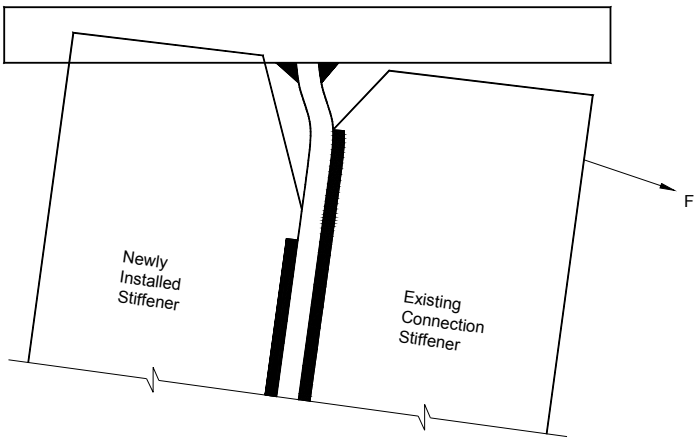

FIGURE 6-37: Schematic Showing Penetration of the Newly Added Stiffener Plate

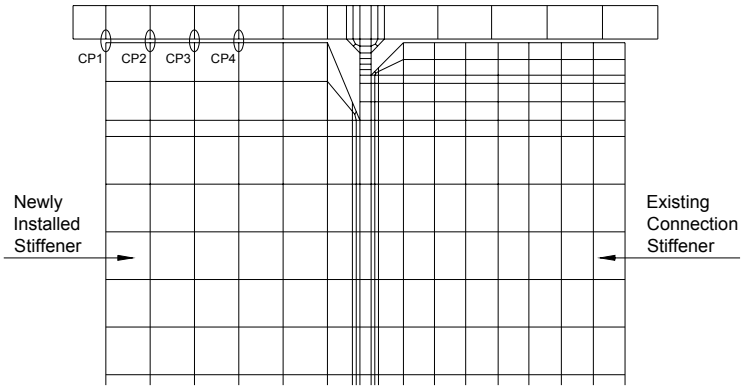

FIGURE 6-38: Coupled Sets Used in Model FM3-p

6.5.2.3 Adding New Stiffener Plate and Removing Truss Members (Model FM3-pr)

Since the current repair method does not successfully reduce the secondary stresses to a satisfactory level, truss chord removal is then considered in addition to the already performed repair method, as modeled by FM3-pr shown in Figure 6-36(d). By using this means of retrofit, stresses can be reduced on average by 87%, 69%, and 83%, respectively, for the highest σ_x, σ_y, and σ_z locations in the web gap. Although the percentage reductions of the corresponding stresses are less than those obtained from the chord removal only repair, all of the

stress range magnitudes are successfully controlled below and close to half of the CAFT of fatigue Detail Category C and C'. As a result, the connection stiffener detail should be able to sustain unlimited number of stress cycles and be free from fatigue cracking after the repair is carried out.

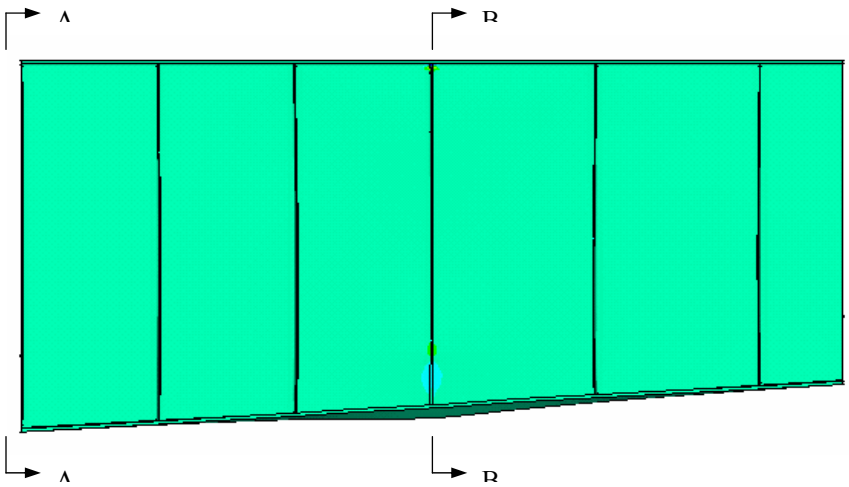

(a) girder elevation

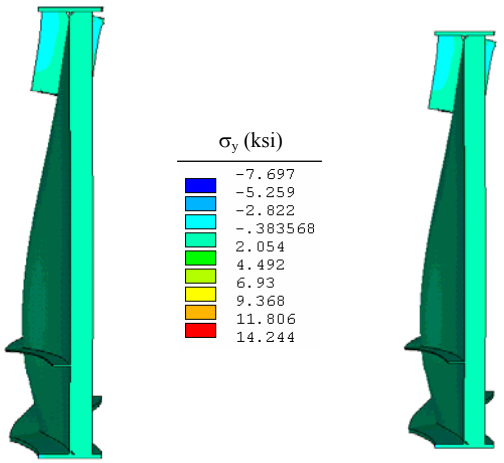

(b) side view (A-A) **(c) connection stiffener section (B-B)**

FIGURE 6-39: Model FM3-p Overall Deformation and □y Stress Distribution for Load Case No. 6

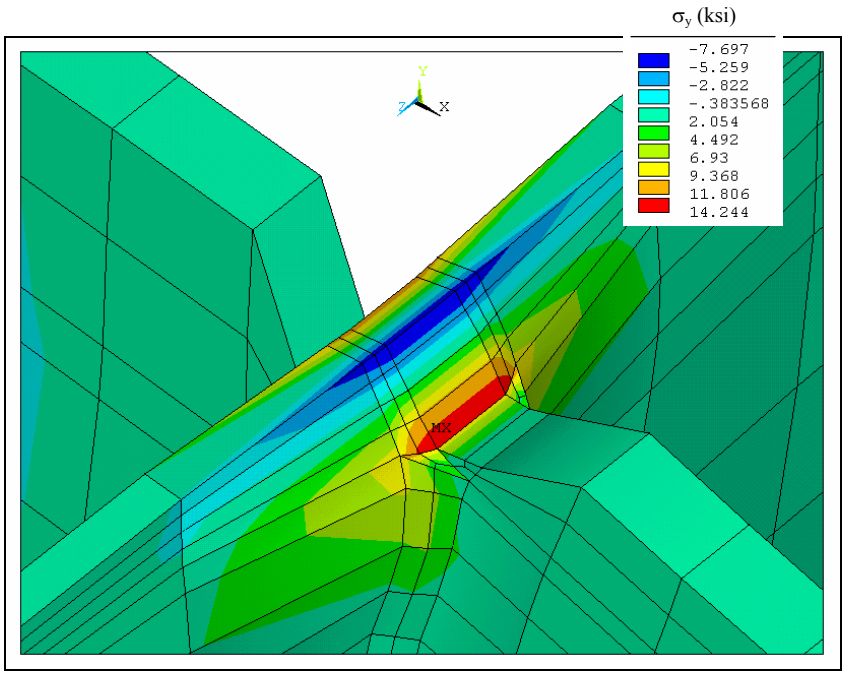

FIGURE 6-40: Model FM3-p Web Gap Stress Contour on the Existing Connection Stiffener Side for Load Case No. 6 (flange elements are hidden)

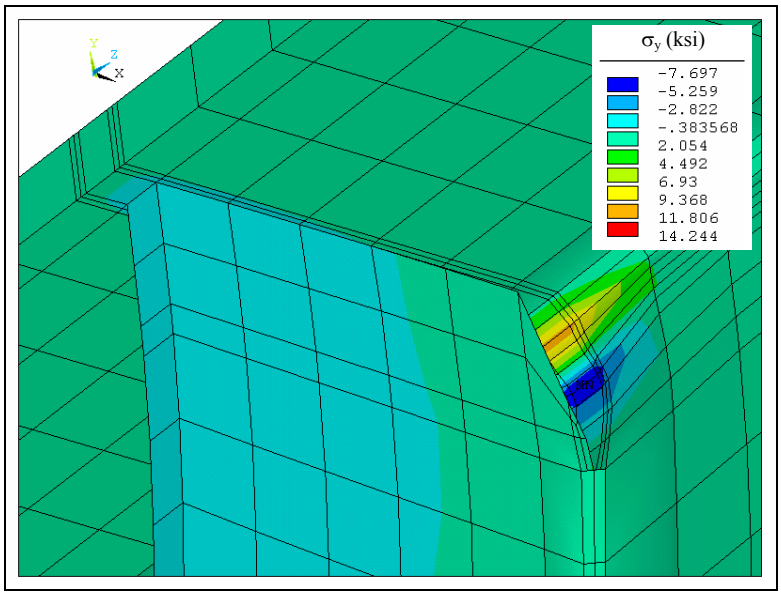

Figure 6-41: Model FM3-p Web Gap Stress Contour on the Newly Installed Stiffener Side for Load Case No. 6

6.5.3 Evaluation of FM3 Model Series

Table 6-5 provides a summary of the maximum web gap stresses obtained from the different repair models and their respective percentage reductions. For illustration purposes, the

out-of-plane displacement and Node A σ_y stress variation of all 16 load cases for the FM3 model series are plotted in Figure 6-42 and 6-43, respectively. Comparison of the web gap stress gradient of the four models is presented in Figure 6-44 and 6-45 for both web surfaces. The effect of chord removal is significant. It is suggested that chord removal be carried out only for the interior floor-beams at the negative moment regions, so the floor trusses at these locations can still lean on the adjacent trusses at the positive moment regions and the bridge piers, and would not rack out of the truss plane during deck replacement. This method thus is recommended to be carried out as a supplementary repair to the negative moment region connections.

TABLE 6-5: Web gap stresses for FM3 model series

	FM3	FM3-p		FM3-r		FM3-pr	
	Maximum Stress (ksi)	Maximum Stress (ksi)	Average Percentage Reduction	Maximum Stress (ksi)	Average Percentage Reduction	Maximum Stress (ksi)	Average Percentage Reduction
σ_x [L.C. No.]	24 [7]	13 [6]	46%	0.55 [5]	98%	3.3 [6]	87%
σ_y [L.C. No.]	20 [7]	14 [6]	34%	2.5 [5]	89%	6.5 [6]	69%
σ_z [L.C. No.]	15 [7]	8.8 [6]	43%	0.50 [5]	97%	2.5 [6]	83%

Note: extreme stresses occur mostly at Load Case No. 5, 6, and 7; percentage reductions are averages of all 16 load cases.

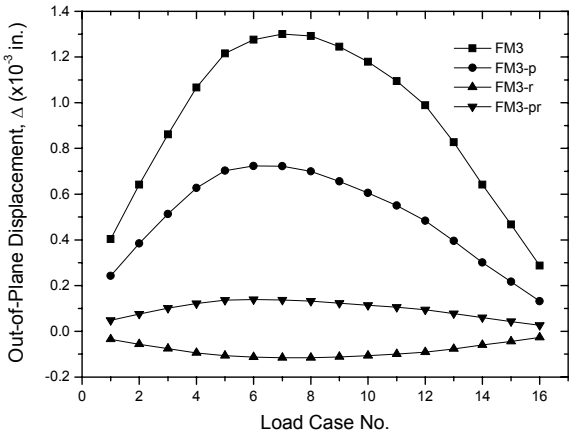

FIGURE 6-42: Variation of Out-of-Plane Displacements for FM3 Model Series

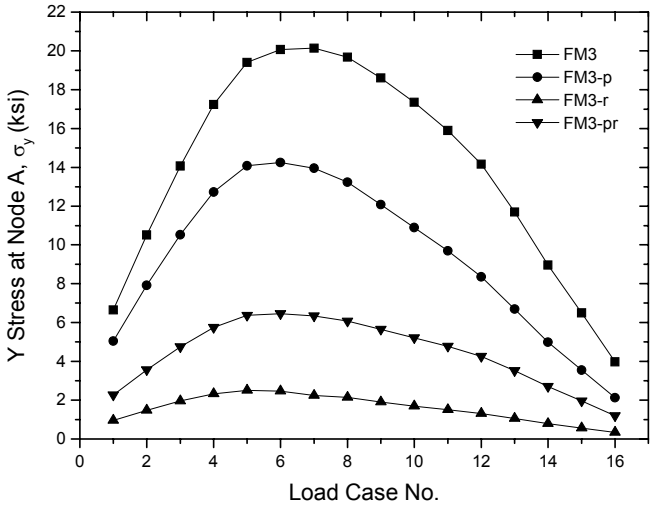

FIGURE 6-43: Node A σ_y Stress Variation for FM3 Model Series

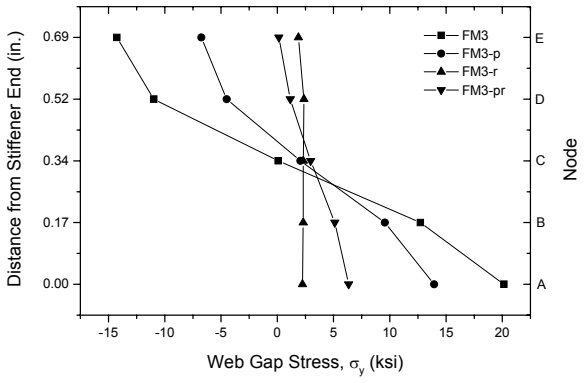

FIGURE 6-44: Load Case No. 7 Web Gap Stress Gradient of FM3 Model Series on the Existing Connection Stiffener Side

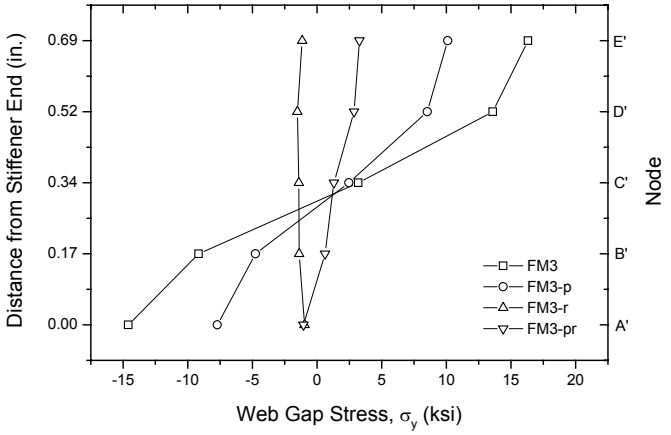

FIGURE 6-45: Load Case No. 7 Web Gap Stress Gradient of FM3 Model Series on the Newly Installed Stiffener Side

6.6 Out-of-Plane Displacement

6.6.1 Definition

Strictly speaking, the out-of-plane displacement Δ should be defined as the differential value between Node A and E transverse displacements:

$$\Delta = \Delta_A - \Delta_E \qquad (6\text{-}1)$$

where Δ_A and Δ_E are X direction translations of Node A and E, as shown in Figure 6-46.

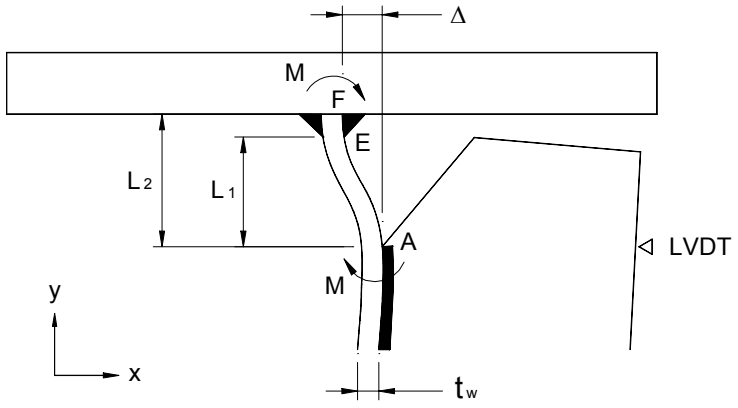

FIGURE 6-46: Dimensions Used for Measurement of Out-of-Plane Displacement and Web Gap Length

However, the displacement of Node A alone is used as out-of-plane displacement in this case study due to the following two reasons. First, in many related experimental studies, the out-of-plane displacement is measured by mounting LVDT (Linear Variable Displacement Transducer) units to the girder top flange and pointing to the outer edge of the connection stiffener at the same elevation corresponding to point A, the bottom of the web gap, as shown in Figure 6-46. It is almost impossible to mount another LVDT at the same location to measure the displacement of point E at the top of the web gap, especially for field test conditions. D'Andrea et al. [2001] did succeed in measuring the differential displacements at the web gap for laboratory testing girders. A special LVDT mounting bracket was used to install the LVDTs, and the connection stiffener end was terminated flat and short of the web gap so that the second LVDT could access the toe of flange-to-web welds. Most of the experimental studies, either conducted in the field or in the laboratory, however, used only one LVDT as shown in Figure 6-46 to measure the out-of-plane displacement, and the displacement obtained from this setup is considered to be equivalent to that of (Δ_A - Δ_F), where Δ_F is the X direction translation of point F at the weld root. Second, the remaining three bridges of this study, the Winfield Bridge, the Hump Yard Bridge, and the Tuttle Creek Bridge, are investigated by shell-to-shell submodeling, where the steel members are modeled all by shell elements and the welds are omitted for simplification purposes. So for these three bridges, the designated web gap length is L_2, as shown in Figure 6-46, and the relative horizontal translation between Node A and F is considered as out-of-plane displacement. In order to keep consistence with the results presented by other research studies and those obtained from the rest three bridges, the differential value between Δ_A and Δ_F is defined as the out-of-plane displacement for the web gap. In this particular case, Δ_F values are extremely small compared to Δ_A and Δ_E for all 16 load cases, so the X direction

deformation of Node A, Δ_A, is specified as the out-of-plane displacement for the Westgate Bridge.

The error caused by using Node A displacement, Δ_A, instead of the differential displacement, (Δ_A - Δ_E), is calculated according to Equation 6-2:

$$Error = \frac{\Delta_A - (\Delta_A - \Delta_E)}{(\Delta_A - \Delta_E)} \times 100\% = \frac{\Delta_E}{(\Delta_A - \Delta_E)} \times 100\% \qquad (6\text{-}2)$$

The average percentage error of all 16 load cases is 15.5% for Model FM1 and 15.1% for Model FM3. This indicates that the influence of Δ_E should not be neglected. However, both Δ_A and (Δ_A - Δ_E) are very small values, and the choice of either Δ_A or (Δ_A - Δ_E) as out-of-plane displacement really does not affect the other parameters much, except when used for Fisher's $\sigma - \Delta$ expression as will be discussed in section 6.6.2. Both Δ_A and (Δ_A - Δ_E) are reasonable displacement values when used to describe the nature and characteristics of out-of-plane distortion. For example, the maximum Δ_A experienced by FM1 model is 1.6×10^{-3} in., and the maximum (Δ_A - Δ_E) of this model is 1.4×10^{-3} in. Both fall into the range of normal distortion measurements of less than 4×10^{-3} in. [NCHRP 336, 1990]. Therefore, the adoption of Δ_A for out-of-plane displacement is considered acceptable for this case study.

6.6.2 Fisher's $\sigma - \Delta$ Expression

For the conditions of web gap distortion shown in Figure 6-46, a relationship between the web gap stress σ and the out-of-plane displacement Δ is established by Fisher [1998] as illustrated by Equation 6-3:

$$\sigma = \frac{M y_c}{I} = \frac{6EI\Delta}{L^2}\left(\frac{t_w}{2}\right)\left(\frac{1}{I}\right) = \frac{3E\Delta t_w}{L^2} \qquad (6\text{-}3)$$

where:

σ = web gap bending stress (ksi)

M = web gap bending moment (Kips-in.)

y_c = distance from neutral axis to extreme fiber (in.)

I = moment of inertia (in.^{4})

E = Young's modulus (ksi)

L = web gap length (in.)

Δ = out-of-plane displacement (in.)

t_w = web thickness (ksi)

This equation assumes that the web gap is subjected to double curvature due to transverse displacement Δ. It is important that the use of web gap length and the out-of-plane displacement should be consistent. In this bridge, the differential displacement between A and E is available, so $\Delta = (\Delta_A - \Delta_E)$ and $L = L_1$. For the other three bridges, $\Delta = \Delta_A - \Delta_F$ and $L = L_2$. Table 6-6 shows the comparison of web gap stresses calculated by using Fisher's formula and obtained directly from ANSYS solution for the Westgate Bridge.

TABLE 6-6: Web Gap Stress Comparison for Load Case No. 7

Model	Out-of-Plane Displacement, Δ (in.)	Fisher $\sigma=3E\Delta t_w/L^2$ (ksi)	ANSYS σ_y (ksi) @ Node			
			A	E	A'	E'
FM1	1.4×10^{-3}	± 97	25	-18	-18	20
FM3	1.1×10^{-3}	± 76	20	-14	-15	16

Note: $t_w = {}^3/_8$ in., L = $^{11}/_{16}$ in., E = 29000 ksi.

The out-of-plane bending stresses yielded by Fisher's expression are apparently too high to be reasonable results. The effectiveness of Equation 6-3 for web gap stress approximation will be further discussed when the analysis of the other three bridges are carried out. Based on the data of Table 6-6, for this bridge a factor of 0.26 can be applied to the Fisher's formula to

reduce the stresses close to the ANSYS results.

6.7 Summary

This chapter presented findings from the finite element analysis of distortion-induced fatigue cracking and pertinent retrofit at connection stiffener details of the Westgate Bridge. Results obtained from this study are summarized as follows:

1. Both the positive and negative moment region model analyses indicated severe stress concentration at the connection stiffener ends close to girder top flanges. The unstiffened web gaps were exposed to stress ranges higher than the fatigue limits and were therefore vulnerable to fatigue cracking. Before crack started to form at the web gap, the area of girder web affected by out-of-plane distortion is within 5 inch on each side of the connection stiffener.
2. The upper chords of the truss frames directly caused the out-of-plane distortion. The retrofit analysis showed that fatigue stresses could be completely eliminated if these members had been removed. However, removal should be performed with caution so that lateral stability of the truss system is guaranteed.
3. In terms of stress reduction, the current repair used at the positive moment region connections for the Westgate Bridge is satisfactory, though the quality of repair welds is a concern and needs to be checked frequently. The repair method performed at the negative moment region connections is not successful; therefore additional chord removal is required. It is expected that an infinite fatigue life can be achieved at all floor-beam to girder connections when this additional repair is performed.
4. About 15 percent error can be resulted from neglecting the effect of differential displacement of the web gap for calculation of out-of-plane displacement. Web gap stress calculated by Fisher's expression does not match the actual stress condition in the bridge.

5. It is recommended that field experiments be performed in the future research in order to measure the stress ranges at the web gaps caused by the actual traffic loading, to verify the effect of the proposed repairs, and to compare the results with what have been obtained from the finite element study.

Chapter 7

Case Study 3: The Winfield Bridge

The Winfield Bridge developed web gap fatigue cracks in the tension zone near the bottom flange of the girder positive moment region. The affected diaphragm-girder connections were repaired by installing additional reinforcing splice plates to the girder web and attaching connection stiffeners to the girder flanges. No structural modification was performed for similar details in the bridge that have not developed fatigue cracking. Concerns are that these details may also be subjected to high magnitude fatigue stresses so that cracks may occur at a later time if the condition is left unchanged. The investigation carried out in this case study focuses on the web gap stress evaluation of typical diaphragm-girder connections. The objectives are to locate the potential crack initiation sites in the bridge, to verify the effectiveness of the existing repair method used for the girder repair, and to provide additional retrofit recommendations in order to inhibit crack occurrence at other diaphragm-girder connections.

7.1 Bridge Structure and Fatigue Cracking

The Winfield Bridge was built in 1972 crossing the Walnut River in Winfield, Kansas. It is composed of two parallel structures carrying US-77 southbound and northbound. The southbound bridge [KDOT Bridge No. 77-18-16.65(009)] has a four-girder/floor-beam/stringer superstructure configuration. The northbound bridge [KDOT Bridge No. 77-18-16.66(074)] has a four-girder/diaphragm system. Both structures are noncomposite and have a skew of 28°-39'-16". The bridge elevation is shown in Figure 7-1. Span No. 3 (125 ft) is the longest of the five continuous spans of the bridge.

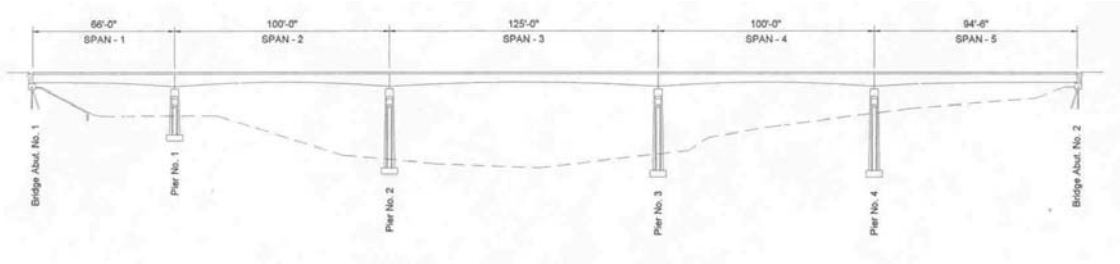

FIGURE 7-1: Elevation of the Winfield Bridge

During the 1996 bridge inspection, web gap fatigue cracks were observed at two diaphragm-girder connections in Span No. 3 of the northbound bridge. The framing plan (Figure 7-2) has a staggered diaphragm arrangement. Both Crack Location No. 1 and 2 were located in the mid-span of Girder G3 close to the bottom flange and were thus subjected to high magnitude of both in-plane and out-of-plane bending moments. The connection stiffeners used at these two locations were welded to the top flange, but not to the bottom flange, so cracks were not seen at the top flange web gaps. Figure 7-3 shows the crack exposure on web surfaces at Location No. 1 using dye penetrant. Figure 7-4 shows schematically the observed crack shape and size of the same detail. Both the horseshoe and the horizontal cracks were identified to have gone through the web thickness. Since the cracks were developed at the stiffener to bottom flange connections and at the mid of the longest span of the bridge, the affected web gap areas were exposed to high tensile flexural stresses which could cause the cracks to propagate continuously upward through the girder depth. The cracking condition of this bridge is thus more severe than those found near the girder top flanges such as seen in the Westgate Bridge.

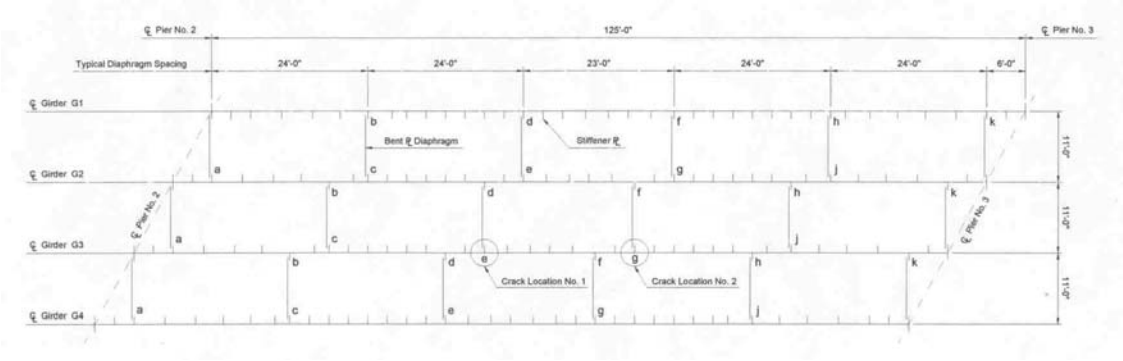

FIGURE 7-2: Span No. 3 Framing Plan and Crack Locations of the Northbound Winfield Bridge

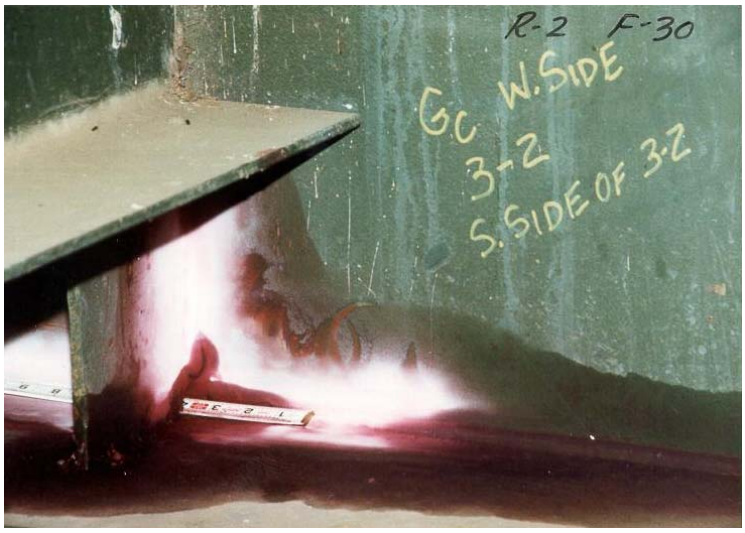

(a) cracks on the interior girder web side

(b) cracks on the exterior girder web side

FIGURE 7-3: Inspection Pictures of Crack Location No. 1

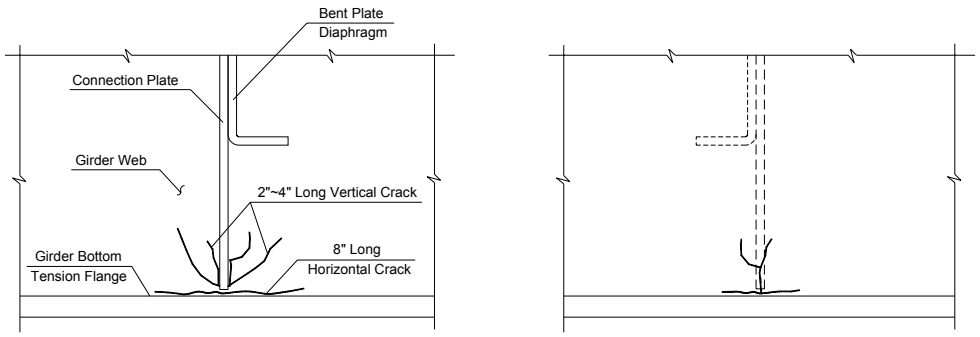

(a) Crack Shape on Diaphragm Side

(b) Crack Shape on No Diaphragm Side

FIGURE 7-4: Crack Shape and Size Observed at Location No. 1

Figure 7-5 shows the cross section of the northbound Winfield Bridge. From east to west (right to left in the figure) the roadway widths are a 10 ft shoulder, two 12 ft traffic lanes, and a 6 ft 4 in. median connecting to the southbound bridge. The current bridge AADT (annual average daily traffic) is 6,970 and the percentage of truck traffic is 11%. The concrete slab is 9 in. thick with compressive strength f_c' of 4000 psi. All plate girders, diaphragms, and stiffeners were fabricated from ASTM A36 steel.

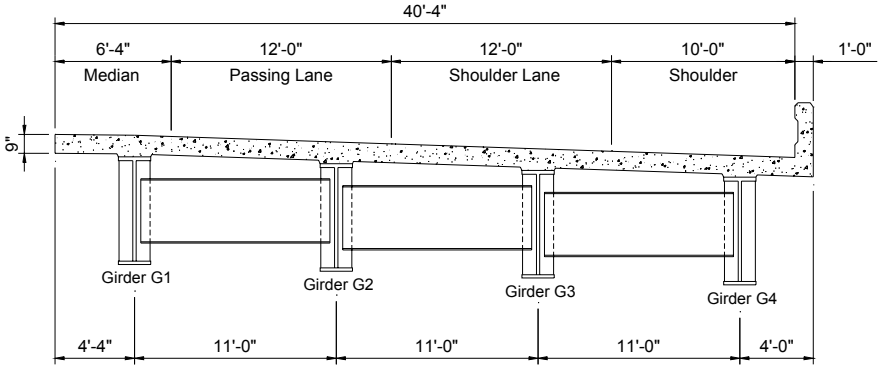

FIGURE 7-5: Cross Section of the Northbound Winfield Bridge
(looking north)

7.2 Evaluation of KDOT Repair Approach

The two crack locations were repaired by KDOT in 1998 using a reinforcing detail shown in Figure 7-6. The complete repair procedure for Girder G3 was carried out as follows:

1. Remove and salvage the bent plate diaphragm for reattachment by detaching the diaphragm to stiffener welds. Remove the existing connection stiffener and grind the remaining weld material from web and top flange.
2. Drill a $^{15}/_{16}$ in. diameter repair hole through the web plate at the end of each horseshoe crack.
3. Drill $^{15}/_{16}$ in. diameter bolt holes in web and bottom flange using the web and flange splice plates as templates. Remove all paint from the existing girder surfaces at the web and bottom flange splice locations. Paint these areas with organic zinc primer. Also paint the contact surfaces of the web and flange splice plates with organic zinc primer.
4. Install new splice plates to girder web and bottom flange. Weld new stiffeners to girder web, top flange, and bottom flange splice plates.
5. Weld the existing diaphragm back to the new connection stiffener.

Unlike the original A36 steel used in the bridge, the newly fabricated splice and stiffener plates used for the girder repair are made of ASTM A709 Grade 36 steel. This repair method not only enhanced the girder cross section and stiffened the web gap area at the crack locations, but provided fatigue resistance of Detail Category B to the web and bottom flange using bolted connections. Chances of crack reinitiation at these two locations are very little with such a conservative repair. In fact, to some extent the repaired girder sections could be considered as overly strengthened, as the stiffener installed on the no-diaphragm side is apparently not necessary. The one used on the other web side for diaphragm connection has already been required to be welded to both girder flanges, which should have provided sufficient resistance to the out-of-plane distortion for the repaired details.

However, since no structural corrections were made to the other diaphragm-girder connections that have the same unstiffened web gap details, those areas are still exposed to high cyclic fatigue stresses and remain as potential sites for future crack development. The repair method proposed by Figure 7-6 is expensive if applied to every diaphragm-girder connections. Therefore, it is necessary that certain preventive measures be taken at those intact but crack-prone details before fatigue cracking finally develops.

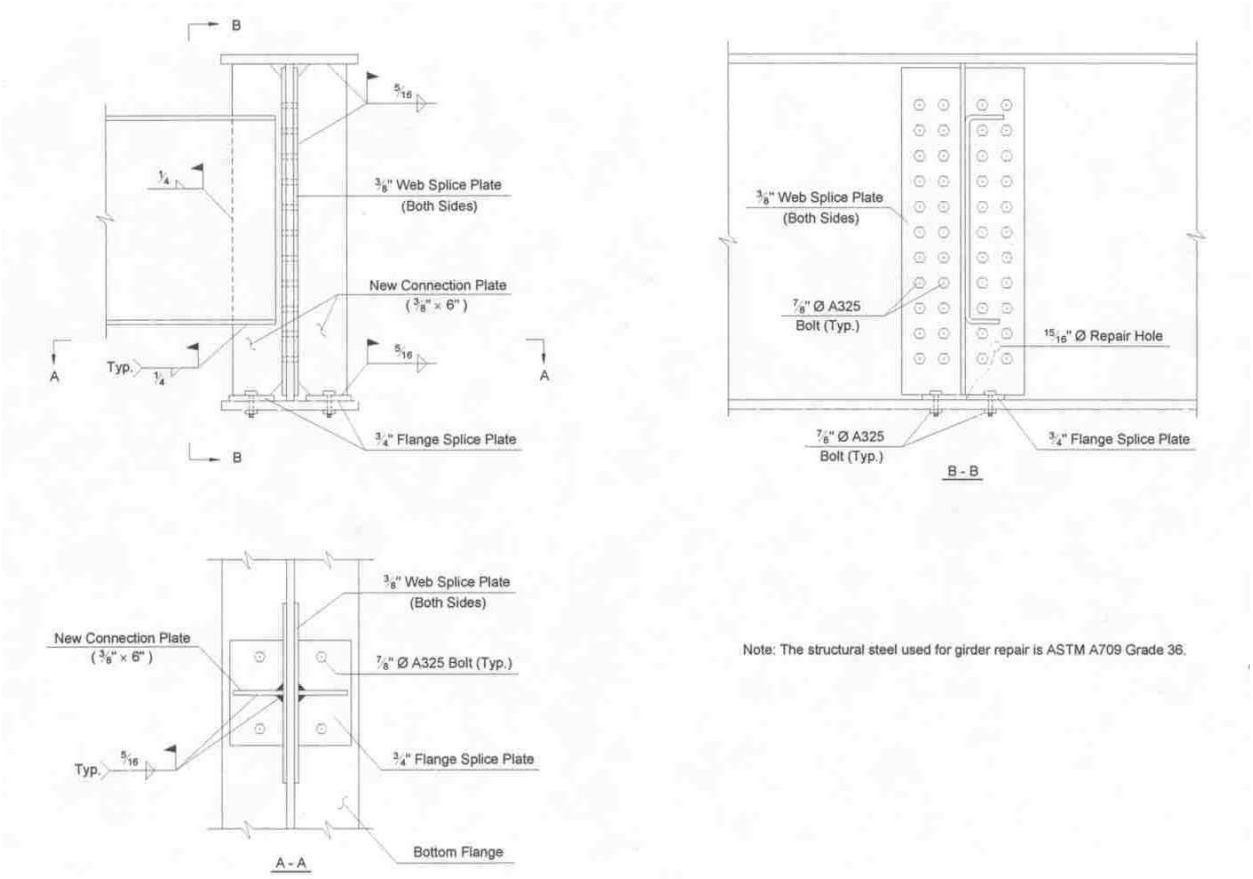

FIGURE 7-6: Crack Repair Details of the Winfield Bridge

7.3 Finite Element Investigation

Submodeling is performed to study the web gap stresses at the diaphragm-girder connections of the Winfield Bridge. As shown in Figure 7-2, for each girder, the connection stiffener locations are marked by a, b, c, d, e, f, g, h, j, and k on the framing plan from Pier No. 2 to No. 3. The

diaphragm-girder connections are thus specified accordingly combining the girder number and the connection stiffener label during the investigation. For example, connection "3e" refers to Crack Location No. 1 and "3g" refers to Crack Location No. 2. The crack susceptible connections of all four girders in Span No. 3 are investigated at the submodel level in order to clearly identify the fatigue stresses developed in the bridge due to the unstiffened web gap details. For issues regarding modeling techniques and fatigue evaluation procedures, see Chapters 4 and 5.

7.3.1 Coarse Model Analysis

As shown in Figure 7-7, the coarse model is constructed including all the superstructure members of Span No. 3. It contains 13,381 elements and 15,338 nodes. A typical girder section of the coarse model is shown in Figure 7-8. The deck slab is modeled by 8-node brick elements (ANSYS Solid 45). The girder, diaphragm, and stiffener plates are modeled by 4-node shell elements (ANSYS Shell 181). Coincident nodes at the top flange and bottom deck slab contact surfaces are coupled for transverse (X) and vertical (Y) DOFs, but not for the longitudinal (Z) DOFs so that the model can behave noncompositely. The end of girder span is assumed fixed to approximate the actual continuous support provided to the bridge at Pier No. 2 and No. 3, so the flange and web nodes on the girder end sections are restrained in all DOFs. Figure 7-9 shows the girder flange, web, and stiffener plate dimensions used for the modeling. Notice that the flange width changes at the field splice location and the web depth varies continuously along the girder length. Figure 7-10 shows the geometry of the bent plate diaphragms. The transverse intermediate stiffener and the transverse connection stiffener to girder flange attachment of this bridge is designed the same as shown in Figure 7-11. The stiffeners are welded to the top flange at girder section "A" and are welded to the bottom flange at girder section "B". Figure 7-12

shows the designated range of section “A”, “B”, and “C” within the girder span. This arrangement indicates that during the original design the transverse stiffeners were required to be welded only to the girder compression flange, i.e., the top flange at the positive moment region “A” and the bottom flange at the negative moment region “B”. Therefore, the stiffeners are not connected to the bottom flange at the positive moment region “A”, the top flange at the negative moment region “B”, and both the top and bottom flanges at the transition region “C”. In order to simplify the coarse model construction, all the stiffener-to-flange interfaces are modeled as fully connected, which literally eliminates the web gap geometry in the coarse model. Because the unstiffened web gaps are highly localized details, excluding them from the coarse model has little effect on the global behavior of the bridge structure. Loading is applied using an HS15 fatigue truck. The truck is placed at the center of the shoulder lane and moved from Pier No. 2 to Pier No. 3 for a total of 20 load cases. Figure 7-12 shows the truck moving direction and the wheel load position for Load Case No. 1. The intervals between adjacent load cases are 6 ft. Figure 7-13 shows, for example, the overall structure deflection of Load Case No. 3 and No. 15 based on the coarse model analysis results.

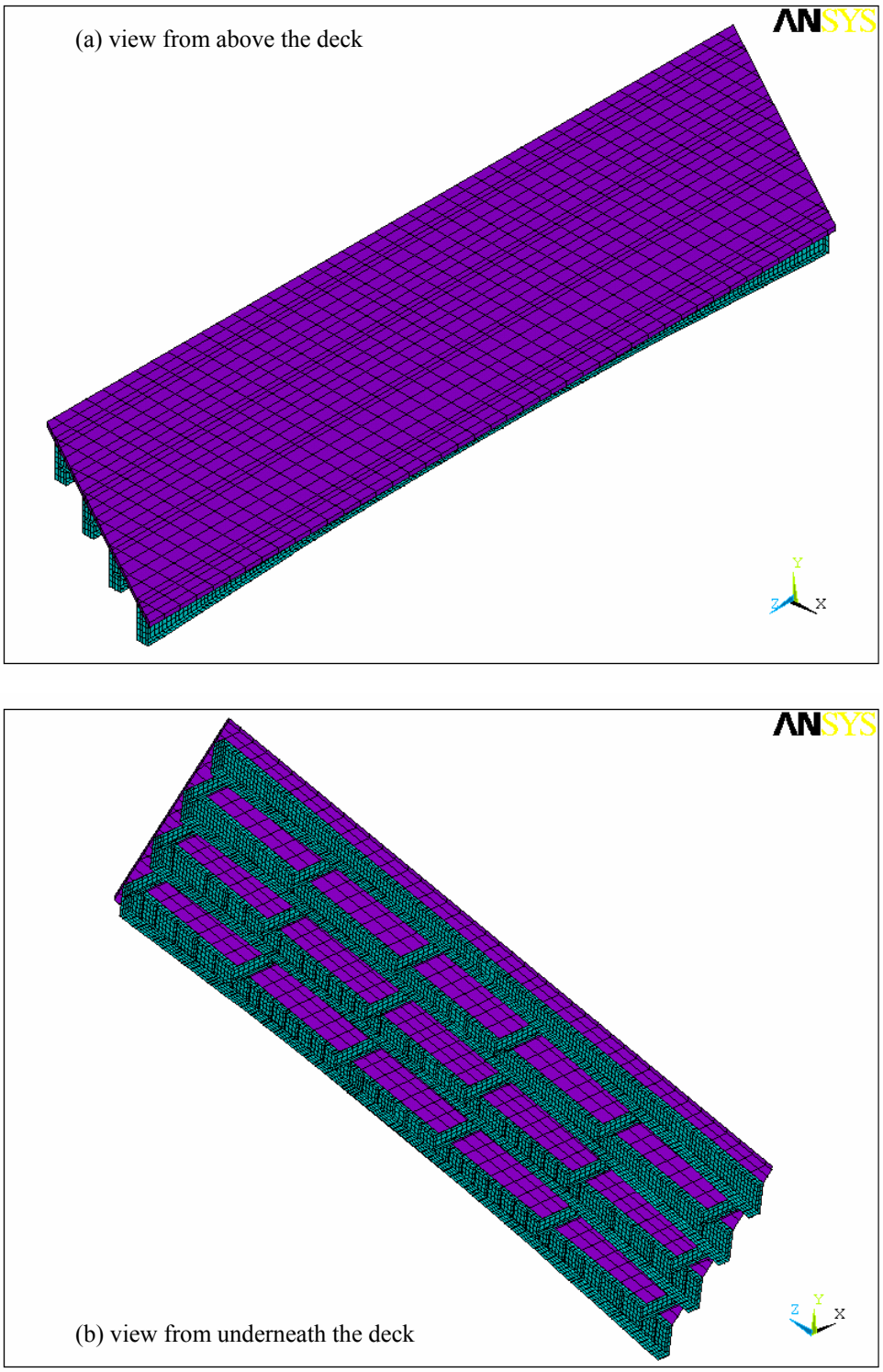

FIGURE 7-7: Coarse Model for Span No. 3 of the Northbound Winfield Bridge

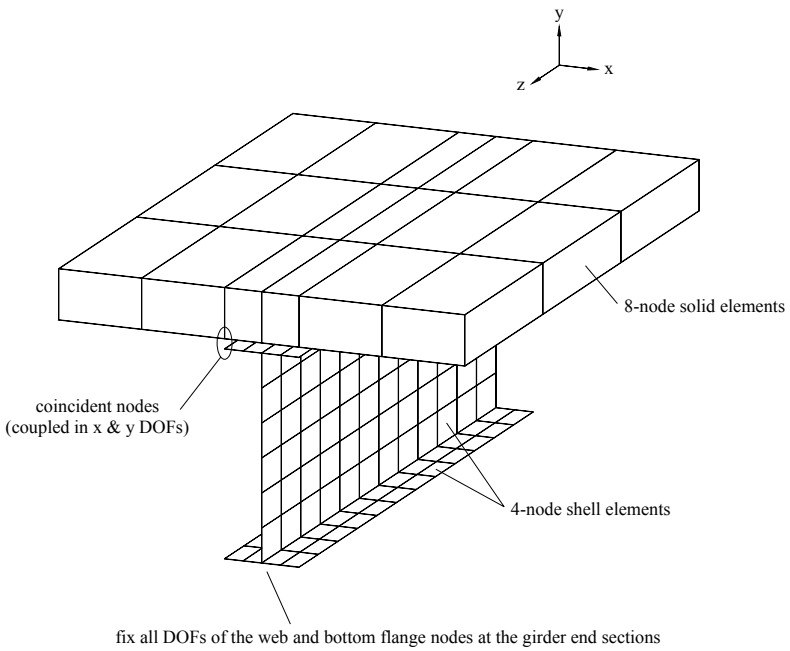

FIGURE 7-8: Typical Girder Section of the Coarse Model

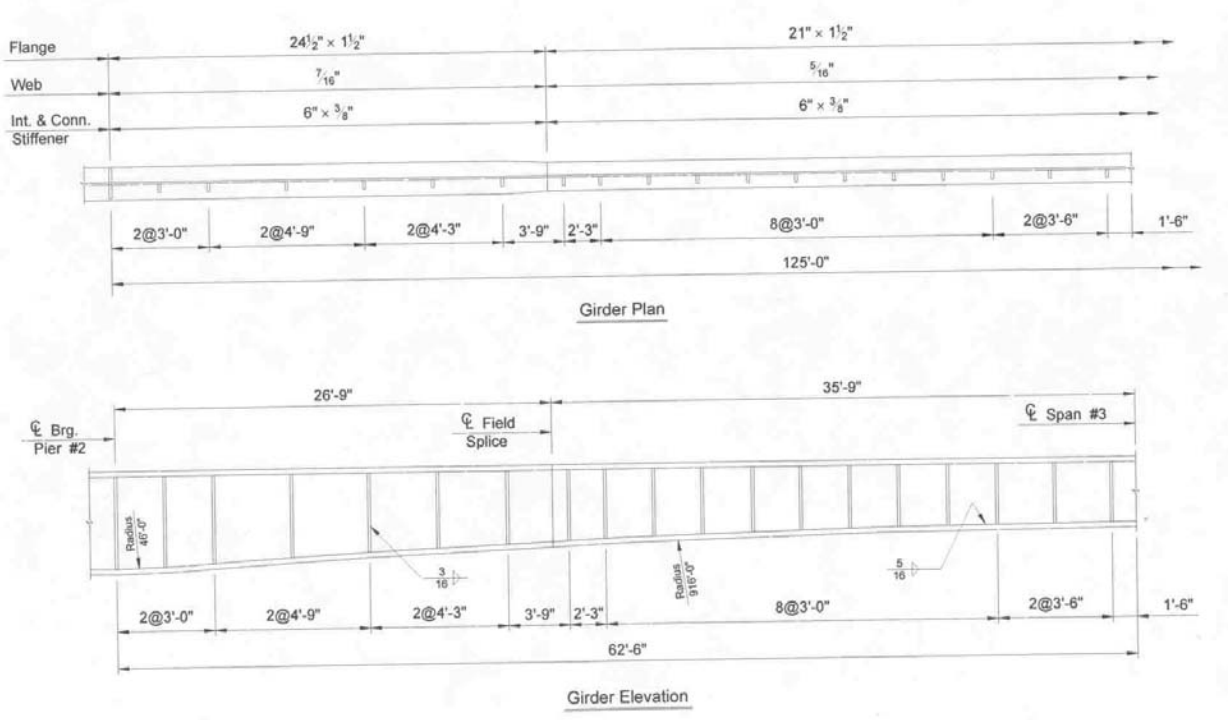

FIGURE 7-9: Half Span Girder Plan and Elevation

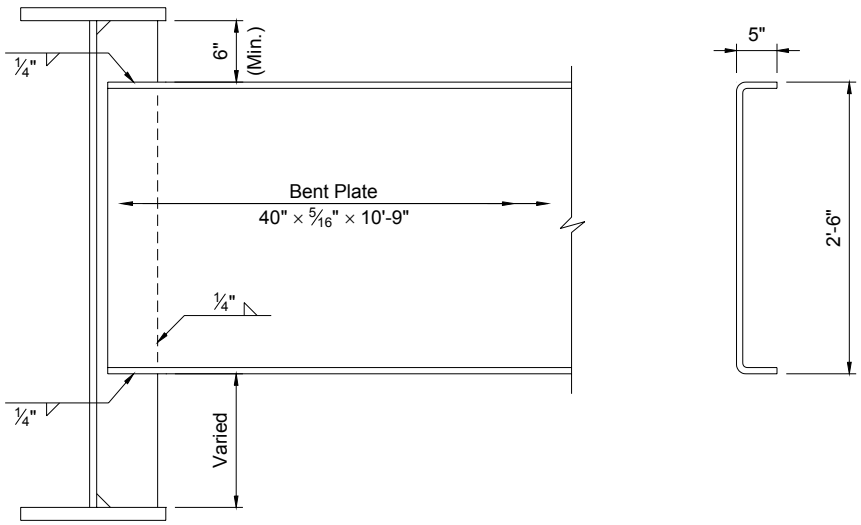

FIGURE 7-10: Intermediate Diaphragm Detail

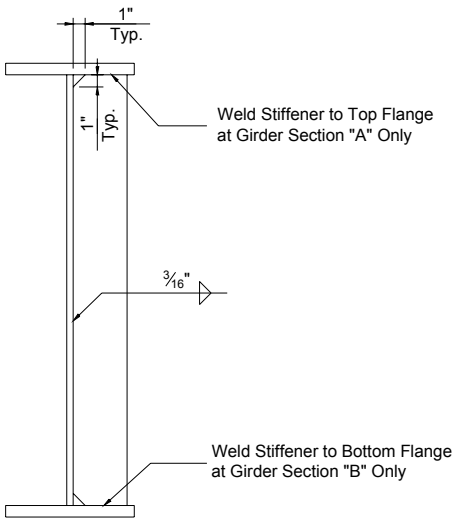

FIGURE 7-11: Intermediate Stiffener Detail

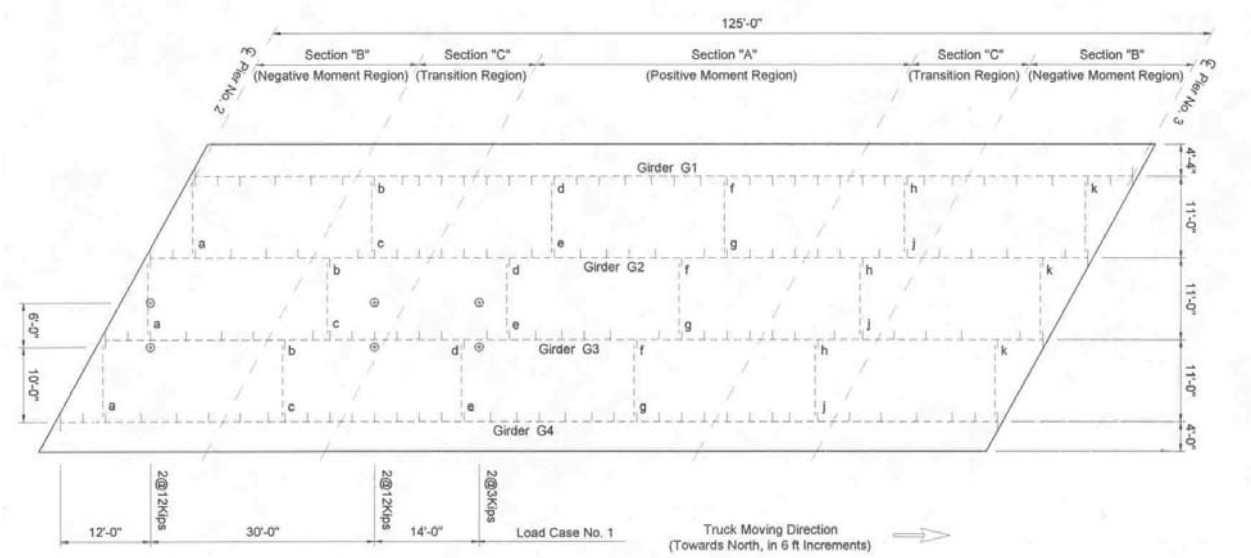

FIGURE 7-12: Truck Position of Load Case No. 1 and Girder Section A, B, and C

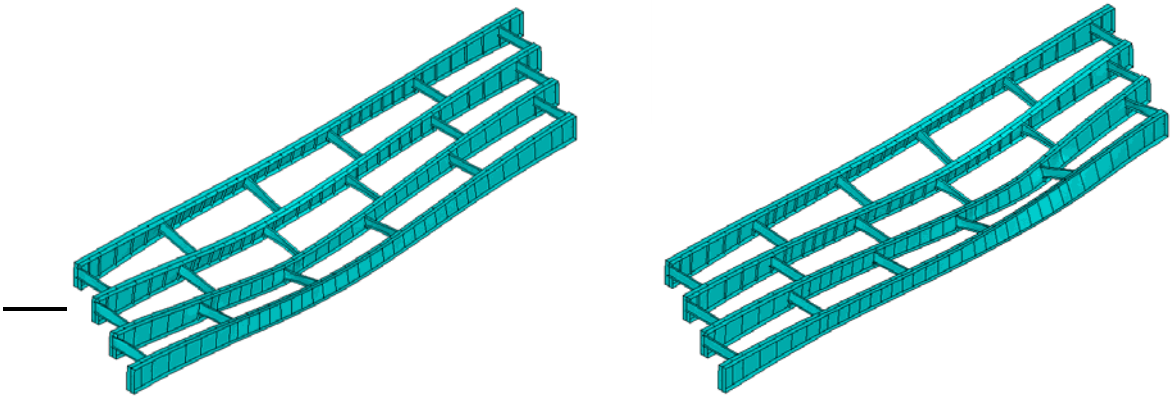

(a) load case No. 3 **(b) load case No. 15**

Figure 7-13 Coarse model deformation (deck elements are hidden)

7.3.2 Submodel Analysis

7.3.2.1 Details of Interest

Submodeling is then performed to investigate the local stress distribution at the unstiffened web gap regions. Figure 7-14 shows the submodel dimension and its correlation with the coarse model. The same cut boundary dimension is also used for the submodels built including the top flange web gap details. Table 7-1 summarizes the overall submodel characteristics of the Winfield Bridge. Altogether 13 diaphragm-girder connections of Span No. 3 are selected and 17 submodels are constructed for web gap stress evaluation. For connections 3b, 3c, 3j, and 3k in the transition region, submodel analysis is carried out for the unstiffened web gap details at both the top and bottom flanges. The element and node number of each submodel are between 4,000 and 6,000.

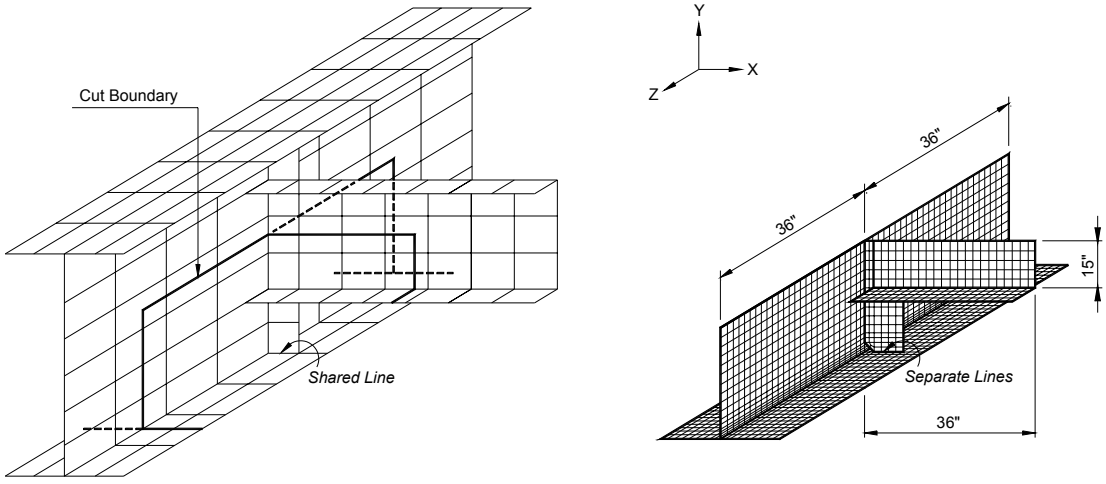

FIGURE 7-14: Submodel with Web Gap Geometry

TABLE 7-1: Girder-Diaphragm Connections Selected for Submodel Study

Connection	Web Gap Location at Top/Bottom Flange	Girder Section	Moment Region	Submodel Size	
				Node #	Element #
3a, 3k	Top	"B"	Negative	4544	4378
3b, 3j	Top	"C"	Transition	4595	4428
	Bottom			5876	5694
3c, 3h	Top	"C"	Transition	4507	4335
	Bottom			5634	5449
3d	Bottom	"A"	Positive	4756	4587
1f, 2f, 3e, 3f	Bottom	"A"	Positive	4674	4506
3g, 4g	Bottom	"A"	Positive	4838	4668

Figure 7-15 shows the mesh grid points specified for web gap stress evaluation. Since all the steel members are modeled using shell elements in this bridge, the plate thickness shown in the figure is fictitious and is only used in order to indicate the grid point designation on both sides of the girder web. To distinguish from those actual nodal grid points shown in Figure 6-11 for the Westgate Bridge, the locations of interest in this case study are called, for example, Points A, B, C, instead of Nodes A, B, C. Point A and A' in Figure 7-15 are actually one node located at the mid surface of the web thickness. However, the ANSYS postprocessor is capable of generating stress solutions on both shell surfaces at the same node, taking into account the plate thickness and bending effect. So Point A and A' can have different stress values. For either top or bottom flange submodels, Point A and A' are the stiffener-to-web connection end of the web gap, and Point E and E' are the flange-to-web connection end of the web gap. Point A to E are on the stiffener side of the girder web and Point A' to E' are on the no-stiffener side of the girder

web. Point E', E'1 to E'10, and E"1 to E"10 are along the flange-to-web connection on the no-stiffener web side. Since the fillet weld is neglected for simplification purposes, the web gap length of the submodel is 1 in.

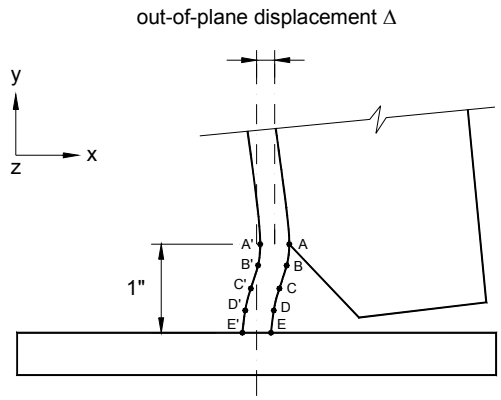

(a) Grid points specified within bottom flange web gap

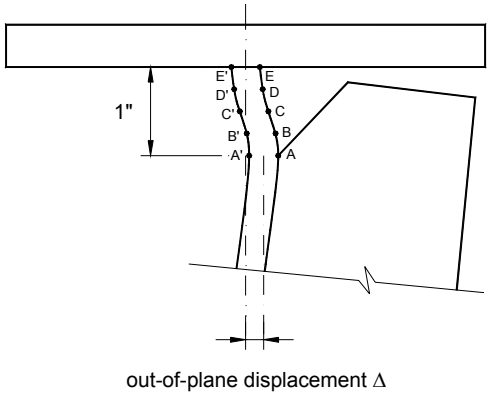

(b) Grid points specified within top flange web gap

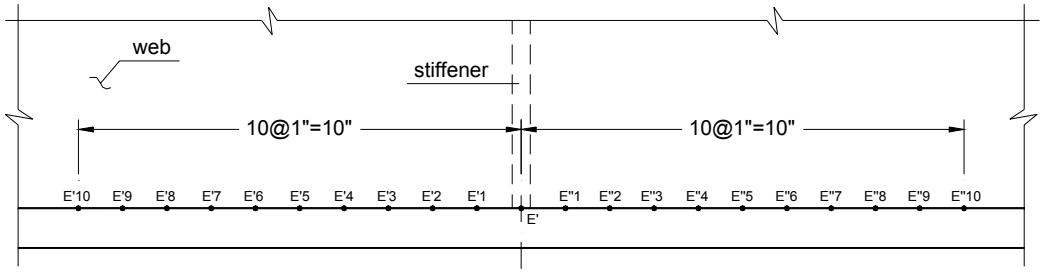

(c) Grid points specified along the bottom-flange-to-web connection on the no-stiffener web side

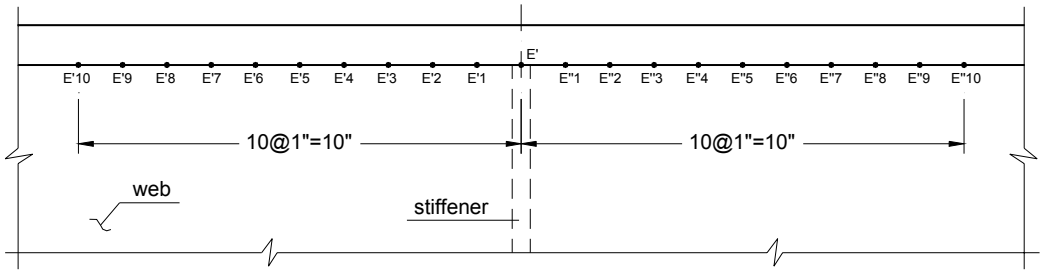

(d) Grid points specified along the top-flange-to-web connection on the no-stiffener web side

FIGURE 7-15: Grid Points Specified for Web Gap Stress Evaluation

The overall element mesh size of the submodels is limited to no greater than 1 in. In particular, within the web gap length, the element size is reduced to ¼ in. in order to properly describe the stress gradient caused by out-of-plane distortion. The out-of-plane displacement, Δ, is specified using relative X-axis translation between Point A and E.

7.3.2.2 Comparison of Web Gap Stresses Developed at Mid-Span Diaphragm-Girder Connections of the Four Main Girders

For each of the four girders, a diaphragm-girder connection close to the girder mid-span is selected for submodel analysis, in order to compare the web gap stresses developed at the similar details of the different girders. The connections chosen for study are 1f, 2f, 3g, and 4g. The unstiffened web gaps of these four connections are all located at the girder bottom flanges, so the grid points specified in Figure 7-15(a) and (c) are used for discussion of the finite element solution. To perform the submodel analysis, cut boundary DOF interpolation needs to be carried out for each submodel and for all 20 load cases. In most cases, the maximum web gap σ_y stress occurs at Point E', corresponding to the horizontal cracks along the flange-to-web welds, and the maximum web gap σ_x and σ_z stresses occur at Point A, corresponding to the vertical and horseshoe cracks along the stiffener-to-web welds.

Figure 7-16 shows the σ_y stress variation corresponding to different load cases of Point E' for the four submodels. The letter "b" in the parenthesis is added to the legend to make it clear that these submodels are built for bottom flange unstiffened web gaps. The σ_y stresses of Point A on the other side and the other end of the web gap are plotted in Figure 7-17. Comparing the curves shown in Figures 7-16 and 7-17, it is noticed that the σ_y stress at Point A is less than 50% that of Point E' for all four girders and at all 20 load cases. Figures 7-18 and 7-19 show the stress variation of Point A for σ_x and σ_z, respectively. An overview of Figures 7-16

to 7-19 shows that, of the four diaphragm-girder connections under investigation, 2f and 3g are exposed to significant magnitude of stress fluctuation, while 1f and 4g hardly experience any stress change during the entire truck movement. Since the connections are selected from the four girders at similar locations, it can be concluded that only the two interior girders of the bridge, G2 and G3, are subjected to out-of-plane distortion-induced fatigue. Cracks due to secondary stresses are not expected to occur at the two exterior girders, G1 and G4.

TABLE 7-2: Maximum Web Gap Stresses for Mid-Span Girder Connections

Connection	1f (b)	2f (b)	3g (b)	4g (b)	AASHTO Fatigue Detail Category	CAFT
Girder	G1	G2	G3	G4		
Moment Region	Positive	Positive	Positive	Positive		
Girder Section	"A"	"A"	"A"	"A"		
$\sigma_{x, max}$	0.44 ksi	6.7 ksi	11 ksi	1.5 ksi	C'	12 ksi
	L.C. # 4	L.C. # 9	L.C. # 9	L.C. # 9		
	Point A	Point A	Point A	Point A		
$\sigma_{y, max}$	1.1 ksi	22 ksi	37 ksi	4.9 ksi	C	10 ksi
	L.C. # 4	L.C. # 9	L.C. # 9	L.C. # 9		
	Point E'	Point E'	Point E'	Point E'		
$\sigma_{z, max}$	0.47 ksi	8.1 ksi	13 ksi	2.1 ksi	C'	12 ksi
	L.C. # 4	L.C. # 9	L.C. # 8	L.C. # 9		
	Point A	Point A	Point A	Point A		

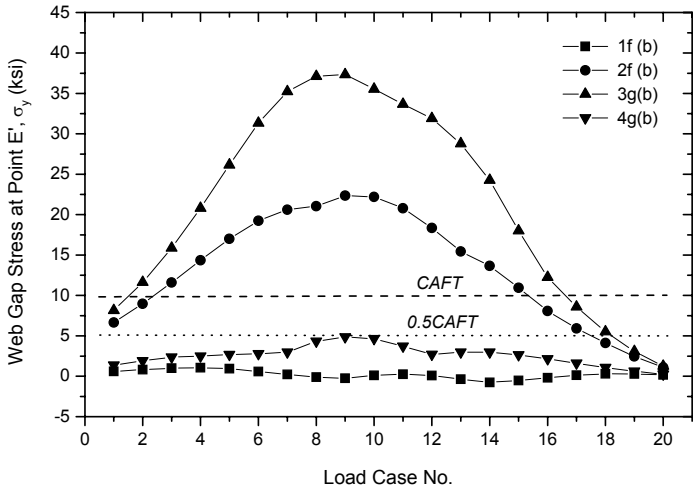

FIGURE 7-16: Point E' σ_y Stress for Mid-Span Diaphragm-Girder Connections

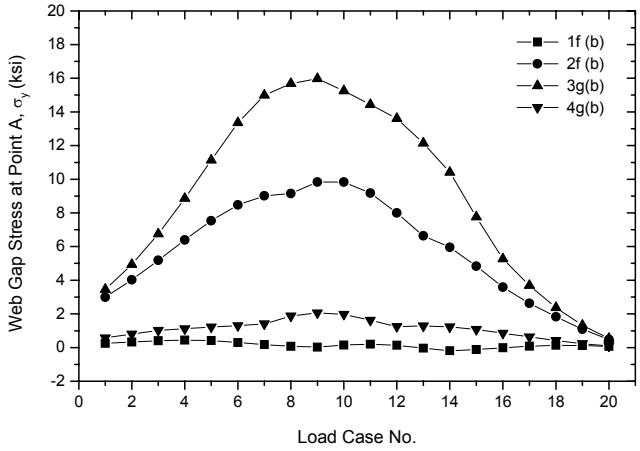

FIGURE 7-17: Point A σ_y Stress for Mid-Span Diaphragm-Girder Connections

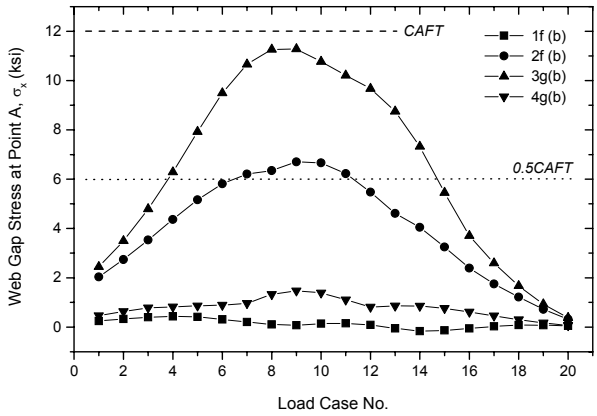

FIGURE 7-18: Point A σ_x Stress for Mid-Span Diaphragm-Girder Connections

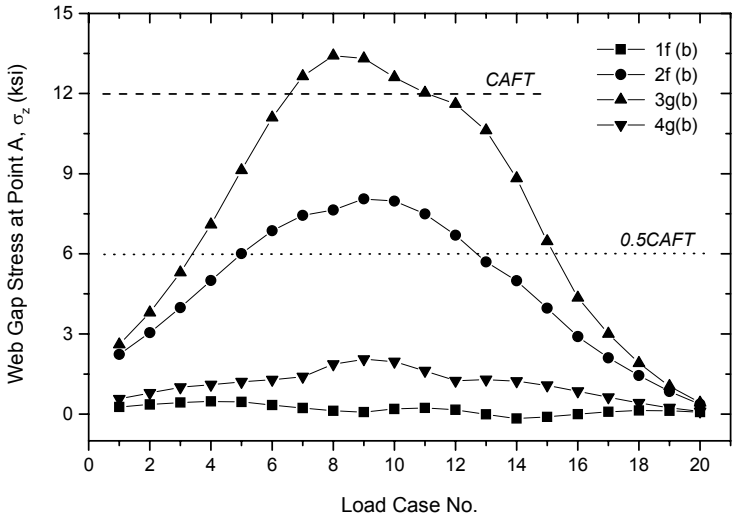

FIGURE 7-19: Point A σ_z Stress for Mid-Span Diaphragm-Girder Connections

The maximum web gap σ_x, σ_y, and σ_z stresses of these four connections are summarized in Table 7-2. The stress range for each detail is defined using the maximum stress value, as the minimum stress is always close to zero. For connections 1f and 4g, the maximum stresses in X, Y, and Z directions are all lower than ½ CAFT, so the diaphragm-girder connections of Girder G1 and G4 are safe even with the web gaps left unstiffened. The maximum σ_x and σ_z stresses of connections 2f and 3g are close to or lower than the CAFT, but higher than ½ CAFT. The maximum σ_y stresses of these two details are much higher than the CAFT. Thus, the diaphragm-girder connections of Girder G2 and G3 are extremely susceptible to web gap fatigue cracking. In particular, stresses developed in connection 3g are higher than those in connection 2f, so Girder G3 is under a more critical situation than G2. In fact, the two locations in the bridge that have already developed fatigue cracks are located at connections 3e and 3g. Based on the above observation, all the diaphragm-girder connections of Girder G3 are therefore studied at submodel level in order to gain full understanding of the web gap stress condition developed in the

Winfield Bridge. The corresponding analysis results are presented in Sections 7.3.2.3 and 7.3.2.4, respectively, for bottom and top flange web gap details.

7.3.2.3 Submodel Analysis for Girder G3 Diaphragm-Girder Connections with Unstiffened Web Gaps at the Bottom Flange

Girder G3 has eight diaphragm-girder connections with unstiffened web gaps at the bottom flange: connections 3b, 3c, 3h, and 3j in the transition region, and connections 3d, 3e, 3f, and 3g in the positive moment region. For all eight connections and at all major truck locations, the maximum σ_y stress occurs at Point E' and the maximum σ_x and σ_z stresses both occur at Point A. The web gap stresses of those most highly stressed nodes of each submodel are plotted in Figures 7-21 to 7-22 and summarized in Table 7-3. Figure 7-20 shows the variation of Point E' σ_y stress versus load cases. Figures 7-21 and 7-22 show the variation of Point A σ_x and σ_z stresses, respectively. Figure 7-23 shows the variation of the out-of-plane displacement. The fluctuation pattern shown in Figures 7-20 to 7-23 suggests that for each diaphragm-girder connection, the high magnitude stress or out-of-plane displacement in the web gap occurs only when the truck moves close to the diaphragm position. Web gap stresses experienced by the positive moment region connections are much higher than those developed in the transition region connections, which indicates that larger differential girder deflection occurs in the mid-span area. For connections 3b, 3c, 3h, and 3j, the maximum σ_x and σ_z stresses are all close to or lower than ½ CAFT, but the maximum σ_y stresses are higher than the CAFT. For connections 3d, 3e, 3f, and 3g, the maximum σ_x and σ_z stresses are close to the CAFT, but still higher than ½ CAFT. The maximum σ_y stresses are all found close to yield strength, which are much higher the CAFT. So all these eight diaphragm-girder connections may have the chance to develop out-of-plane fatigue cracks in the unstiffened bottom flange web gaps. Connections 3e and 3g had already been identified with fatigue cracks and repaired by KDOT. Connections 3d and 3f may

experience fatigue cracking in the near future as the maximum web gap σ_x, σ_y, and σ_z stress magnitudes developed in these two connections are almost the same as those developed in connections 3e and 3g. Cracks are expected to occur at both the horizontal flange-to-web welds and the vertical stiffener-to-web welds. The maximum σ_y stresses observed in the transition region connections 3b, 3c, 3h, and 3j are much lower than those of the positive moment region connections, but the stress magnitudes are still high enough to introduce horizontal fatigue cracking along the flange-to-web welds. Vertical or horseshoe cracks may not be able to develop in these four connections as the maximum σ_x and σ_z stresses are all of low magnitudes close to ½ CAFT.

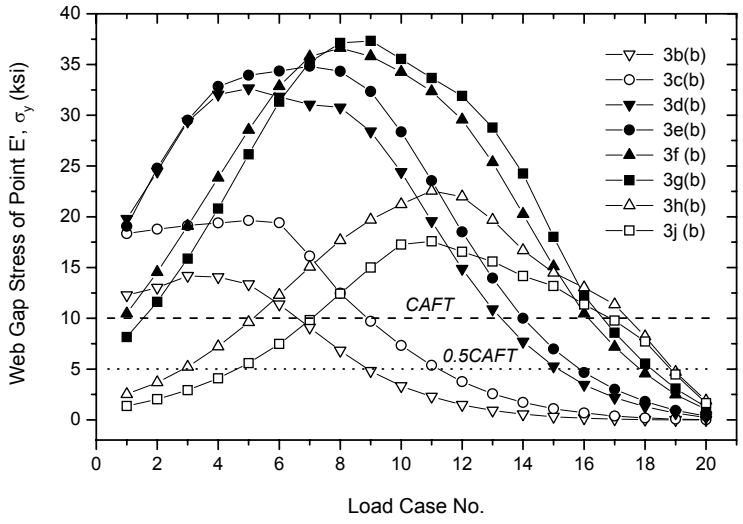

FIGURE 7-20: Point E' σ_y Stress Variation for Girder G3 Bottom Flange Submodels

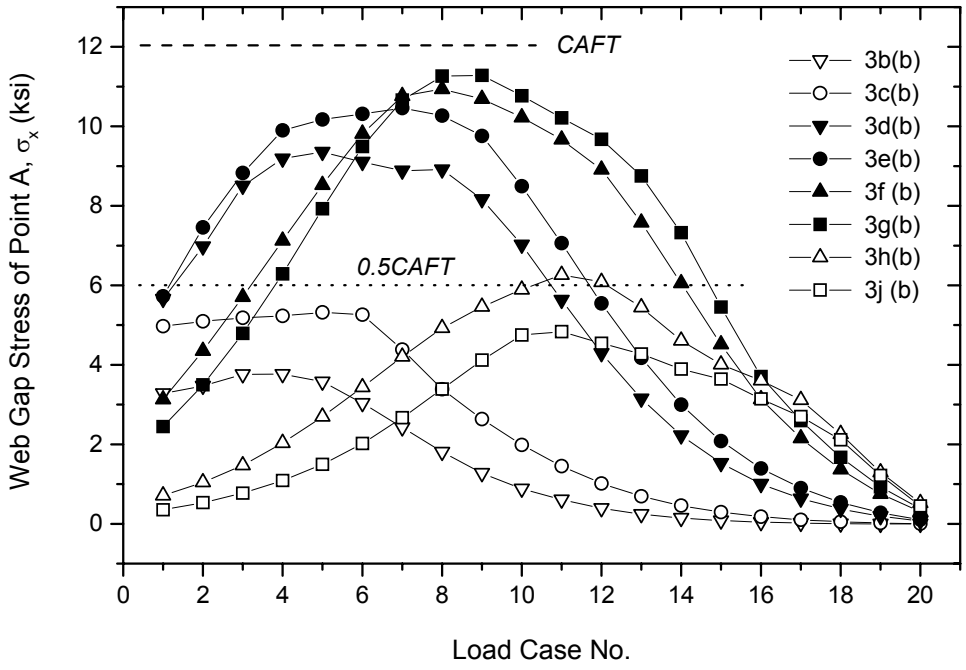

FIGURE 7-21: Point A σ_x Stress Variation for Girder G3 Bottom Flange Submodels

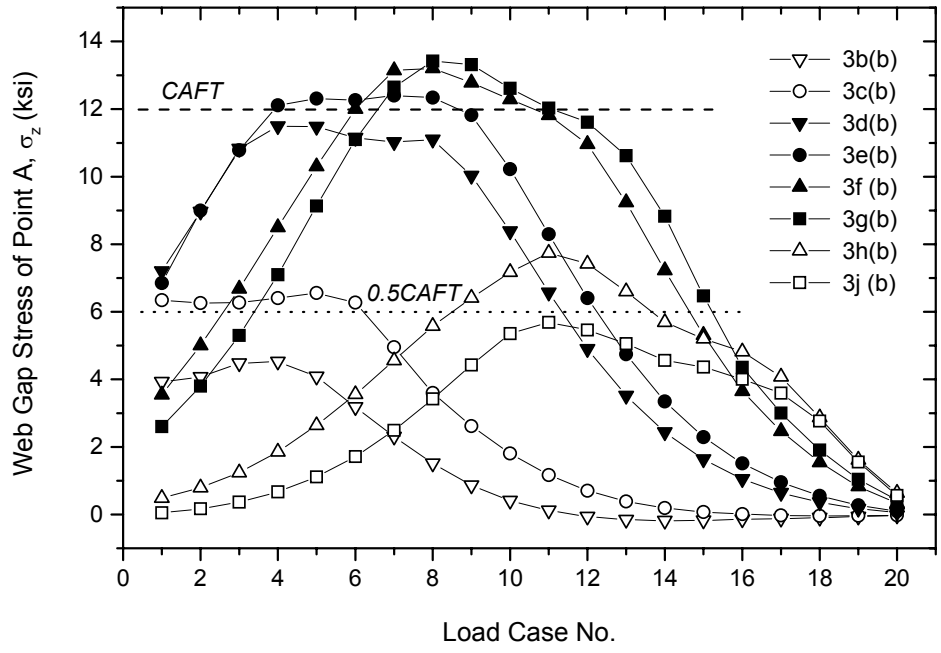

FIGURE 7-22: Point A σ_z Stress Variation for Girder G3 Bottom Flange Submodels

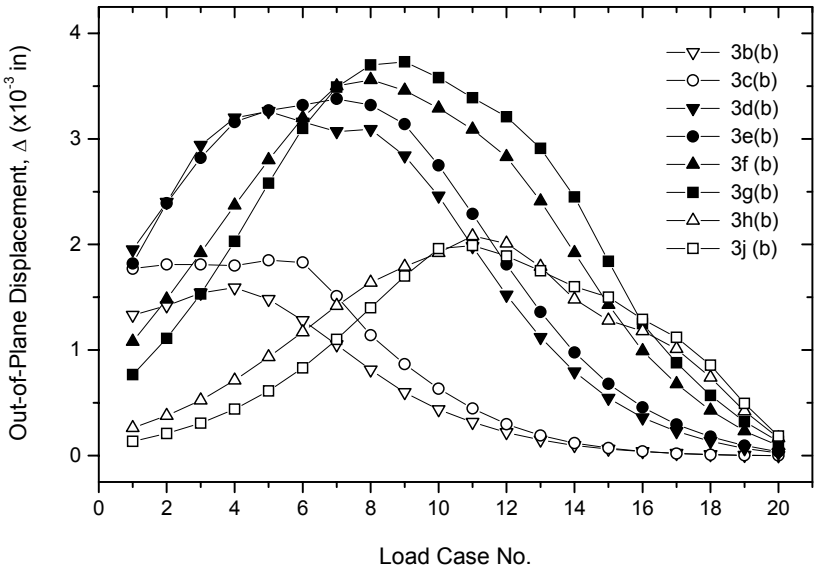

FIGURE 7-23: Variation of Out-of-Plane Displacement for Girder G3 Bottom Flange Submodels

Figures 7-24 and 7-25 show the maximum web gap stress gradient of the diaphragm-girder connections in the positive and transition moment regions, respectively. The effect of out-of-plane distortion is very clear. Connections in the positive moment region are apparently subjected to more dramatic stress variation within the web gap than those in the transition region. For all the eight connections, the σ_y stresses at the bottom end of the web gaps (Points E' and E) are more than two times of those occurring at the top end (Points A and A'). So theoretically, in terms of stress range, the horizontal bottom-flange-to-web welds would develop fatigue cracks at an earlier stage than the vertical stiffener-to-web welds. Symmetry is found about the mid web surface, for the stresses on each side of the girder web, but is not found about the mid web gap length. The locations of zero stresses are about $^1/_3$ of the web gap length down below the top web gap end (Point A or A').

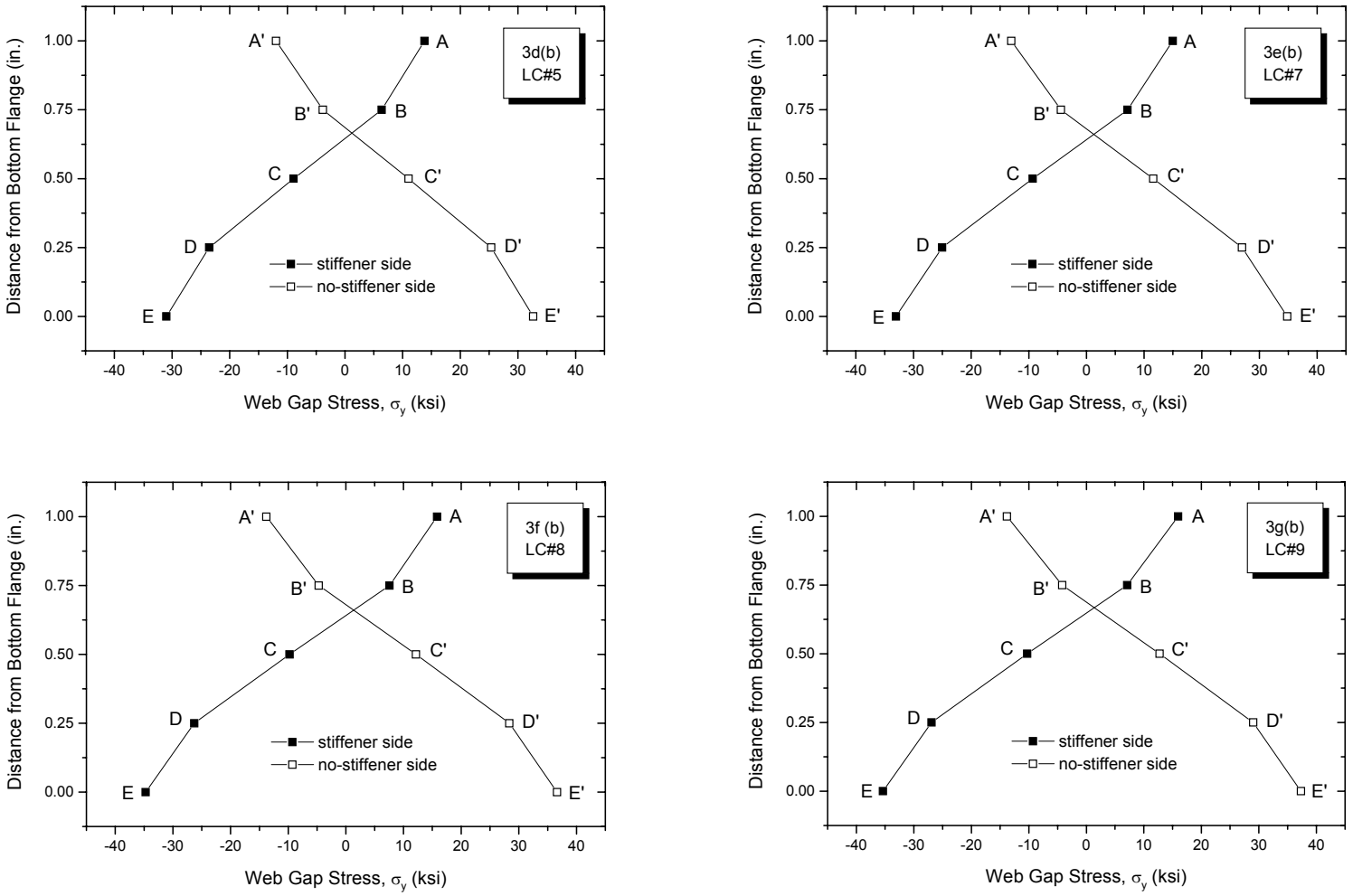

FIGURE 7-24: Web Gap Stress Gradient for Bottom Flange Submodels of Girder G3 Positive Moment

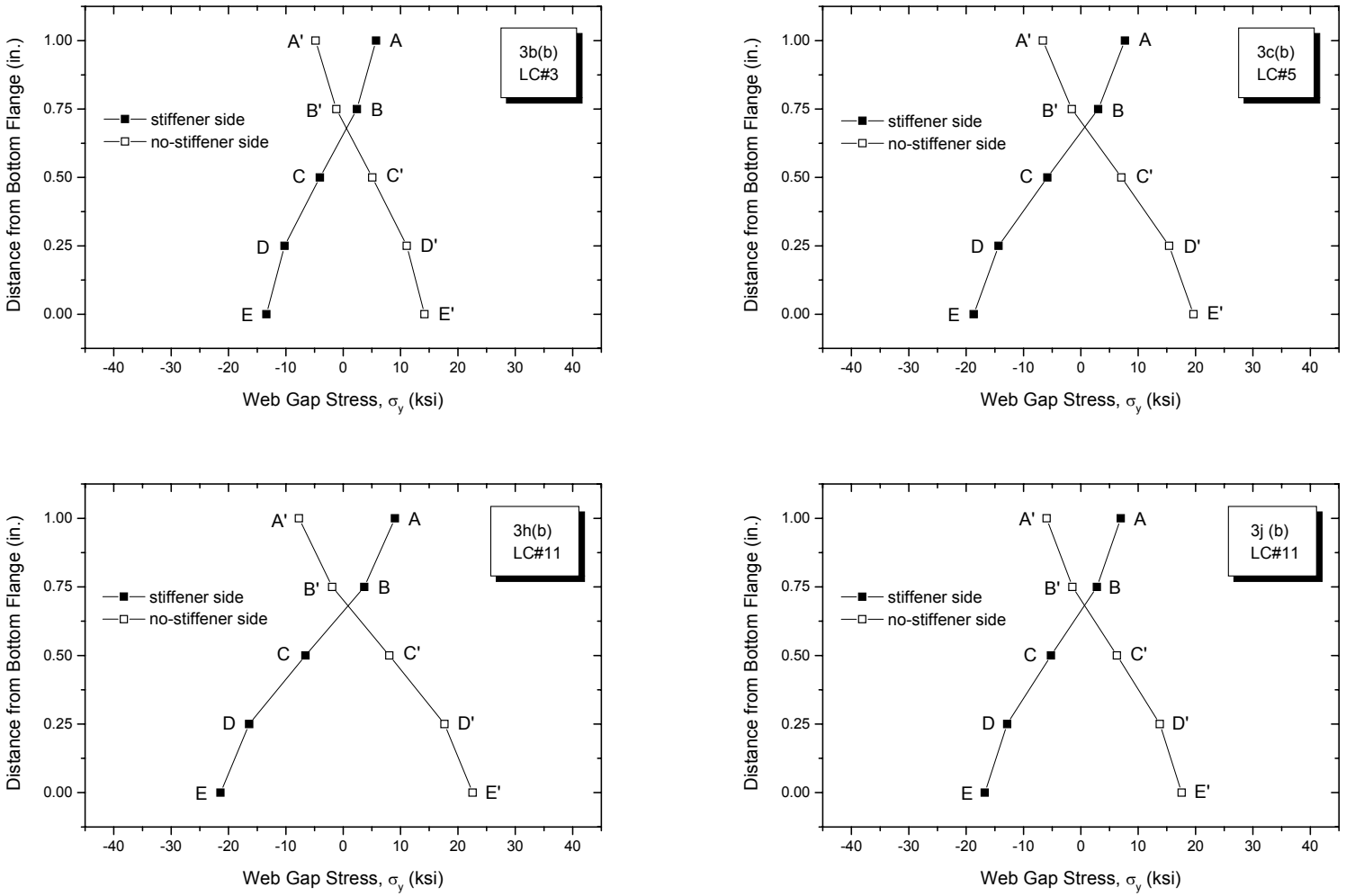

FIGURE 7-25: Web Gap Stress Gradient for Bottom Flange Submodels of Girder G3 Transition Region

TABLE 7-3: Maximum Web Gap Stresses of Girder G3 Bottom Flange Submodels

Connection	3b (b)	3c (b)	3d (b)	3e (b)	3f (b)	3g (b)	3h (b)	3j (b)	AASHTO Fatigue Detail Category	CAFT
Moment Region	Transition	Transition	Positive	Positive	Positive	Positive	Transition	Transition		
Girder Section	"C"	"C"	"A"	"A"	"A"	"A"	"C"	"C"		
Δ_{max}	1.59×10^{-3} in.	1.85×10^{-3} in.	3.26×10^{-3} in.	3.38×10^{-3} in.	3.56×10^{-3} in.	3.73×10^{-3} in.	2.08×10^{-3} in.	1.99×10^{-3} in.		
	L.C. # 4	L.C. # 5	L.C. # 5	L.C. # 7	L.C. # 8	L.C. # 9	L.C. # 11	L.C. # 11		
$\sigma_{x, max}$	3.8 ksi	5.3 ksi	9.4 ksi	10 ksi	11 ksi	11 ksi	6.3 ksi	4.8 ksi	C'	12 ksi
	L.C. # 4	L.C. # 5	L.C. # 5	L.C. # 7	L.C. # 8	L.C. # 9	L.C. # 11	L.C. # 11		
	Point A	Point A	Point A	Point A	Point A	Point A	Point A	Point A		
$\sigma_{y, max}$	14 ksi	20 ksi	33 ksi	35 ksi	37 ksi	37 ksi	23 ksi	18 ksi	C	10 ksi
	L.C. # 3	L.C. #5	L.C. # 5	L.C. # 7	L.C. # 8	L.C. # 9	L.C. # 11	L.C. # 11		
	Point E'	Point E'	Point E'	Point E'	Point E'	Point E'	Point E'	Point E'		
$\sigma_{z, max}$	4.5 ksi	6.6 ksi	11 ksi	12 ksi	13 ksi	13 ksi	7.7 ksi	5.7 ksi	C'	12 ksi
	L.C. # 4	L.C. #5	L.C. # 4	L.C. # 7	L.C. # 8	L.C. # 8	L.C. # 11	L.C. # 11		
	Point A	Point A	Point A	Point A	Point A	Point A	Point A	Point A		

Figures 7-26 and 7-27 illustrate, for example, the σ_y stress contour of submodel 3g at Load Case No. 9. The overall stress distribution on both web sides indicates mild, close to zero stress magnitude, but significant stress concentration effect is observed in the small web gap region. The maximum and minimum σ_y stresses at Points E' and E, respectively, are all beyond the yield strength. Figure 7-28 shows the web gap σ_x stress contour of the same connection at Load Case No. 9 and Figure 7-29 shows the corresponding σ_z stress contour. Both have the maximum stresses at Point A on the stiffener side of the girder web. Figure 7-30 shows the σ_y stress distribution along the flange-to-web welds on the no-stiffener side of the girder web. The peak stress occurs at Point E' with an amplitude of 37 ksi. Stress within the next adjacent 3 in. on each side of the stiffener decreases dramatically and in approximately a linear pattern. The σ_y stresses at Points E'3 and E"3 are 4.5 ksi and 5.8 ksi, respectively. From Point E'3 to E'10 and E"3 toE"10, stress decreases gradually in a relatively flat slope. At Points E'5 and E"5, the σ_y magnitudes are 1.3 ksi and 2.5 ksi, respectively. So generally speaking, a total of 10 in. wide area, 5 in. on each side of the connection stiffener, can be defined as the affected zone due to the web gap stress concentration. The other seven Girder G3 connections have the same web gap stress distribution pattern, with similar or lower stress magnitudes. This 10 in. affected zone is thus suggested as a general size for the stress concentration regions of the unstiffened bottom flange web gaps.

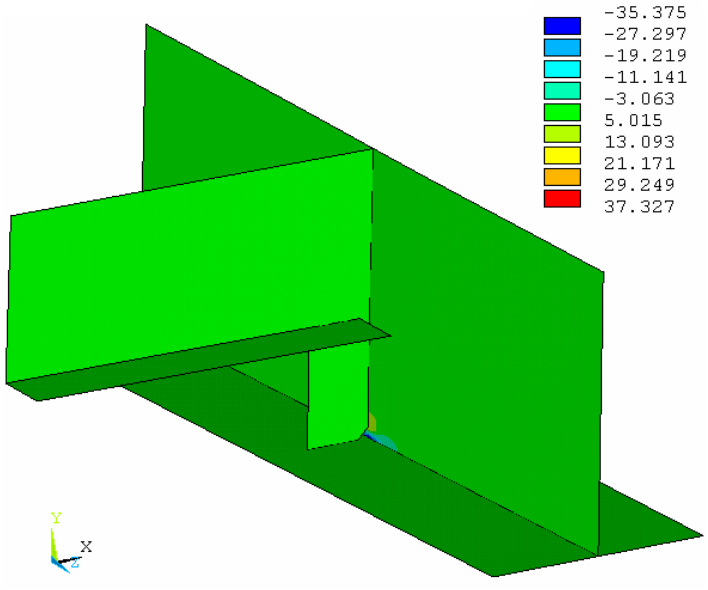

(a) overall σ_y stress distribution of the submodel (ksi)

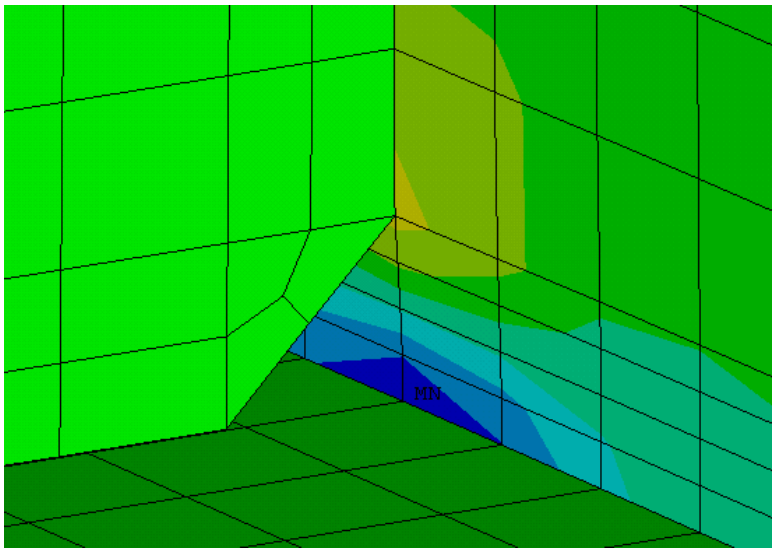

(b) web gap σ_y stress distribution (maximum compressive stress at Point E)

FIGURE 7-26: Load Case No. 9 σ_y Stress Contour of Submodel 3g on the Stiffener Side

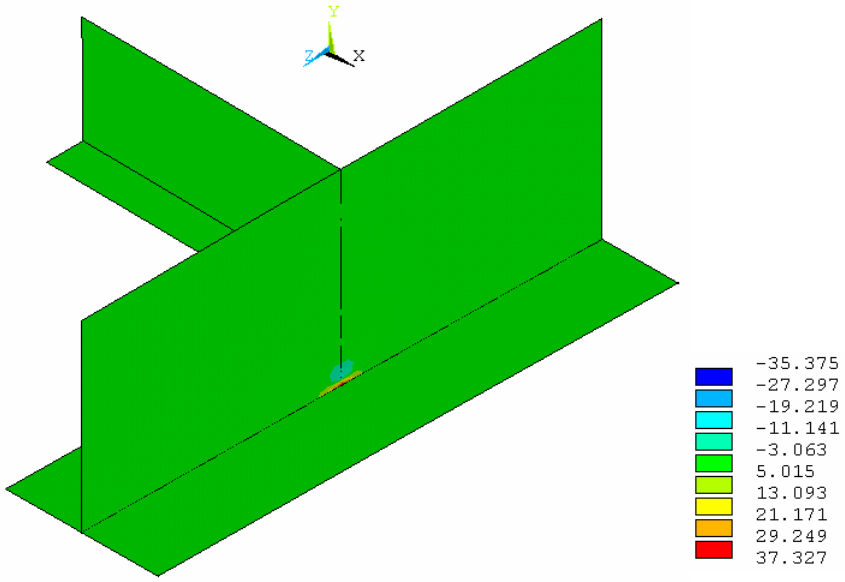

(a) overall σ_y stress distribution of the submodel (ksi)

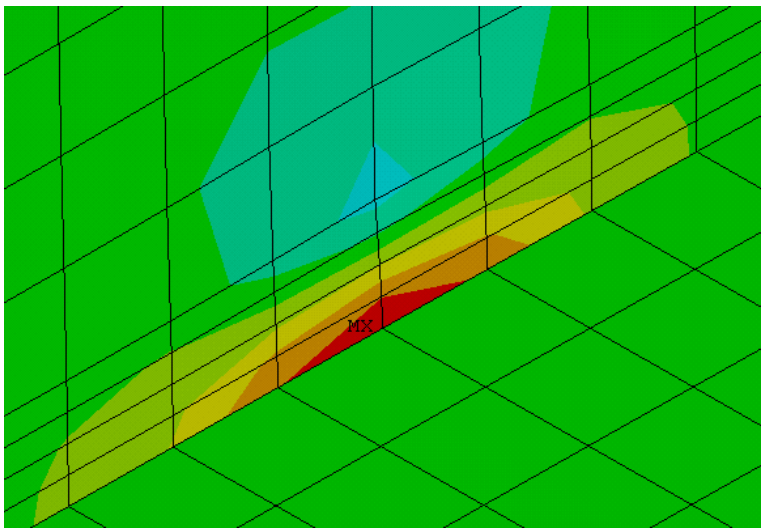

(b) web gap σ_y stress distribution (maximum tensile stress at Point E')

FIGURE 7-27:Load Case No. 9 σ_y Stress Contour of Submodel 3g on the No-Stiffener Side

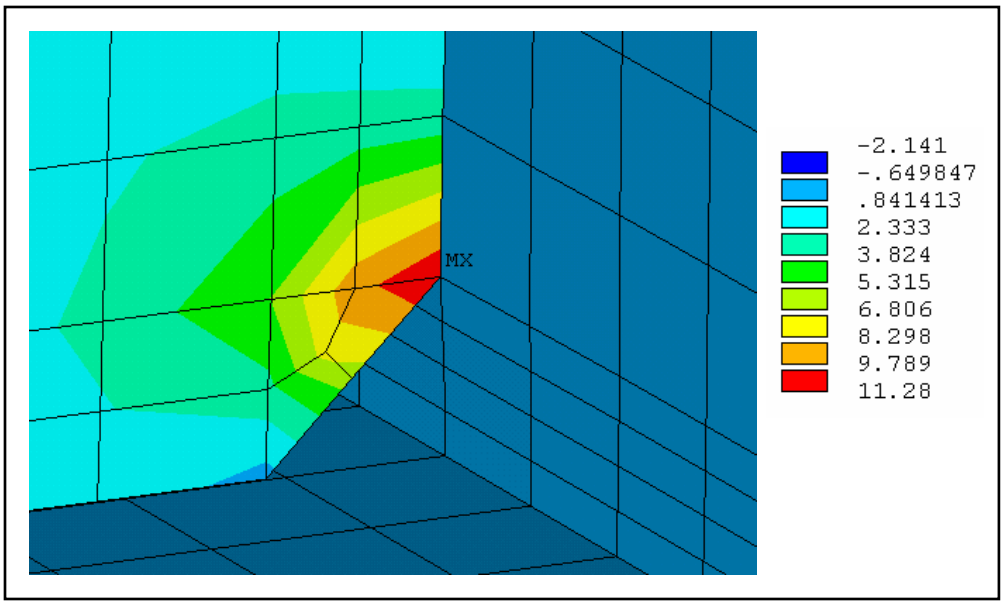

FIGURE 7-28: Load Case No. 9 Web Gap σ_x Stress Contour of Submodel 3g

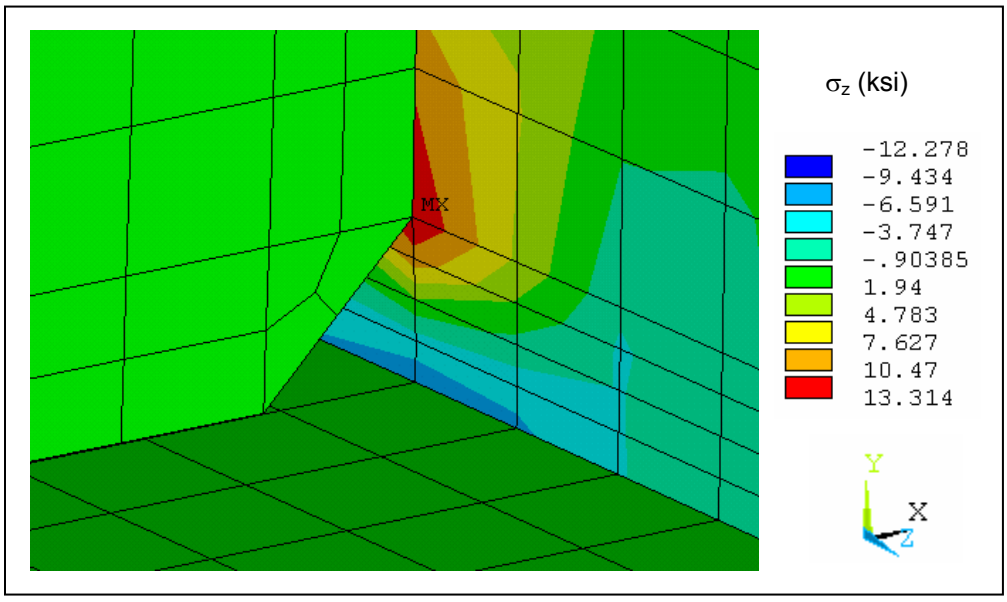

FIGURE 7-29: Load Case No. 9 Web Gap σ_z Stress Contour of Submodel 3g

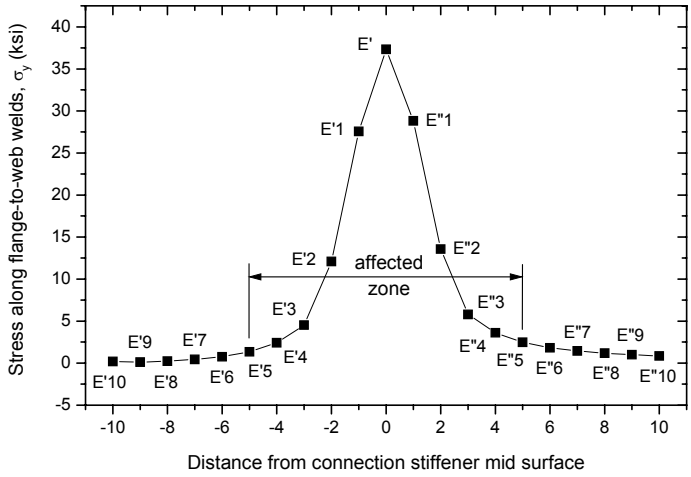

FIGURE 7-30: Load Case No. 9 σ_y Stress Distribution of Submodel 3g along the Flange-to-Web Welds

7.3.2.4 Submodel Analysis for Girder G3 Diaphragm-Girder Connections with Unstiffened Web Gaps at the Top Flange

Girder G3 has six diaphragm-girder connections that have unstiffened web gaps at the top flange: connections 3a and 3k in the negative moment region, and connections 3b, 3c, 3h, and 3j in the transition region. The grid points shown in Figure 7-15(b) and (d) are used to explain the analysis results of the top flange submodels.

For all 20 load cases, the web gaps of connections 3a and 3k in the negative moment region are pushed outward and distort in double curvature as shown in Figure 7-31(a). The maximum σ_y stress thus occurs at Point E on the stiffener side of the web and the σ_x and σ_z stresses at Point A are always in compression. For connections 3b, 3c, 3h, and 3j in the transition region, except at a few low stress magnitude load cases where the distortion is found the same as of Figure 7-31(a), for most truck locations the web gaps are pulled inward and deflect in a reversed curvature as shown in Figure 7-31(b). The maximum σ_y stress occurs mostly at Point E' on the no-stiffener side of the web and the maximum σ_x and σ_z stresses occur

mostly at Point A. Figure 7-32 shows the web gap σ_y stress variation for the six top flange submodels. The data plotted in the diagram are stresses at Point E for connections 3a and 3k and Point E' for connections 3b, 3c, 3h, and 3j. The letter "t" in the parenthesis is added to the legend to make it clear that these submodels are for top flange unstiffened web gaps. Connections 3a, 3b, and 3c are subjected to only one stress cycle per truck passage, while connections 3h, 3j, and 3k are subjected to two stress cycles per truck passage. The maximum σ_y stresses of connections 3b, 3c, and 3h are below ½ CAFT. Those of connections 3a, 4j, and 3k are close to the CAFT, but still higher than ½ CAFT, so horizontal cracks could develop at the flange-to-web welds. Figures 7-33 and 7-34 show the Point A stress variation for σ_x and σ_z, respectively. Both the maximum σ_x and σ_z stresses of all six connections are below ½ CAFT, so vertical or horseshoe cracks along the stiffener-to-web welds are not likely to occur at these locations. Figure 7-35 shows the variation of out-of-plane displacement for the six top flange submodels. The bridge is skewed at Pier No. 2 and No. 3, so connections 3a and 3k in the negative moment region experience larger out-of-plane displacement than the other four connections in the transition region. Table 7-4 summarizes the maximum out-of-plane displacement as well as the maximum σ_x, σ_y, and σ_z stresses of the six top flange submodels. Compared with the analysis results obtained for the bottom flange submodels (Table 7-3), the fatigue stresses developed in the top flange unstiffened web gaps are much lower. All maximum stresses are below the CAFT and most of them are below ½ CAFT. This is why no cracks have been found in the top flange web gaps of the Winfield Bridge. However, since the maximum σ_y stresses in connections 3a, 3j, and 3k are still higher than ½ CAFT, it is recommended that some repair action also be taken at these unstiffened top flange web gap details, so that possible crack development at these locations can be prevented.

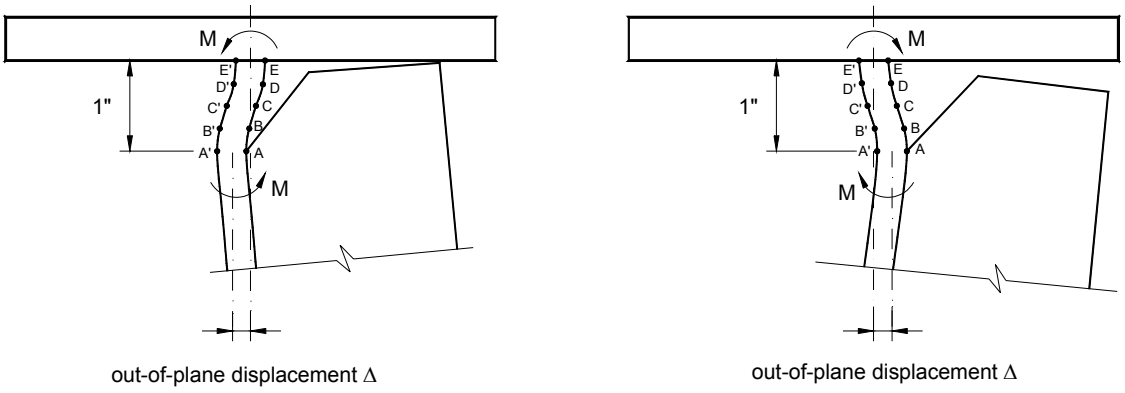

(a) web gap pushed outward

(b) web gap pulled inward

FIGURE 7-31: Schematic of Different Web Gap Distortion Curvature

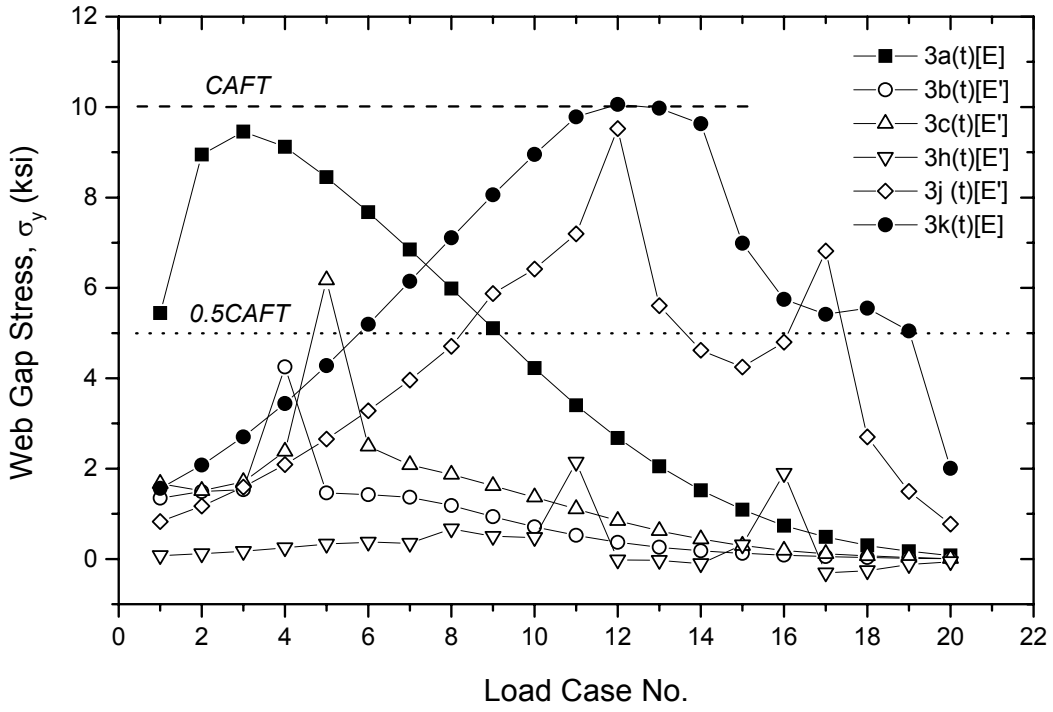

FIGURE 7-32: Web Gap σ_y Stress Variation for Girder G3 Top Flange Submodels

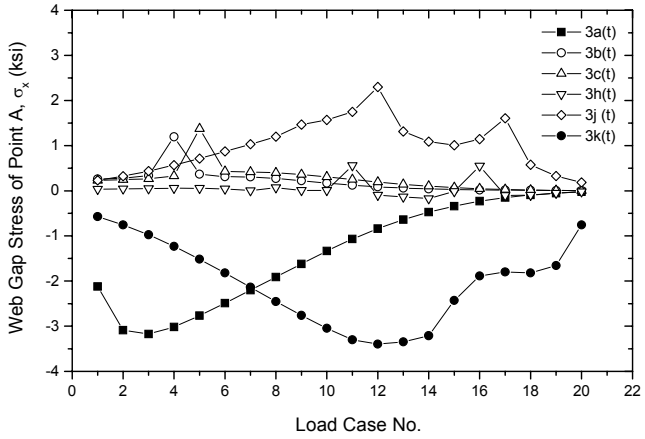

FIGURE 7-33: Point A σ_x Stress Variation for Girder G3 Top Flange Submodels

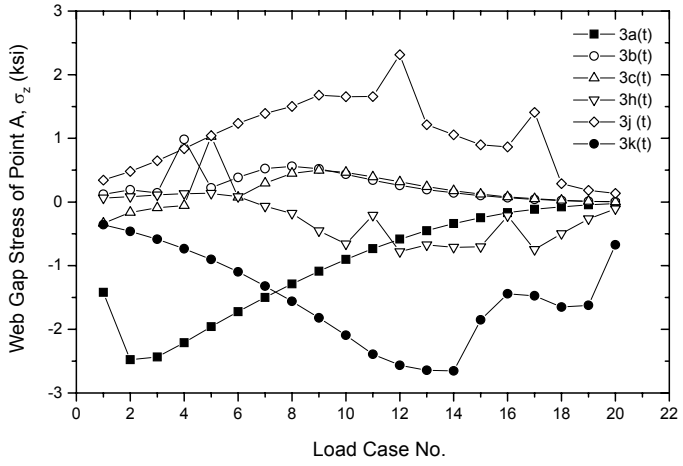

FIGURE 7-34: Point A σ_z Stress Variation for Girder G3 Top Flange Submodels

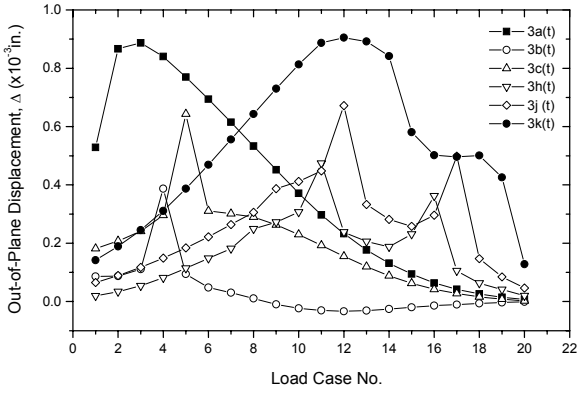

FIGURE 7-35: Variation of Out-of-Plane Displacement for Girder G3 Top Flange Submodels

TABLE 7-4: Significant Web Gap Stresses of Girder G3 Top Flange Submodels

Connection	3a (t)	3b (t)	3c (t)	3h (t)	3j (t)	3k (t)	AASHTO Fatigue Detail Category	CAFT
Moment Region	Negative	Transition	Transition	Transition	Transition	Negative		
Girder Section	"B"	"C"	"C"	"C"	"C"	"B"		
Δ_{max}	8.87×10^{-4} in.	3.87×10^{-4} in.	6.43×10^{-4} in.	4.74×10^{-4} in.	6.72×10^{-4} in.	9.05×10^{-4} in.		
	L.C. # 3	L.C. # 4	L.C. # 5	L.C. # 11	L.C. # 12	L.C. # 12		
$\sigma_{x, max}$	< 0	1.2 ksi	1.4 ksi	0.56 ksi	2.3 ksi	< 0	C'	12 ksi
	all load cases	L.C. # 4	L.C. # 5	L.C. # 11	L.C. # 12	all load cases		
	Point A	Point A	Point A	Point A	Point A	Point A		
$\sigma_{y, max}$	9.5 ksi	4.3 ksi	6.2 ksi	2.1 ksi	9.5 ksi	10 ksi	C	10 ksi
	L.C. # 3	L.C. # 4	L.C. # 5	L.C. # 11	L.C. # 12	L.C. # 12		
	Point E	Point E'	Point E'	Point E'	Point E'	Point E		
$\sigma_{z, max}$	< 0	0.98 ksi	1.0 ksi	0.14 ksi	2.3 ksi	< 0	C'	12 ksi
	all load cases	L.C. # 4	L.C. # 5	L.C. # 5	L.C. # 12	all load cases		
	Point A	Point A	Point A	Point A	Point A	Point A		

Figures 7-36 and 7-37 show the maximum web gap σ_y stress gradient of the top flange submodels, for connections at negative and transition moment regions, respectively. Compared to those observed in the bottom flange submodels (Figures 7-24 and 7-25), both the stresses and the stress variation amplitudes within the top flange web gaps are of much lower magnitude. For all six connections, stresses on each side of the girder web are symmetric about the web mid surface, but are not symmetric about the mid web gap length. The σ_y stresses at the top, flange end of the web gaps (Points E and E') are at least two times of those occurring at the bottom, stiffener end (Points A' and A). For connections 3a and 3k, the locations of zero stresses are about $^1/_3$ of the web gap length up above the bottom web gap end (Point A or A'). For connections 3b, 3c, 3h, and 3j, the locations of zero stresses are about $^1/_4$ of the web gap length up above the bottom web gap end (Point A or A').

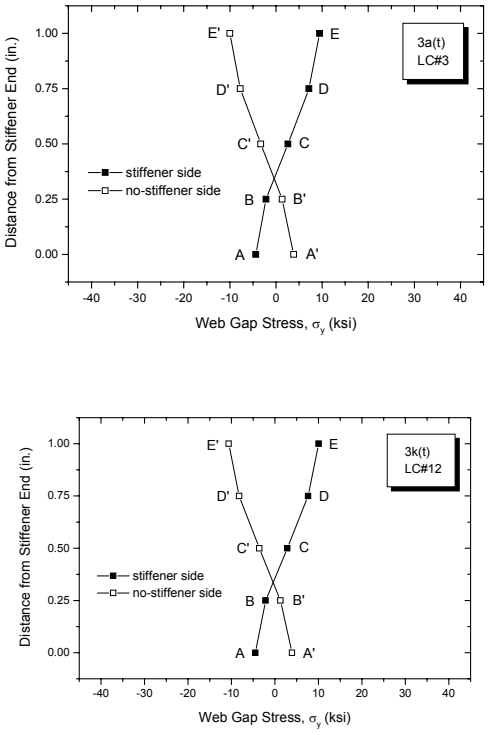

FIGURE 7-36: Web Gap Stress Gradient for Top Flange Submodels of Girder G3 Negative Moment Region Connections

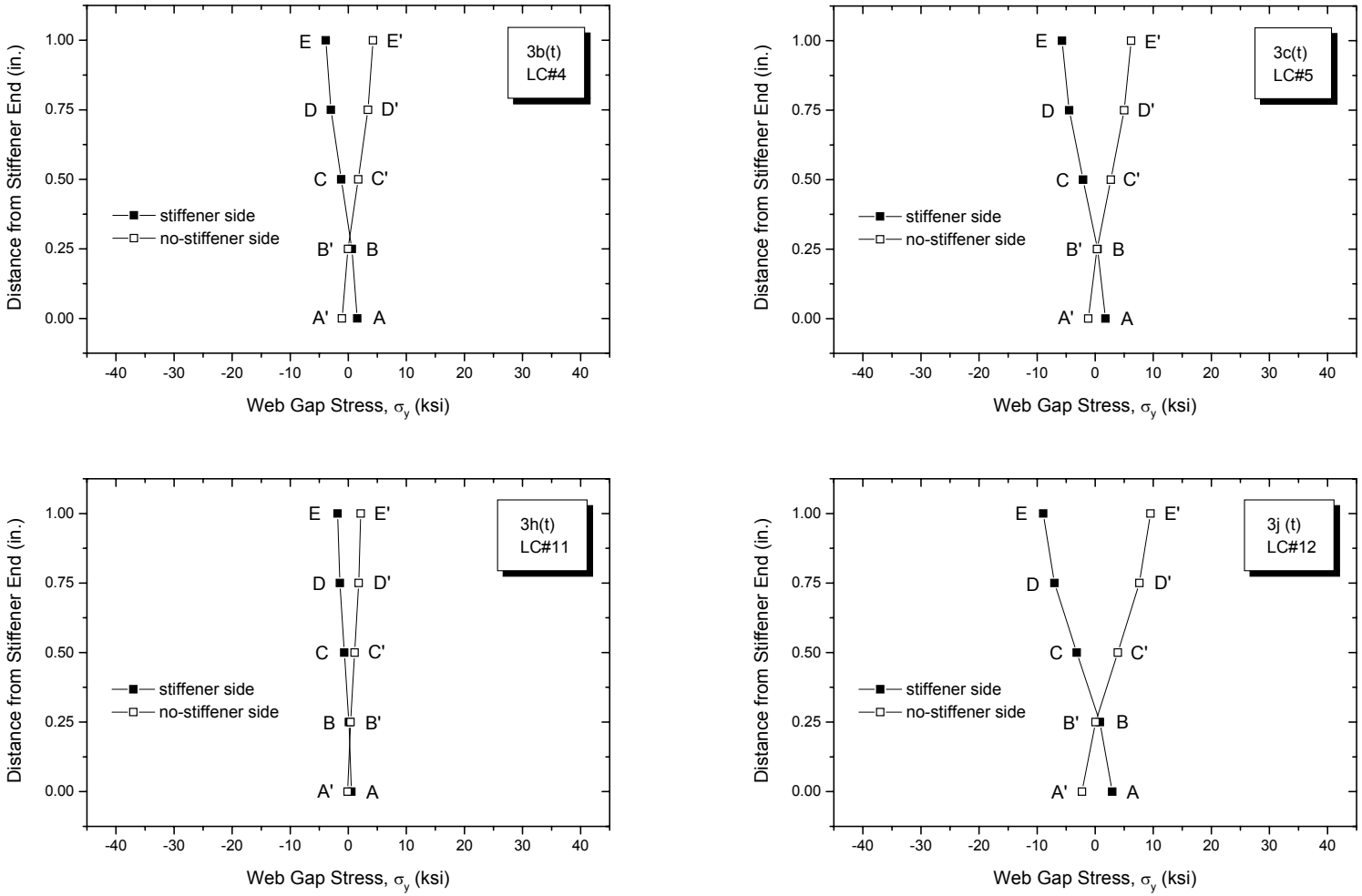

FIGURE 7-37: Web Gap Stress Gradient for Top Flange Submodels of Girder G3 Transition Region Connections

Figures 7-38, 7-39, and 7-40 show the stress contours of submodel 3j for σ_y, σ_x, and σ_z, respectively, at Load Case No. 12 for the stiffener side of the girder web. Figures 7-41, 7-42, and 7-43 show the corresponding stress contours of submodel 3k at the same load case. The corresponding web gap stresses at the same point of the two models are of different signs. For example, the σ_x and σ_z stresses at Point A and the σ_y stress at Point E are all in minimum compressive stresses for submodel 3j, but the same stresses at the same locations are all in maximum tensile stresses for submodel 3k. Though not plotted, the stresses of those points on the no-stiffener side of the girder web are also in opposite signs for the two submodels. This indicates that the web gaps of these two models are bent in opposite curvatures when subjected to out-of-plane distortion. The overall stress distribution of both submodels is close to zero. Stress concentration is only confined to the small web gap region. Figures 7-44 and 7-45 show, respectively, the σ_y stress distribution along the top-flange-to-web welds for submodels 3j and 3k. The data points E'1 to E'10 and E"1 to E"10 plotted in Figure 7-45 for submodel 3k are on the stiffener side of the girder web. The web gap of this connection is deflected with a curvature of Figure 7-31(a), so the fatigue stresses responsible for horizontal cracks are located on this web side. The peak stresses at Point E' of connection 3j and Point E of connection 3k are both about 10 ksi. Compared to the curve shown in Figure 7-30 for bottom flange submodel, the stress amplitudes of top flange submodels are much lower. Nevertheless, a 10 in. affected zone (5 in. on each side of the connection stiffener) can still be specified for the area around the web gap for the stress concentration effect.

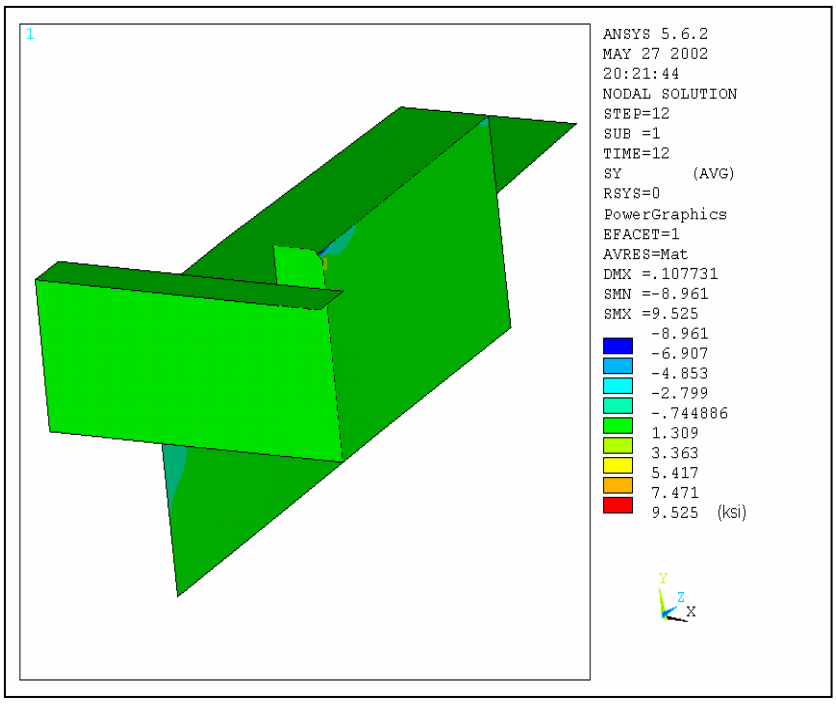

(a) overall σ_y stress distribution of the submodel

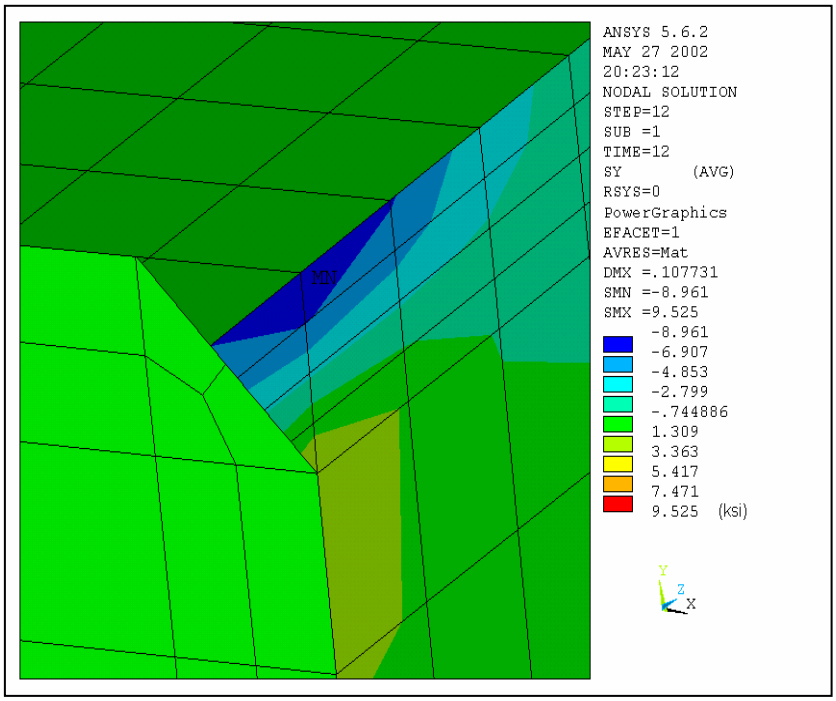

(b) web gap σ_y stress distribution (minimum compressive stress at Point F)

FIGURE 7-38: Load Case No. 12 σ_y Stress Contour of Submodel 3j on the Stiffener Side

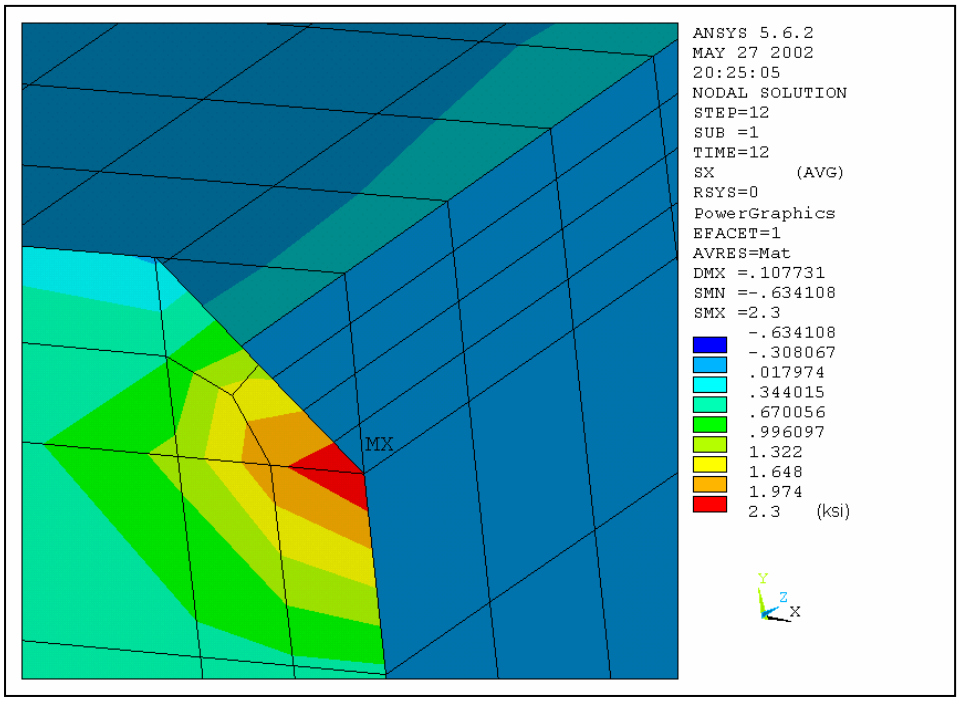

FIGURE 7-39: Load Case No. 12 σ_x Stress Contour of Submodel 3j

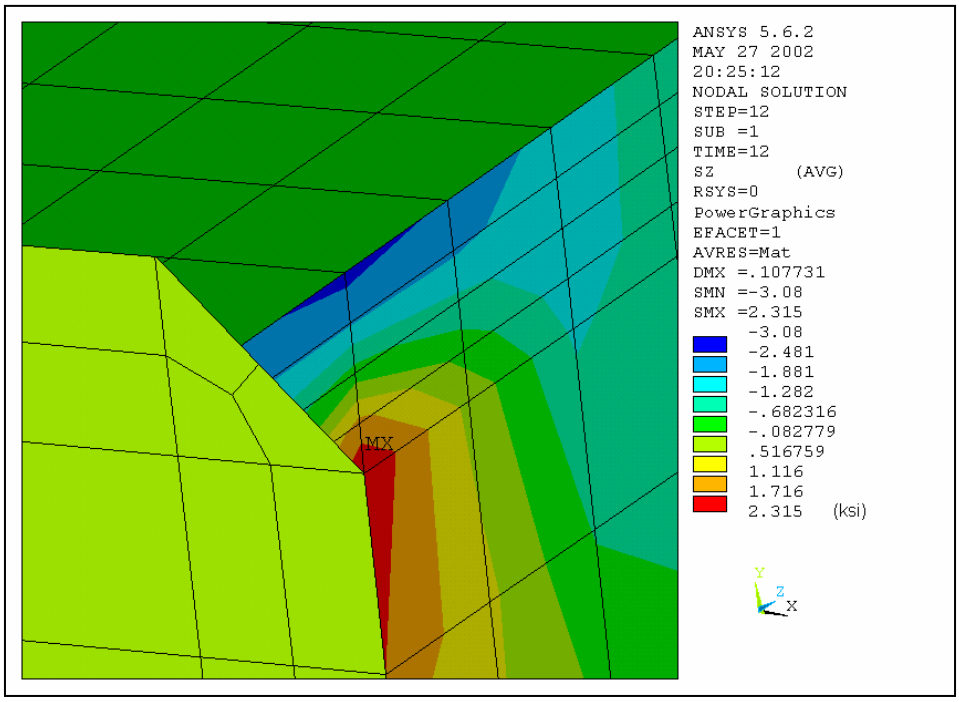

FIGURE 7-40: Load Case No. 12 σ_z Stress Contour of Submodel 3j

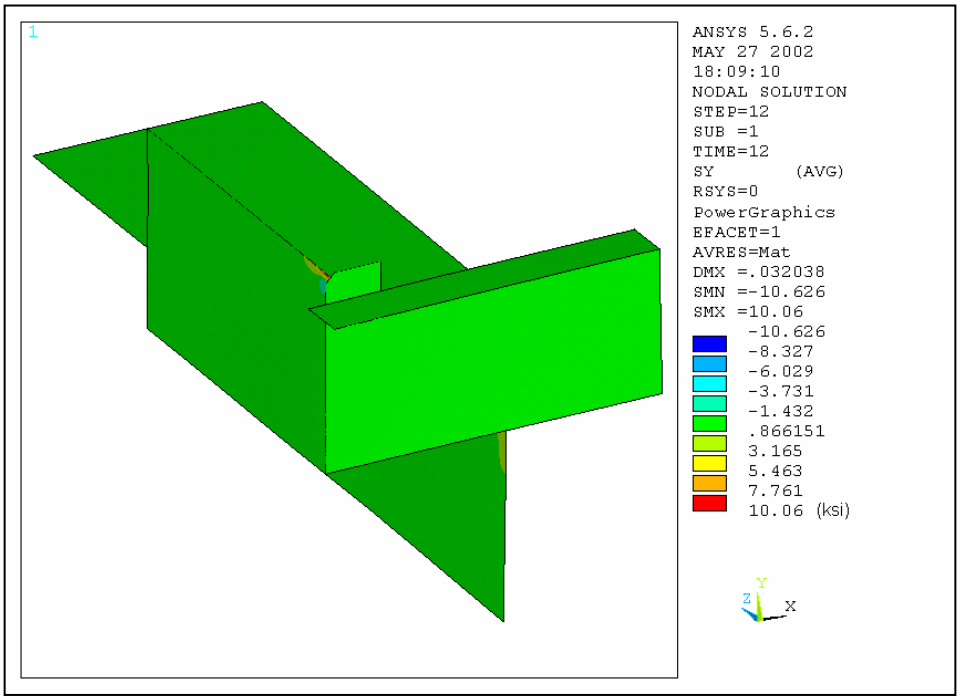

(a) overall σ_y stress distribution of the submodel

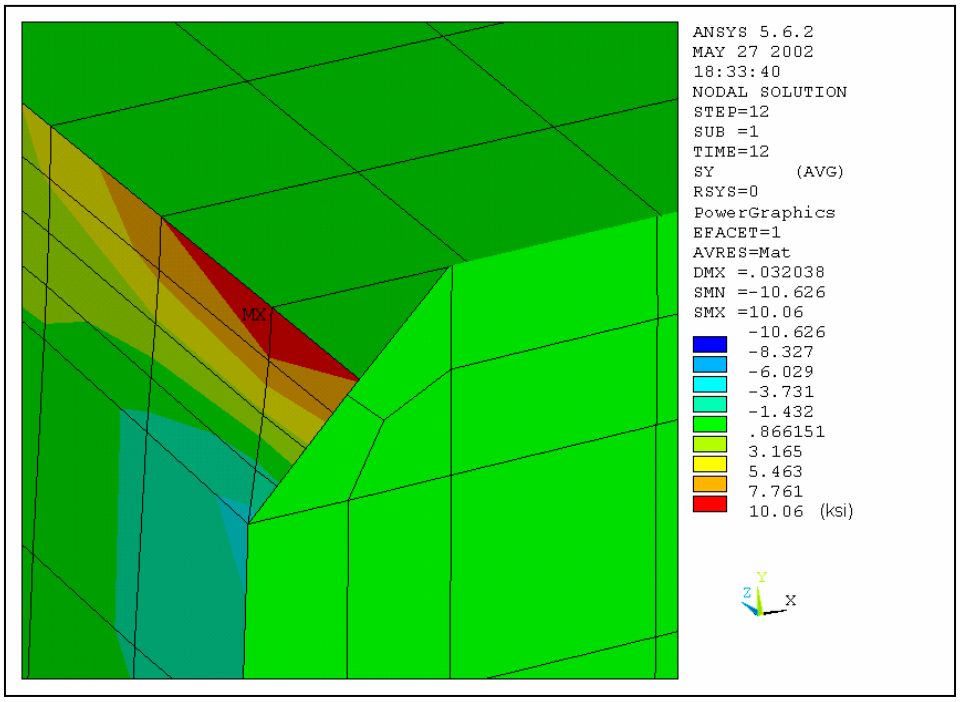

(b) web gap σ_y stress distribution (maximum tensile stress at Point E)

FIGURE 7-41: Load Case No. 12 σ_y Stress Contour of Submodel 3k on the Stiffener Side

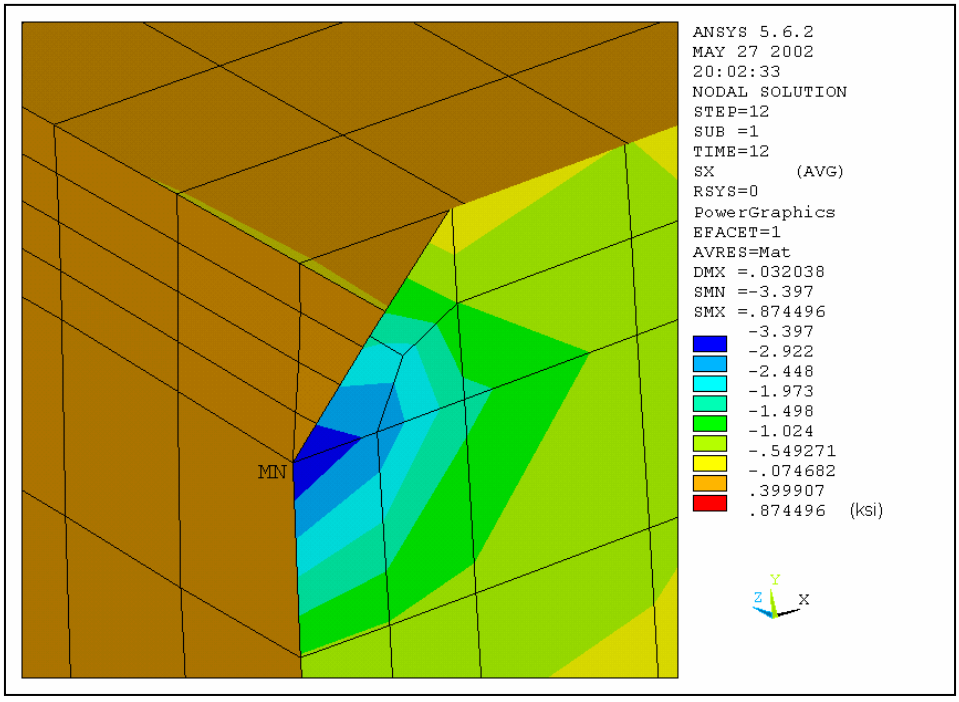

FIGURE 7-42: Load Case No. 12 σ_x Stress Contour of Submodel 3k

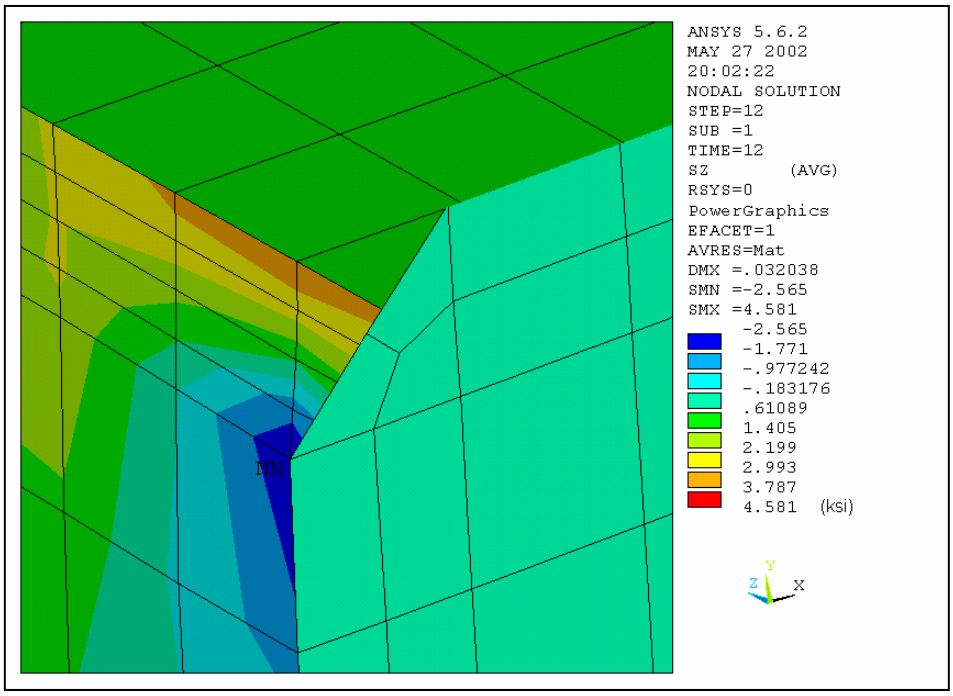

FIGURE 7-43: Load Case No. 12 σ_z Stress Contour of Submodel 3k

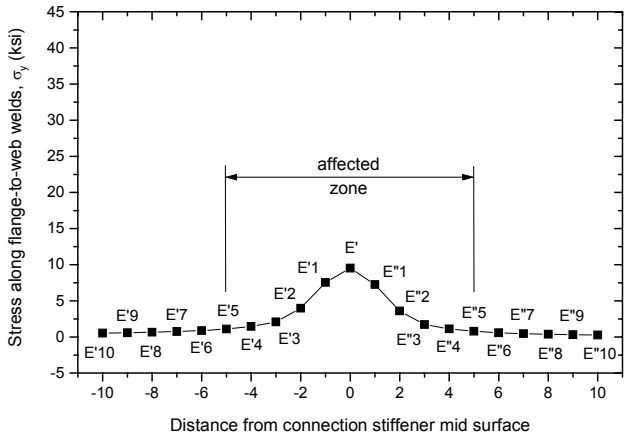

FIGURE 7-44: Load Case No. 12 σ_y Stress Distribution of Submodel 3j along the Flange-to-Web Welds on the No-Stiffener Side of the Girder Web

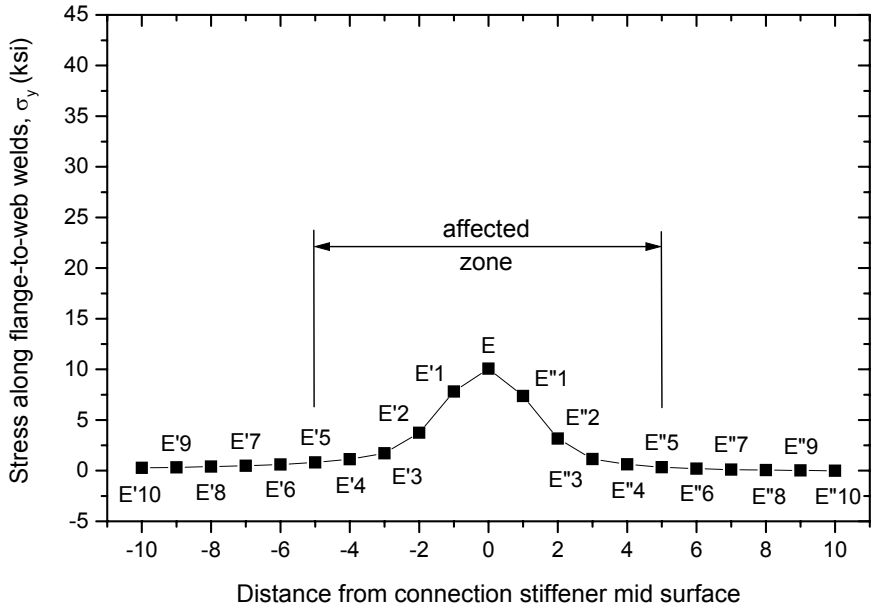

FIGURE 7-45: Load Case No. 12 σ_y Stress Distribution of Submodel 3k along the Flange-to-Web Welds on the Stiffener Side of the Girder Web

7.3.3 Importance of the Diaphragm-Girder Connections in Span No. 3

The NCHRP Report 336 [1990] points out in its literature survey that "*Measurements were not available on staggered diaphragms, but the degree of cracking in actual bridges appeared comparable to floorbeam girder bridges. Also, the bottom flange web gap often cracked in structures with staggered diaphragms*." The findings of this case study thus support,

to some extent, the observations of the NCHRP Report 336. The finite element investigation of the Winfield Bridge shows that the bottom flange web gaps of the interior girders are exposed to higher magnitude of out-of-plane distortion and are more likely to develop fatigue cracks than the top flange web gaps. Based on the analysis results presented in Sections 7.3.2.2 to 7.3.2.4, the web gap stress conditions and the degree of urgency for repair of the diaphragm-girder connections in Span No. 3 of the Winfield Bridge is summarized as follows.

1. The secondary stresses developed in the two exterior girders G1 and G4 are not high enough to cause fatigue cracking. Structural repairs are thus only needed for the two interior girders G2 and G3.
2. The four diaphragm-girder connections in the mid-span of Girder G3, connections 3d, 3e, 3f, and 3g, are subjected to the highest magnitude fatigue stresses in the bridge. Stresses developed in the bottom flange web gaps of these four connections are close to the yield strength. Cracks had been previously observed in connections 3e and 3g, and corresponding girder retrofit had been carried out by KDOT at these two locations. It is important that repair measures also be taken at connections 3d and 3f.
3. The transition and negative moment region connections experience much lower web gap fatigue stresses than those in the positive moment region. The maximum bottom flange web gap stresses of the transition region connections are about 20 ksi, and the maximum top flange web gap stresses of both the transition and negative moment region connections are about 10 ksi. However, since these stresses are higher than ½ CAFT, fatigue cracking can still occur in these locations. Therefore, structural repair is also required for the diaphragm-girder connections in the transition and negative moment regions.
4. Fatigue stresses developed in the corresponding connections of Girder G2 are much lower than those of Girder G3, but at some web gap details the stress magnitudes are still high enough to cause fatigue cracking. In addition, though with much less frequency, higher magnitude secondary stresses occur occasionally in the connections of Girder G2 when trucks drive along the passing

lane. For conservative and simplification purposes, it is thus recommended that all the diaphragm-girder connections of Girder G2 be repaired, using the same method as for Girder G3.

7.4 Repair Analysis

7.4.1 KDOT Repair for Cracked Connections

The two cracked diaphragm-girder connections 3e and 3g were repaired by KDOT using the details shown in Figure 7-6. By changing the model geometries to simulate the repair condition, coarse-to-fine submodel analysis is conducted again for connection 3g, so that the stresses developed before and after the repair can be compared.

The clip end dimension is 2-in. by 1-in. for the newly installed stiffeners, so the web gap length built into the repair model is 2 inches. The flange and web splice plate thicknesses are added to those of the corresponding shell elements at the areas where they were bolted to the original girder section. A new stiffener is added on the side of the girder web and both stiffeners are connected to the bottom flange. The finite element results indicate that Load Case No. 9 is again found to be the truck location that causes the highest stresses in the model.

Figure 7-46 shows the web gap σ_y stress gradient on the no-diaphragm side of the web for Load Case No. 9 both before and after the repair. Significant stress reduction can be observed. The stress variation between Point A' and E' is 51 ksi before the repair, but was decreased to 2.6 ksi after the repair. The σ_x and σ_z stresses at Point A are also decreased to about zero. The web gap region is therefore "cooled" down and fatigue cracking should not occur at this location after the repair.

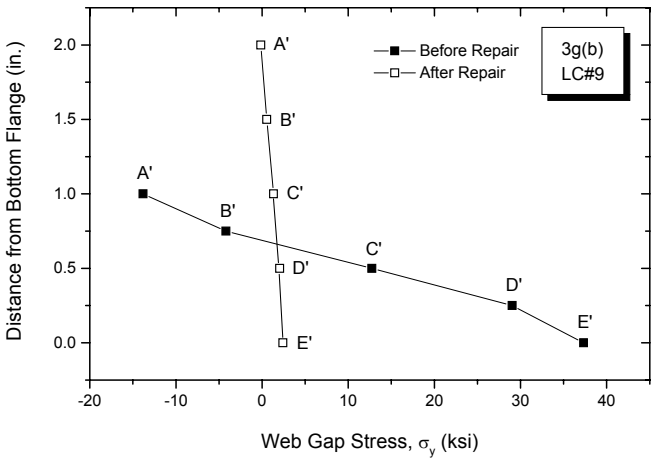

FIGURE 7-46: Connection 3g Web Gap Stress Gradient Before and After the Repair

However, the maximum stresses are noticed to have shifted to the diaphragm-to-stiffener weld ends, as shown by Point L in Figure 7-47. Figures 7-48 and 7-49 show the post-retrofit stress contours of σ_x and σ_y, respectively, for connection 3g at Load Case No. 9. The maximum σ_x stress (10 ksi) and σ_y stress (16 ksi) both occur at Point L and are higher than ½ CAFT. Both the horizontal and vertical diaphragm-to-stiffener welds are considered as Category C details, in terms of the stresses normal to the weld lengths. So the area around the bottom diaphragm-to-stiffener weld junction becomes a new stress concentration zone and fatigue cracking could develop along either the horizontal or the vertical welds.

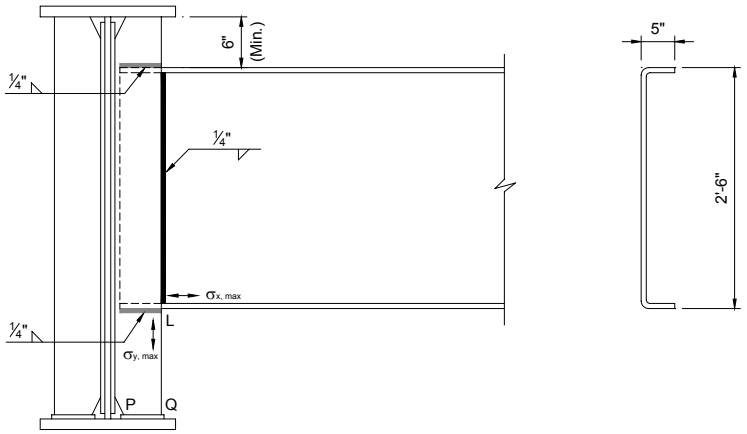

FIGURE 7-47: Locations of Maximum σ_x and σ_y Stresses using KDOT Repair

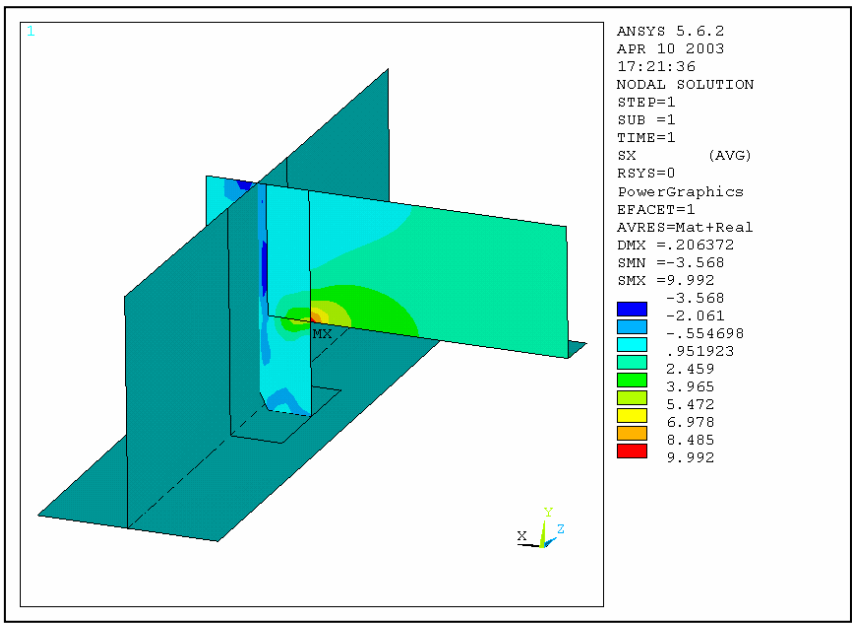

FIGURE 7-48: Post Retrofit σ_x Stress Contour of Connection 3g at Load Case No. 9

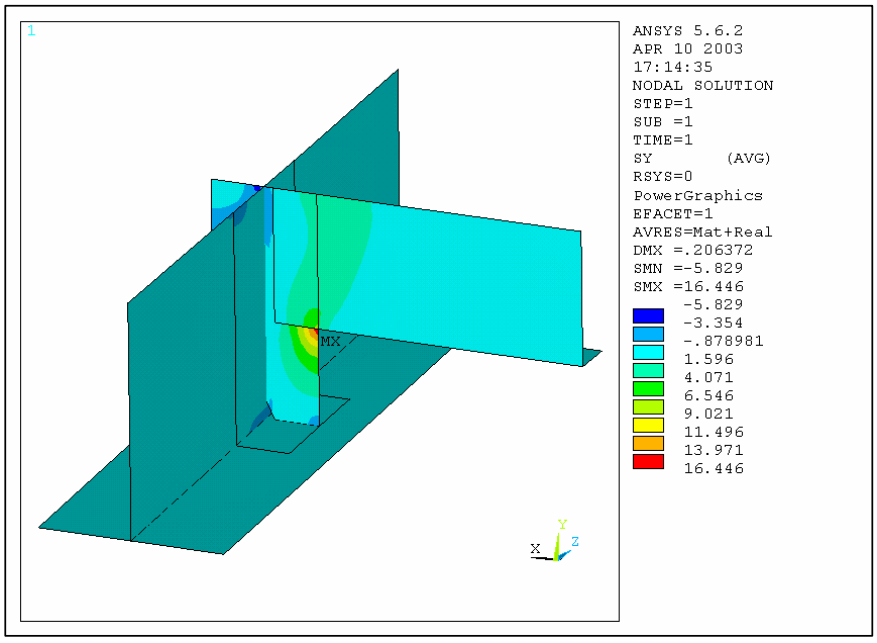

FIGURE 7-49: Post Retrofit σ_y Stress Contour of Connection 3g at Load Case No. 9

A bolted diaphragm-to-stiffener connection could have been used during the retrofit to avoid possible fatigue cracking at the connecting welds. The stress magnitudes of the new concentration area are much lower than those previously developed in the web gap region. The potential crack initiation point is also moved to a location away from the girder web, which gives the inspectors enough time to identify the problem before cracks start to propagate. So in general, the KDOT repair method is acceptable. However, special attention needs to be paid to both horizontal and vertical diaphragm-to-stiffener welds during future bridge inspections. If cracks are found at these locations, it is important that additional retrofit be carried out to prevent cracks from growing into the diaphragm, the stiffener, or even further into the girder web.

Another area of interest of the repair model is the bolted attachment between the connection stiffener and bottom flange, as indicated by line PQ in Figure 7-47. Both of the stresses developed in the connection plate (σ_y) and bottom flange (σ_z) normal to this line are found much less than ½ CAFT of Detail Category B, so cracks would not develop at this region after the repair. A summary of the stresses developed at Point L and line PQ is provided in Table 7-5.

TABLE 7-5: Stresses of Potential Crack Locations in Connection 3g after the Repair

L.C. # 9	Stress	Before Repair	After Repair	AASHTO Fatigue Detail Category	CAFT
Point L	$\sigma_{x,\,max}$	5.0 ksi	10 ksi	C	10 ksi
	$\sigma_{y,\,max}$	10 ksi	16 ksi	C	10 ksi
Line PQ	σ_y	–	< 1.2 ksi	B	16 ksi
	σ_z	–	< 1.0 ksi	B	16 ksi

The repair analysis for connection 3e is not performed as it is expected to experience lower fatigue stresses than connection 3g, based on the results given in Section 7.3.2.3.

7.4.2 Repair Analysis for Uncracked Connections

Possible repair options for the uncracked connections are: removing the diaphragms, cutting the connection stiffeners short, or attaching the connection stiffeners to girder flanges. Since stability is a concern to skewed structures, diaphragm removal is not suggested. As for the cut-short repair, the available cut-short length is only about 6 in. near the top flange, and about 8-10 in. near the bottom flange at the mid-span connections due to the varied girder depth (Figure 7-10). These dimensions are usually considered inadequate for web gap stress release. The 6 in. length at the top flange does not provide enough room for construction either. In addition, it is very time and labor consuming to grind smooth the cut-short area, in order to meet satisfactory surface finish criteria and to prevent cracks from reinitiating. The cut-short repair method is therefore not considered. To be consistent with the KDOT repair used at the two cracked locations, a rigid stiffener-to-flange attachment, either by welding or bolting, is recommended as the structural repair or correction for those uncracked diaphragm-girder connections. The following finite element analyses are carried out at connections 3f, 3h, and 3k, respectively, in order to study the repair performance of the positive, transition, and negative moment region connections.

7.4.2.1 Repair Analysis for Connection 3f

The geometry of submodel 3f is changed by connecting the stiffener to the bottom flange. The coarse-to-submodel cut boundary DOF interpolation is performed again and the repair model is analyzed for all 20 load cases. Figure 7-50 shows the change of web gap stress gradient on the no-stiffener side of the web at Load Case No. 8. The stress variations between

Nodes A' and E' before and after the repair are 50 ksi and 4.5 ksi, respectively. Table 7-6 summarizes the results of those mostly stressed points within the web gap. The σ_x stress at Point A is always below zero after the connection stiffener is attached to the bottom flange; the σ_y stress at Point E' is reduced to 5.2 ksi; and the σ_z stress at Point A is reduced to 1.7 ksi. The average percentage reductions of all 20 load cases are 102%, 86%, and 91%, respectively, for σ_x, σ_y, and σ_z stresses. Since the stresses at those potential crack initiation points are all decreased to equal or below ½ CAFT, fatigue cracking is not expected to occur at the web gap region after the retrofit.

TABLE 7-6: Comparison of Connection 3f Web Gap Stresses Before and After the Repair

	Before Repair	After Repair	Average Percentage Reduction	Fatigue Detail Category	CAFT
σ_x	11 ksi	< 0	102%	C'	12 ksi
	L.C. # 8	all load cases			
	Point A	Point A			
σ_y	37 ksi	5.2 ksi	86%	C	10 ksi
	L.C. # 8	L.C. # 8			
	Point E'	Point E'			
σ_z	13 ksi	1.7 ksi	91%	C'	12 ksi
	L.C. # 8	L.C. # 7			
	Point A	Point A			

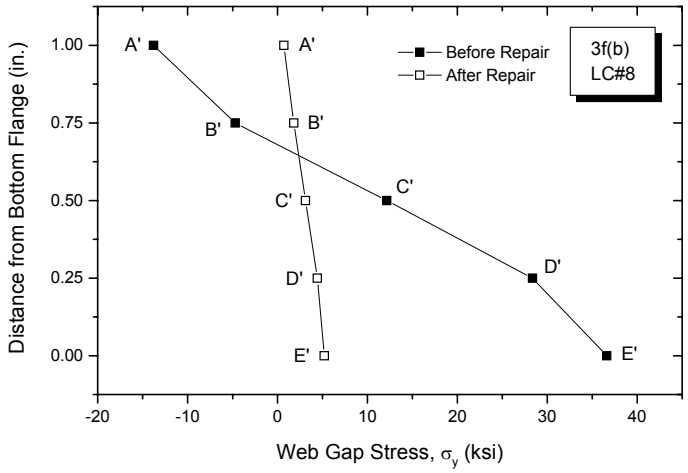

FIGURE 7-50: Connection 3f Web Gap Stress Gradient Before and After the Repair

Figure 7-51 shows schematically the areas of interest in the connection 3f repair model and Table 7-7 summarizes the corresponding stresses developed at these locations. As in connection 3g, the maximum post-retrofit stresses in the model are observed shifting to the vertical and horizontal diaphragm-to-stiffener weld intersection, Point L [Figure 7-51(a)]. The σ_x and σ_y stresses developed at this point are 7.7 ksi and 15 ksi, both higher than ½ CAFT. This new concentration zone, therefore, needs to be checked frequently and carefully during future bridge inspection. As in connection 3g, since the detail is in a relatively low stress range (less than CAFT), the overall performance of the repair at this location is still considered acceptable.

TABLE 7-7: Stresses of Potential Crack Locations in Connection 3f after the Repair

L.C. # 8	Stress	Before Repair	After Repair	AASHTO Fatigue Detail Category	CAFT
Point L	$\sigma_{x,\,max}$	4.8 ksi	7.7 ksi	C	10 ksi
	$\sigma_{y,\,max}$	9.1 ksi	15 ksi	C	10 ksi
Line PQ	σ_y	–	< 2.0 ksi	B or C	16 or 10 ksi
	σ_z	–	< 2.6 ksi	B or C	16 or 10 ksi

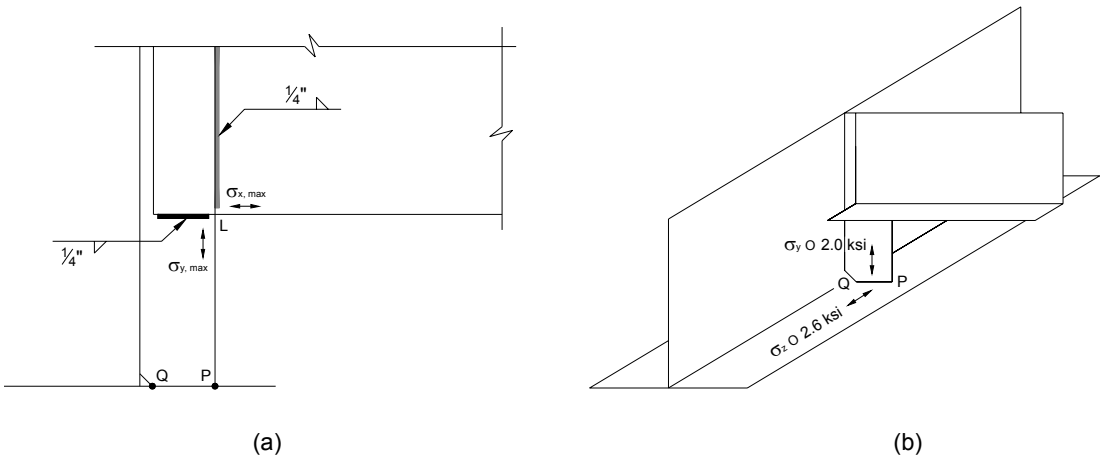

FIGURE 7-51: Areas of Interest in the Connection 3f Repair Model

The stresses normal to line PQ are also checked, as illustrated in Figure 7-51(b), because the stiffener is now connected to the bottom flange. For all 20 load cases, the σ_y stresses at the stiffener plate are below 2.0 ksi and the σ_z stresses at the girder flange are below 2.6 ksi. Since the stress magnitudes are lower than ½ CAFT of either a Category B or C' detail, both welded and bolted attachments can be used for the flange-to-stiffener connections without creating a new stress concentration site at this detail after the repair.

The repair analysis for the other positive moment region connection 3d is not performed as it is supposedly subjected to lower magnitude fatigue stresses than connection 3f as per the previous investigation.

7.4.2.2 Repair Analysis for Connection 3h

The repair analysis carried out for connection 3h bottom flange detail yields similar results as those of connection 3f except that lower stress magnitudes are obtained. As tabulated in Table 7-8, all the web gap stresses are decreased to below ½ CAFT and the average percentage reductions for σ_x, σ_y, and σ_z are 102%, 87% and 103%, respectively. Figure 7-52

illustrates the change of web gap σ_y stress gradient before and after the repair at Load Case No. 11. Table 7-9 summarizes the stresses of the areas of interest in the repair model. The maximum σ_x and σ_y stresses again occur at Point L [Figure 7-53(a)]. The maximum σ_x (5.1 ksi) is close to ½ CAFT, but the maximum σ_y (11 ksi) is higher still than ½ CAFT, so cracks may have the chance to develop along the horizontal diaphragm-to-stiffener welds during future service. Figure 7-53(b) shows the σ_y and σ_z stresses normal to line PQ at the flange-to-stiffener connection. Both are close to zero for all 20 load cases, so fatigue cracks should not occur at this detail no matter a welded or bolted detail is used. Repair analysis for the bottom flange details of the other transition region connections 3b, 3c, and 3j are not conducted, as the fatigue stresses developed in these connections are lower than that of connection 3h.

TABLE 7-8: Comparison of Connection 3h Web Gap Stresses Before and After the Repair

	Before Repair	After Repair	Average Percentage Reduction	Fatigue Detail Category	CAFT
σ_x	6.3 ksi	< 0	102%	C'	12 ksi
	L.C. # 11	all load cases			
	Point A	Point A			
σ_y	23 ksi	2.9 ksi	87%	C	10 ksi
	L.C. # 11	L.C. # 11			
	Point E'	Point E'			
σ_z	7.7 ksi	0.81 ksi	103%	C'	12 ksi
	L.C. # 11	L.C. # 16			
	Point A	Point A			

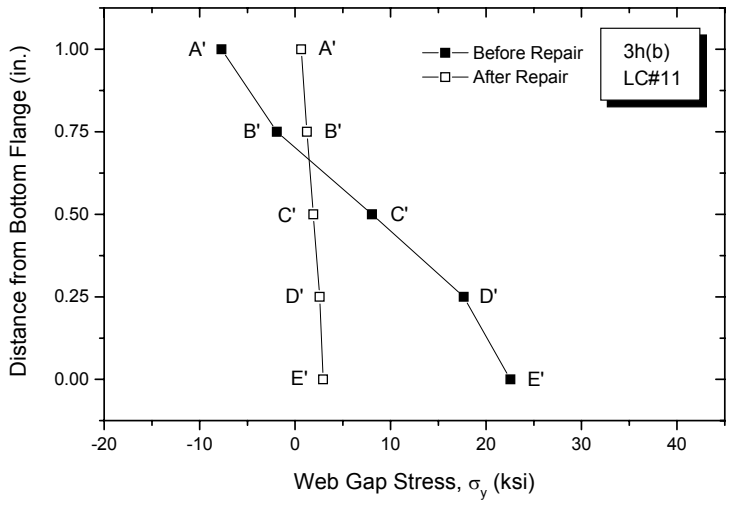

FIGURE 7-52: Connection 3h Web Gap Stress Gradient Before and After the Repair

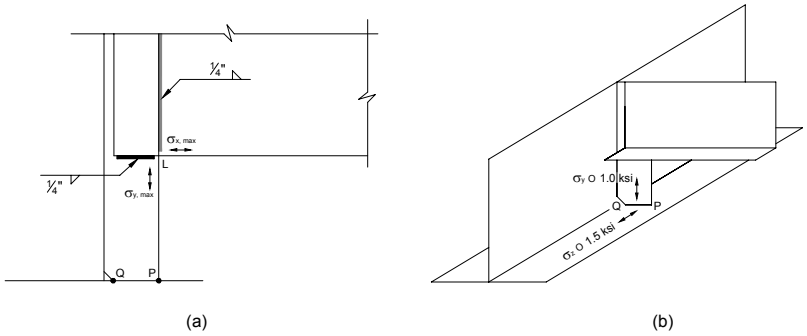

FIGURE 7-53: Areas of Interest in the Connection 3h Repair Model

TABLE 7-9: Stress of Potential Crack Locations in Connection 3h After the Repair

16 or 10 ksi	Stress	Before Repair	After Repair	AASHTO Fatigue Detail Category	CAFT
Point L	$\sigma_{x,\,max}$	4.1 ksi	5.1 ksi	C	10 ksi
	$\sigma_{y,\,max}$	8.9 ksi	11 ksi	C	10 ksi
Line PQ	σ_y	–	< 1.0 ksi	B or C	16 or 10 ksi
	σ_z	–	< 1.5 ksi	B or C	

7.4.2.3 Repair Analysis for Connection 3k

For those diaphragm-girder connections with unstiffened top flange web gap details, only the flange-to-web welds are subjected to stress magnitudes that can cause fatigue cracking. The crack opening stresses are also much lower than those developed in the bottom flange details. Finite element repair analysis is carried out only for connection 3k, since the web gap stresses developed in this connection are the highest among those of the same group of details. Table 7-10 shows the web gap stresses of connection 3k both before and after the repair. The post-retrofit stresses are all close to zero and the average percentage reductions for σ_x, σ_y, and σ_z stresses are 102%, 85%, and 126%, respectively. Figure 7-54 shows the comparison of web gap σ_y stress gradient before and after the repair on the stiffener side of the girder web at Load Case No. 12. Though the stress variation is not as dramatic as seen in the bottom flange web gap details, the effect of stress reduction after the repair is still obvious. The repair model of connection 3k also indicates a curvature of out-of-plane web gap deflection as of Figure 7-31(a). Though with much less degree of distortion than the unstiffened condition, it still places Point E on the stiffener side of the web in tension and Point E' on the no-stiffener side of the web in compression.

TABLE 7-10: Comparison of Connection 3k Web Gap Stresses Before and After the Repair

	Before Repair	After Repair	Average Percentage Reduction	Fatigue Detail Category	CAFT
σ_x	< 0 ksi	0.058 ksi	102%	C'	12 ksi
	all load cases	L.C. # 9			
	Point A	Point A			
σ_y	10 ksi	1.6 ksi	85%	C	10 ksi
	L.C. # 12	L.C. # 12			
	Point E	Point E			
σ_z	< 0 ksi	0.72 ksi	126%	C'	12 ksi
	all load cases	L.C. # 10			
	Point A	Point A			

TABLE 7-11: Stresses of Potential Crack Locations in Connection 3k After the Repair

L.C. # 12	Stress	Before Repair	After Repair	AASHTO Fatigue Detail Category	CAFT
Point L	$\sigma_{x, max}$	< 0	-2.4 ksi	C	10 ksi
	$\sigma_{y, max}$	< 0	-4.2 ksi	C	10 ksi
Line PQ	σ_y	–	< 2.6 ksi	B or C	16 or 10 ksi
	σ_z	–	< 1.5 ksi	B or C	16 or 10 ksi

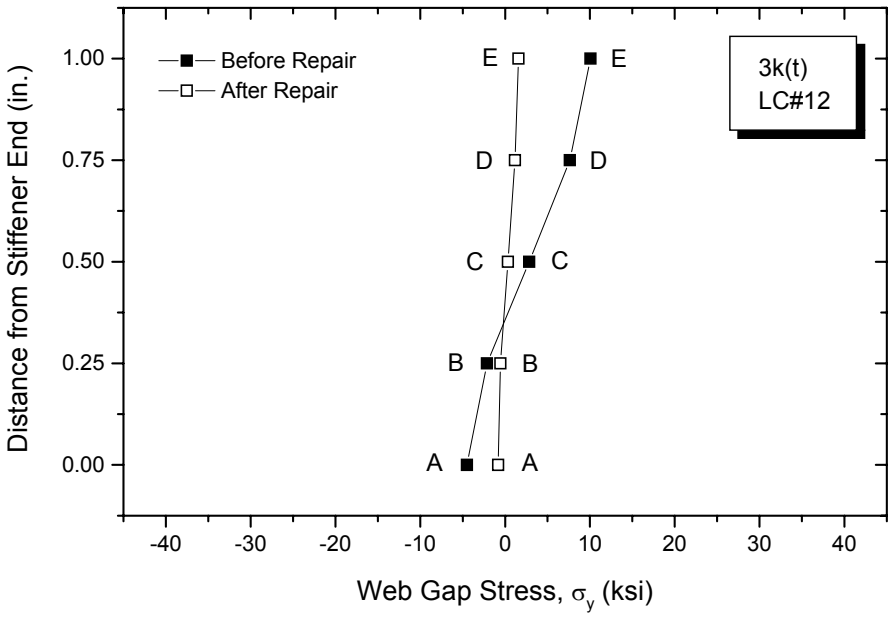

FIGURE 7-54: Connection 3k Web Gap Stress Gradient Before and After the Repair

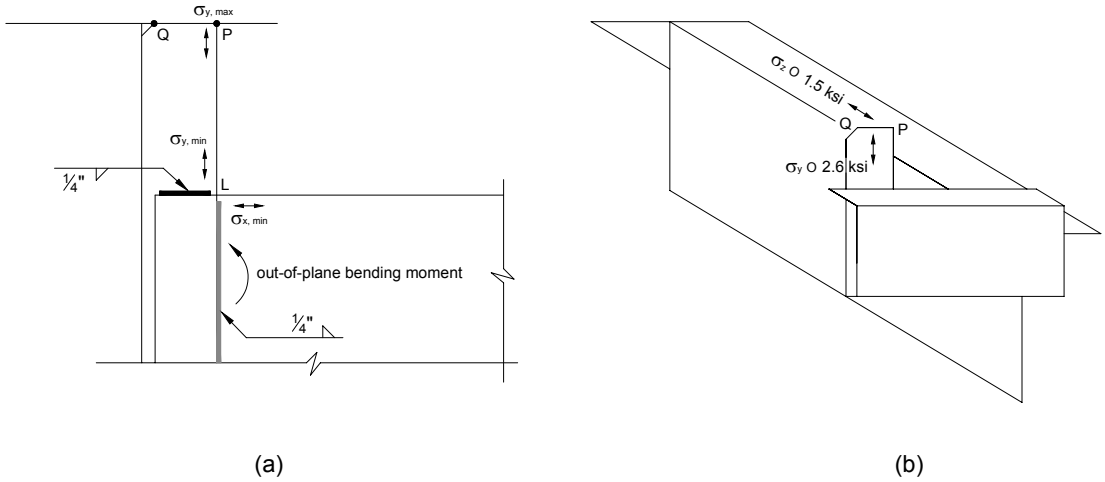

FIGURE 7-55: Areas of Interest in the Connection 3k Repair Model

For all 20 load cases, the end of the diaphragm is subjected to positive out-of-plane bending moment. Therefore, as shown in Figure 7-55(a), Point L at the horizontal and vertical weld intersection is placed in a field of compressive stress. The minimum σ_x and σ_y stresses of

the repair model are -2.4 ksi and -4.2 ksi, respectively, occurring at Load Case No. 12. Since both stresses are compressive, fatigue cracking will not occur at the diaphragm-to-stiffener connection welds. Figures 7-56 and 7-57 plot the σ_x and σ_y stress contours of Load Case No 12 for the repair model of connection 3k. The maximum σ_y stress now occurs at Point P, with a magnitude of 2.6 ksi at Load Case No. 14. Figure 7-55(b) shows the stresses along line PQ at the flange-to-stiffener connection. The σ_y stresses are lower than 2.6 ksi and the σ_z stresses are lower than 1.5 ksi for all 20 load cases. Thus, either a bolted or a welded connection can be used for the repair and fatigue cracking will not develop in the flange or the stiffener at the attachment. Table 7-11 summarizes the stresses developed at Point L and line PQ in the repair model.

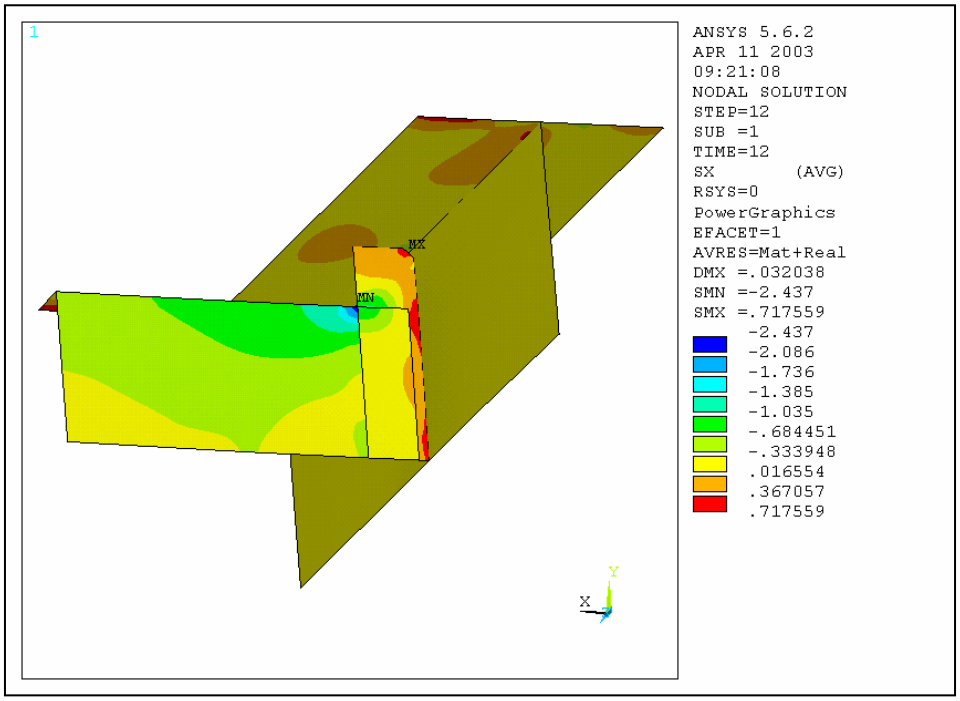

FIGURE 7-56: Post Retrofit σ_x Stress Contour of Connection 3k at Load Case No. 12

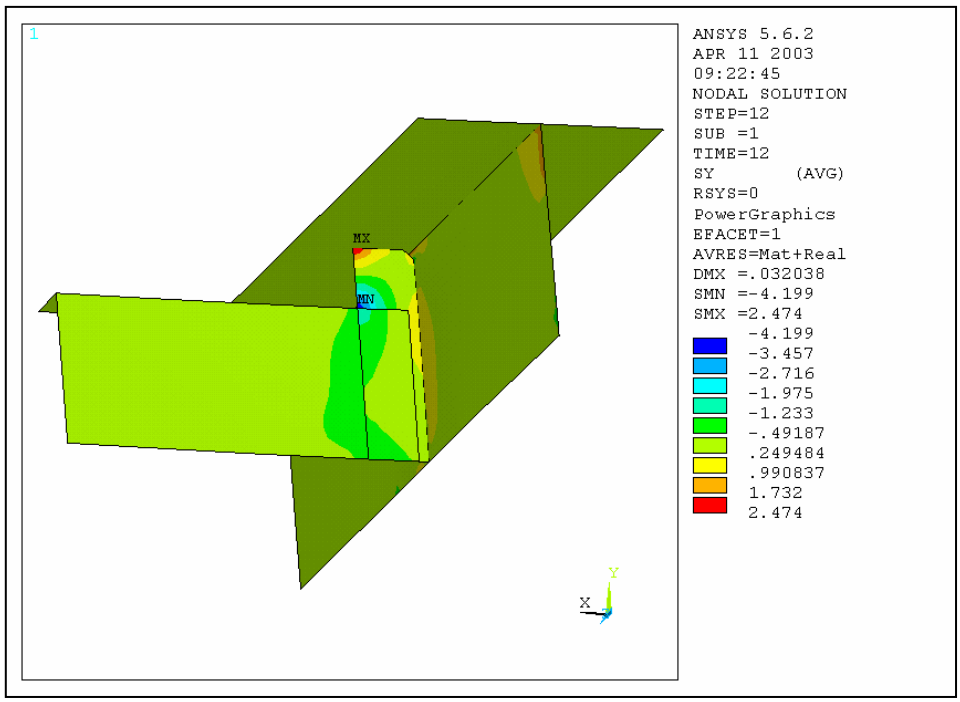

FIGURE 7-57: Post Retrofit σ_y Stress Contour of Connection 3k at Load Case No. 12

Connection 3a has the same stress condition as connection 3k, since both of them are in the negative moment region. But for the four connections with unstiffened top flange web gaps in the transition region, the stresses developed in the repair models are mostly in opposite signs, due to the negative out-of-plane bending moments occurring at the diaphragm ends. Thus, for connections 3b, 3c, 3h, and 3j, the σ_x and σ_y stresses developed at Point L are in tension. However, since the overall stresses of the submodels with top flange web gap details are much lower than those of the bottom flange submodels, the stresses at Point L and its vicinity are expected to be lower than ½ CAFT. The σ_y and σ_z stresses along line PQ should also be close to zero. Therefore, fatigue cracks will not develop at the top horizontal and vertical diaphragm-to-stiffener connection welds and the top-flange-to-stiffener attachment after the repair.

7.4.3 Repair Recommendations

The following repair recommendations are proposed based on the foregoing finite element study of the Winfield Bridge:

1. Repair is only needed for the unstiffened web gaps of Girder G2 and G3. The corresponding connections of the two girders should be repaired using the same method.
2. Although the repair analysis shows that, for all the diaphragm-girder connections, the stresses normal to the flange-to-stiffener attachment (line PQ) are below ½ CAFT of either the Category B or C' detail, it is recommended that bolted connections (Category B details) be used for the repair of the positive moment region bottom flange web gaps, since the differential girder deflections are the largest and the out-of-plane fatigue stresses are the highest at these girder sections. Figure 7-58 shows a repair option of using a bolted angle at the flange-to-stiffener connection. The top flange web gaps in the negative moment region and the bottom and top flange web gaps in the transition region can be repaired using the welded connections (Category C' details), as shown in Figure 7-59, since the fatigue stresses developed in these locations are relatively low.
3. The repair analysis indicates that a new crack initiation site will develop at the bottom of the diaphragm-to-stiffener weld intersection (Point L) after the repair, especially for those connections in the positive moment region. It is recommended that peening or ultrasonic impact treatment (UIT) be performed at these details for both the horizontal and the vertical diaphragm-to-stiffener welds. Either one of these two repair methods can improve the fatigue resistance by one category.
4. Since the stresses developed at the top flange web gaps are relatively low (less than CAFT of detail Category C), it is recommended that field testing be carried out before the repair for one transition region connection and one negative moment region connection, preferably connections 3j and 3k, to see if a welded repair at these stiffener ends is a must. Strain gauging along bottom diaphragm-to-stiffener connection welds at a positive moment region connection is also recommended after the repair to see if additional peening or UIT treatment at these locations is necessary.
5. It is recommended that all the structural repairs be accomplished while the bridge is closed to traffic.

A summary of the repair recommendations for the Winfield Bridge is given in Table 7-12.

TABLE 7-12: Repair Recommendations for the Winfield Bridge

Connection	Moment Region	Web Gap Location	Repair Recommendations	Remarks
3e, 3g	Positive	Bottom Flange	Perform peening or UIT treatment to the bottom diaphragm-to-stiffener connection welds.	Peening or UIT treatment can be disregarded upon field testing results.
2d, 2e, 2f, 2g 3d, 3f	Positive	Bottom Flange	Bolt the connection stiffener to the bottom flange. Perform peening or UIT treatment to the bottom diaphragm-to-stiffener connection welds.	
2b, 2c, 2h, 2j 3b, 3c, 3h, 3j	Transition	Bottom and Top Flange	Weld the connection stiffener to both the top and bottom flanges.	Weld repair at the top flanges can be disregarded upon field testing results.
2a, 2k 3a, 3k	Negative	Top Flange	Weld the connection stiffener to the top flange.	

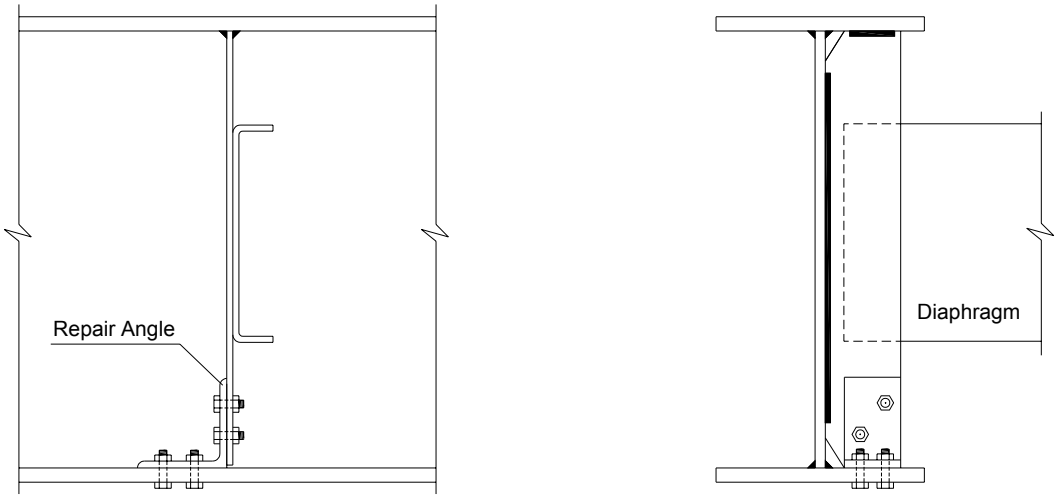

FIGURE 7-58: Bolted Repair Used for the Positive Moment Region Connections

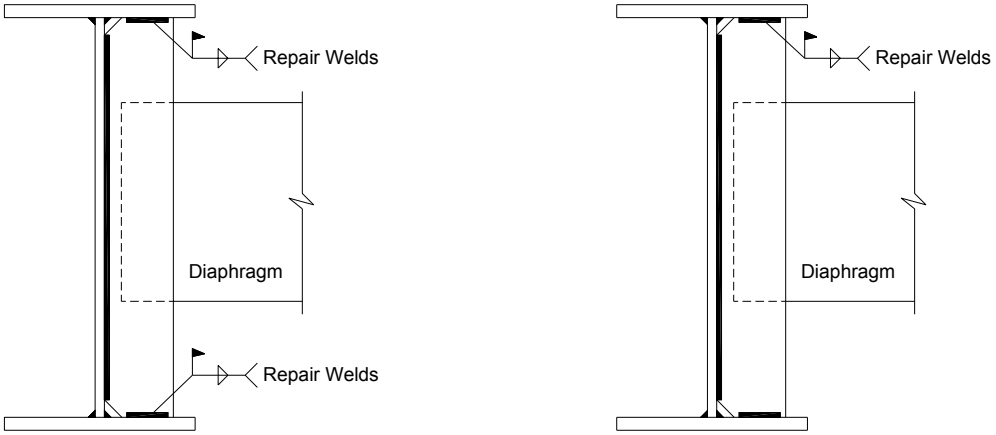

(a) transition region (b) negative moment region

FIGURE 7-59: Welded Repair Used for the Transition and Negative Moment Region Connections

7.5 Fisher's σ – Δ Expression

Though the submodel analyses indicate that the zero web gap stresses are not located at the middle of the web gap length, Fisher's formula for out-of-plane stress calculation is still used assuming equal double curvature. The results are then compared with those obtained directly from the ANSYS solution, as shown in Table 7-13. For all the 14 web gap details of Girder G3, the stresses calculated by Fisher's formula are more than two times of the maximum stress values yielded by ANSYS at Point E or E'. Since the out-of-plane displacement values are in a reasonable range, the Fisher's formula apparently needs an additional adjustment factor in order to produce close to actual web gap stresses in the bridge. Using the highest web gap stresses from the ANSYS solution, the average ratio of $\sigma_{y,\,ANSYS} / \sigma_{y,\,Fisher}$ for the 14 Girder G3 details under investigation is 0.38.

TABLE 7-13: Web Gap Stresses Obtained from Fishers's Formula and ANSYS Analysis

Connection or Submodel	Load Case No.	Out-of-Plane Displacement Δ (in.)	Fisher $\sigma=3E\Delta t_w/L^2$ (ksi)	ANSYS σ_y (ksi) @ Point			
				A	E	A'	E'
3a (t)	3	8.87×10^{-4}	± 24	-4.4	9.5	3.8	-10
3b (t)	4	3.87×10^{-4}	± 11	1.5	-3.9	-1.1	4.3
3b (b)	4	1.59×10^{-3}	± 43	5.7	-13	-4.8	14
3c (t)	5	6.43×10^{-4}	± 17	1.8	-5.7	-1.2	6.2
3c (b)	5	1.85×10^{-3}	± 50	7.7	-19	-6.6	20
3d (b)	5	3.26×10^{-3}	± 89	14	-31	-12	33
3e (b)	7	3.38×10^{-3}	± 92	15	-33	-13	35
3f (b)	8	3.56×10^{-3}	± 97	16	-35	-14	37
3g (b)	9	3.73×10^{-3}	± 101	16	-35	-14	37
3h (t)	11	4.74×10^{-4}	± 13	0.54	-1.8	-0.13	2.1
3h (b)	11	2.08×10^{-3}	± 57	9.0	-21	-7.7	23
3j (t)	12	6.72×10^{-4}	± 18	2.9	-9.0	-2.3	9.5
3j (b)	11	1.99×10^{-3}	± 54	7.0	-17	-6	18
3k (t)	12	9.05×10^{-4}	± 25	-4.5	10	3.9	-11

Note: $t_w = {}^5/_{16}$ in., L = 1 in., E = 29000 ksi.

7.6 Summary

Conclusions and recommendations are drawn as follows based on the coarse-to-fine submodeling procedures conducted in this chapter for the investigation of the Winfield Bridge. The finite element analysis is carried out only for Span No. 3, but the conclusions can be extended to the other four spans as long as they have the similar structural layout.

1. The diaphragm-girder connections of the two interior girders are subjected to stress amplitudes that can cause fatigue cracking. In particular, those bottom flange web gaps located in the mid-span positive moment region connections are

exposed to stress ranges close to yielding, so expeditious structural repair should be carried out for these details before cracks start to initiate.

2. The stress gradient diagrams show that the unstiffened web gaps of the Winfield Bridge are not subjected to equal double curvature under the out-of-plane distortion. The locations of zero stresses are always closer to the stiffener end and further away from the flange end of the web gaps.
3. Retrofit should be carried out using rigid attachments between the connection stiffeners and the girder flanges. A bolted repair is recommended for the positive moment region connections and a welded repair is recommended for the transition and negative moment region connections. The connections of the two exterior girders need no repair even with the web gaps left unstiffened.
4. For the positive moment region connections, a new crack initiation site may develop after the repair at the bottom horizontal and vertical diaphragm-to-stiffener weld intersection. It is recommended that peening or ultrasonic impact treatment be carried out at these details to improve the fatigue resistance of the weld toes and to inhibit the potential crack initiation as well.
5. Strain measurements of staggered diaphragms are not available from previous research studies. Thus, it is recommended that field testing be performed for the Winfield Bridge before the retrofit is applied, so that the stress data under the real traffic loading can be collected and used to compare with the analytical solution. The field experimental results can also help to determine whether the repairs are necessary for those details with relatively low fatigue stresses, such as the welded repair for the top flange web gaps and the peening or the ultrasonic impact treatment for the diaphragm-to-stiffener connection welds.
6. The web gap stresses calculated by Fisher's formula are significantly higher than what can actually occur in the field. The average ratio of the maximum ANSYS web gap stresses vs. Fisher's results is 0.38. It is therefore recommended that this adjustment factor be applied to the equation in order to generate reasonable stress predictions for the bridge.

Chapter 8

Case Study 4: The Hump Yard Bridge

The Hump Yard Bridge developed bottom flange web gap fatigue cracks at the cross-frame to girder connections near the piers. The repair procedure proposed by KDOT is to drill stop holes at the crack tips and to weld the connection stiffeners to the girder flanges. In-depth finite element studies are presented in this chapter, at both the coarse model and the submodel levels, in order to explore the development of existing cracks observed in the bridge and to identify other potential crack initiation sites during future service. Investigations are also conducted to evaluate the KDOT repair plan and other possible retrofit alternatives that can effectively reduce or eliminate the secondary stresses. The goal is to provide a comprehensive study of the bridge structure, to reveal the fundamental behavior of out-of-plane distortion-induced fatigue at the cross-frame to girder connections, and to recommend appropriate repair methods to extend the bridge's life.

8.1 Description of the Bridge

The Hump Yard Bridge was built in 1970 on highway I-635 in Kansas City, Kansas. It is a skewed multiple-girder bridge with twin structures: the west bridge [KDOT Bridge No. 635-105-3.55(040)] carries southbound traffic and the east bridge [KDOT Bridge No. 635-105-3.56(041)] carries northbound traffic. Both structures have 6 units and 35 spans, with varied span lengths and cross section widths. Figure 8-1 shows, for example, the framing plan of Span No. 8 between Piers No. 7 and No. 8. In most circumstances, intermittent transverse cross-frames were designed for the bridge; i.e. the cross-frames were not installed continuously, but only in every other bay across the bridge width. At a very few locations, however, floor-beam/stringer arrangement was

used instead of the cross-frames (Figure 8-4b). Figure 8-2 shows the traffic lanes of Spans No. 6 and No. 7 between Piers No. 5 and No. 7. For the west bridge, the roadway width includes a 6 ft inside shoulder, four 12 ft driving lanes, a variable width transition section for the off ramp, and a 6 ft outside shoulder. The east bridge has the similar lane divisions except that there are only three driving lanes within these two spans. The noncomposite deck slab is uniform 7¼ in. thickness with compressive strength f_c' of 4000 psi. Structural steels are A36 except at the hinges and the shear transfer devices, where A242 is used. The 2002 AADT of the bridge is 80,000 vpd (vehicles per day) with 10% trucks.

8.2 Crack Scenario and KDOT Repair Plan

During the 1997 bridge inspection, fatigue cracks were first observed in Span No. 8 of the west bridge at three cross-frame to girder connections. As shown in Figure 8-1, the cracks were identified at the negative moment region close to Pier No. 8 in Girders 2-2W, 2-5W, and 2-8W. All the cracks were found at the small web gaps close to the girder bottom flanges and had propagated through the web thickness. Figure 8-3 shows the inspection pictures of the three locations with the cracks marked by arrows pointing toward the crack tips. The yellow (greyer) arrows were placed during the 1997 inspection. The white (brighter) arrows were placed during a later inspection in 2000. Fatigue crack growth between these two inspections can be noticed clearly by the distance between the ends of the two sets of arrows.

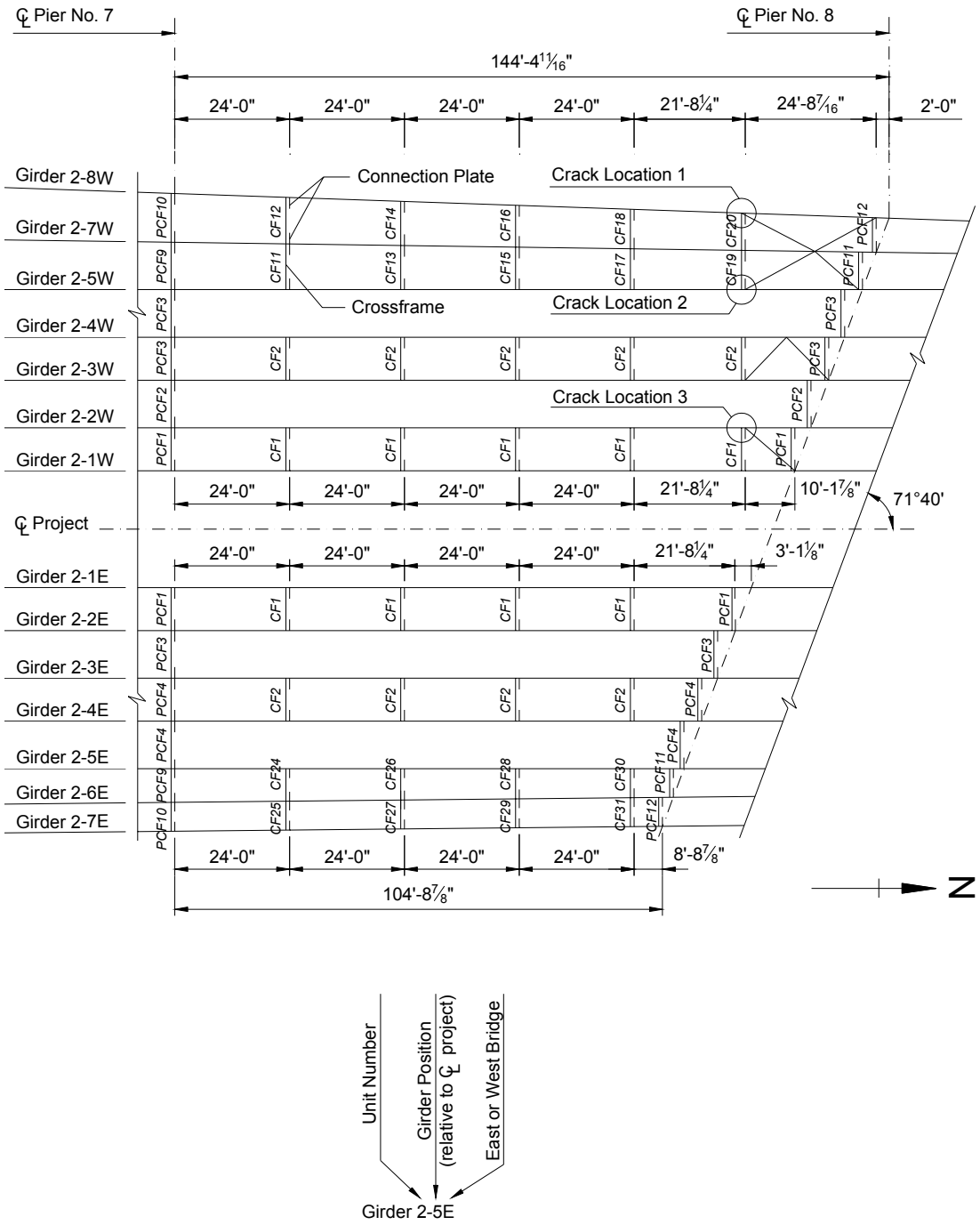

FIGURE 8-1: Steel Framing Plan and Crack Locations of the Hump Yard Bridge Span No. 8

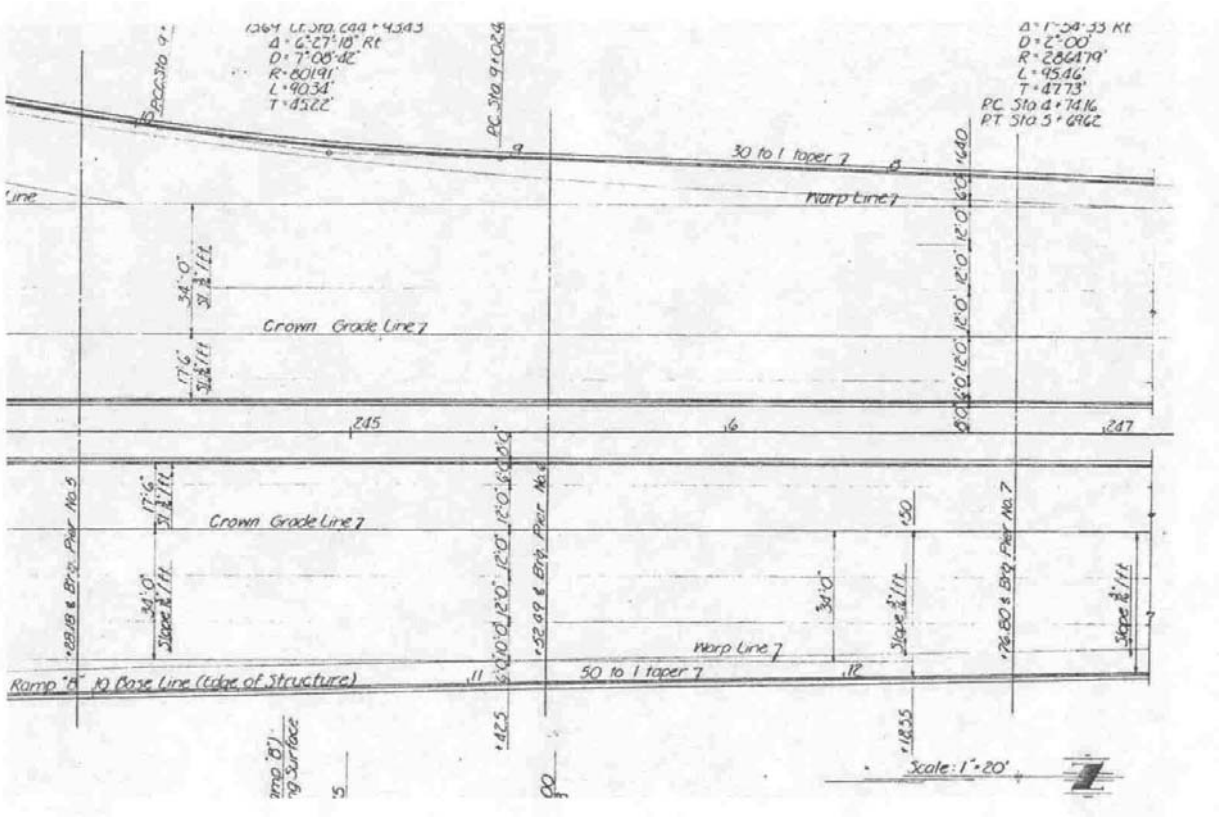

FIGURE 8-2: Bridge Plan Showing Traffic Lanes between Pier No. 5 and No. 7

(a) Girder 2-2W

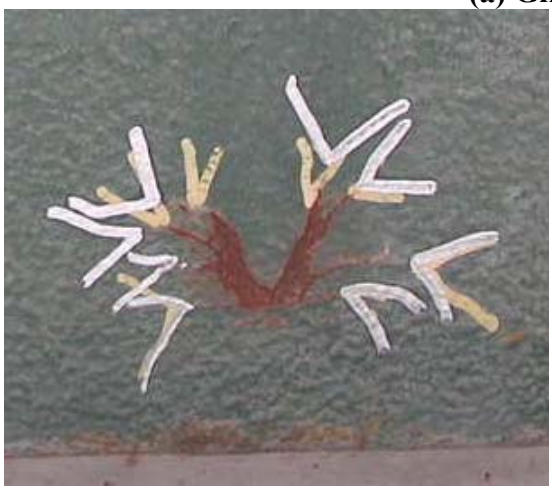

(b) Girder 2-5W

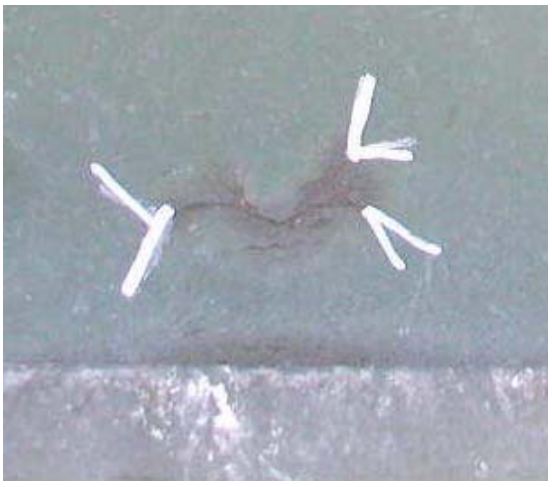

(c) Girder 2-8W

FIGURE 8-3: Inspection Pictures Showing Bottom Flange Web Gap Cracks in Span No. 8

New crack locations and crack types were found in other spans of the bridge during the 2000 inspection. A repair plan was prepared by KDOT in late 2001. The construction will not

be carried out until after 2002. These cracks found in 2000 and their corresponding repair methods are described as follows:

1) **Type A Repair**: Additional web gap cracks were found in Spans No. 20 and No. 33 during the 2000 bridge inspection, as shown in Figure 8-4. A1 refers to the horseshoe cracks and A2 refers to the horizontal cracks. The crack detail in Span No. 20 occurred at a cross-frame to girder connection in the bottom flange web gap. This is the same as those developed in Span No. 8. Cracks in Span No. 33, however, occurred at two floor-beam to girder connections in the top flange web gaps, as shown in Figure 8-5. Repairs of these web gap cracks, including those developed in Span No. 8, are categorized as Type A repairs. As illustrated in Figure 8-6, the retrofit plan is to drill 1 in. diameter holes at the crack tips, cold work and enlarge the holes by $^{1}/_{16}$ in. using a mandrel, and fill the holes by ASTM A325 bolts. The connection stiffener will then be attached to both the top and bottom girder flanges by welding. Type A1 and A2 cracks are the focus of the finite element study.

2) **Type B Repair**: Two new crack details were also found in Abutment No. 2 at the floor-beam to girder connections during the 2000 bridge inspection, as shown in Figures 8-7 and 8-8. The cracks initiated from the top end of the vertical stiffener-to-web welds and then propagated downward into the stiffener plate. The repair method proposed by KDOT is to arrest the crack propagation by drilling holes at the crack tips, increasing the hole size by cold expansion, and installing A325 bolts, as for the Type A repair. Then the cracks will be mended by square-groove welds and the stiffeners will be connected to the top flanges by fillet welds. Repairs applied at these two locations are categorized as Type B repairs. The out-of-plane distortion mechanism at the abutments is due to end constraint of the floor-beams. Type B repairs are discussed briefly below but are not the subject of the finite element study.

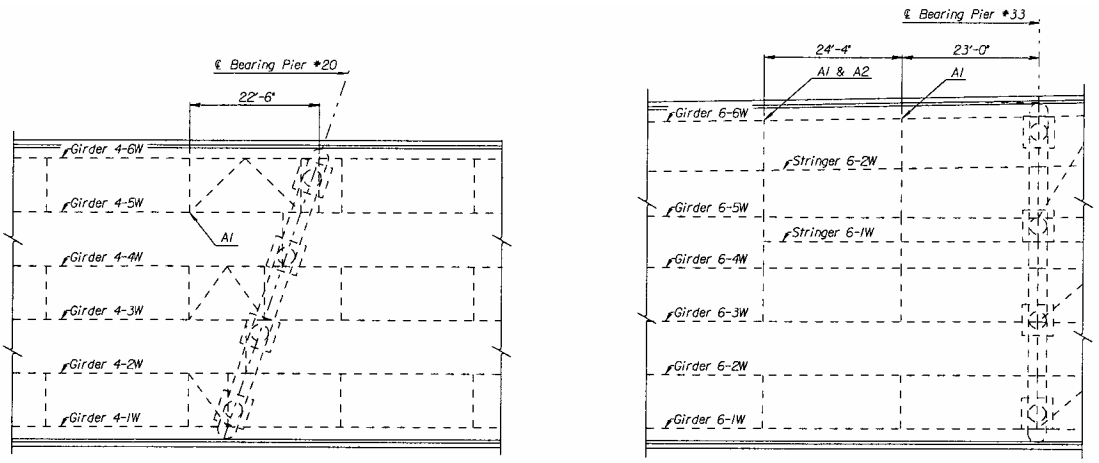

(a) Span No. 20 (b) Span No. 33

FIGURE 8-4: Crack Locations in Span No. 20 and No. 33

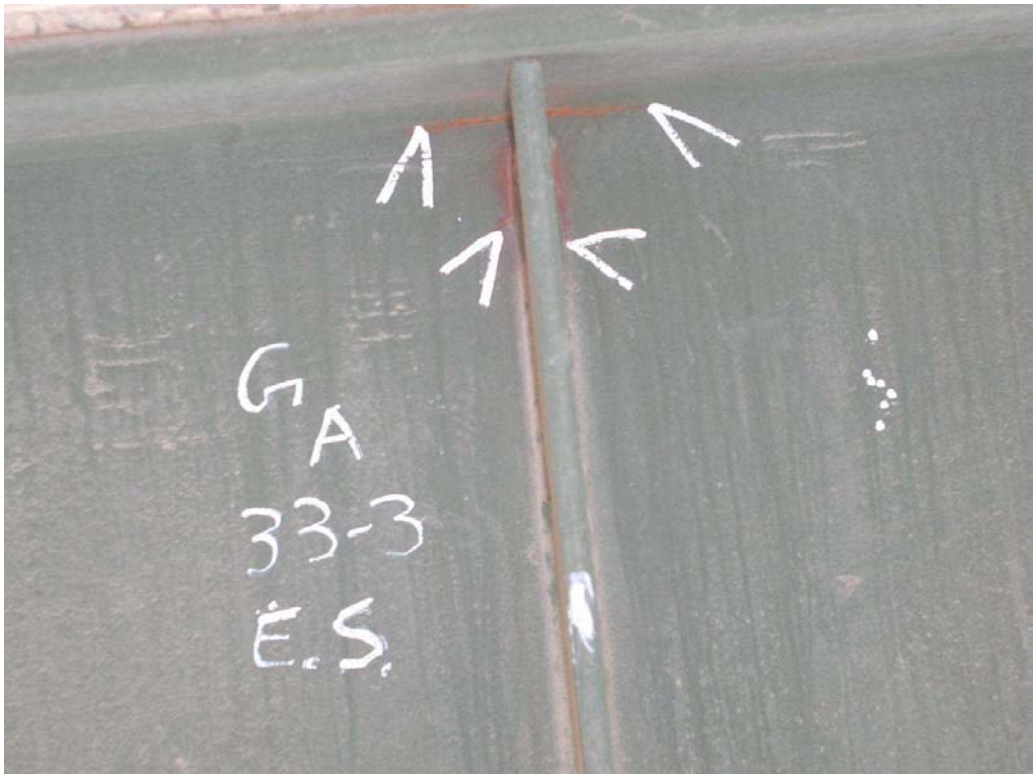

FIGURE 8-5: Top Flange Web Gap Cracks Developed in Span No. 33

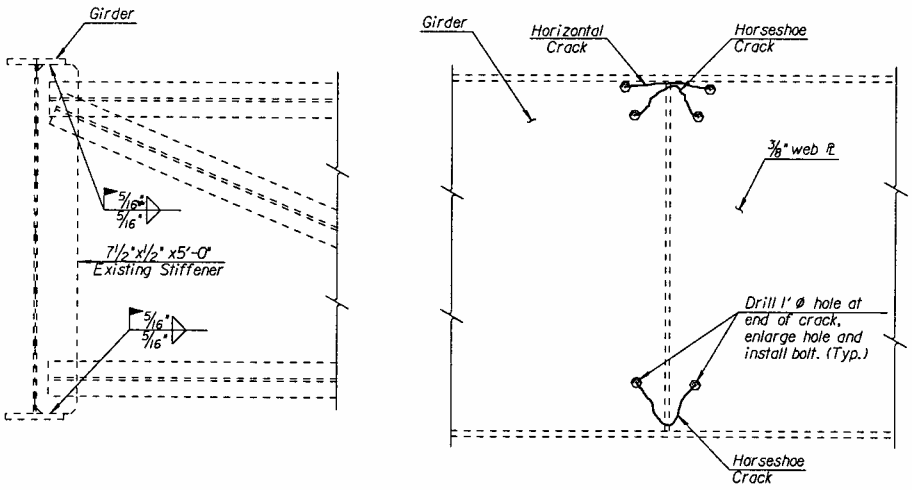

FIGURE 8-6: Type A Repair for Web Gap Cracks

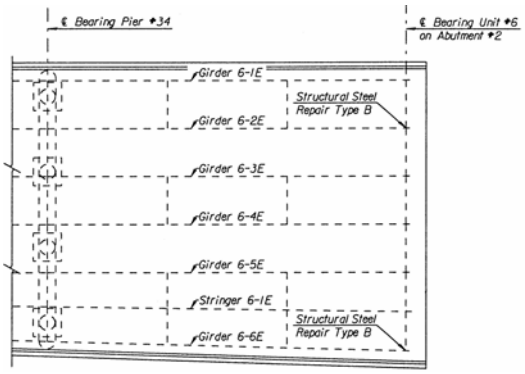

FIGURE 8-7: Type B Crack Locations at Abutment No. 2

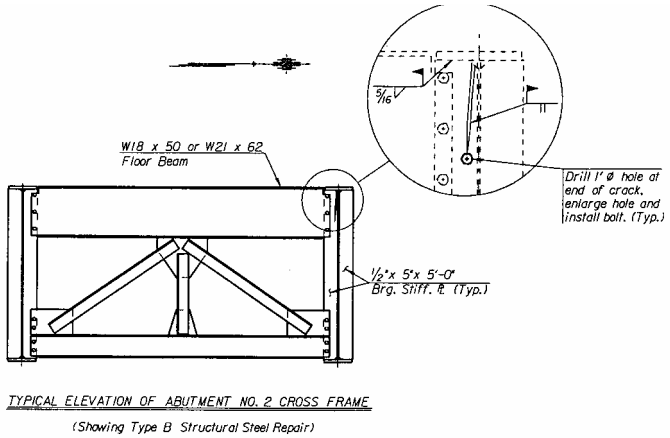

FIGURE 8-8: Type B Repair for Cracks in Bearing Stiffener Plate

Both Type A and B repairs will be accomplished while the bridge is closed to traffic. After reviewing the KDOT repair plan, it is believed that the application of cold expansion in both Type A and B repairs is not appropriate. As previously stated in Section 2.4.2, the existence of a crack on the drilled hole circumference may invalidate the formation of the hoop and radial compressive stress fields in the hole neighborhood, since the crack could open up when the tapered mandrel is pulled from one side of the hole to the other [Figure 2-9(c)]. This concern has been reported to KDOT and an agreement has been reached that cold working will not be used during the actual bridge repair. For the Type B crack, it is believed that the appropriate repair procedures should be to drill a hole at the crack tip, groove-weld the vertical crack, grind the plate surface smooth, and then drill a larger hole or use some other method to remove the end of the welds before the bolt is installed. In fact, bolt installation may not be needed, as the crack path should be eliminated after the repair welding. These suggestions will be submitted to KDOT at a later time together with the finite element analysis results.

The bottom flange web gap cracks are the main research interest of this case study since they are rare in KDOT bridges. Similar cracking conditions have been observed only in the Winfield Bridge at the mid girder span positive moment region (Chapter 7). The four bottom flange web gap crack locations found in the Hump Yard Bridge (three in Span No. 8 and one in Span No. 20), however, all occurred at the negative moment regions close to the bridge piers and at the cross-frame to girder connections with lateral bracings [Figures 8-1 and 8-4(a)]. Span No. 8 of the west bridge has three such crack details and is thus chosen for detailed investigations using the finite element methods.

8.3 Finite Element Study

It is interesting to note that fatigue cracks were not observed at the girder mid-span regions of the

bridge where the differential girder deflections are larger and the out-of-plane distortion magnitudes are higher. Cracks in Span No. 8 are all located at the bottom flange web gaps in the negative moment regions close to bridge piers, where the girder deflections are relatively small and the bottom flanges are mostly in compression. These areas are seemingly the most unlikely crack susceptible details of the bridge structure. To reveal the cause of crack occurrence at these locations and to evaluate the repair methods proposed by KDOT, submodeling procedures are carried out for selected cross-frame to girder connections of Span No. 8, including both the mid-span and the first interior section cross-frame to girder connections, and for both the top and bottom flange web gap details. For issues regarding modeling techniques and fatigue evaluation procedures, see Chapters 4 and 5.

8.3.1 Coarse Model Analysis

8.3.1.1 Assumptions and Simplifications

The structural configuration of Span No. 8 makes it difficult to model the bridge geometry exactly. As shown in Figures 8-1 and 8-2, Girders 2-7W and 2-8W are not parallel to the other girders, so the bridge cross section width changes along the girder span length. Figure 8-9 shows the intermediate cross-frame details of the west bridge. The cross-frame width of CF11 to CF20 in Span No. 8 (see also Figure 8-1) thus also varies for different bridge cross sections. The connection stiffeners are not attached to either the top or the bottom flange and are clipped at both the inside and the outside edges of the plate width when fitting tight to girder flanges. All the cross-frame members are ST4M11.25, which is equivalent to the current steel shape designation of MT4×11.25 structural tees. Figure 8-10 shows the lateral bracing details in Span No. 8 of the west bridge. The lateral bracing members were only designed for those first interior bays close to Pier No. 8 with cross-frames (see also Figure 8-1). The braces were all

fabricated using ST4M14 tees (not available any more from the current steel shape specifications) and were welded to the girder bottom flanges through gusset plates (or lateral connection plates, as termed by the current AASHTO LRFD Specifications [1998]). Figure 8-11 shows the details of Girder 2-4W. The flange width and thickness change frequently within the span length. The other six girders have the similar geometry pattern and have splices and tapers at different locations. In order to avoid intensive modeling work with consideration of these details, the following assumptions and simplifications are made during the coarse model construction:

1) The girder flanges are assumed uniform 18 in. wide and 1 in. thick along the span length for all seven girders. This could change the girder in-plane flexural stresses, but should have little effect on the web gap out-of-plane behavior.
2) Girders 2-7W and 2-8W are assumed parallel to the project centerline with equal spacings as between the other adjacent girders (Figure 8-12). The cross-frame width is thus also assumed constant over the entire span.
3) The roadway width of the bridge cross section is also assumed constant along the span length. The deck slab width built into the coarse model is 63 ft. (Figure 8-13), including four equal traffic lanes and two shoulders, one on each side of the bridge cross section.
4) The connection plate width is assumed half of the flange width. Clip geometries are neglected. Actual plate width will be used later during the submodel analysis.
5) All the stiffeners are assumed attached to the girder flanges to simplify the coarse model construction. Because the connection stiffener to web and flange intersection is away from the submodel cut boundary, this simplification does not cause much difference to the results of DOF interpolation. The actual unconnected stiffener-flange detail will be considered during the submodel analysis.

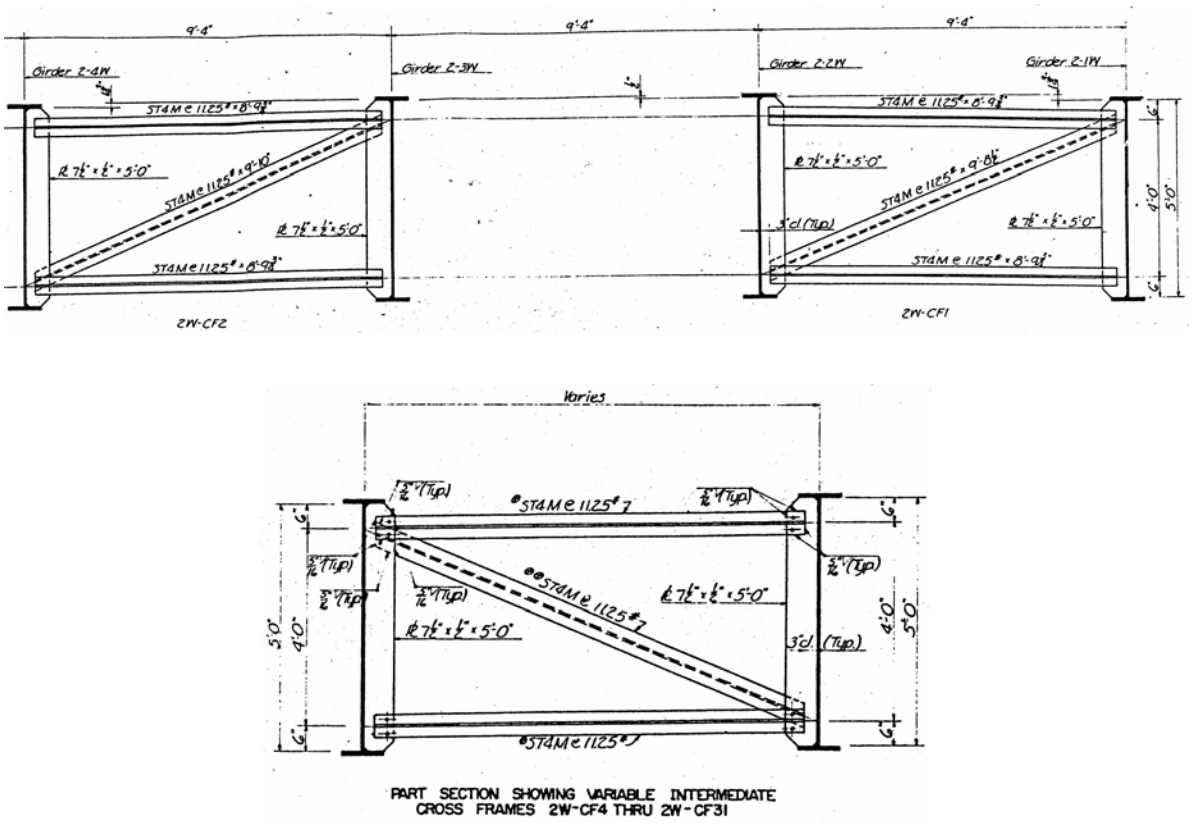

FIGURE 8-9: Intermediate Cross-Frame Details of the West Hump Yard Bridge Span No. 8

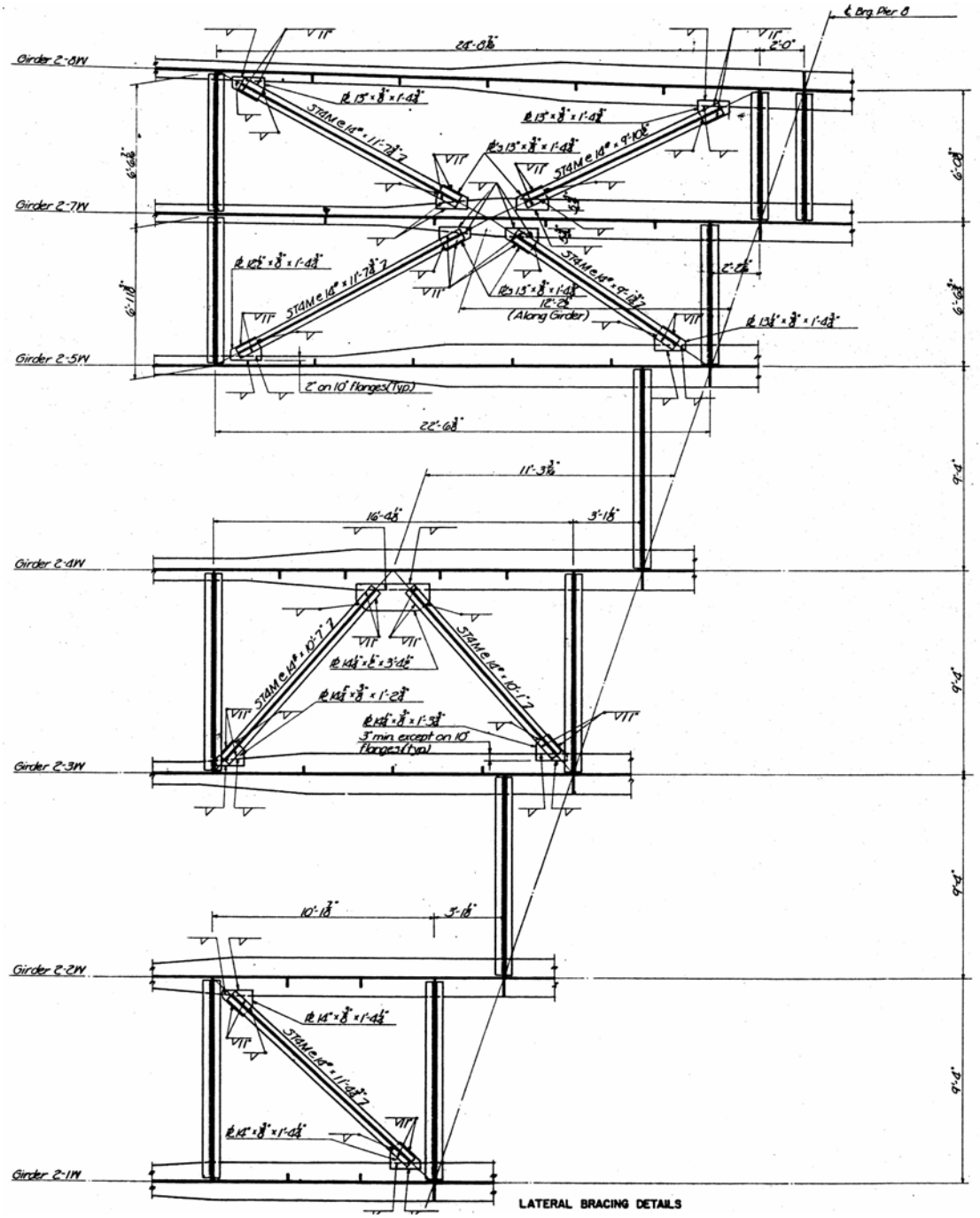

FIGURE 8-10: Lateral Bracing Details of the West Hump Yard Bridge Span No. 8

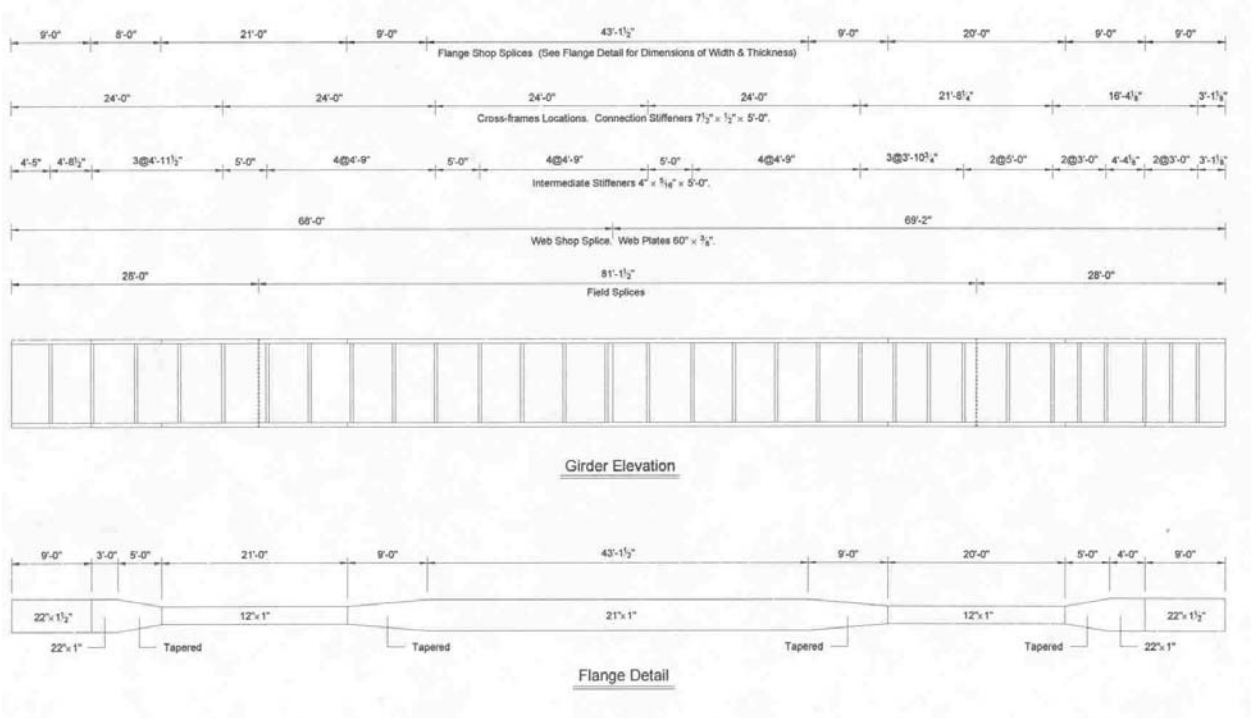

FIGURE 8-11: Girder 2-4W Details of the Hump Yard Bridge

8.3.1.2 Numbering and Designation

Figures 8-12 and 8-13 show the bridge plan and cross section of Span No. 8 revised for the coarse model investigation. An HS15 fatigue truck is placed at the center of Lane 1 and moved in increments of 4 ft from Pier No. 8 to Pier No. 7 for a total of 40 load cases. The wheel load positions of Load Case No. 21 are shown in Figure 8-12 for illustration. Axes A-A to E-E in Figure 8-12 refer to the locations of bridge cross sections with interior cross-frames. To distinguish the standard cross-frames CF1 and CF2 at different cross section locations, the original designation of these cross-frames in the bridge plan (Figure 8-1) is suffixed with the cross section label, as shown in Figure 8-12. For example, CF1 and CF2 at cross section E-E are now changed to CF1E and CF2E. The corresponding numbering of each individual cross-frame member is then denoted affixing the member position to the new cross-frame designation, as shown in Figure 8-14, for example, for cross sections C-C and E-E. The bracing members are

designated BRC1 to BRC7 as shown on the revised bridge plan in Figure 8-12. The cross-frame to girder connections are named combining the respective girder number and cross section label. In particular, as indicated by the square marks in Figure 8-12, connections 2e, 3e, 5e, 8e, 2c, 3c, 5c, and 8c will be studied in detail through submodeling in order to determine the magnitude and distribution of the fatigue stresses developed in the web gap areas.

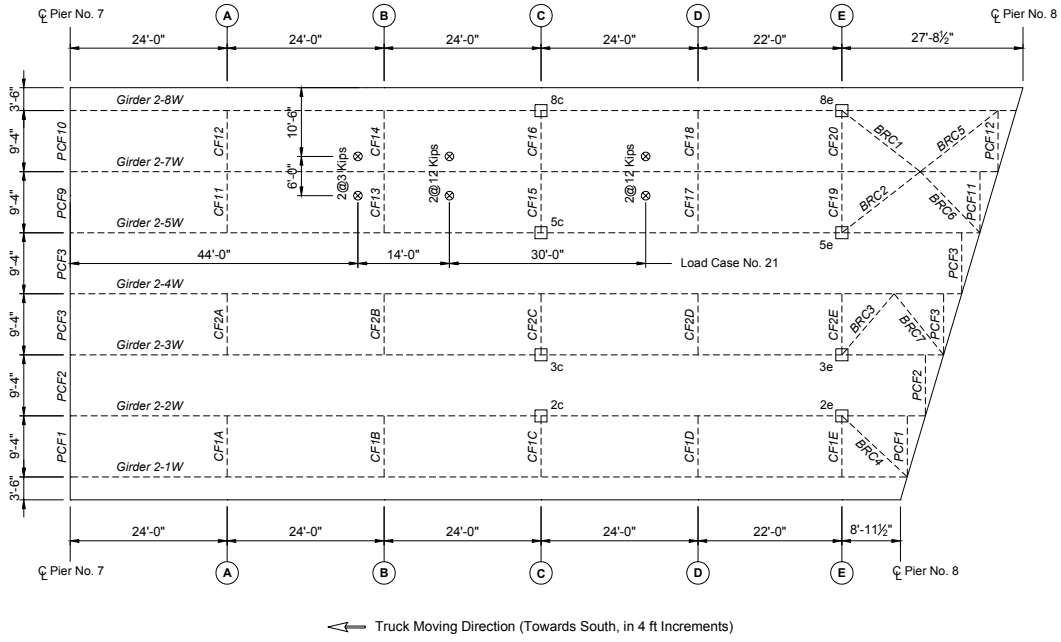

FIGURE 8-12: Revised Bridge Plan of Span No. 8 for Coarse Model Construction

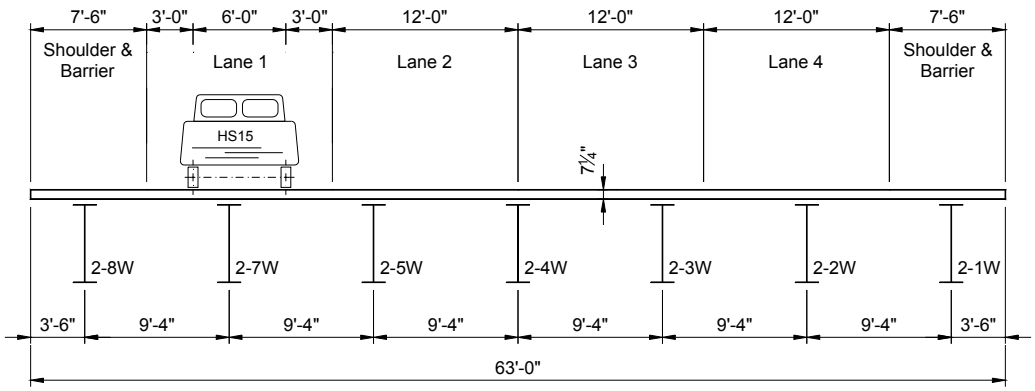

FIGURE 8-13: Revised Bridge Cross Section and Fatigue Truck Location for Coarse Model Investigation

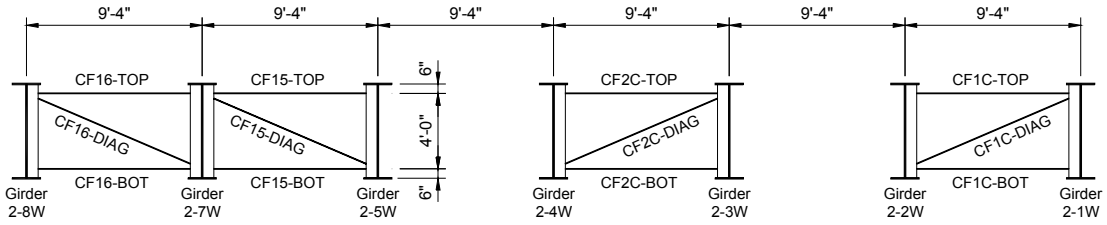

(a) cross section C-C

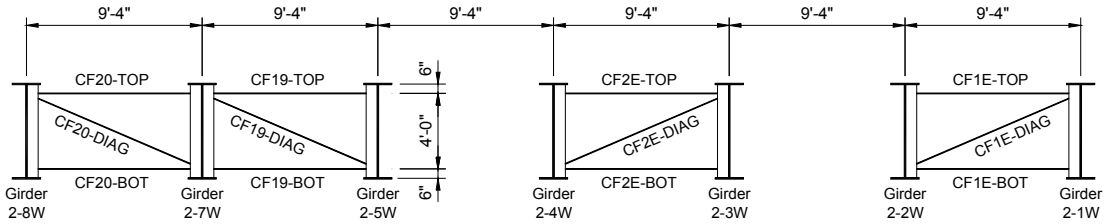

(b) cross section E-E

FIGURE 8-14: Designation of Cross-Frame Members

8.3.1.3 Coarse Model Structure

As shown in Figure 8-15, all the superstructural members of the west bridge Span No. 8 are built into a coarse model composed of 14,500 elements and 19,400 nodes. Figure 8-16 shows schematically the element combination of the coarse model. The concrete deck is modeled using 8-node brick elements (ANSYS Solid 45). The girder components (flanges, webs, and stiffeners) are modeled by 4-node shell elements (ANSYS Shell 181). The cross-frame and bracing members are modeled using 3-D truss elements (ANSYS Link 8). Coupled X and Y DOF sets are generated for coincident nodes at the deck slab and top flange interface. The longitudinal Z direction DOFs are not coupled for these coincident nodes in order to simulate the noncomposite behavior. Assuming the bridge cross sections are fixed at Piers No. 7 and No. 8, the deck and girder end section nodes are fixed to all DOFs.

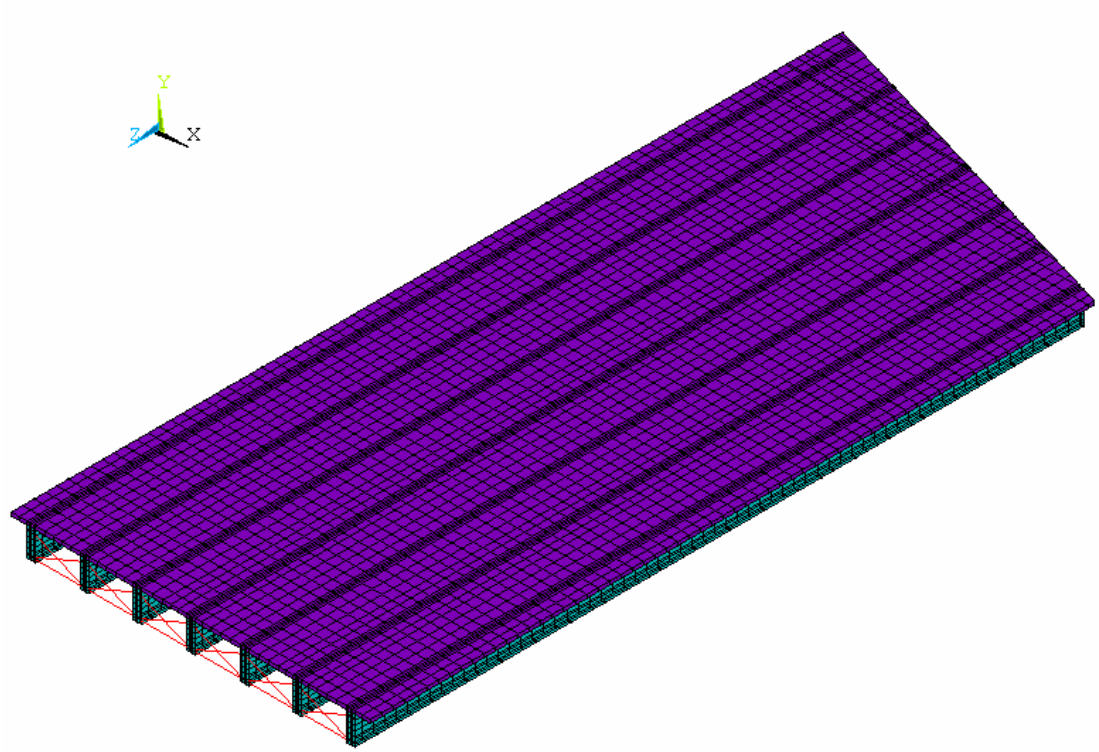

a) isometric view

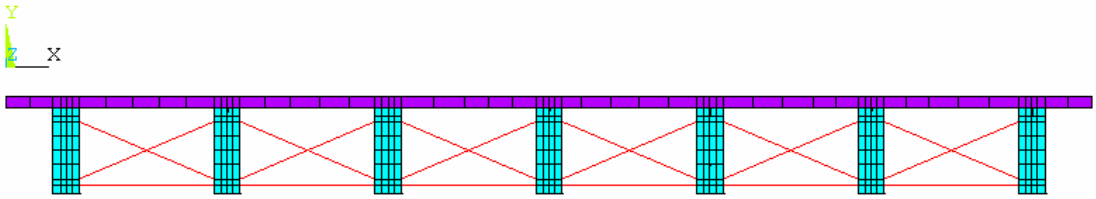

(b) cross section at the bridge pier

FIGURE 8-15: Coarse Model of the Hump Yard Bridge Span No. 8

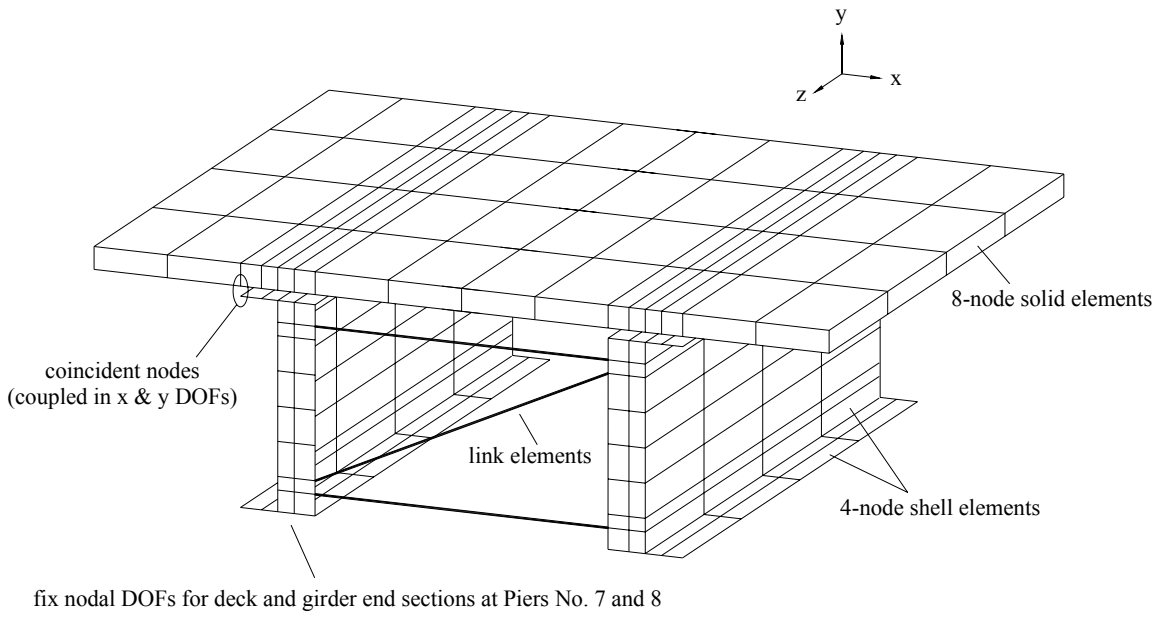

FIGURE 8-16: Typical Girder Section of the Coarse Model Showing Element Combination

Although all the four driving lanes carry southbound traffic, it is believed that Lane 1 close to the outside shoulder is the most heavily loaded and the HS15 fatigue truck is only centered in this lane for the coarse model analysis. Figure 8-17 plots, for example, the overall deformation and vertical deflection (Y direction) contour of the coarse model at Load Case No. 13. The structural members directly underneath or close to the wheel loads apparently yield higher responses than those away from them. Although the web gap fatigue behavior will be studied in detail during the submodel investigation, it can be expected that, since the truck is loaded in Lane 1, higher magnitude fatigue stresses will develop in the cross-frame to girder connections close to the west side of the bridge than in those close to the east side.

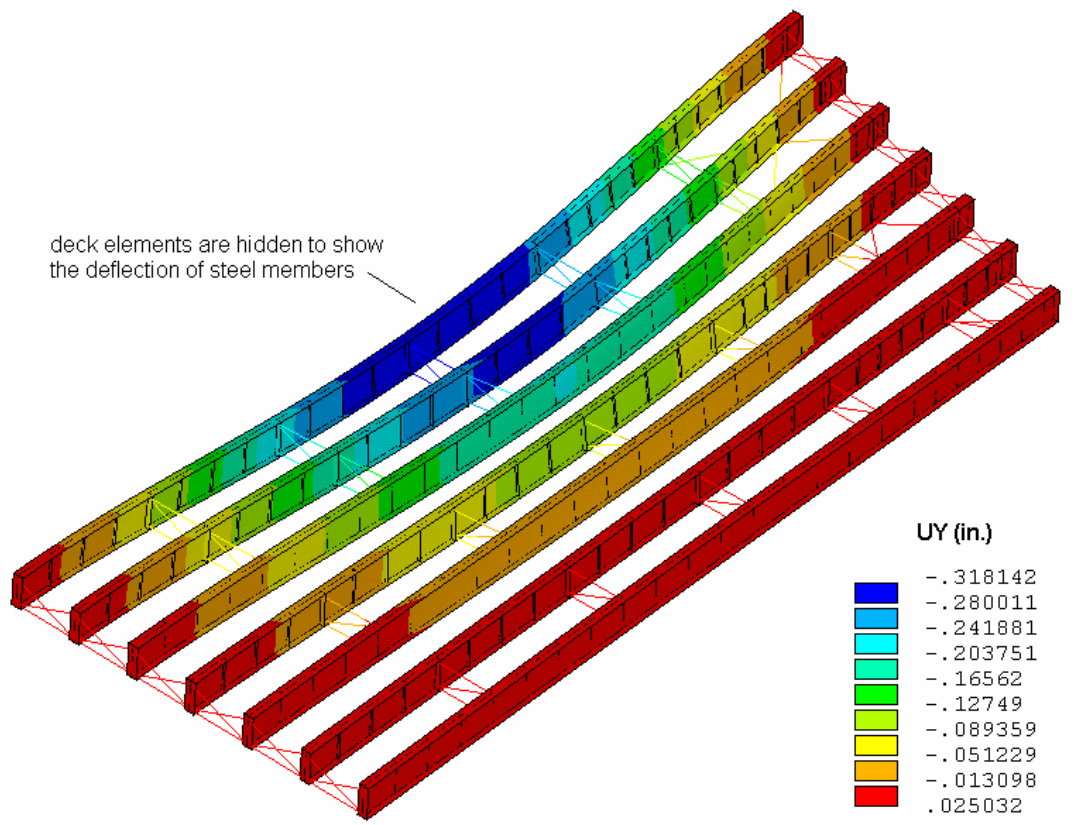

FIGURE 8-17: Coarse Model Contour Showing Vertical Deflection at Load Case No. 13

8.3.1.4 Cross-Frame and Bracing Member Forces

Figures 8-18 to 8-21 present the axial forces of the corresponding cross-frame members in the first interior cross section E-E and the mid-span cross section C-C, as a function of load case numbers (or truck locations). Figure 8-22 plots schematically the member forces of Load Case No. 21 on the cross-frame elevations. Figure 8-23 shows the change of bracing member forces vs. the truck locations. The maximum and minimum axial forces observed in these cross-frame and bracing members, as well as their corresponding load case numbers, are summarized in Table 8-1.

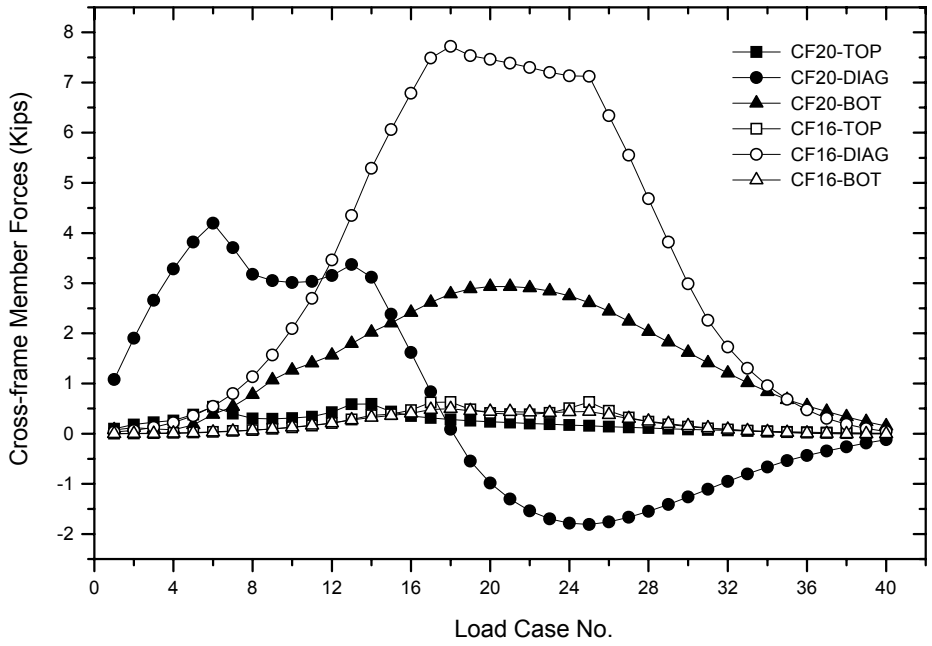

FIGURE 8-18: Cross-Frame Member Forces of CF20 and CF16

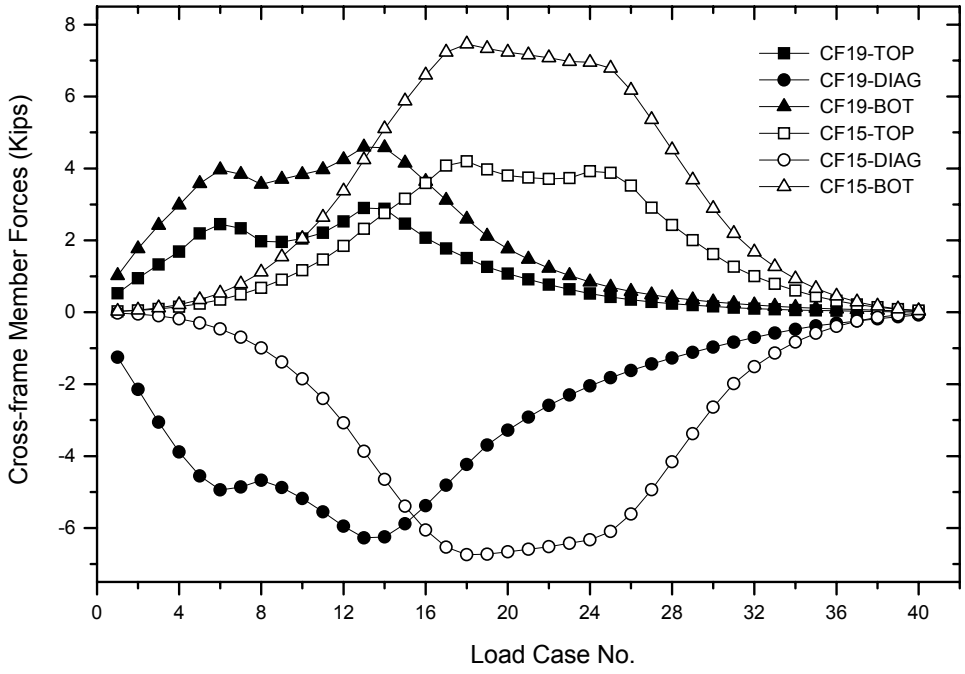

FIGURE 8-19: Cross-Frame Member Forces of CF19 and CF15

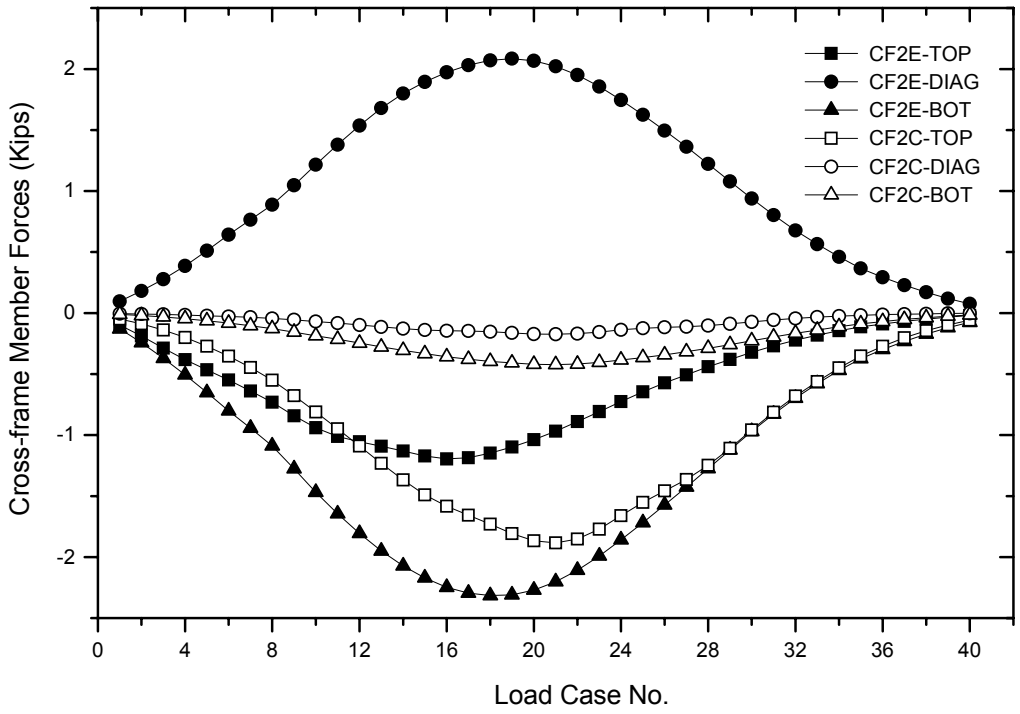

FIGURE 8-20: Cross-Frame Member Forces of CF2E and CF2C

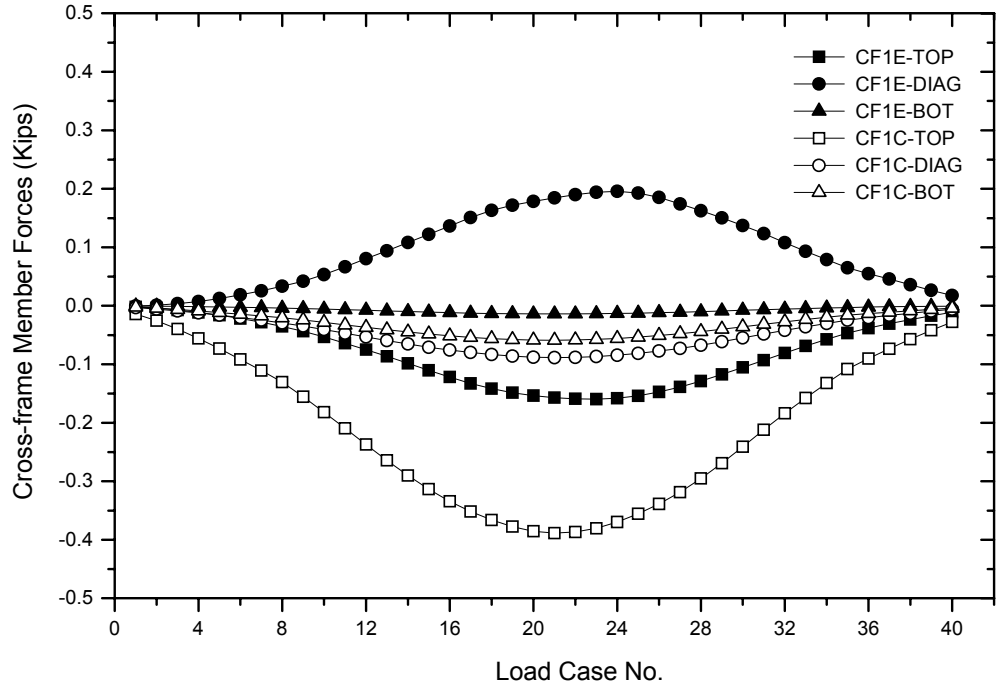

FIGURE 8-21: Cross-Frame Member Forces of CF1E and CF1C

To reveal the cause of fatigue cracking developed in the Hump Yard Bridge, the coarse model analysis results of Load Case No. 21 shown in Figure 8-22 are selected for further discussion. Comparing the bottom chord axial forces of CF16 and CF20, for example, it is noticed that although the truck wheel loads are over section C-C and away from section E-E, as shown in Figure 8-12, the force developed in CF20-BOT (2.9 Kips) is unexpectedly much larger than that of CF16-BOT (0.44 Kips). At this load case, the fatigue truck is located approximately in the middle of the bridge span. The girder sections close to the bridge piers are thus subjected to high magnitude negative bending moment and the adjacent bracing members are also highly stressed. According to Table 8-1, brace BRC1 is in its maximum compression at Load Case No. 21 (-4.4 Kips). The X component of this compressive force (2.7 Kips) pushes the bottom flange outward and at the same time increases the tensile force of the bottom chord CF20-BOT, as shown in Figure 8-24(a). These two horizontal forces literally form a couple, distort the unstiffened web gap out-of-plane, and introduce a site of stress concentration at the bottom flange detail of connection 8e. Though the forces are of very low magnitude, they are still large enough to cause fatigue cracking at the web gap area. For connection 8c, however, as shown in Figure 8-24(b), there are no bracing members connecting to the bottom flange and there are no additional structural members that can balance the horizontal X direction force with CF16-BOT, so the axial force developed in the bottom chord has to be close to zero. As a result, out-of-plane distortion is not able to form at this connection and its web gap region can stay free from fatigue cracking even though it is unstiffened.

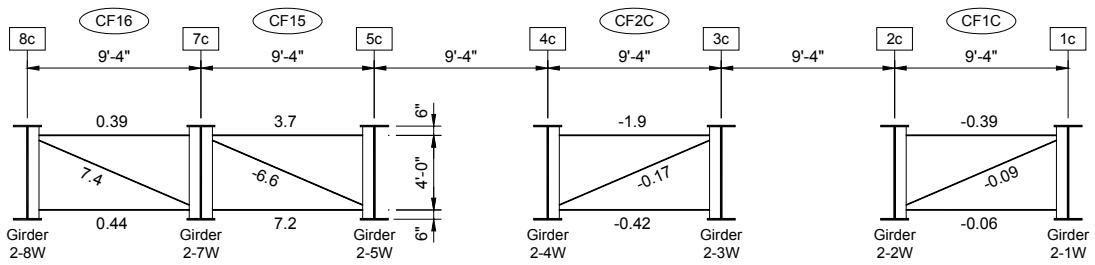

(a) cross-frame member forces of section C-C (Kips)

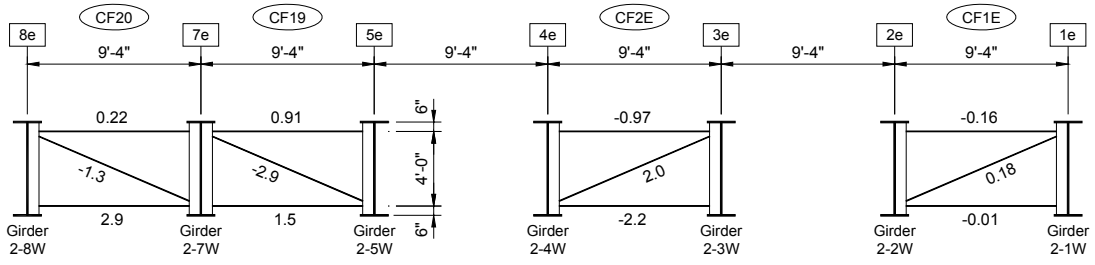

(b) cross-frame member forces of section E-E (Kips)

FIGURE 8-22: Cross-Frame Member Forces of Sections C-C and E-E at Load Case No. 21

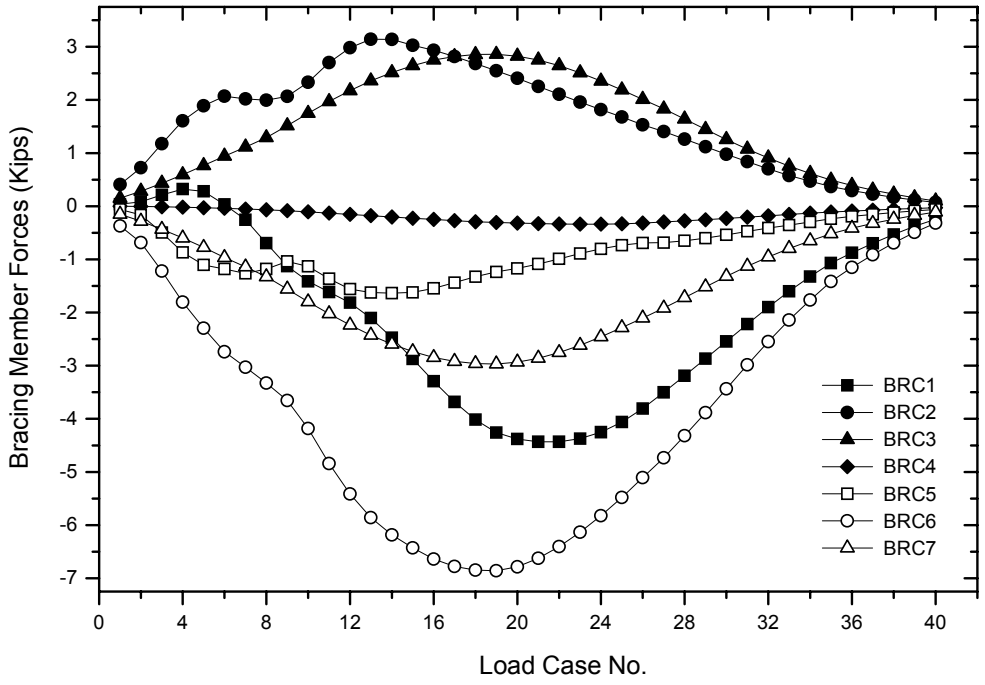

FIGURE 8-23: Bracing Member Forces

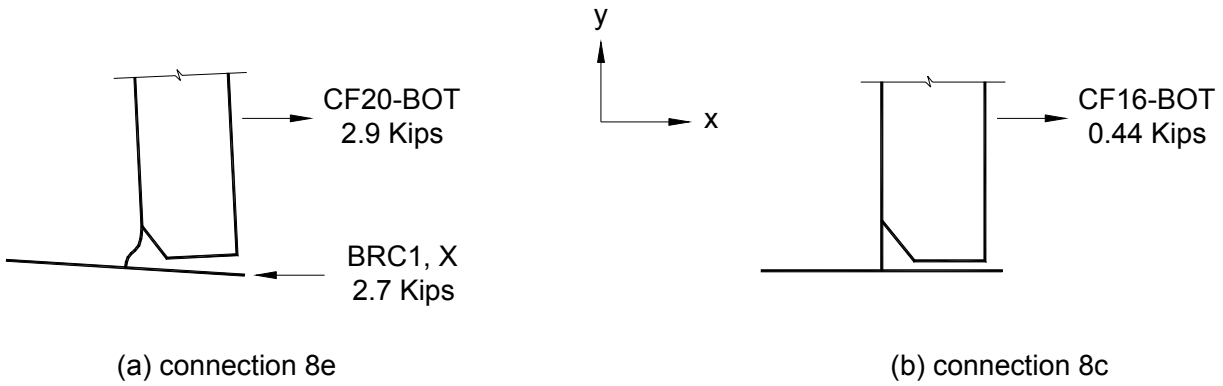

FIGURE 8-24: Load Case No. 21 Bottom Flange Details of Connections 8e and 8c

Other corresponding bottom flange connection details of cross sections C-C and E-E yield similar results. This explains why the web gap cracks in the Hump Yard Bridge developed only in the cross-frame to girder connections with a lateral bracing terminating at the bottom flange. A simple repair method to avoid future crack development could be to remove these bracing members. The detailed web gap stress results presented later in this chapter through submodel investigation support this observation.

Though cracks were not found in the top flange web gaps, the cross-frame member force results of Figure 8-22 indicate that high magnitude fatigue stresses could also develop in these locations. Figure 8-25 shows, for example, the top flange loading diagrams of connections 8c and 5c. In both cases, the X direction components of the cross-frame member forces are larger than those acting on the bottom flange detail of connection 8e, which has already been found with fatigue cracks under the loading condition shown in Figure 8-24(a). Since the bridge top flange is embedded in the concrete slab, the end condition of the web gap is fixed at the top and an equivalent shear force Q can be developed in the direction opposite to the X component of the

cross-frame member forces acting on the stiffener.The top flange connections are more constrained and stiffer than the bottom flange connections, so they can withstand higher magnitude of shear forces and out-of-plane bending moments developed at the web gaps. As a result, the sum of the cross-frame member forces acting on the top flange detail is mostly larger than that acting on the bottom flange detail at the same cross-frame to girder connection, as can be observed from the results of Figure 8-22(a) for cross section C-C. The situation should be the same for the connections of cross sections A-A, B-B, and D-D. For connections of cross section E-E, however, as can be observed from Figure 8-22(b), the cross-frame member force summations are sometimes larger at the bottom flange details, due to the existence of bracing members. Nevertheless, further submodel analysis performed in Section 8.3.2 indicates that stresses developed in the top flange details of cross sections C-C and E-E are both high enough to cause fatigue cracking. Therefore, repair investigations should also be conducted to prevent future crack development at the top flange web gaps.

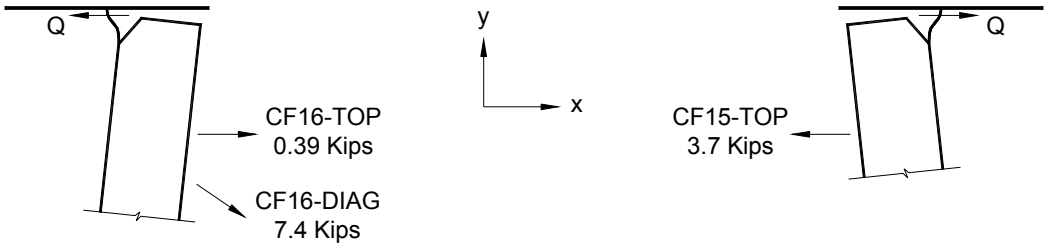

FIGURE 8-25: Load Case No. 21 Top Flange Details of Connections 8c and 5c

TABLE 8-1: Summary of Cross-Frame and Bracing Member Forces

Section	Cross-frame Members		Maximum Forces		Minimum Forces	
			(Kips)	L.C. #	(Kips)	L.C. #
Cross Section E-E	CF20-	TOP	0.59	14	0.01	40
		DIAG	4.2	6	-1.8	25
		BOT	2.9	21	0.08	1
	CF19-	TOP	2.9	13	0.01	40
		DIAG	-0.08	40	-6.3	13
		BOT	4.6	13	0.02	40
	CF2E-	TOP	-0.02	40	-1.2	16
		DIAG	2.09	19	0.08	40
		BOT	-0.08	40	-2.3	18
	CF1E-	TOP	0	1	-0.16	23
		DIAG	0.20	24	0	1
		BOT	0	1	-0.01	21
Cross Section C-C	CF16-	TOP	0.63	18	0	1
		DIAG	7.7	18	0.03	1
		BOT	0.50	18	-0.01	39
	CF15-	TOP	4.2	18	0.02	1
		DIAG	-0.02	1	-6.7	18
		BOT	7.5	18	0.03	1
	CF2C-	TOP	-0.05	1	-1.9	21
		DIAG	0	40	-0.17	21
		BOT	-0.01	1	-0.42	21
	CF1C-	TOP	-0.01	1	-0.39	21
		DIAG	0	1	-0.09	21
		BOT	0	1	-0.06	21
Bracings	BRC1		0.32	4	-4.4	21
	BRC2		3.1	13	0.07	40
	BRC3		2.9	19	0.10	40
	BRC4		0	1	-0.34	23
	BRC5		-0.06	40	-1.6	14
	BRC6		-0.32	40	-6.9	19
	BRC7		-0.11	40	-3.0	19

8.3.2 Submodel Analysis

8.3.2.1 Submodel Structure

The next step of the investigation is to solve the web gap stresses using submodeling techniques. The selected cross-frame to girder connections for submodel analysis are the four connections 2e, 3e, 5e, and 8e at cross section E-E with brace intersections, and the four corresponding connections 2c, 3c, 5c, and 8c at cross section C-C (Figure 8-12). Figure 8-26 shows schematically the relationship between the coarse model and the submodel at a bottom flange cross-frame to girder connection. The same cut dimension is also used for the submodel construction of top flange connections. Unlike the coarse model, the submodel includes the web gap detail and uses the actual connection stiffener width. The element mesh size is controlled at approximately 1 in. but with special refinement at the web gap region in order to capture the local stress concentration effect. The overall submodel sizes are 5,100 elements and 5,300 nodes.

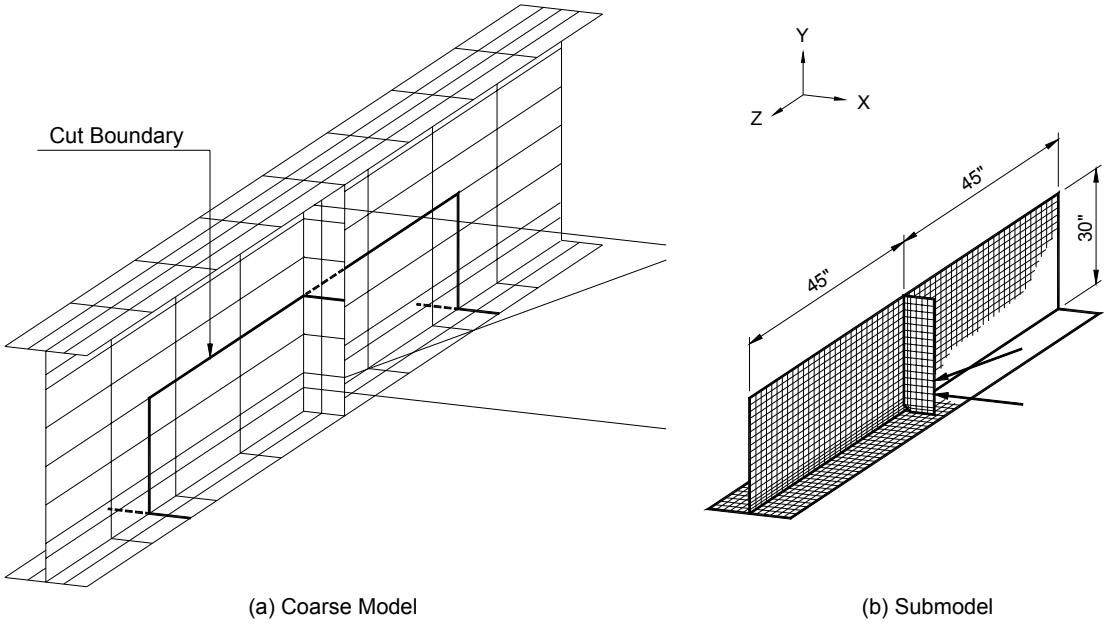

FIGURE 8-26: Schematic Relationship between Coarse Model and Submodel

As shown in Figure 8-26, since ANSYS can only perform cut boundary DOF interpolation for solid and shell elements, the link elements are not intercepted and included in the submodel. In order to take into account the contribution of cross-frame and bracing members, the forces of connecting link elements obtained from the coarse model solution are then converted to nodal forces and assigned to the submodel at the corresponding nodes [Figure 8-26(b)]. Figure 8-27 shows, for example, an ANSYS screen shot of the cut boundary DOFs and the bottom chord and brace forces (in X, Y, and Z components) applied to the bottom flange submodel of connection 8e. The submodel analysis conducted for this bridge thus uses a combination of imposed displacements and imposed loads.

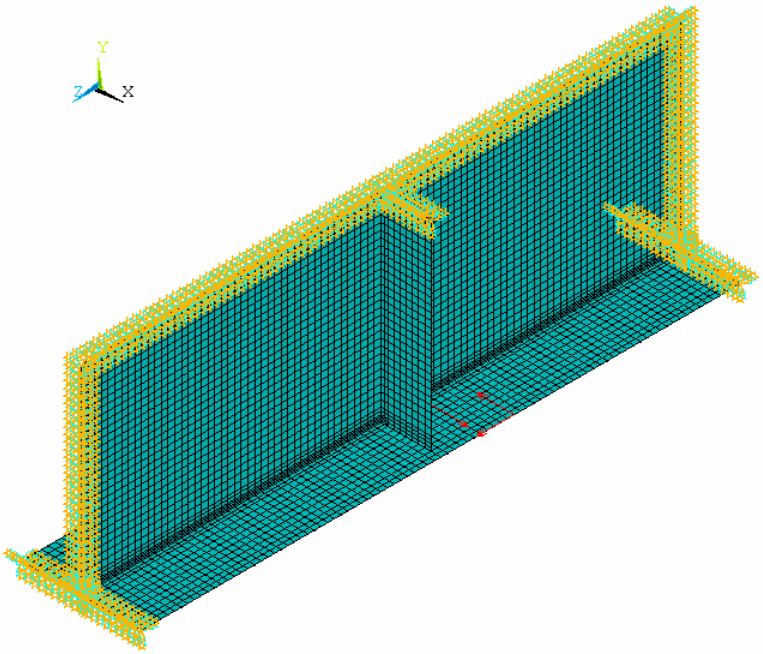

FIGURE 8-27: ANSYS Screen Capture Showing the Cut Boundary DOFs and the Bottom Chord and Brace Forces Applied to Submodel 8e

For each submodel, the cut boundary DOFs can be generated automatically using built-in ANSYS commands. It thus takes little effort to save this DOF information into load case files (e.g., SUB.S01 to SUB.S40 for 40 load cases). However, those nodal forces have to be assigned individually to the corresponding nodes for each load case by the modeler. This procedure is very time consuming and introduces the possibility of input errors. Three Microsoft Excel [2000] macros are thus programmed during the research for automatic data input. The nodal force information is first converted to a format acceptable by ANSYS and then attached to the end of each load case files.

Figure 8-28 shows the area of interest for the submodel web gap stress evaluation. Points A to E are on the stiffener side and Points A' to E' are on the no-stiffener side of the web. For both the bottom and top flange submodels, Points A and A' are at the stiffener end and Points E and E' are at the flange end of the web gap. Points E'1 to E'10 and E"1 to E"10 are 1 in. apart on each side of the stiffener plate and on the side of the web with significant tensile stresses normal to the flange-to-web welds. For each load case, the web gap out-of-plane displacement is measured by the difference between the X direction translations of Points A and E.

8.3.2.2 Bottom Flange Submodels

Submodel analyses are carried out for the bottom flange web gap details of all eight selected cross-frame to girder connections at cross sections C-C and E-E. The results indicate that the maximum web gap stresses all occur when the truck moves close to the mid-span of the bridge. This is true even for the four connections at cross section E-E close to the bridge piers. The maximum tensile σ_y stress always occurs at the flange end of the web gap, either at Point E or E', depending on the curvature of the out-of-plane distortion. The maximum σ_x and σ_z stresses both occur at Point A, either in tension or compression. Figure 8-29 shows the

maximum tensile σ_y stress variation of the corresponding connections in the two cross sections. The information given by the legend includes the designation of the connection, the location of the web gap ("b" for bottom flange and "t" for top flange), and the point where the stress is located (Point E or E'). Except for connection 2e where no significant fatigue stress is observed during the entire truck passage, the other three connections 8e, 5e, and 3e at cross section E-E all experience stress fluctuations higher than CAFT. However, for the entire 40 load cases, stresses developed in the four connections 8c, 5c, 3c, and 2c at cross section C-C are all close to zero. This confirms the coarse model results that bottom flange web gap fatigue cracking could only develop in the connections at cross section E-E with brace intersections. Cracks had already been observed in connections 8e, 5e, and 2e. The stress range experienced by connection 3e suggests that this location will become the next site of bottom flange fatigue cracking if not repaired. The stresses occurring at connection 2e are found close to zero from the submodel analysis. This is because the truck is only placed in Lane 1 (Figures 8-12 and 8-13) during this study, so it has little effect on Girder 2-2W in terms of lateral load distribution. Since this span of the bridge has four southbound lanes, trucks frequently use the other lanes closer to Girder 2-2W, introducing web gap stresses in connection 2e and causing fatigue cracking.

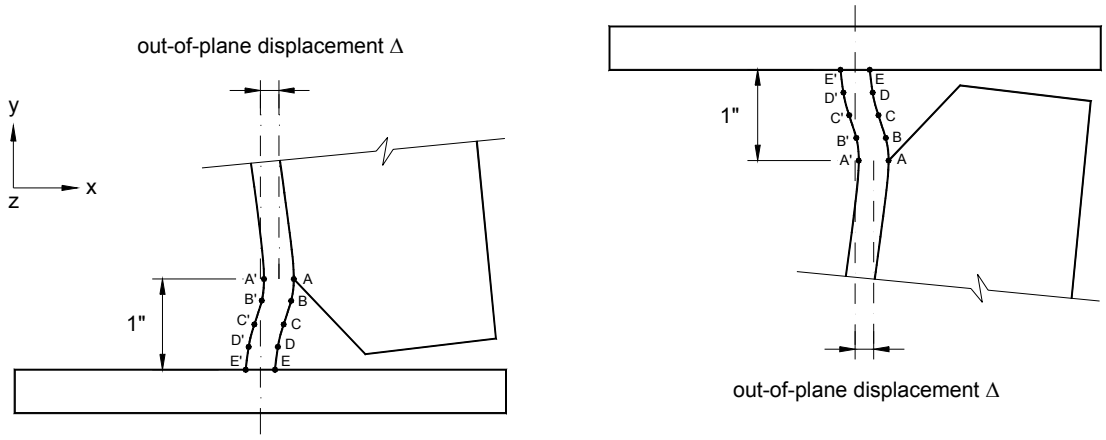

(a) Grid points within the bottom flange web gap

(b) Grid points within the top flange web gap

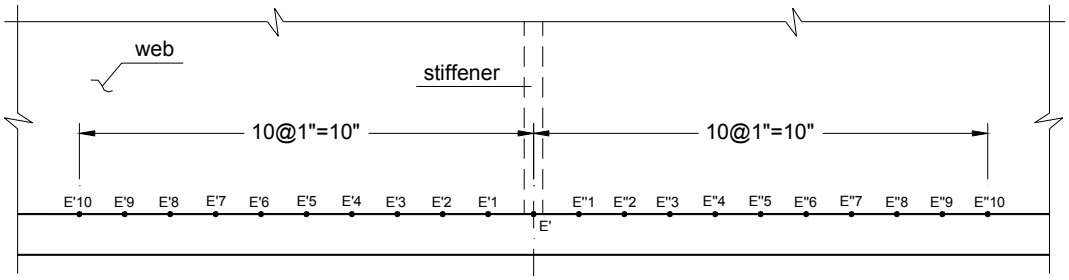

(c) Grid points along the bottom-flange-to-web connection

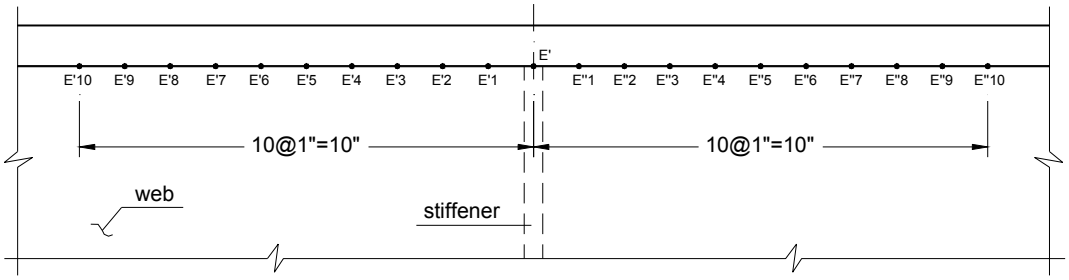

(d) Grid points along the top-flange-to-web connection

FIGURE 8-28: Area of Interest for the Web Gap Stress Evaluation

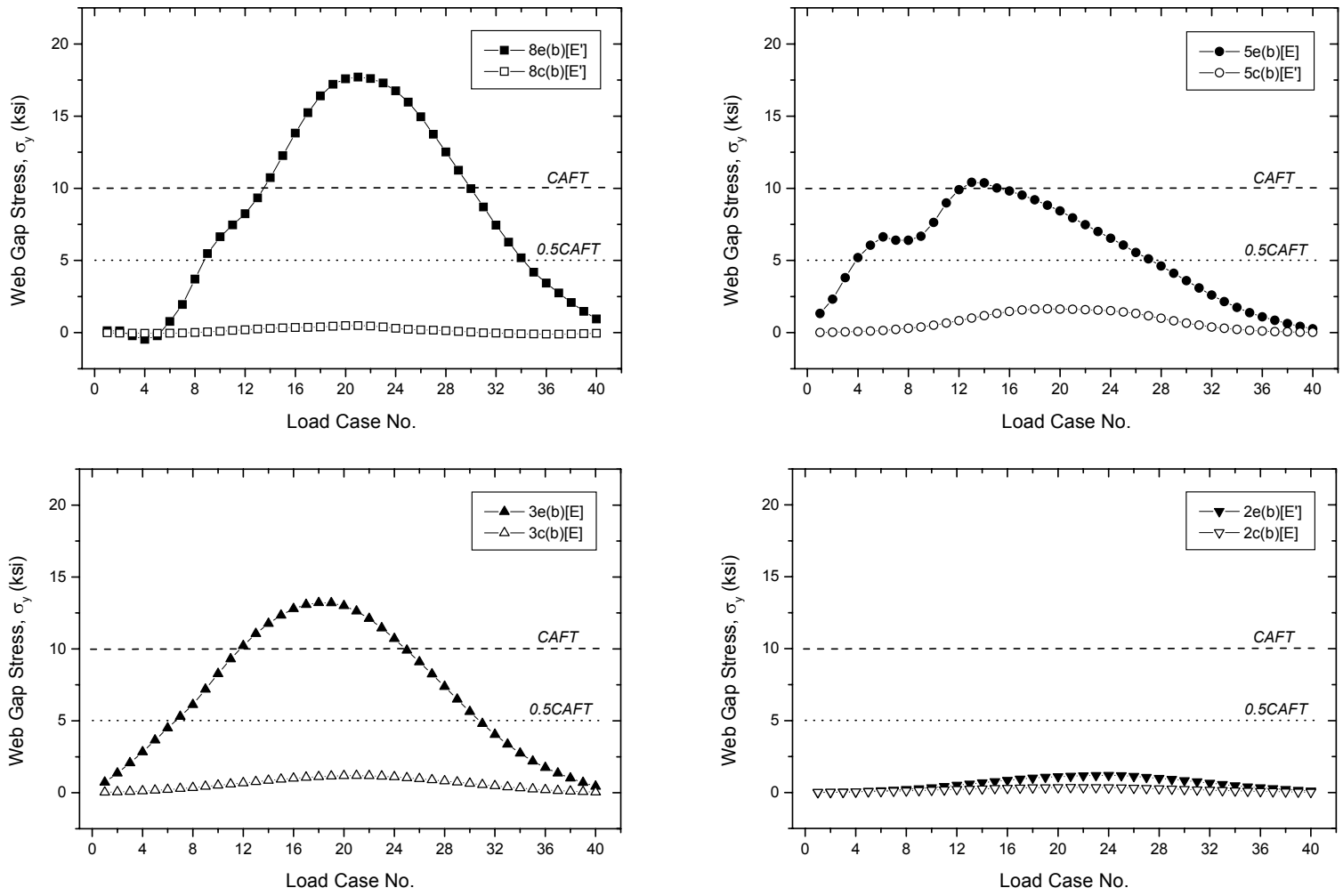

FIGURE 8-29: Maximum Web Gap σ_y Stress Variation of the Bottom Flange Submodels

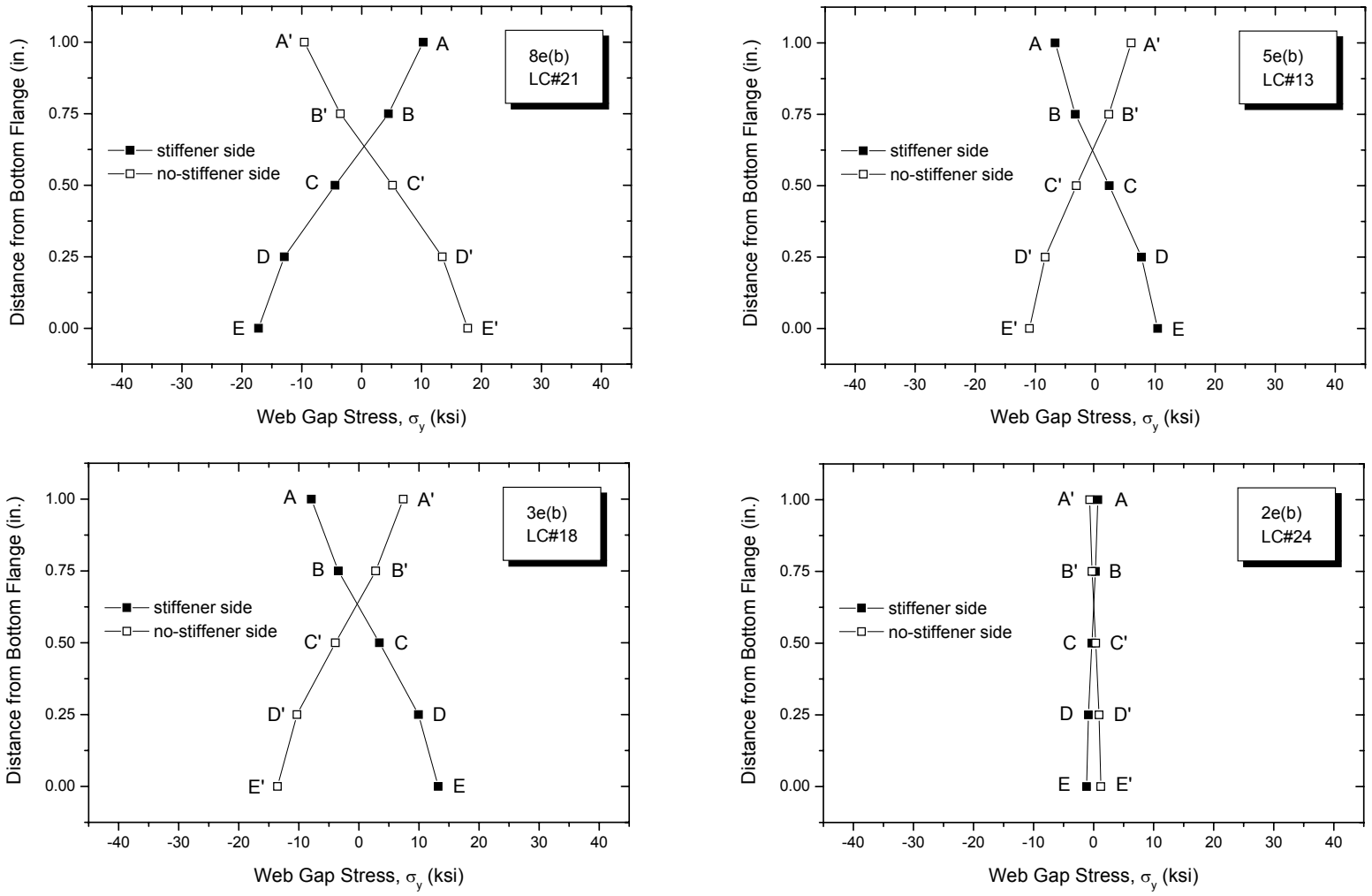

FIGURE 8-30: Bottom Flange Web Gap Stress Gradient of the Connections at Cross Section E-E

Figure 8-30 shows the bottom flange web gap σ_y stress gradient of the four connections at cross section E-E. Stresses on both sides of the girder web are symmetric about the mid web thickness, but are not symmetric about the mid web gap length. The zero stresses are all located at about $^3/_8$ of the web gap length close to the stiffener ends (Points A or A'). The σ_y stresses developed at the same locations of cross section C-C are all close to zero, so stress gradients are not plotted for these connections.

Figures 8-31 and 8-32 show the σ_y stress contours of submodel 8e at Load Case No. 21 on both sides of the girder web. Stress concentration is confined to a very small area in the web gap region. The maximum compressive σ_y stress occurs at Point E [Figure 8-31(b)] and the maximum tensile σ_y stress occurs at Point E' [Figure 8-32(b)]. Figures 8-33 and 8-34 show the web gap σ_x and σ_z stress contours of submodel 8e at the same load case. Both indicate maximum tensile stresses at Point A. Figure 8-35 plots the σ_y stress distribution along the flange-to-web welds. A 10 in. affected zone, 5 in. on each side of the stiffener plane, covers the region of stress concentration. Stresses outside this region are close to zero.

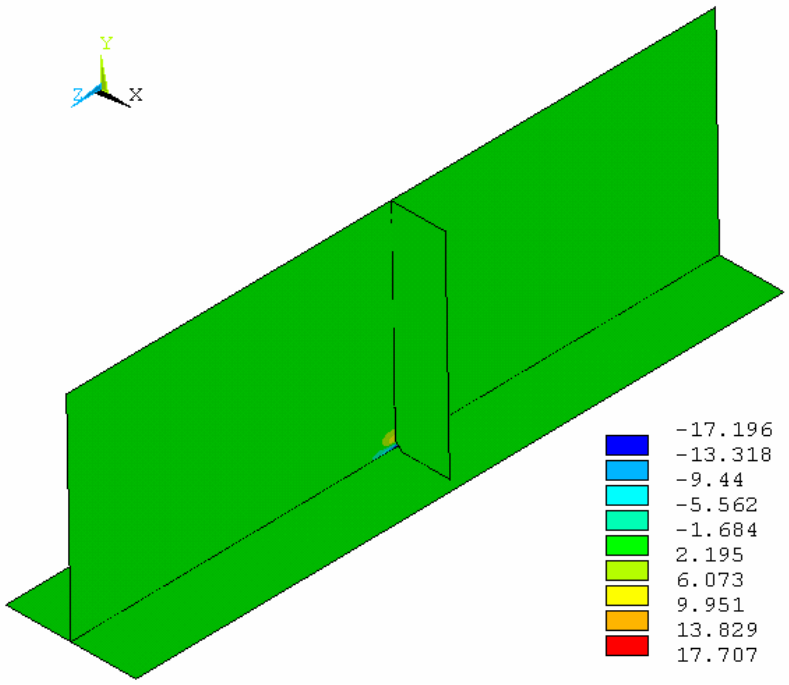

(a) overall σ_y stress distribution of the submodel (ksi)

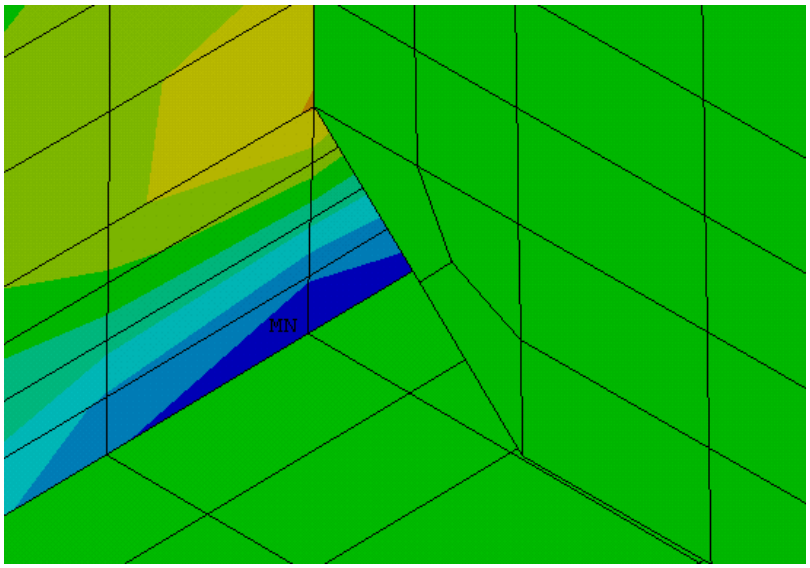

(b) web gap σ_y stress distribution (maximum compressive stress at Point E)

FIGURE 8-31: Load Case No. 21 σ_y Stress Contour of Submodel 8e on the Stiffener Side

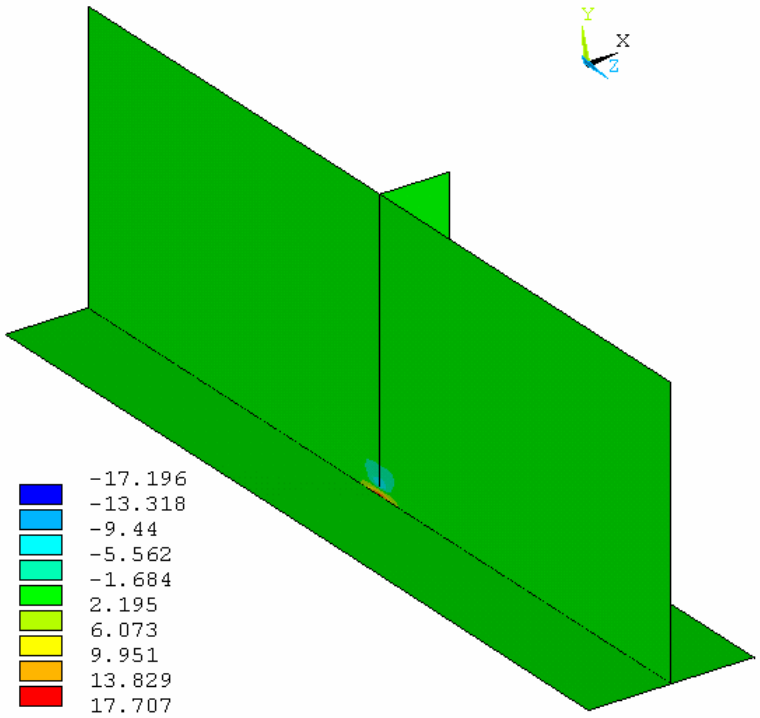

(a) overall σ_y stress distribution of the submodel (ksi)

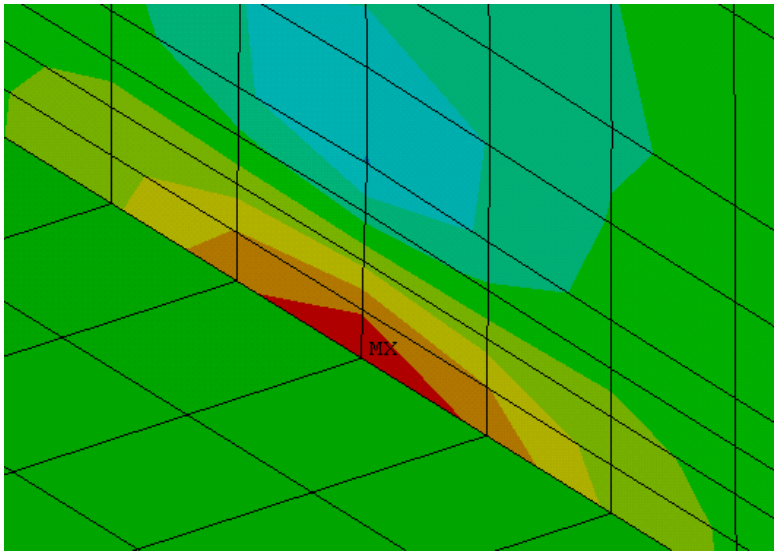

(b) web gap σ_y stress distribution (maximum tensile stress at Point E')

FIGURE 8-32: Load Case No. 21 σ_y Stress Contour of Submodel 8e on the No-Stiffener Side

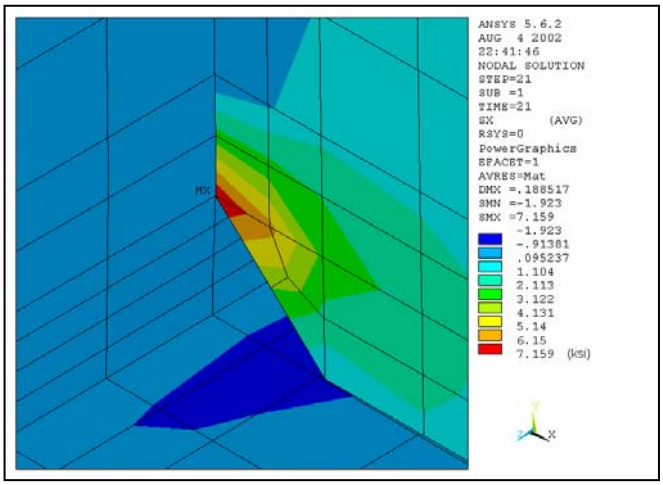

FIGURE 8-33: Load Case No. 21 σ_x Stress Contour of Submodel 8e

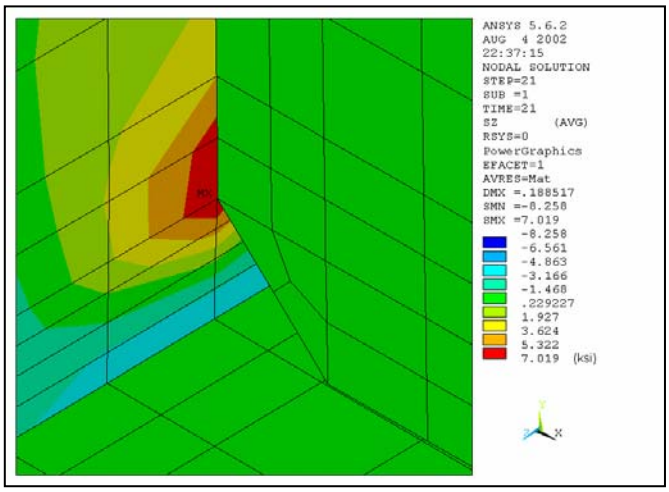

FIGURE 8-34: Load Case No. 21 σ_z Stress Contour of Submodel 8e

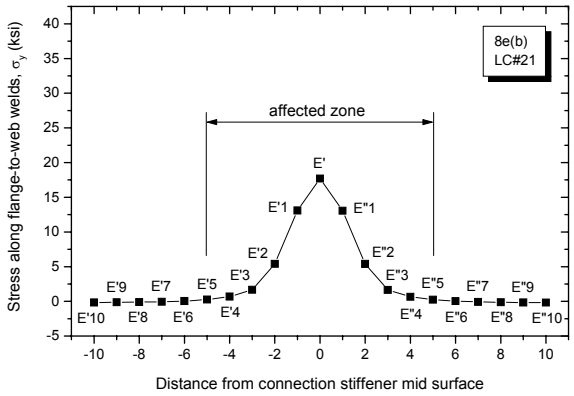

FIGURE 8-35: Load Case No. 21 σ_y Stress Distribution of Submodel 8e along Flange-to-Web Welds

The maximum web gap σ_x, σ_y, and σ_z stresses of the eight bottom flange submodels are summarized in Table 8-2. For connections 8e, 2e, 8c, and 5c, as shown in Figure 8-36(a), the top end of the web gap is deflected towards the stiffener side of the girder web for the most stressed load case, so the maximum σ_x and σ_z stresses occurring at Point A are in tension. For connections 5e, 3e, 3c, and 2c, as shown in Figure 8-36(b), the top end of the web gap is deflected towards the no-stiffener side of the girder web for the most stressed load case, so the maximum σ_x and σ_z stresses occurring at Point A are in compression. In general, for the connections at cross section C-C, the bottom flange web gap σ_x, σ_y, and σ_z stresses are all close to zero. This result can also be extended to the cross-frame to girder connections at cross sections A-A, B-B, and D-D, since the structural layout and web gap detail at these cross sections are the same as those at cross section C-C. For this span of the bridge, only the four connections 8e, 5e, 3e, and 2e at cross section E-E can be exposed to bottom flange web gap stresses higher than ½ CAFT. So structural repair of the bottom flange web gap is only needed at these four locations.

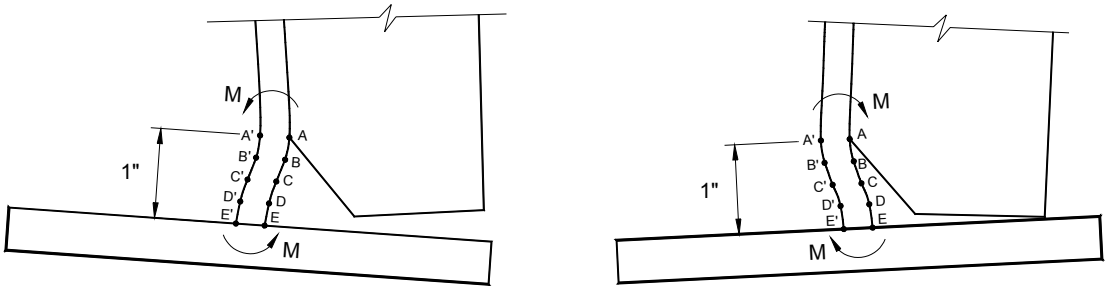

(a) web gap pulled inward for connections 8e, 2e, 8c, 5c

(b) web gap pushed outward for connections 5e, 3e, 3c, 2c

FIGURE 8-36: Connections Subjected to Different Curvatures of Out-of-Plane Distortion

TABLE 8-2: Maximum Web Gap Stresses of the Bottom Flange Submodels

Cross Section	E-E				C-C				AASHTO Fatigue Detail Category	CAFT
Connection	8e (b)	5e (b)	3e (b)	2e (b)	8c (b)	5c (b)	3c (b)	2c (b)		
Δ_{max}	1.93×10^{-3} in.	1.27×10^{-3} in.	1.49×10^{-3} in.	1.36×10^{-3} in.	5.24×10^{-4} in.	7.04×10^{-4} in.	8.38×10^{-4} in.	2.32×10^{-4} in.		
	L.C. # 21	L.C. # 13	L.C. # 19	L.C. # 24	L.C. # 19	L.C. # 21	L.C. # 21	L.C. # 11		
$\sigma_{x, max}$	7.2 ksi	-4.5 ksi	-5.5 ksi	0.49 ksi	0.23 ksi	0.64 ksi	-0.45 ksi	-0.13 ksi	C’	12 ksi
	L.C. # 21	L.C. # 13	L.C. # 18	L.C. # 24	L.C. # 21	L.C. # 18	L.C. # 21	L.C. # 21		
	Point A	Point A	Point A	Point A	Point A	Point A	Point A	Point A		
$\sigma_{y, max}$	18 ksi	10 ksi	13 ksi	1.2 ksi	0.49 ksi	1.6 ksi	1.2 ksi	0.35 ksi	C	10 ksi
	L.C. # 21	L.C. #13	L.C. # 18	L.C. # 24	L.C. # 21	L.C. # 19	L.C. # 21	L.C. # 21		
	Point E’	Point E	Point E	Point E’	Point E’	Point E’	Point E	Point E		
$\sigma_{z, max}$	7.0 ksi	-4.6 ksi	-6.0 ksi	0.53 ksi	2.1 ksi	2.2 ksi	-0.27 ksi	-0.16 ksi	C’	12 ksi
	L.C. # 20	L.C. # 16	L.C. # 18	L.C. # 24	L.C. # 21	L.C. # 18	L.C. # 21	L.C. # 21		
	Point A	Point A	Point A	Point A	Point A	Point A	Point A	Point A		

8.3.2.3 Top Flange Submodels

Connections 8e and 5e at the first interior cross section E-E and connections 8c and 5c at the mid-span cross section C-C are selected for top flange submodel analysis. Connections 5e, 8c, and 5c experience web gap distortion as shown in Figure 8-37(a) for all 40 load cases. The bottom end of the web gap is pulled towards the stiffener side of the girder web, so the maximum tensile σ_y stress always occurs at Point E'. For connection 8e, the web gap distortion is as Figure 8-37(a) for the first 18 load cases, where the maximum tensile σ_y stress also occurs at Point E'. The curvature of out-of-plane distortion is then changed to that shown in Figure 8-37(b) where the bottom end of the web gap is pushed towards the no-stiffener side of the girder web. The maximum tensile σ_y stress is therefore found at Point E for each of the remaining 22 load cases. However, the maximum σ_y stress of submodel 8e of all 40 load cases is found at Point E' at Load Case No. 6. Thus, Point E' σ_y stress variation is plotted in Figure 8-38 for the four top flange submodels under investigation.

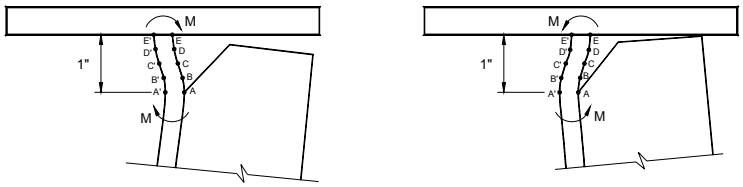

(a) web gap pulled inward (b) web gap pushed outward

FIGURE 8-37: Variation of Out-of-Plane Displacement for the Top Flange Submodels

Figure 8-38 shows that the highest web gap stress of each submodel occurs at the load case where the truck is close to the connection. Stresses developed in the two mid-span connections 8c and 5c are higher than those developed in the corresponding connections 8e and 5e close to the bridge piers, because the girder differential deflection and out-of-plane distortion

are larger at the bridge mid-span sections. The Point E' σ_y stress of submodel 8e is positive for Load Cases No. 1 to 18 and negative for Load Cases No. 19 to 40, due to the change of web gap distortion curvature. The maximum σ_y stress occurring at Point E' is 21 ksi at Load Case No. 6, but the stress range experienced at this point for the entire truck passage is 28 ksi. Both stress measures are high enough to introduce fatigue cracks along the flange-to-web welds. All four submodels have maximum σ_y stresses or stress ranges higher than CAFT. This indicates that fatigue cracks can develop at the unstiffened top flange web gaps during future bridge service.

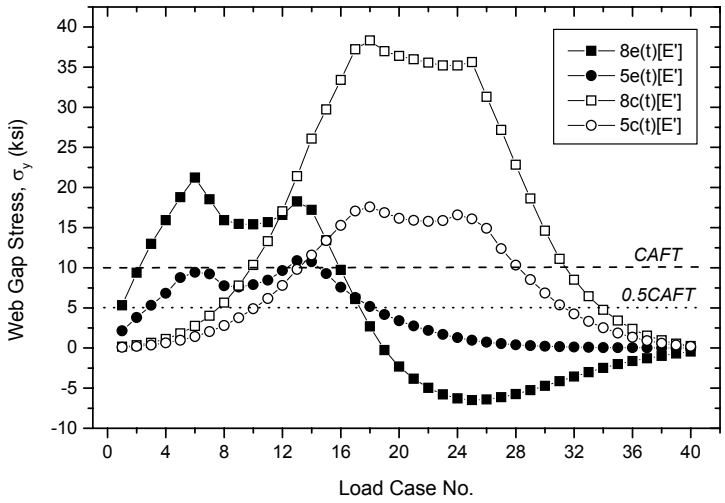

FIGURE 8-38: Point E' Web Gap σ_y Stress Variation of the Top Flange Submodels

Figure 8-39 shows the web gap stress gradient of the four top flange submodels. Compared to Figure 8-30, the overall web gap stress magnitude and variation gradient are both higher at the top flange than at the bottom flange. Though the top flange submodel analysis is not performed at the other cross-frame to girder connections, it is expected that stresses higher than the fatigue limit can also develop at these locations when the fatigue truck is in the other lanes or at other load cases. To prevent future crack development, an appropriate repair solution is thus needed for the top flange web gaps of all the cross-frame to girder connections.

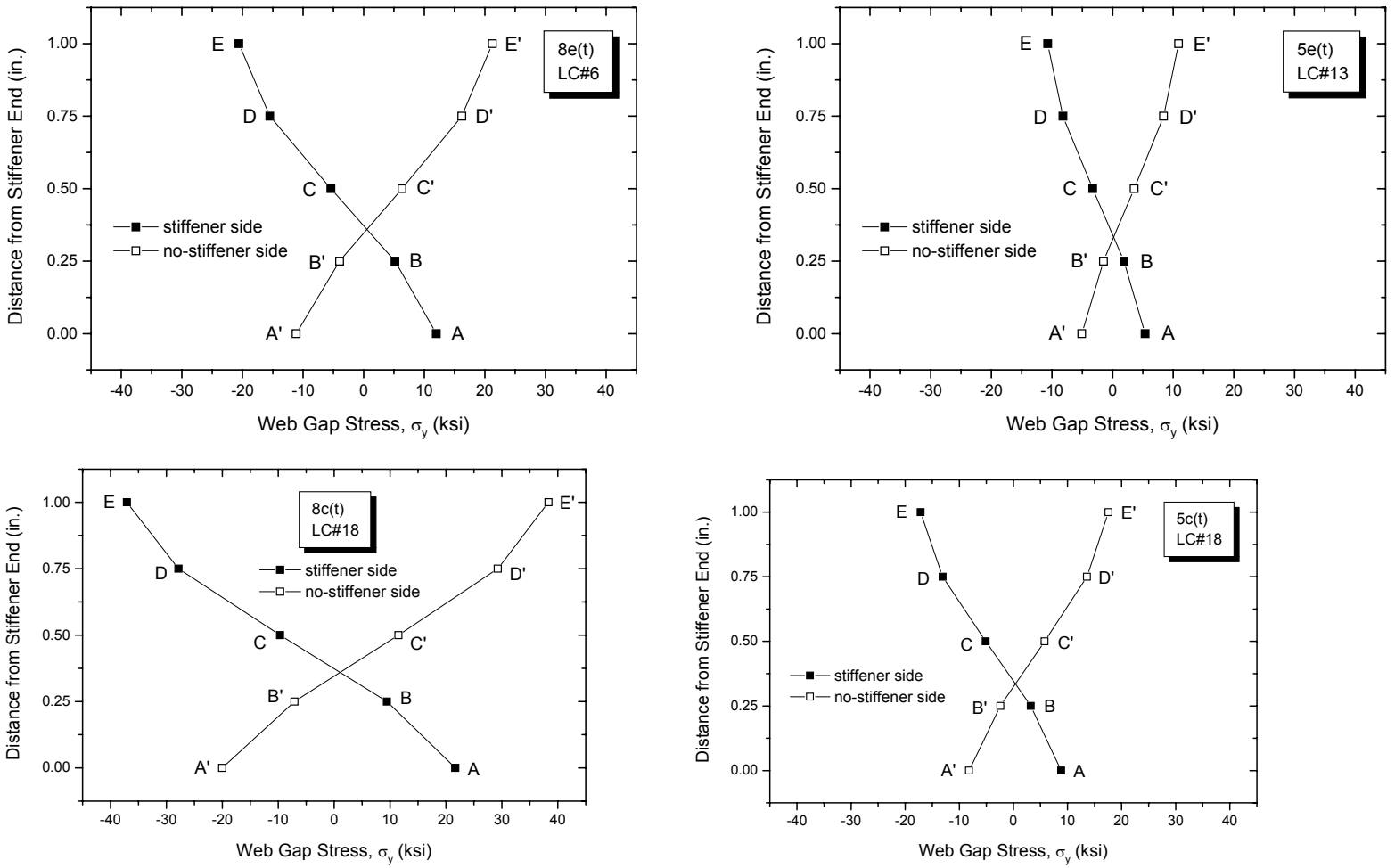

FIGURE 8-39: Top Flange Web Gap Stress Gradient

Table 8-3 summarizes the maximum web gap stress and out-of-plane displacement results of the four top flange submodels. Connection 8c is the most highly stressed. Figures 8-40 and 8-41 show the σ_y stress contours of submodel 8c on the stiffener and no-stiffener sides of the girder web at Load Case No. 18. The overall stress distribution on both web sides is close to zero, but high magnitude stresses, both in tension and in compression, and dramatic stress variations are observed at the web gap area. The maximum σ_y stress at Point E' is 38 ksi, which has exceeded the yield point. Cracks could develop very soon at the flange-to-web welds when subjected to such a high stress magnitude. Figures 8-42 and 8-43 show the stress contours of the submodel at the same load case for σ_x and σ_z. The maximum σ_x stress is 15 ksi and the maximum σ_z stress is 14 ksi. Both occur at Point A. The combination of these two stresses could cause the cracks to develop in a short time along the stiffener-to-web welds. The same distribution contours are also seen in the other three submodels 5e, 8e, and 5c, but with lower stress magnitude. During the actual bridge service, it is believed that this "hot" stress concentration zone can be found at all the unstiffened top flange web gaps, and the stresses developed at the mid-span positive moment region connections should be higher than those developed at the corresponding transition and negative moment region connections.

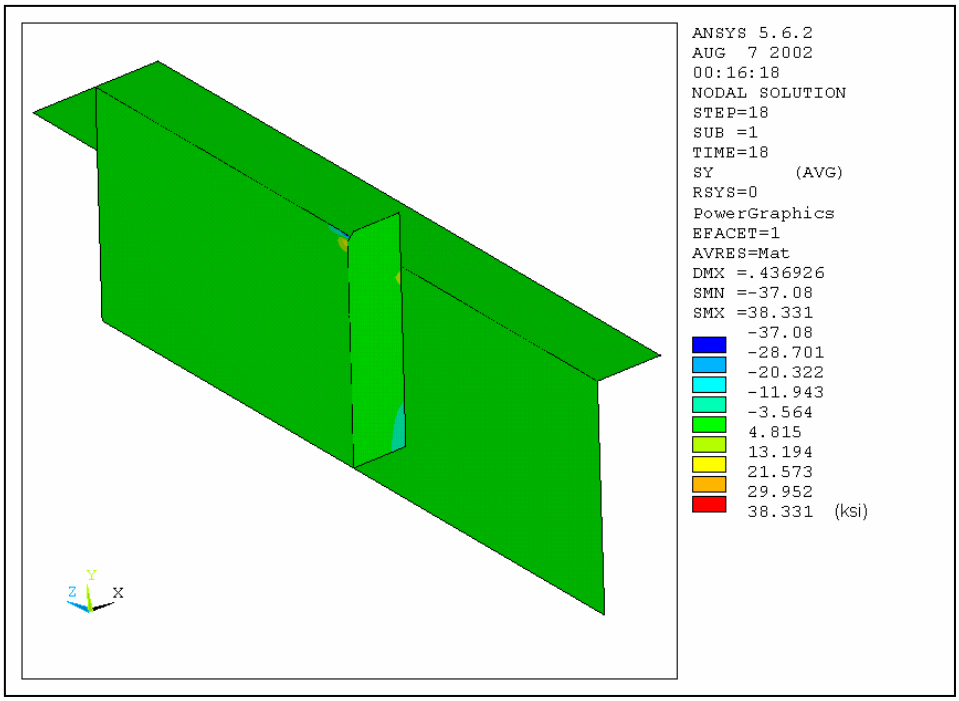

(a) overall stress distribution of the submodel

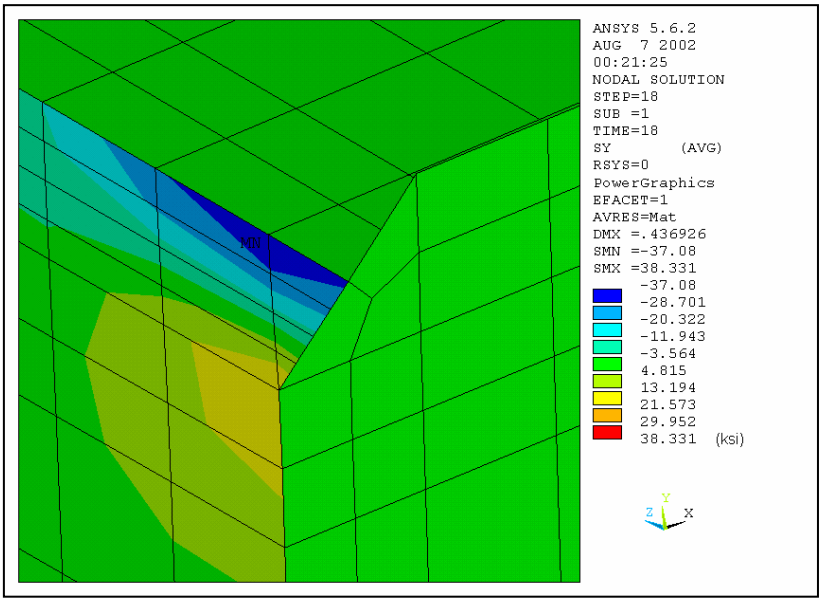

(b) web gap stress distribution (maximum compressive σ_y stress at Point E)

FIGURE 8-40: Load Case No. 18 σ_y Stress Contour of Submodel 8c on the Stiffener Side

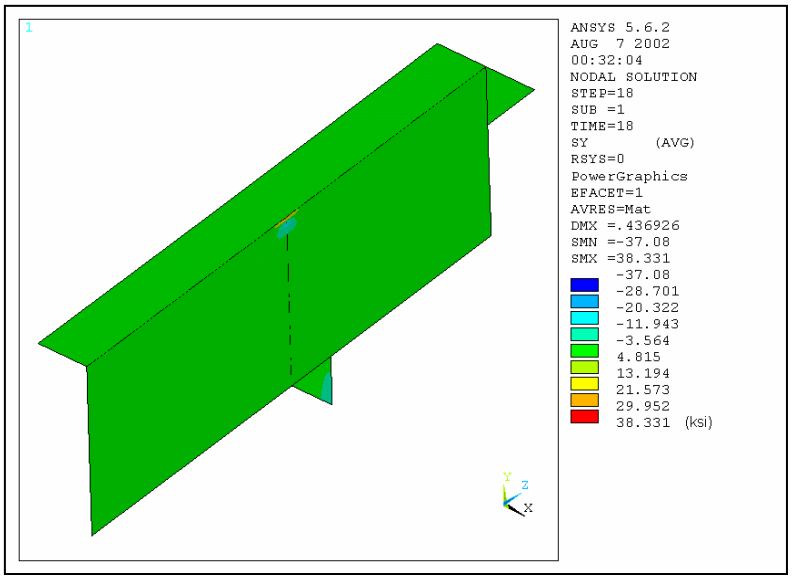

(a) overall stress distribution of the submodel

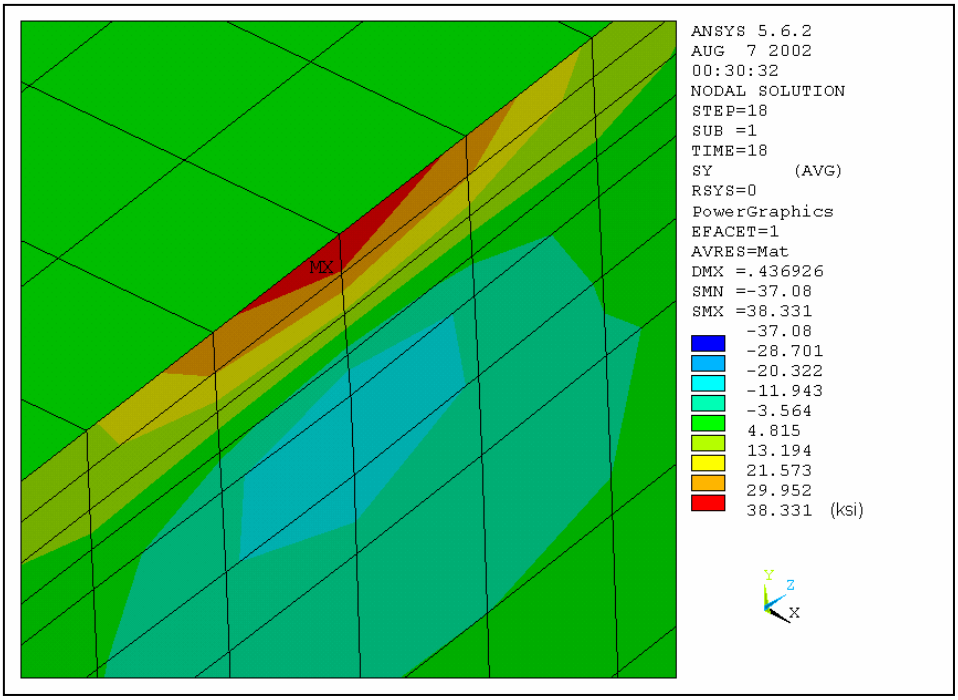

(b) web gap stress distribution (maximum tensile σ_y stress at Point E')

FIGURE 8-41: Load Case No. 18 σ_y Stress Contour of Submodel 8c on the No-Stiffener Side

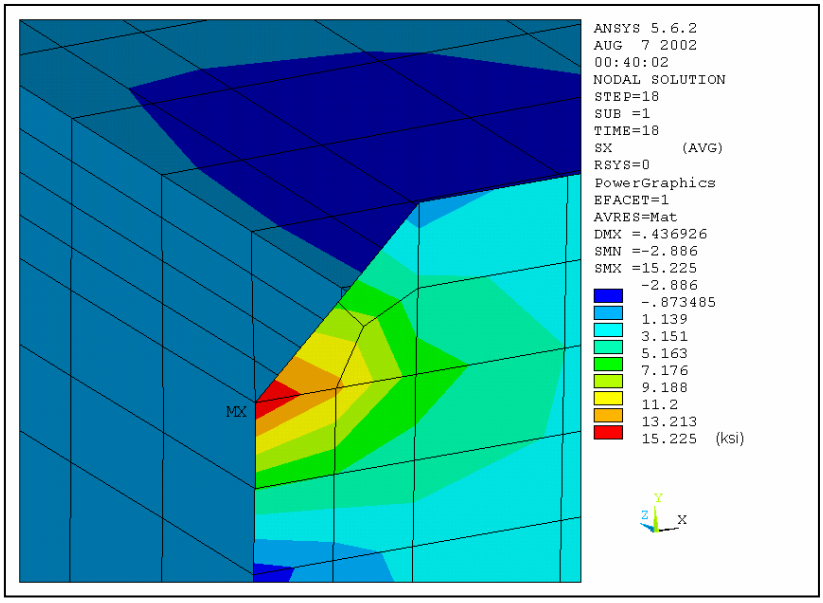

FIGURE 8-42: Load Case No. 18 σ_x Stress Contour of Submodel 8c

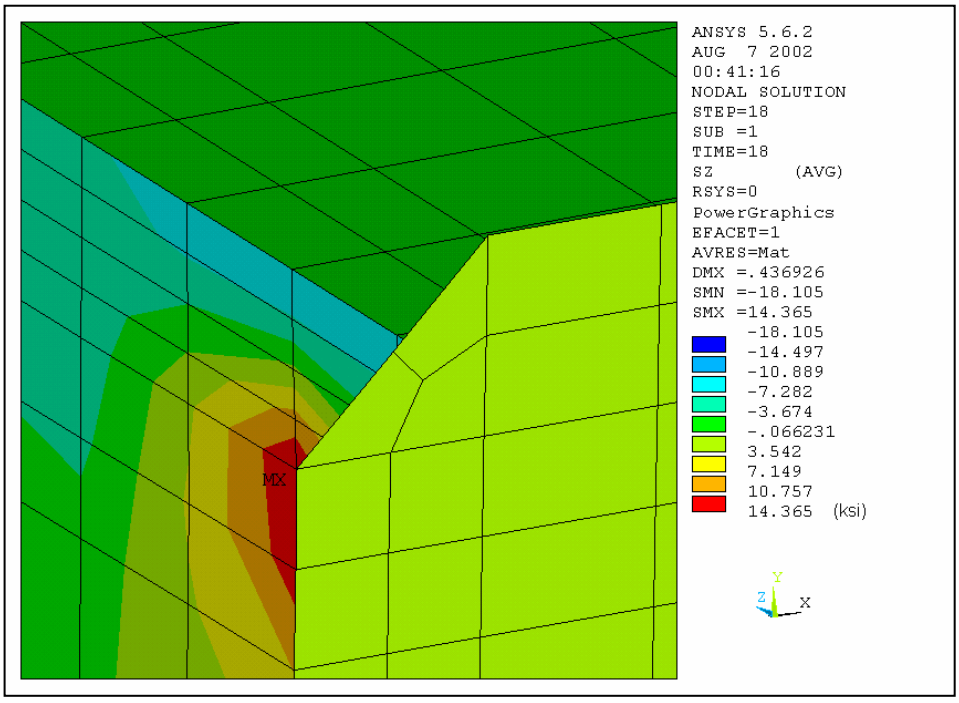

FIGURE 8-43: Load Case No. 18 σ_z Stress Contour of Submodel 8c

TABLE 8-3: Maximum Web Gap Stresses of the Top Flange Submodels

Cross Section	E-E		C-C		AASHTO Fatigue Detail Category	CAFT
Connection	8e (t)	5e (t)	8c (t)	5c (t)		
Δ_{max}	2.31×10^{-3} in.	7.12×10^{-4} in.	4.67×10^{-3} in.	8.43×10^{-4} in.		
	L.C. # 6	L.C. # 6	L.C. # 18	L.C. # 18		
$\sigma_{x, max}$	8.5 ksi	4.1 ksi	15 ksi	6.5 ksi	C'	12 ksi
	L.C. # 6	L.C. # 13	L.C. # 18	L.C. # 18		
	Point A	Point A	Point A	Point A		
$\sigma_{y, max}$	21 ksi	11 ksi	38 ksi	18 ksi	C	10 ksi
	L.C. # 6	L.C. # 13	L.C. # 18	L.C. # 18		
	Point E'	Point E'	Point E'	Point E'		
$\sigma_{z, max}$	8.7 ksi	4.4 ksi	14 ksi	5.7 ksi	C'	12 ksi
	L.C. # 6	L.C. # 13	L.C. # 18	L.C. # 18		
	Point A	Point A	Point A	Point A		

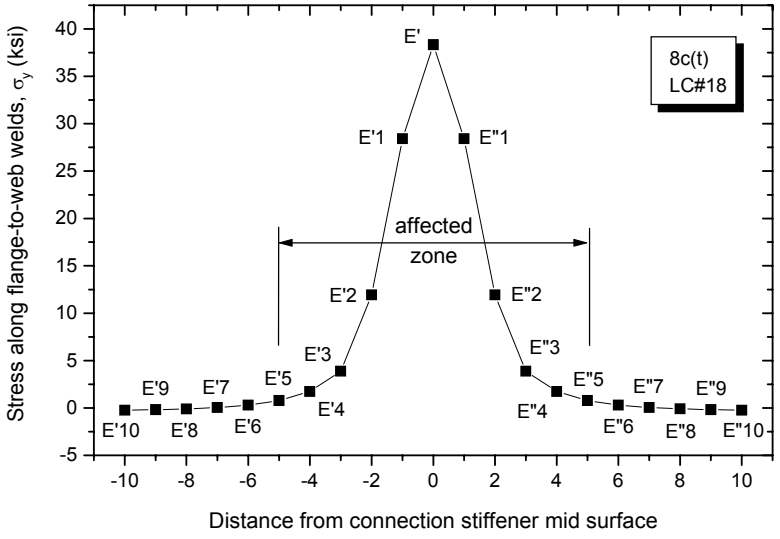

FIGURE 8-44: Load Case No. 18 σ_y Stress Distribution of Submodel 8c along Flange-to-Web Welds

Figure 8-44 plots the σ_y stress distribution along the flange-to-web welds for connection 8c at Load Case No. 18. Compared to the stress condition shown in Figure 8-35 for the bottom flange submodel 8e, the maximum σ_y stress developed at Point E' of the top flange submodel 8c is much higher. However, the 10 in. affected zone for stress concentration is still applicable.

8.4 Repair Analysis

Two repair approaches are considered during the study. One is to remove the bracing members. The other is to weld the connection stiffeners to the girder flanges, as proposed by KDOT. Changes in the web gap stresses are evaluated using submodeling analysis, as discussed in Sections 8.4.1 and 8.4.2 for the two different repair methods. Final repair recommendations are presented in Section 8.4.3.

8.4.1 Brace Removal

The first repair option is to remove the horizontal plane of bracing between cross section E-E and Pier No. 8, i.e., members BRC1 to BRC7 shown in Figure 8-12. The coarse model of Figure 8-15 is modified to exclude the brace elements and the analysis is performed again for all 40 truck locations. Figure 8-45 shows the cross-frame member forces of section E-E for Load Case No. 21 both before and after the brace removal. The axial forces all decrease for this load case after the braces are removed. Figures 8-46 to 8-49 show the change in these cross-frame member forces for all 40 load cases. Cross-frames CF20 (Figure 8-46), CF19 (Figure 8-47), and CF2E (Figure 8-48) experience noticeable axial force changes in at least one or two of their structural components, mostly in the diagonal or bottom chords. Forces developed in the cross-frame members of CF1E (Figure 8-49), however, are close to zero both before and after the brace removal. Thus, no further web gap stress evaluation of connection 2e is performed.

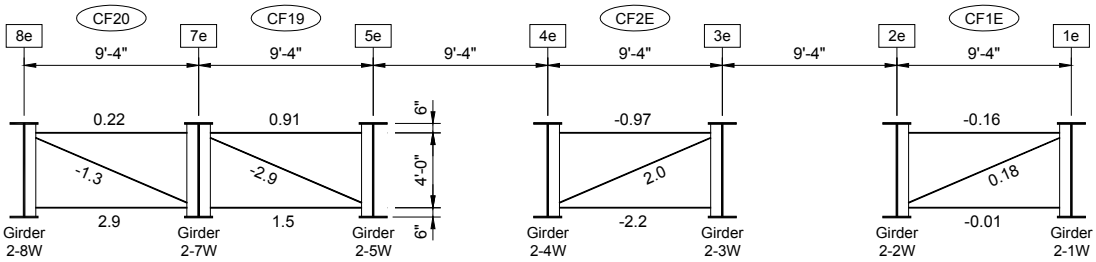

(a) before brace removal (Kips)

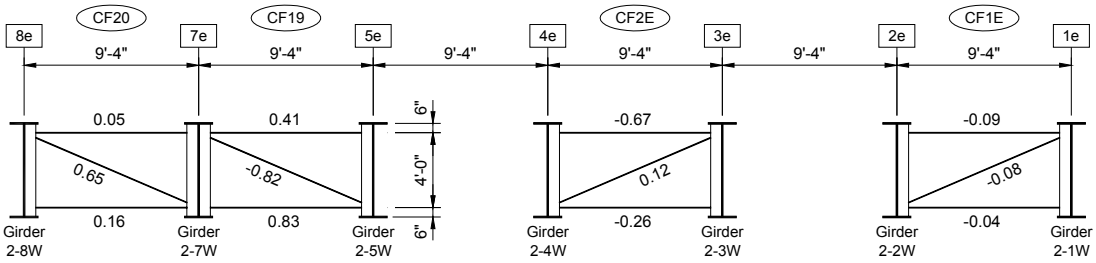

(b) after brace removal (Kips)

FIGURE 8-45: Load Case No. 21 Section E-E Cross-Frame Member Forces

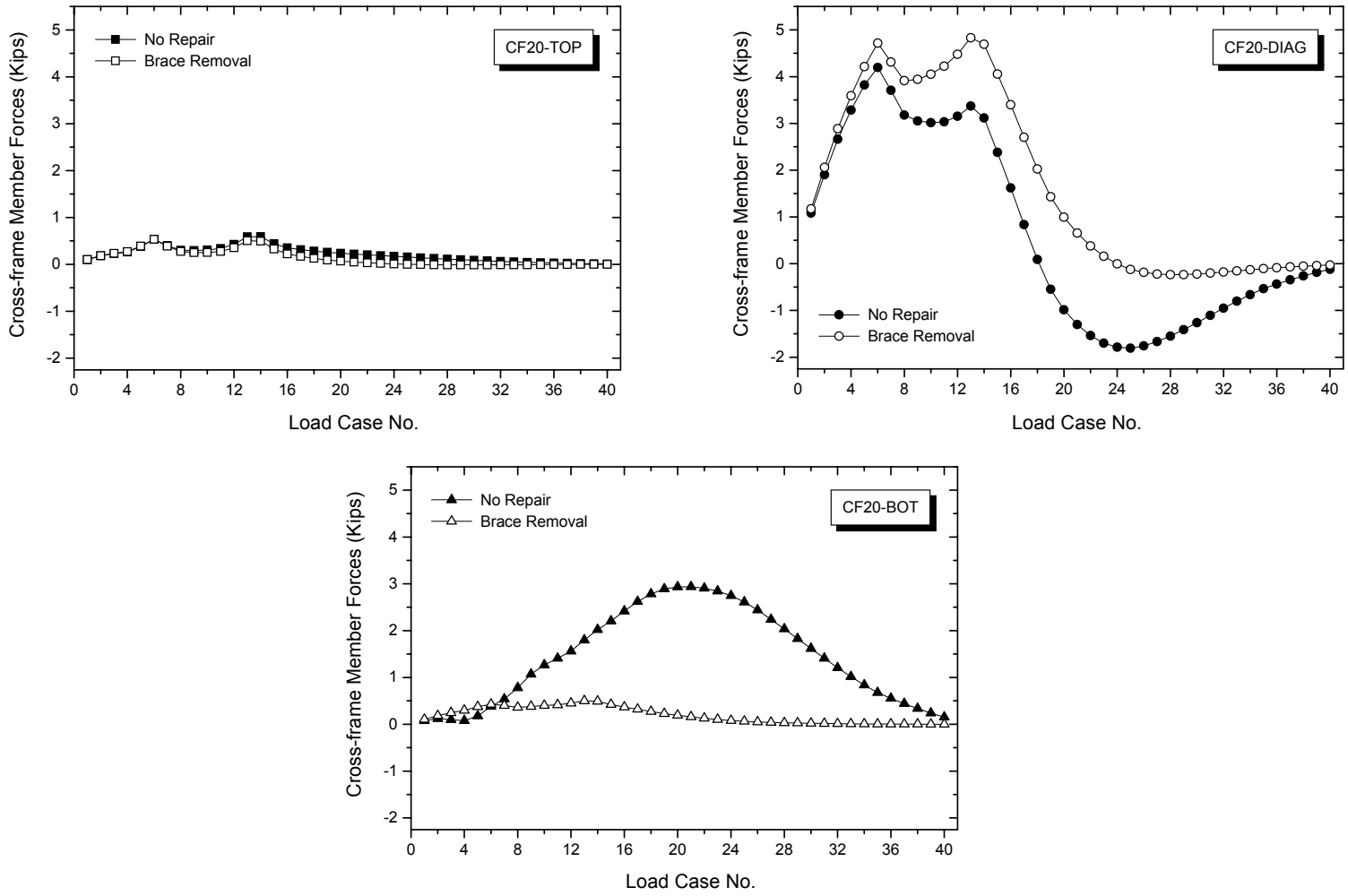

FIGURE 8-46: CF20 Cross-Frame Member Forces Before and After Brace Removal

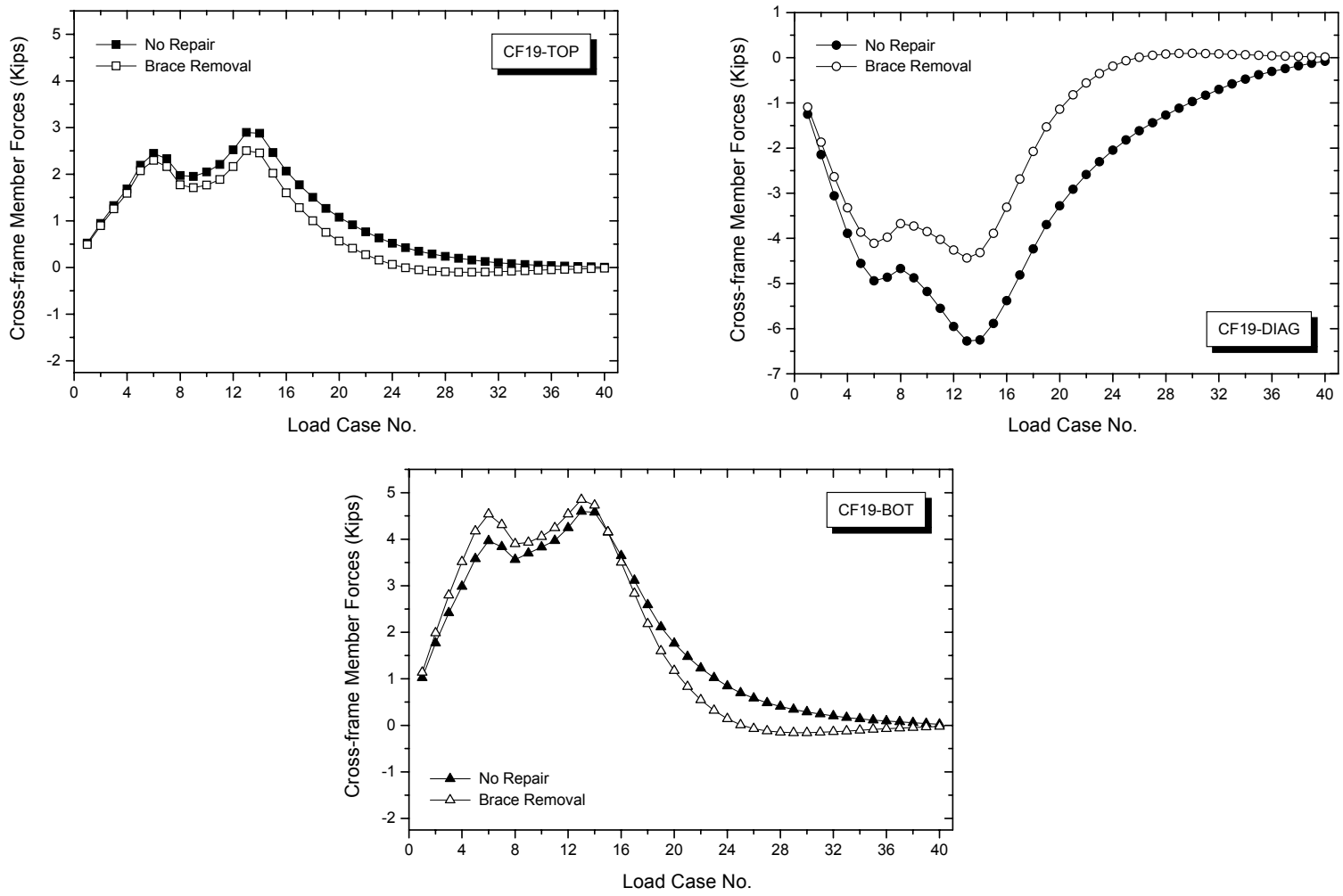

FIGURE 8-47: CF19 Cross-Frame Member Forces Before and After Brace Removal

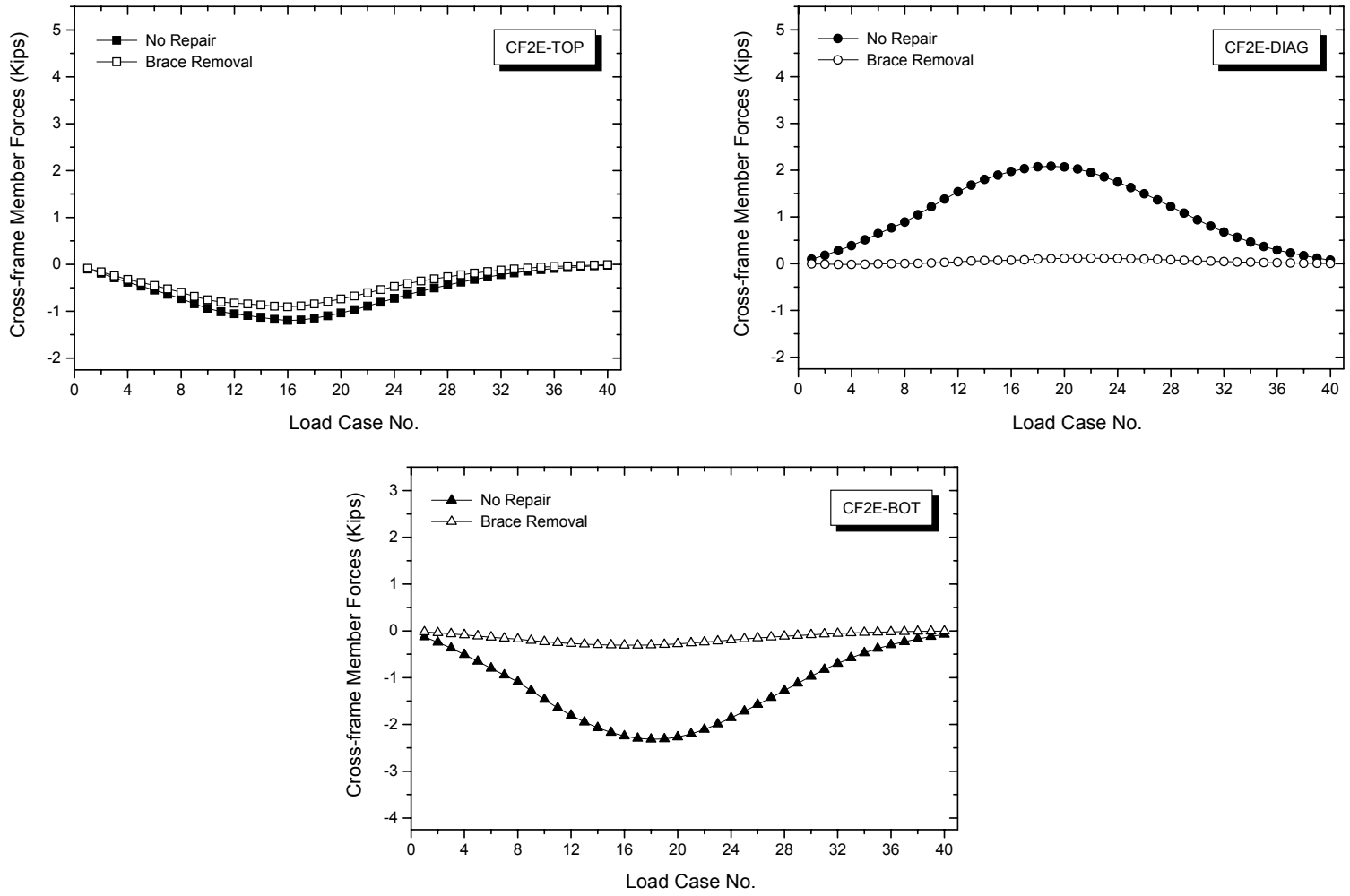

FIGURE 8-48: CF2E Cross-Frame Member Forces Before and After Brace Removal

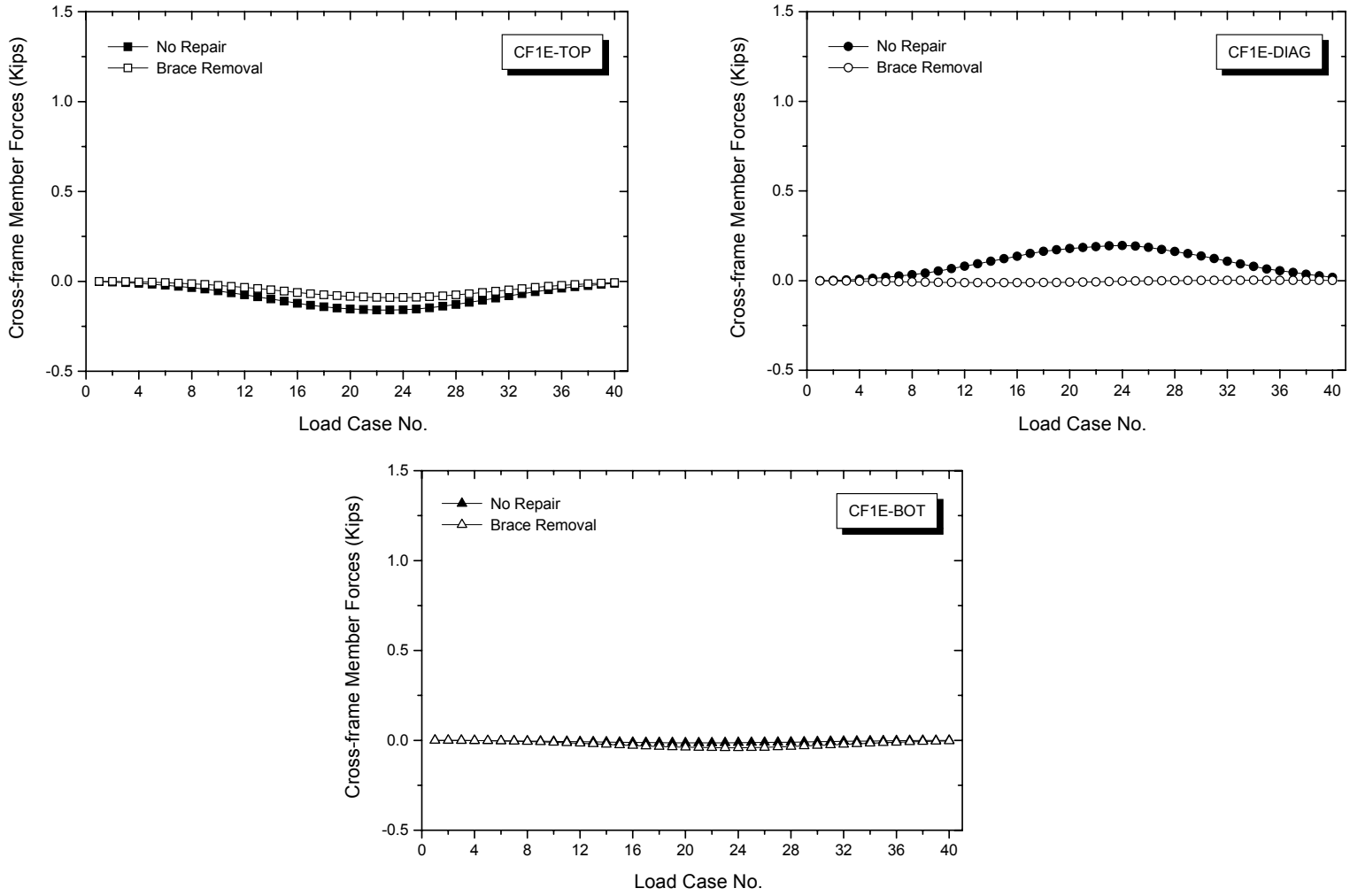

FIGURE 8-49: CF1E Cross-Frame Member Forces Before and After Brace Removal

The procedures of cut boundary DOF interpolation and cross-frame member force assignment are then carried out for the bottom flange submodels of connections 8e, 5e, and 3e. The maximum web gap σ_y stress solutions obtained from the submodel analysis are plotted in Figure 8-50, together with the corresponding results under the condition of no repair. Significant stress reduction is observed after the brace removal. The maximum σ_y stresses of the three submodels all decrease to below ½ CAFT. Figure 8-51 shows the comparison of web gap σ_y stresses before and after the repair, for the load cases associated with the maximum stress gradient. Stress variation within the web gap length is also greatly reduced after the brace removal. For example, the difference between the σ_y stresses of Point A' and E' of connection 8e is a maximum of 27 ksi with the braces at Load Case No. 21, but is reduced to a maximum of 2 ksi without the braces at Load Case No. 12. The major analytical results of the three submodels are summarized in Table 8-4. The maximum web gap σ_x, σ_y, and σ_z stresses are all reduced to below ½ CAFT by the brace removal. About 90% stress reduction is obtained.

The submodel analysis conducted for the first repair approach again indicates the bracing members as the cause of bottom flange web gap fatigue cracking. Both the out-of-plane bending moments and stresses developed at the web gap ends can be eliminated if the braces are removed. However, lack of bottom flange bracing members could result in lateral torsional buckling of the girder sections at the negative moment region, especially in this span as the bridge is skewed at Pier No. 8. Also, an additional repair approach is needed to prevent the top flange web gap cracking. The welded repair is therefore studied in Section 8.4.2 to see if this method can reduce the web gap stresses to a satisfactory level without removing the lateral braces.

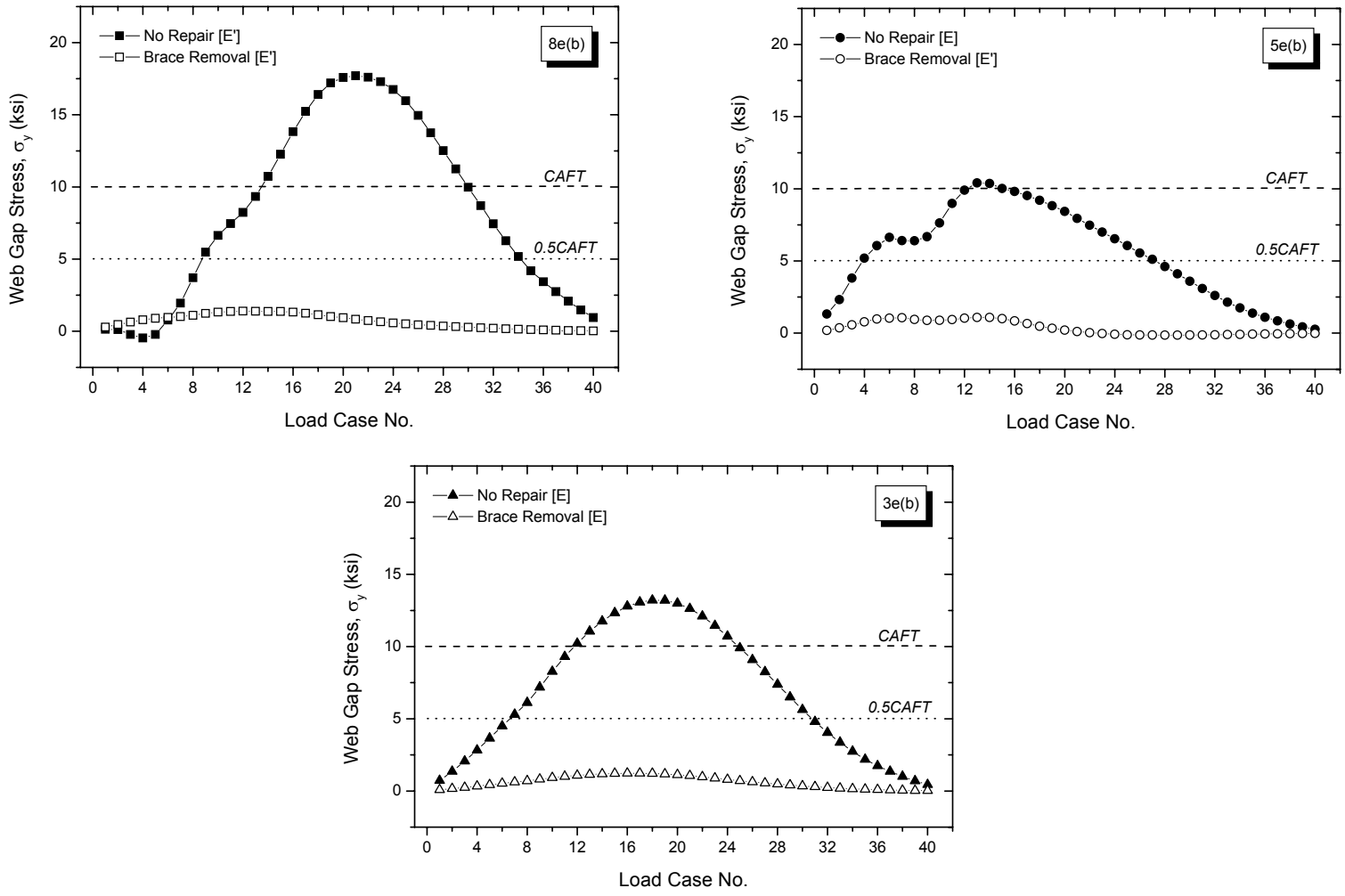

FIGURE 8-50: Bottom Flange Maximum Web Gap σ_y Stress Variation Before and After Brace Removal

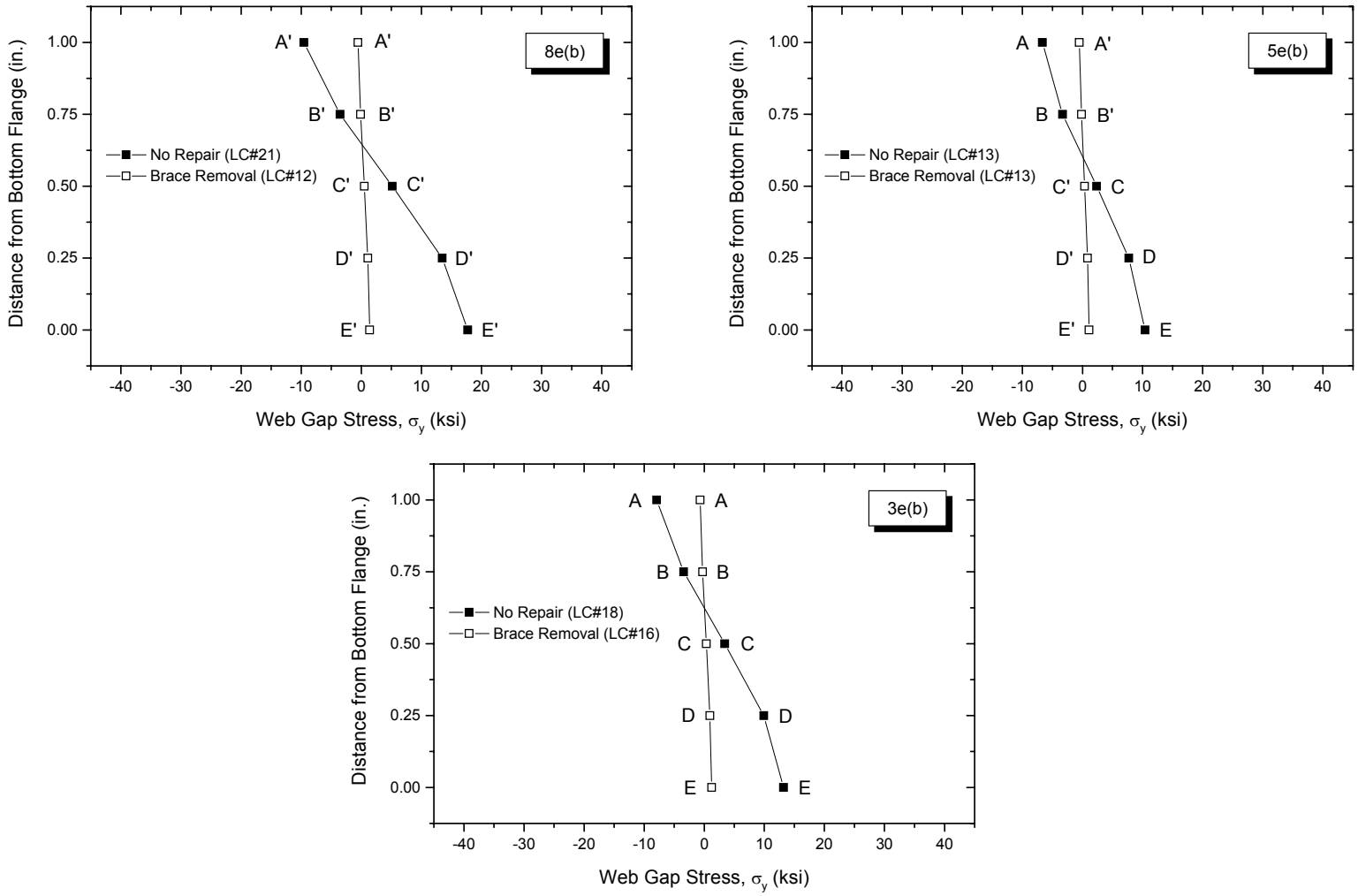

FIGURE 8-51: Bottom Flange Maximum Web Gap σ_y Stress Gradient Before and After Brace Removal

8.4.2 Welded Repair

The second repair option is to stiffen the small web gaps by welding the connection stiffener to the girder flange. Based on the results of Section 8.3.2, the bottom flange web gap cracks could only develop at the cross section E-E brace intersections, while the top flange web gap cracks could develop in any of the cross- frame to girder connections at cross sections A-A to E-E. The welded repair can be used at both the top and bottom flanges to keep the web gaps from deflecting out-of- plane. Finite element studies are conducted for connections 8e and 5e at both the top and bottom flanges and for connections 8c and 5c at the top flange only.

The submodels chosen for the welded repair investigations are modified by connecting the stiffener end to the girder flange. The same cut boundary displacements and cross-frame member forces specified in Section 8.3.2 are then applied to the revised models for repair analysis. Figures 8-52 and 8-53 plot the web gap σ_y stress results of the bottom flange submodels in comparison with the data obtained prior to the repair. Figures 8-54 and 8-55 present the same type of curves for the top flange submodels. The maximum web gap σ_x, σ_y, and σ_z stresses of the bottom and top flange submodels are tabulated in Tables 8-5 and 8-6. For the six details under investigation, at least 85% stress reductions are achieved after the repair. The post-retrofit stresses all decrease to below ½ CAFT, so cracks are not expected to occur by the welded repair even for an unlimited number of load cycles.

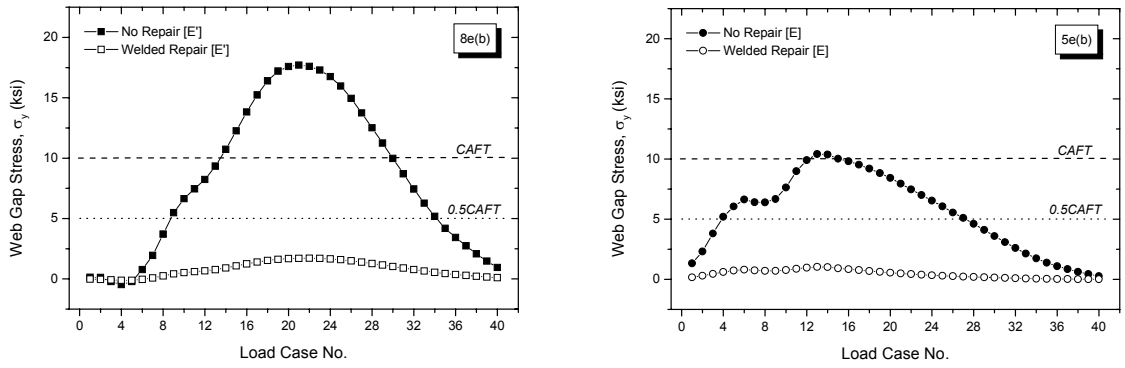

FIGURE 8-52: Bottom Flange Maximum Web Gap σ_y Stress Variation Before and After Welded Repair

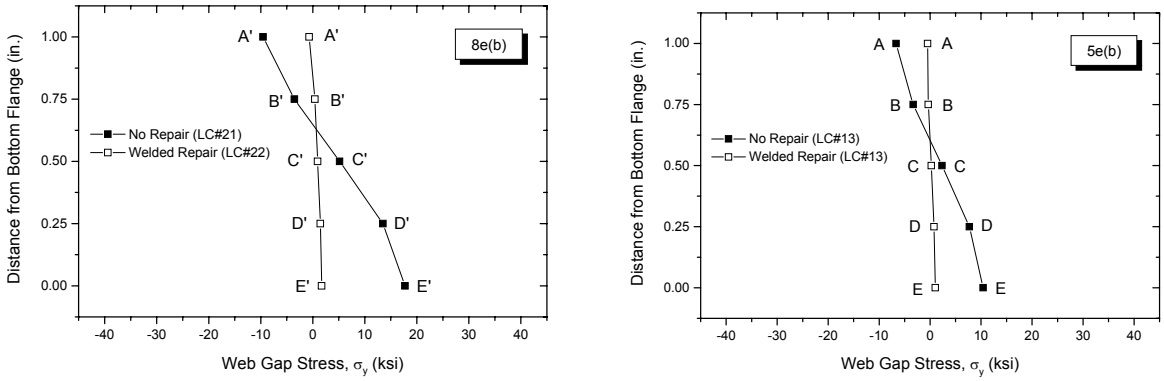

FIGURE 8-53: Bottom Flange Maximum Web Gap σ_y Stress Gradient Before and After Welded Repair

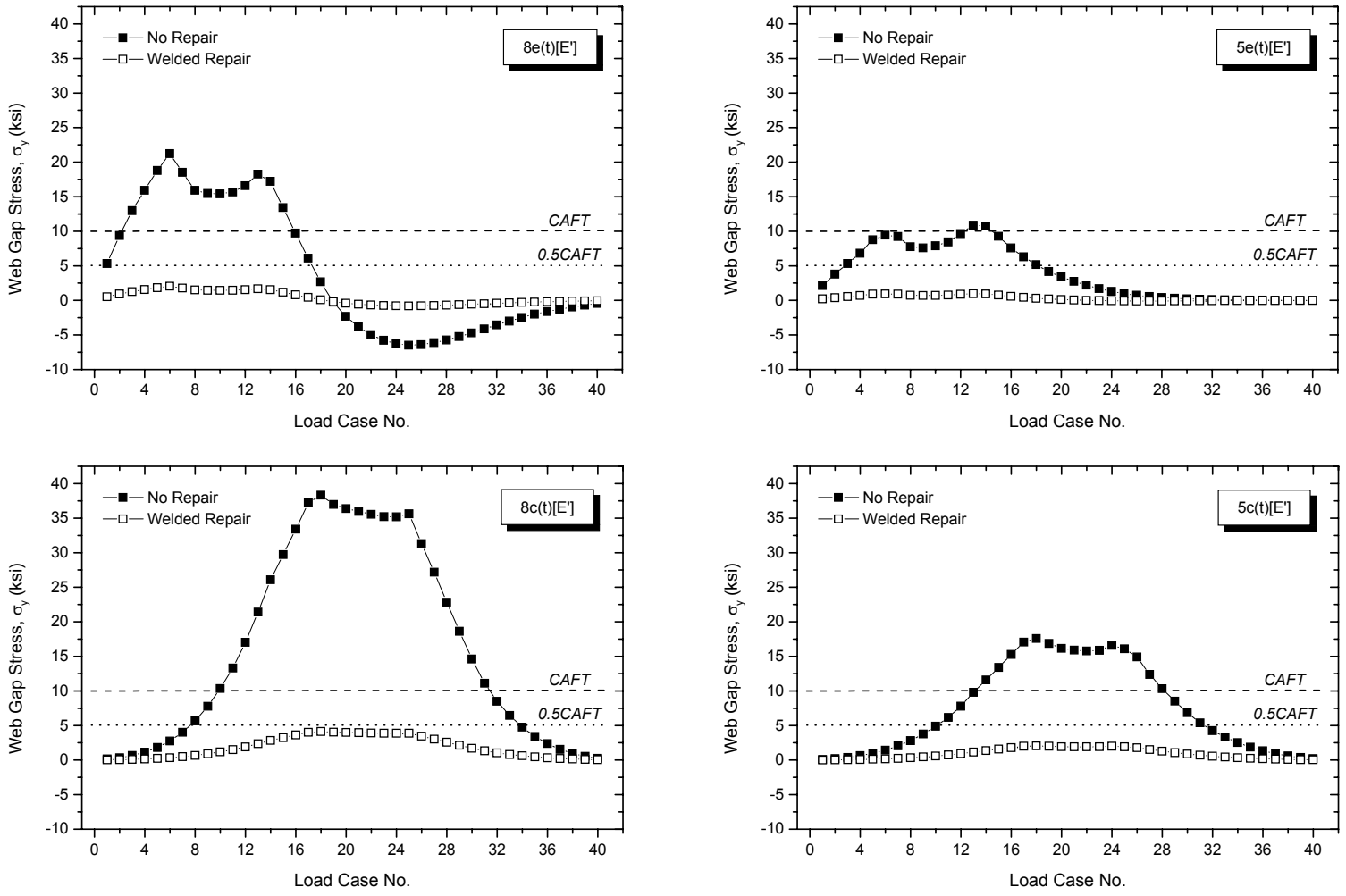

FIGURE 8-54: Top Flange Maximum Web Gap σ_y Stress Variation Before and After Welded Repair

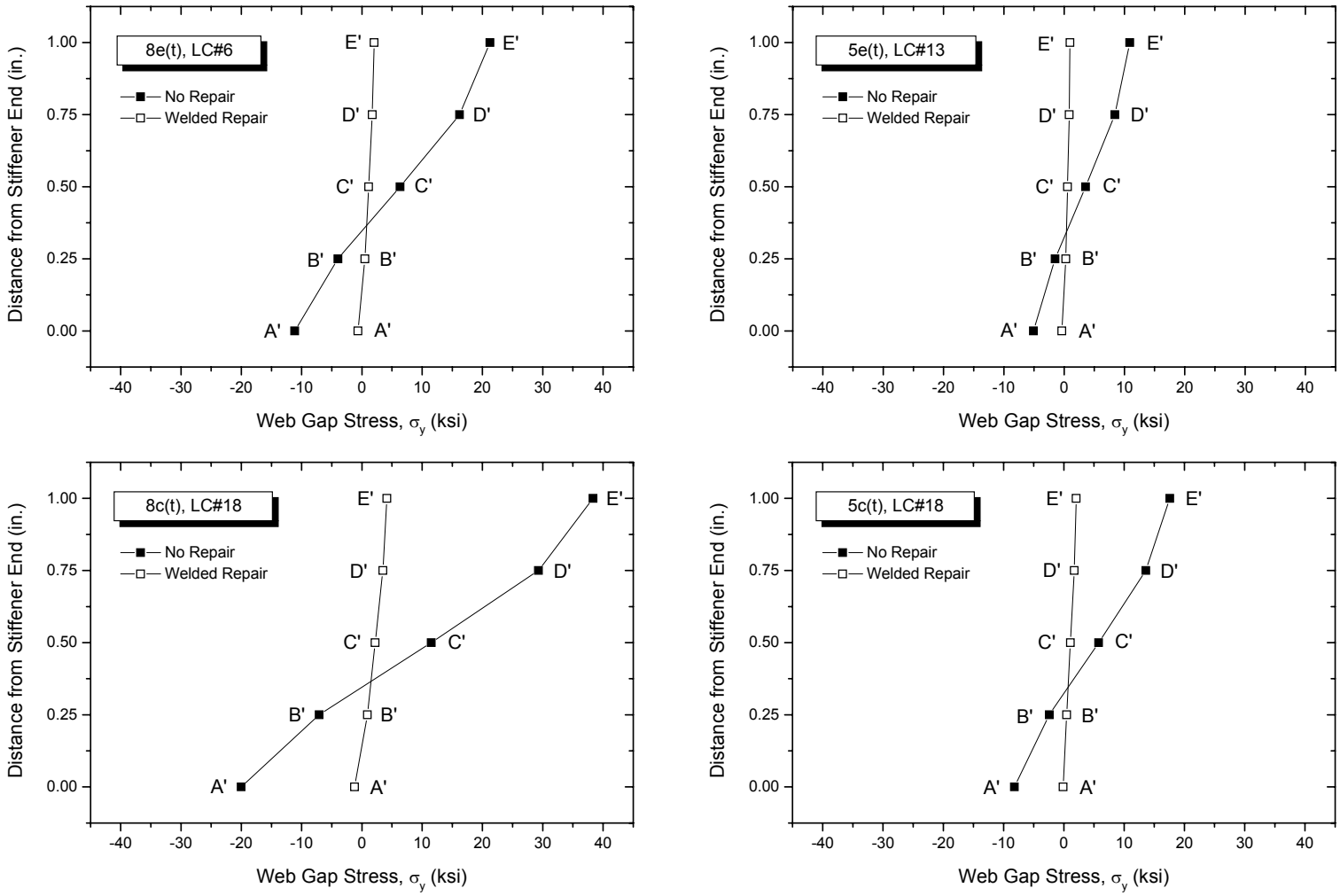

FIGURE 8-55: Top Flange Maximum Web Gap σ_y Stress Gradient Before and After Welded Repair

8.4.3 Repair Recommendations

The retrofit studies performed in this research indicate that both the brace removal and the welded repair are effective approaches in terms of lowering the web gap stress concentration caused by out-of-plane distortion. The original bridge plan shows that the lateral bracing was included for some, but not all of the skewed piers (Figure 8-1). Since no evaluation of girder lateral bracing requirements is made here, it is preferred that these bracing members be retained. The welded stiffener-to-flange connection is thus recommended as the repair approach for the Hump Yard Bridge. Retrofit is recommended for all the top flange connections and for the bottom flange connections with lateral braces. Actual web gap fatigue cracks have already been found in the bridge at the bottom flange of cross-frame to girder connections and at the top flange of floor-beam to girder connections. It is important that repair be carried out as soon as reasonable in order to limit the number of new cracks, especially for the most highly stressed web gap details at the top flange of mid-span sections and at the bottom flange with brace terminations.

TABLE 8-4: Comparison of the Maximum Web Gap Stresses Before and After Brace Removal for the Bottom Flange Submodels

Connection	8e (b)			5e (b)			3e (b)			AASHTO Fatigue Detail Category	CAFT
	No Repair	Brace Removal	% Reduc-tion	No Repair	Brace Removal	% Reduc-tion	No Repair	Brace Removal	% Reduc-tion		
$\sigma_{x, max}$	7.2 ksi	0.50 ksi	93%	-4.5 ksi	0.382 ksi	N.A.*	-5.5 ksi	-0.54 ksi	90%	C'	12 ksi
	L.C. #21	L.C. #14		L.C. #13	L.C. #13		L.C. #18	L.C. #17			
	Point A	Point A		Point A	Point A		Point A	Point A			
$\sigma_{y, max}$	18 ksi	1.4 ksi	92%	10 ksi	1.1 ksi	90%	13 ksi	1.2 ksi	91%	C	10 ksi
	L.C. #21	L.C. #12		L.C. #13	L.C. #13		L.C. #18	L.C. #16			
	Point E'	Point E'		Point E	Point E'		Point E	Point E			
$\sigma_{z, max}$	7.0 ksi	0.68 ksi	90%	-4.6 ksi	0.538 ksi	N.A.*	-6.0 ksi	-0.70 ksi	88%	C'	12 ksi
	L.C. #20	L.C. #10		L.C. #16	L.C. #13		L.C. #18	L.C. #17			
	Point A	Point A		Point A	Point A		Point A	Point A			

Note: * Due to the sign change from the maximum negative stress to the maximum positive stress, the percentage reduction is not calculated.

TABLE 8-5: Comparison of the Maximum Web Gap Stresses Before and After Welded Repair for the Bottom Flange Submodels

Connection	8e (b)			5e (b)			AASHTO Fatigue Detail Category	CAFT
	No Repair	Welded Repair	% Reduc-tion	No Repair	Welded Repair	% Reduc-tion		
$\sigma_{x, max}$	7.2 ksi	0.10 ksi	99%	-4.5 ksi	-0.08 ksi	98%	C'	12 ksi
	L.C. #21	L.C. #21		L.C. #13	L.C. #14			
	Point A	Point A		Point A	Point A			
$\sigma_{y, max}$	18 ksi	1.7 ksi	90%	10 ksi	1.0 ksi	90%	C	10 ksi
	L.C. #21	L.C. #22		L.C. #13	L.C. #13			
	Point E'	Point E'		Point E	Point E			
$\sigma_{z, max}$	7.0 ksi	-0.36 ksi	105%	-4.6 ksi	-0.68 ksi	85%	C'	12 ksi
	L.C. #20	L.C. #26		L.C. #16	L.C. #23			
	Point A	Point A		Point A	Point A			

TABLE 8-6: Comparison of the Maximum Web Gap Stresses Before and After Welded Repair for the Top Flange Submodels

Connec-tion	8e (t)			5e (t)			8c (t)			5c (t)			AASHTO Fatigue Detail Category	CAFT
	No Repair	Welded Repair	% Reduc-tion	No Repair	Welded Repair	% Reduc-tion	No Repair	Welded Repair	% Reduc-tion	No Repair	Welded Repair	% Reduc-tion		
$\sigma_{x, max}$	8.5 ksi	0.07 ksi	99%	4.1 ksi	0.06 ksi	99%	15 ksi	0.17ksi	99%	6.5 ksi	0.08 ksi	99 %	C'	12 ksi
	L.C. #6	L.C. #7		L.C. #13	L.C. #15		L.C. #18	L.C. #26		L.C. #18	L.C. #19			
	Point A	Point A		Point A	Point A		Point A	Point A		Point A	Point A			
$\sigma_{y, max}$	21 ksi	2.0 ksi	90%	11 ksi	0.97 ksi	91%	38 ksi	4.1 ksi	89%	18 ksi	2.0 ksi	88%	C	10 ksi
	L.C. #6	L.C. #6		L.C. #13	L.C. #13		L.C. #18	L.C. #18		L.C. #18	L.C. #18			
	Point E'	Point E'		Point E'	Point E'		Point E'	Point E'		Point E'	Point E'			
$\sigma_{z, max}$	8.7 ksi	0.46 ksi	95%	4.4 ksi	0.59 ksi	87%	14 ksi	-1.1 ksi	108%	5.7 ksi	-0.91 ksi	116 %	C'	12 ksi
	L.C. #6	L.C. #21		L.C. #13	L.C. #21		L.C. #18	L.C. #22		L.C. #18	L.C. #23			
	Point A	Point A		Point A	Point A		Point A	Point A		Point A	Point A			

8.5 Fisher's σ – Δ Expression

Assuming the web gaps deflect with equal double curvature under out-of-plane distortion, the σ_y stresses calculated by Fisher's formula are shown in Table 8-7 for the eight submodel details studied in this chapter. The results are much higher than those obtained from the ANSYS solution. The average stress ratio of the maximum ANSYS results vs. the Fisher's results is 0.35, based on the data provided in Table 8-7. Therefore, for this particular bridge with transverse cross-frame to girder connections, it is recommended that an adjustment factor of 0.35 be included in the Fisher's σ – Δ expression for prediction of web gap stresses.

TABLE 8-7: Web Gap Stresses Obtained from Fisher's Formula and ANSYS Analysis

Connection or Submodel	Load Case No.	Out-of-Plane Displacement Δ (in.)	Fisher $\sigma=3E\Delta t_w/L^2$ (ksi)	ANSYS σ_y (ksi) @ Point			
				A	E	A'	E'
8e (b)	21	1.93×10^{-3}	± 63	10	-17	-10	18
5e (b)	13	1.27×10^{-3}	± 41	-6.7	10	6.0	-11
3e (b)	18	1.49×10^{-3}	± 49	-7.9	13	7.4	-14
2e (b)	24	1.36×10^{-4}	± 4.4	0.71	-1.2	-0.65	1.2
8e (t)	6	2.31×10^{-3}	± 75	12	-21	-11	21
5e (t)	13	6.86×10^{-4}	± 22	5.4	-11	-5.1	11
8c (t)	18	4.67×10^{-3}	± 152	22	-37	-20	38
5c (t)	18	8.43×10^{-4}	± 27	8.8	-17	-8.2	18

Note: $t_w = {}^3/_8$ in., L = 1 in., E = 29000 ksi.

8.6 Summary

Finite element investigations are performed in this chapter for the typical cross-frame to girder connections of the Hump Yard Bridge. Analyses are carried out for selected web gap details at both the positive and negative moment regions and for both the top and bottom flanges. The key

elements of this case study are summarized below:

1. The out-of-plane fatigue cracks at the bottom flange cross-frame to girder connections are caused by the lateral bracing members used at the negative moment regions. Removing these members can successfully decrease the web gap stresses to below the infinite life fatigue limit, but is not recommended for the retrofit due to the concern of girder lateral torsional buckling.
2. The details susceptible to web gap fatigue cracking are the top flange of all the cross-frame to girder connections and the bottom flange of those connections with horizontal brace intersections. The recommended retrofit is to weld the connection stiffener to the girder flange. The web gap stresses developed at the bottom flange of cross-frame to girder connections with no brace intersections are not high enough to cause distortion-induced fatigue. These details can be left unmodified.
3. For the Type B cracks at Abutment No. 2, it is recommended that hole drilling be performed both before and after the crack repair welding. Bolt installation can be neglected since the crack path is removed after the repair.
4. The web gap stresses developed at both the top and bottom flanges are symmetric about the mid web thickness. The stress distribution along the web gap depth is not symmetric. The majority of the details under investigation have a zero stress location at about $^3/_8$ of the web gap length close to the stiffener end.
5. A modification factor of 0.35 is recommended for the use of Fisher's formula in estimating the web gap σ_y stress of this bridge.
6. Fatigue cracking at the bottom flange web gap is not seen very often in KDOT bridges. It is recommended that field testing be performed for the Hump Yard Bridge both before and after the repair to obtain actual strain measurements under traffic loading and to examine the role of the horizontal braces in development of the distortion-induced stresses.

Chapter 9

Case Study 5: The Tuttle Creek Bridge

The Tuttle Creek Bridge developed horizontal and horseshoe cracks at small web gaps close to the girder top flange. Repair had been previously performed by softening the connection plate end with a slot retrofit, but cracks were recently found to have reinitiated at some of the repaired details and are again propagating. This chapter presents a complete finite element study of the cracking behavior observed in the bridge and the appropriate retrofit methods that can be used for bridge repair. Investigations are also performed to examine the potential crack development in the girder bottom flange web gaps. The intent is to provide an effective repair method that can be applied to permanently arrest the crack growth.

9.1 Bridge Structure

The Tuttle Creek Bridge [KDOT Bridge No. 16-81-2.24(017)] was built in 1962 about 2.24 miles east of US-77 over the Big Blue River (Tuttle Creek Reservoir). It is a two-girder bridge with pin and hanger connections consisting of 10 units and 38 spans. The overall bridge length is 5350.1 feet. Currently, this is the fourth longest bridge in the state of Kansas. Figure 9-1 shows the cross section of the bridge. The total roadway width is 28 ft, including two 12-ft traffic lanes and two 2-ft shoulders. The noncomposite deck slab is $7^3/_8 \sim 10$ in. thick with compressive strength f_c' of 3000 psi. The cross-frame members were first bolted and then welded to the connection stiffeners. All transverse stiffeners were only connected to the girder web with intermittent welds, as shown in Figure 9-2. The major steel members were fabricated conforming to ASTM A373-54T, and the expansion devices were fabricated conforming to ASTM A7-56T. The 2002 AADT of the bridge is 520 vpd (vehicles per day) with 13% truck traffic. Figure 9-3

shows the framing plans of the typical end and intermediate bridge spans. The member properties of the cross-frames (Fig. 9-1) and the bottom flange diagonal bracings (Fig. 9-3) are summarized in Table 9-1. The girder detail of a typical intermediate span is shown in Figure 9-4.

TABLE 9-1: Cross-Frames and Diagonal Bracings

Cross-frames (Figures 9-1 and 9-3)

Type	Upper Chords	Bottom Chords	Diagonals	Cross-frame Height, h	Girder Height, d
F1	WT 5×16.5	WT 5×16.5	WT 4×8.5	6'- $4\frac{7}{8}$"	6'- 10"
F2	WT 5×16.5	WT 5×16.5	WT 4×8.5	6'- $8\frac{3}{16}$"	7'- $1\frac{5}{16}$"
F3	WT 5×16.5	WT 5×19.5	WT 4×8.5	7'- $6\frac{1}{4}$"	7'- $11\frac{3}{8}$"
F4	WT 5×16.5	WT 5×22.5	WT 4×8.5	8'- $11\frac{7}{16}$"	9'- $4\frac{1}{16}$"
FP	WT 5×16.5	WT 5×22.5	WT 4×8.5	10'- $7\frac{3}{8}$"	11'- 0"

Bottom Flange Diagonal Bracings (Figure 9-3)

Type	Member Designation
D1, D2	WT 5×12.5
D3, D4	WT 5×10.5
D5, D6	WT 5×14.5
D7, D8	WT 5×19.5
D9, D10	WT 5×22.5
D11, D12	WT 5×16.5

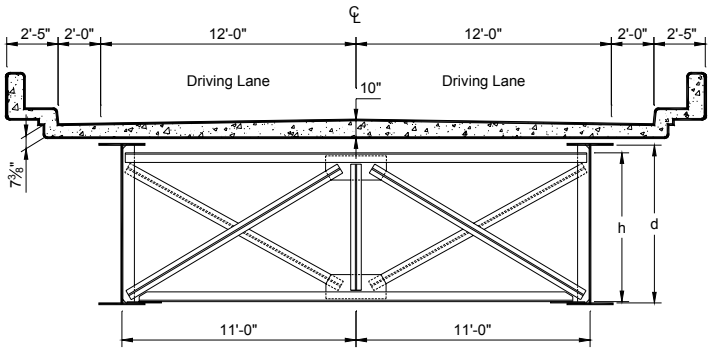

FIGURE 9-1: Cross Section of the Tuttle Creek Bridge

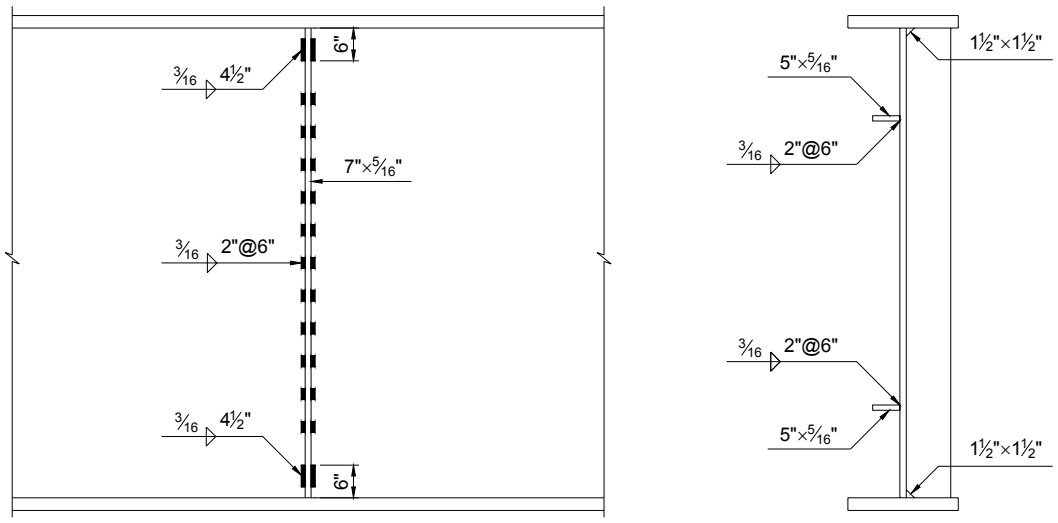

FIGURE 9-2: Intermediate and Connection Stiffener Details

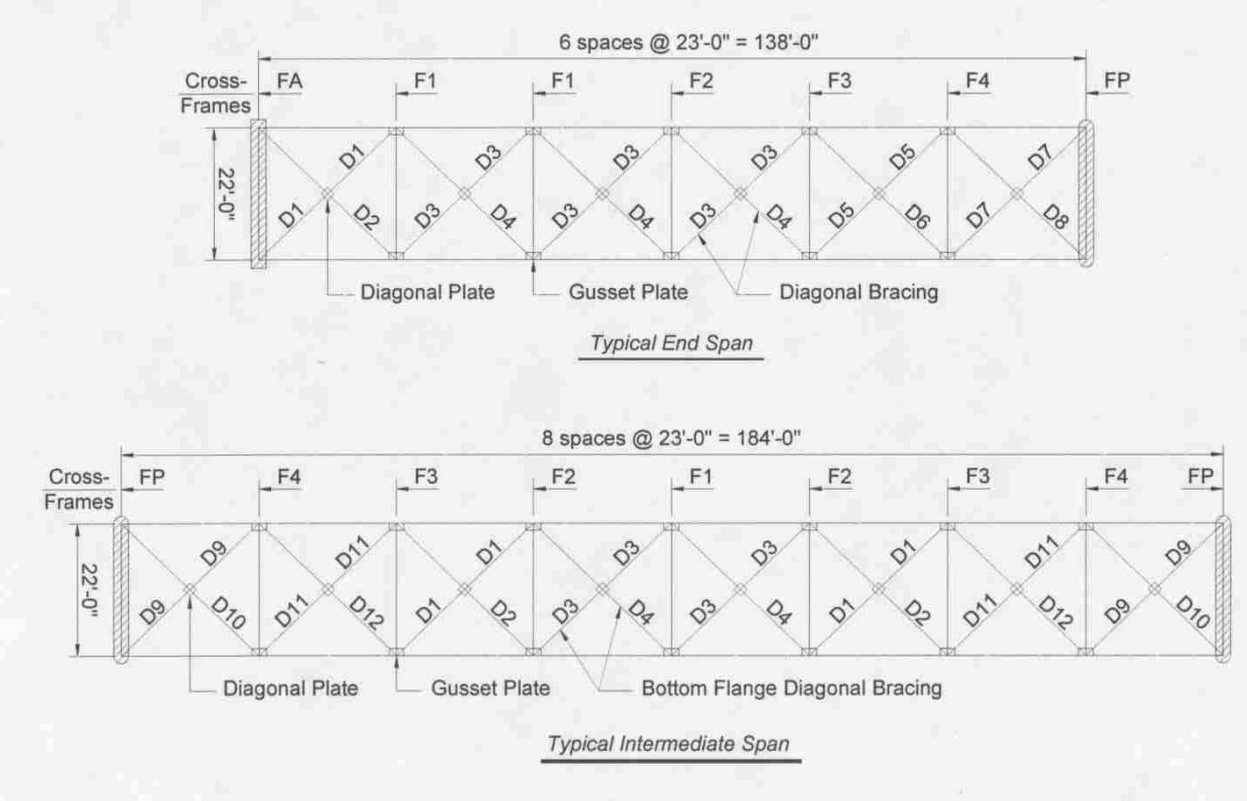

FIGURE 9-3: Framing Plan of Typical end and Intermediate Spans of the Bridge

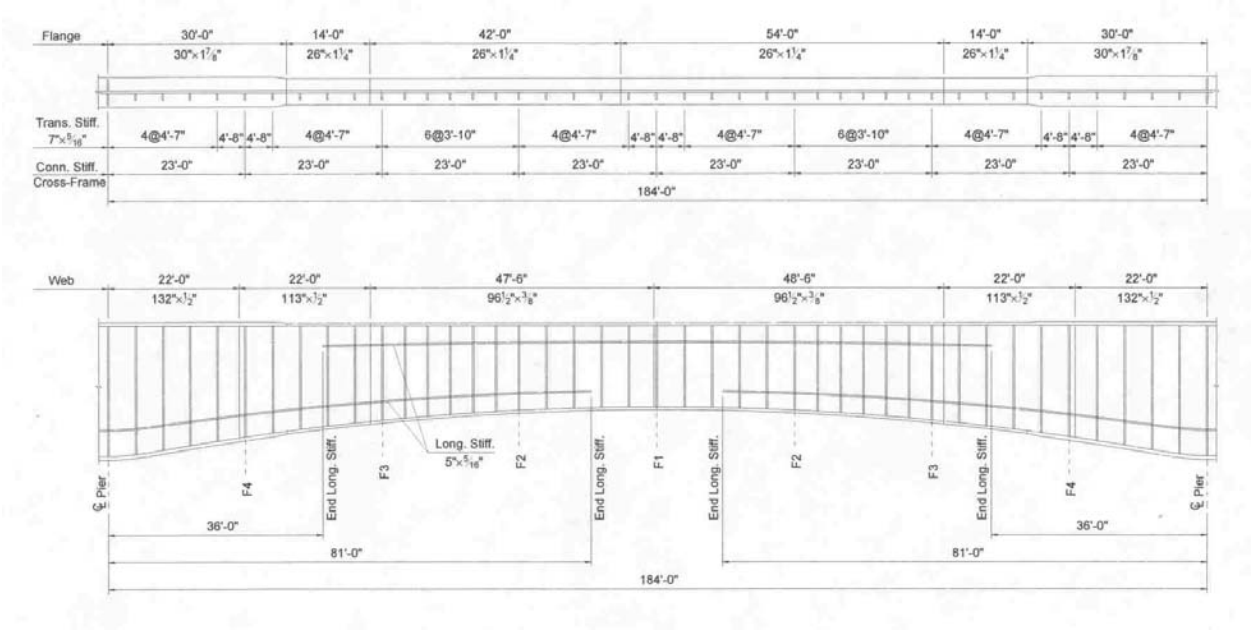

FIGURE 9-4: Girder Details of Typical Intermediate Spans

9.2 Crack Observation and KDOT Repair Recommendations

Figure 9-5 shows the horizontal and horseshoe cracks developed in the top flange web gaps and the KDOT retrofit applied in 1986. To soften the high constraint and stress intensity at the crack details, the web gap was lengthened by cutting a slot along the welded side of the connection plate. The slot was terminated 1 in below the observed crack end with a ½ in radius. For cracks located in both the web (Type A crack) and the connection stiffener (Type B crack), a burr free ¾ in diameter hole was placed at the end of the cracks with an intent to prevent from further propagation. However, this repair method turned out to be unsuccessful. Continuous crack growth and reinitiation have been reported from the field inspections carried out since the bridge was repaired. As shown in Figures 9-6 and 9-7, cracks were found passing over the slot ends or drilled holes at many repaired locations. The recent inspection report issued in 2000 shows that there are currently 382 cross-frame to girder connections in this bridge that have developed fatigue cracking. Compared to the 1996 inspection results, 10 of them are newly developed crack

details and 75 of the previously identified crack locations have been found with crack growth. To date, none of the inspections have reported crack formation at the bottom flange web gaps.

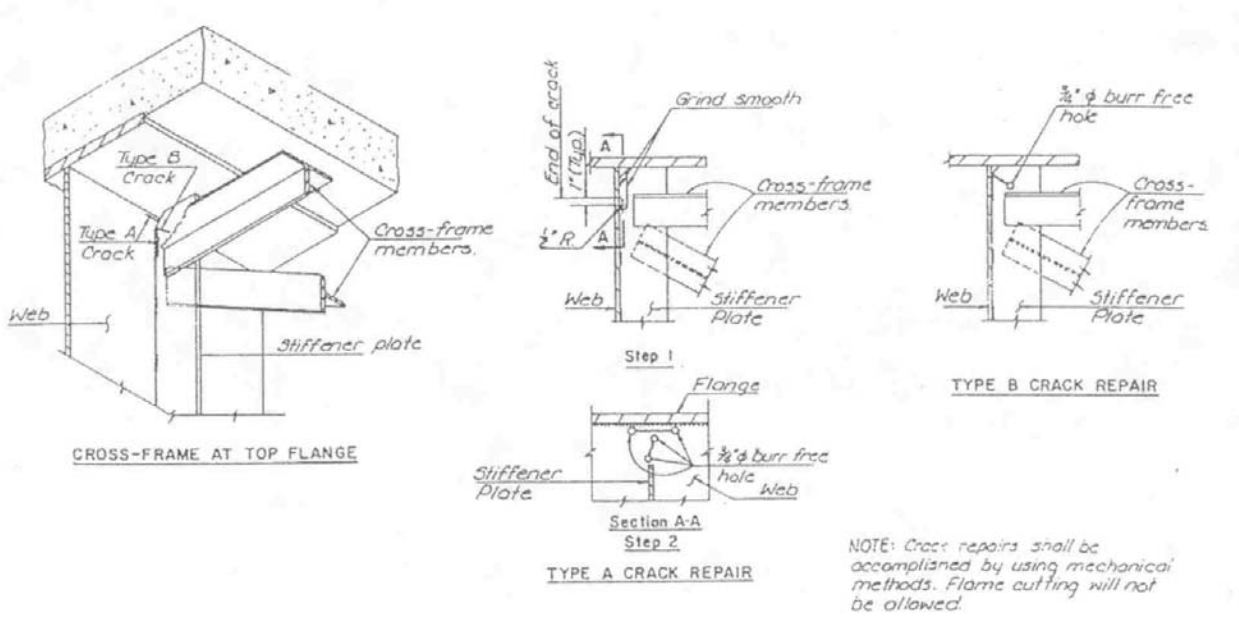

FIGURE 9-5: Crack Repair Detail Used in 1986 Bridge Retrofit

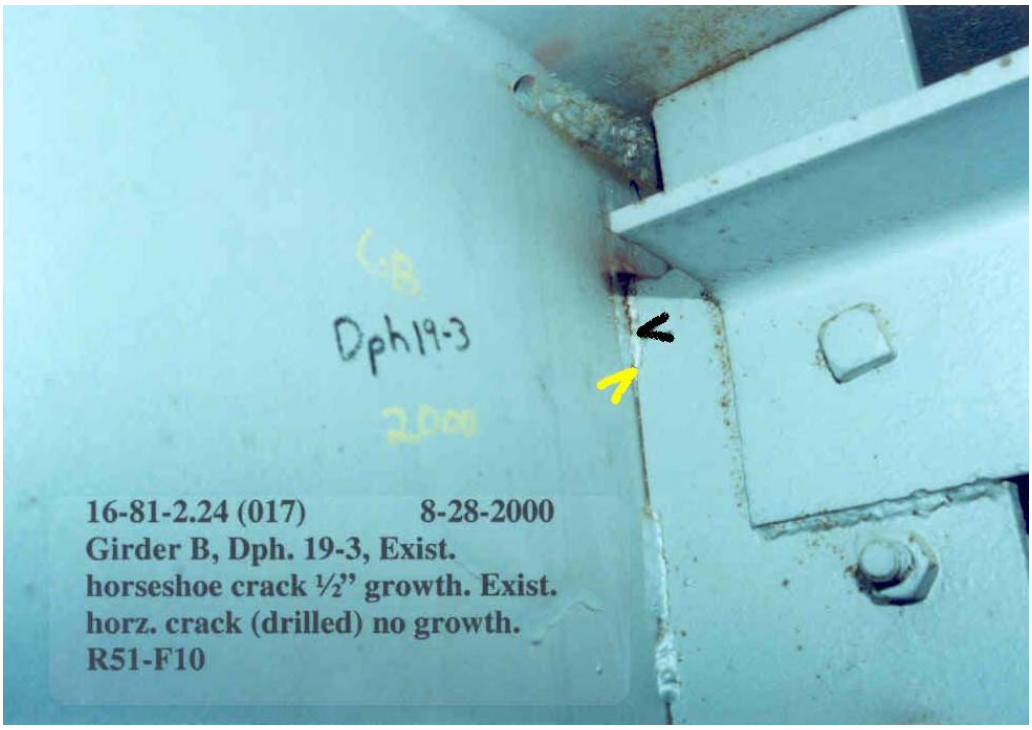

FIGURE 9-6: Crack Growth along the Vertical Stiffener-to-Web Welds

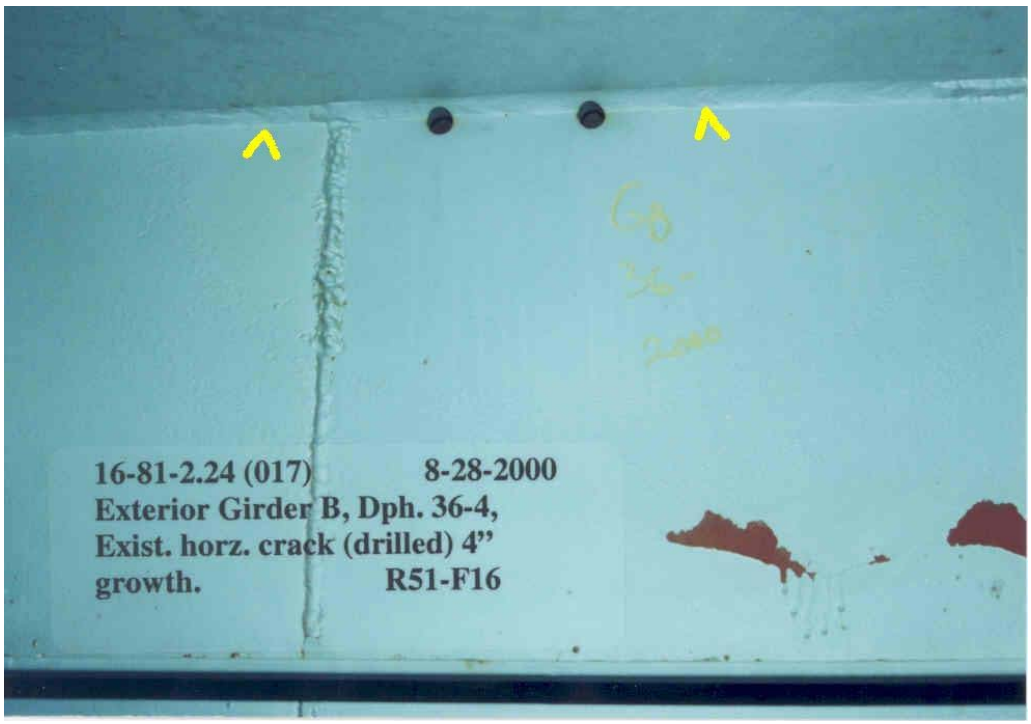

FIGURE 9-7: Crack Growth along the Horizontal Flange-to-Web Welds

It is believed that the following two aspects have caused the crack reinitiation. One is the defect formed at the weld end after the slot cut, and the other is the unsufficient slot length. At some repaired areas, the cut surface was not ground smooth, especially at the end of the vertical welds, which resulted in a new crack initiation site after the repair. Though a ½ in. radius was required for the slot end, in many cases the finished surface was ground to a flatter taper at the weld termination. Defects could always exist in the weld roots and the unfused region between the stiffener-web fillet weld roots was now exposed to the surface. This condition thus promoted crack reinitiation at some of the repaired details. As shown in Figure 9-2, both the transverse intermediate and connection stiffeners used in this bridge were attached to the girder web by intermittent welds. The top and bottom welds are 4½ in. long and those in between are 2 in. long with 6 in. spacing from center to center. The slot cut applied in 1986 at all the repaired locations

ended within the top first weld, so the removed portions of the connection stiffeners were all less than 6 inches. As previously mentioned in Chapter 2, in order to effectively release the web gap stress field, a minimum removal length of 12-in or 20 times of the web thickness should be used for a cut-short repair [NCHRP 336, 1990]. The slot lengths used in this bridge repair were apparently not long enough to provide adequate stress relaxation at the web gap areas, consequently leading to crack reinitiation and propagation.

The repair recommendations documented in the 2000 KDOT inspection report suggested that stop holes be drilled at the tips of the horizontal cracks that either have propagated past holes placed during the 1986 repair or have appeared after the repair. The horseshoe cracks were not recommended for additional hole drilling, as they appear to be self-stabilizing after the first pair of intermittent welds is broken. While it seems reasonable that once the first intermittent welds are cracked through, the web gap is lengthened to 12 inches so that the stress field can be greatly relived, this is more of a "passive" strategy and concerns still remain as to the effectiveness of the repair. Most of the previously repaired details have not reached the point where the first intermittent welds are completely broken, as were observed during the 2000 inspection. So cracks could continue to propagate into the web and even again past the holes drilled supposedly to arrest the horizontal crack extension. This has already happened to many of the repaired details. The same situation may also occur to those cracked but unrepaired details and those uncracked but crack-prone details. On the other hand, even though the web gap stresses decrease significantly after the first intermittent welds are broken, discontinuity and lack of fusion at the intermittent weld roots may again cause crack reinitiation or propagation along the second intermittent welds.

9.3 Similar Cases

A literature review found two other bridges with similar cracking scenarios: the Chamberlain Bridge in South Dakota [Fisher, 1984] and the I-65 Mobile Delta Crossing Bridge in Alabama [Stallings et al., 1993]. Both bridges developed fatigue cracks at girder top flange web gaps.

The Chamberlain Bridge is a multi-girder/cross-frame bridge that also used intermittent welds for the connection between the transverse stiffeners and the girder web. Cracks were found to have propagated downward through the weld throat or along the leg attached to the girder web at a few intermittent welds. In other words, cracks did not stop growing after the first intermittent welds were broken. The repair method used in this bridge was to weld the connection stiffeners to both girder top and bottom flanges.

The I-65 Mobile Delta Crossing Bridge is a two-girder/floor-truss bridge that used continuous fillet welds at transverse stiffener to girder web connections. Field test was performed at two selected locations using 6 in. and 10 in. slot repair. The 6 in. slot repair provided a web gap length of 12 times the web thickness (½ in.). The 10 in. slot represented a compromise between the recommended minimum of 20 times the web thickness ($^{7}/_{16}$ in.) and 12 in. The test data indicated that the 6 in. slot was ineffective, as it produced relatively small stress reductions and even some stress elevations at critical locations while increasing the out-of-plane displacements by 2 to 3.5 times. The 10 in. slot repair reduced the stress ranges at critical locations by approximately 50~75% while limiting the out-of-plane displacements to an acceptable level, so the overall performance of the 10 in. slot was considered to be satisfactory. However, the test results also indicated that the 10 in. slot would not eliminate all possibility of fatigue cracking at the floor-truss/girder connections. The stress range reductions corresponded to an increase in remaining fatigue life by factors of 27 to 64. Thus, the 10 in. slot may not

provide a permanent repair, but should prevent crack reinitiation for several years.

Based on the experience of the above two studies, it is believed that an "active" retrofit solution, such as a rigid connection stiffener to girder flange attachment, should be used in the Tuttle Creek Bridge to effectively eliminate the secondary stresses and to permanently stop the crack recurrence. The remaining part of this chapter provides detailed finite element study of the fatigue behavior observed in the bridge and the different repair methods mentioned above that can be used to inhibit crack growth. For issues regarding modeling techniques and fatigue evaluation procedures, see Chapters 4 and 5.

9.4 Finite Element Study

9.4.1 The Coarse Model

The coarse model is constructed including a typical intermediate span of the bridge, as shown in Figure 9-8. It has 13,731 elements and 21,024 nodes. The deck slab is modeled by 8-node brick elements (ANSYS Solid 45). The girder flanges, webs, and stiffeners are modeled by 4-nodel shell elements (ANSYS Shell 181). The cross-frame members and lateral bracings are modeled by 3-D spar elements (ANSYS Link 8). Coincident nodes are built at the girder top flange in contact with the bottom of the deck slab. Each pair of the coincident nodes is coupled for the X and Y DOFs. The Z DOFs are left uncoupled so that the bridge can act noncompositely. The girder and deck end sections are assumed fixed to simulate the continuous support at the piers, so the deck, flange, and web nodes at the model end sections are restrained to all DOFs. An HS15 fatigue truck with 10% wheel load increment of impact effect is considered for the model loading. As shown in Figure 9-9, the truck is placed at the center of the traffic lane close to Girder A (the westbound lane) and moved toward west for a total of 40 load cases. The distance between the adjacent truck locations is 5 feet. The cross-frame to girder

connections are named combining girder designation, cross-frame type, and the location corresponding to mid-span cross-frame F1. For example, A2E refers to the connection at Girder A and cross-frame F2 on the east side of girder mid-span, B3W refers to the connection at Girder B and cross-frame F3 on the west side of girder mid-span, and A1 refers to the connection at Girder A and mid-span cross-frame F1. Since this is a two-lane bridge with symmetric girder span and cross section, the structural response is expected to be axisymmetric about the intersection of the girder mid-span and the center of the roadway width when the same truck loading is applied to the traffic lane close to Girder B (the eastbound lane). In other words, the stress variation of connection A3E due to the westbound traffic should be the same as that of connection B3W due to the eastbound traffic. Therefore, only the bridge behavior under the westbound truck loading is investigated in this case study.

9.4.2 The Submodels

Submodel analyses are performed for selected cross-frame/girder connections as presented in the following sections. The overall submodel sizes are about 8,000 to 9,500 elements and nodes. Though cracks were only identified in the top flange web gaps, both the top and bottom flange submodel analyses are carried out for this bridge, because the connection stiffener is only welded to the girder web. Figure 9-10 shows schematically the correlation between the coarse model and the submodels. The submodel cut boundary DOFs are interpolated from the coarse model displacement results and the submodel nodal loads are obtained from the coarse model cross-frame and bracing member element forces. Mesh sizes are controlled within 1 in. with special refinement of ¼ in. at the web gap regions. Figure 9-11 shows the area of interest for web gap stress evaluation. Points A to G are on the interior web side and Points A' to G' are on the exterior web side. For both top and bottom flange submodels, Points A and A'

are close to the stiffener end and Points G and G' are close to the flange end of the web gap. Points G'1 to G'10 and G"1 to G"10 are nodes 1 in. apart, 10 in. from each side of the stiffener plate, on the side of the web with tensile σ_y stresses along the flange-to-web welds.

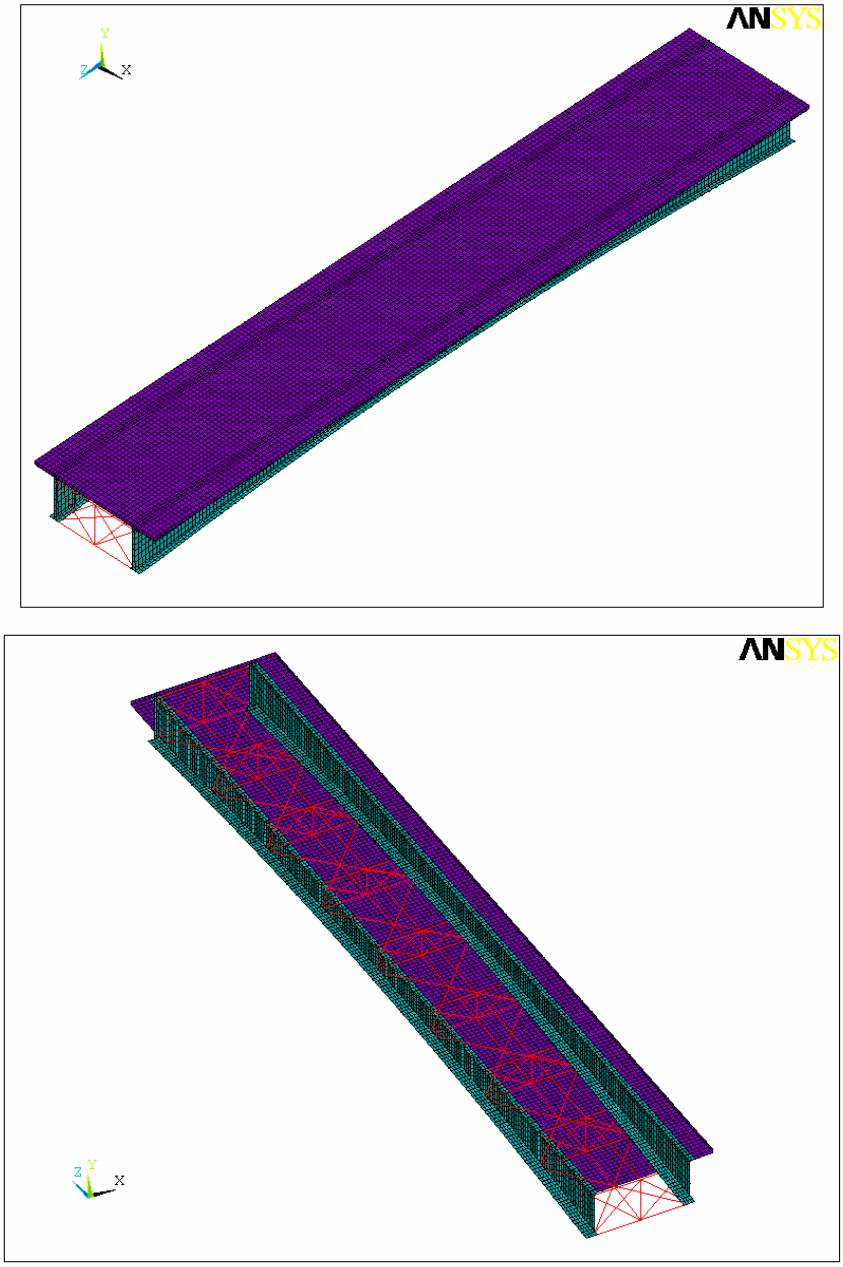

FIGURE 9-8: The Coarse Model

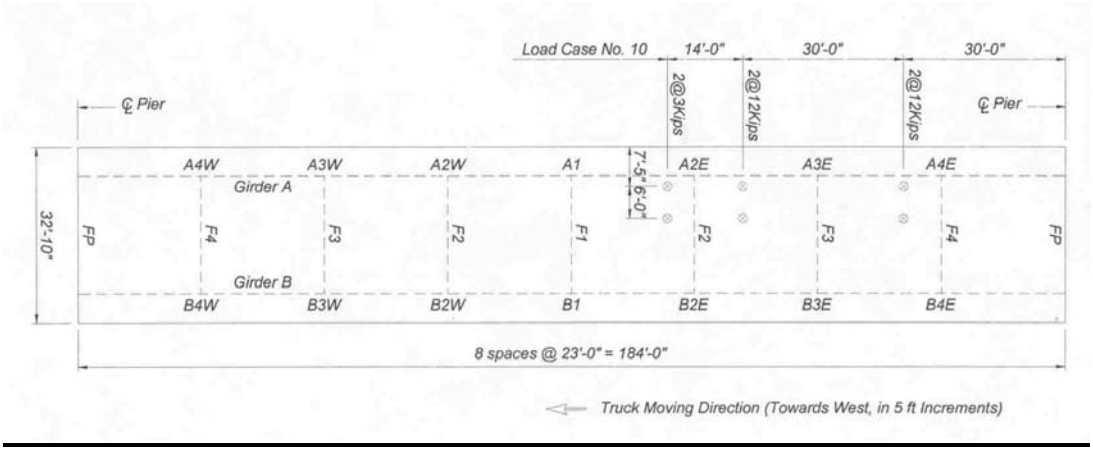

FIGURE 9-9: Coarse Model Track Moving Direction

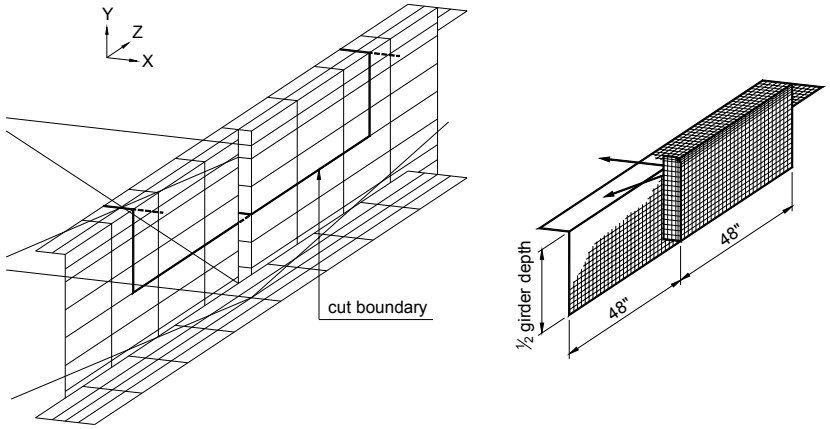

(a) Top Flange Submodeling

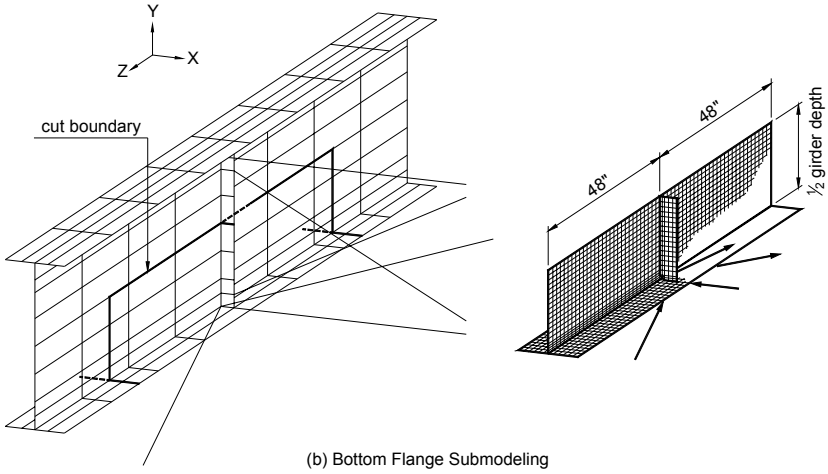

(b) Bottom Flange Submodeling

FIGURE 9-10: Coarse Model vs. Submodel

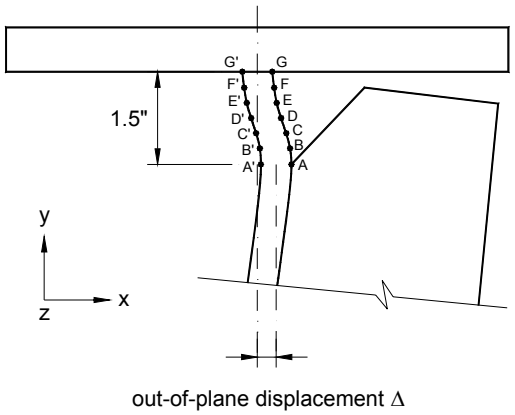

(a) Grid points within the top flange web gap

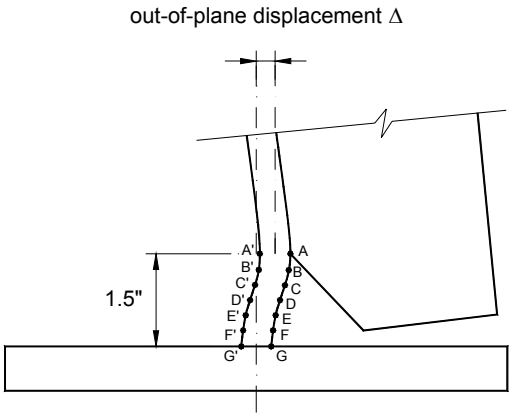

(b) Grid points within the bottom flange web gap

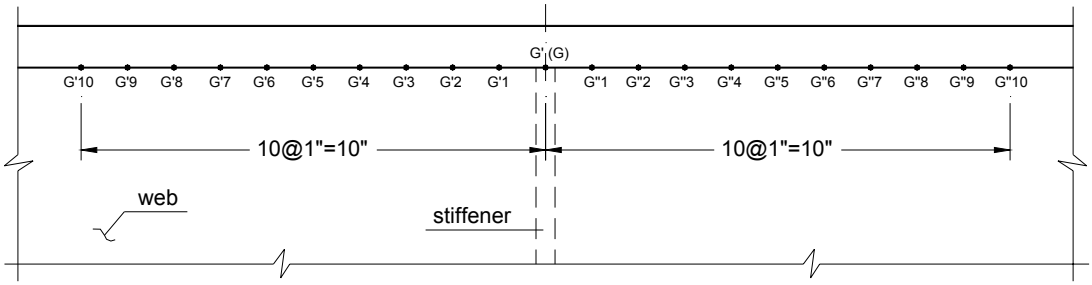

(c) Grid points along the top-flange-to-web connection

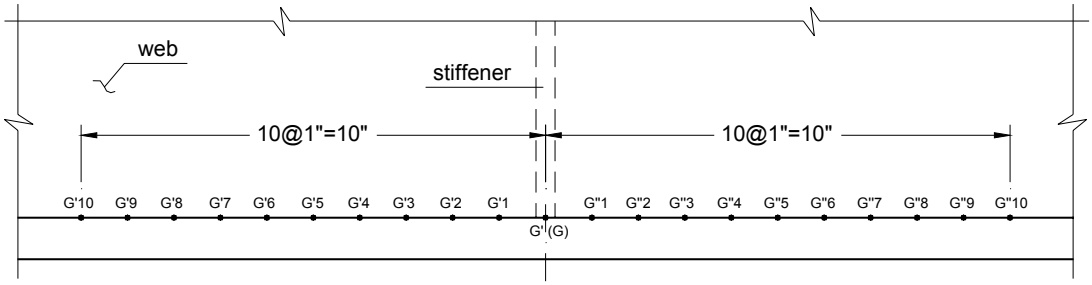

(d) Grid points along the bottom-flange-to-web connection

FIGURE 9-11: Web Gap Grid Points Specified for Submodel Stress Evaluation

9.4.2.1 Mid-Span Connections

Connections A1 and B1 at girder mid-span are investigated first to see which girder details would experience higher fatigue stresses due to the westbound truck traffic. Figure 9-12 shows the top flange web gap σ_y stress variation of connections A1 and B1. The legend in the graph gives information such as the designation of the cross-frame/girder connection, the location of the web gap ("t" for top flange and "b" for bottom flange), and the grid point where the stress is recorded (Point G' or G in most cases). The maximum σ_y stress of connection B1 is 46 ksi occurring at Load Case No. 17, which exceeds yielding. The maximum σ_y stress of connection A1 is 12 ksi occurring at Load Case No. 16. It is about 25% of the maximum σ_y stress developed in connection B1, but is still higher than CAFT. It is interesting to notice that while the truck moves on the lane close to Girder A, it actually causes much higher top flange web gap stresses in Girder B connection B1 than Girder A connection A1. Figure 9-13 shows the bottom flange web gap σ_y stress variation of the two mid-span connections. This time, stresses developed in connection A1 are higher than those of connection B1. Figure 9-14 shows the σ_y stress gradient of both the top and bottom flange submodels of connections A1 and B1 at their respective load cases with the highest magnitude of fatigue stresses. The maximum out-of-plane displacements and stresses obtained from the submodel analyses of these four details are summarized Table 9-2.

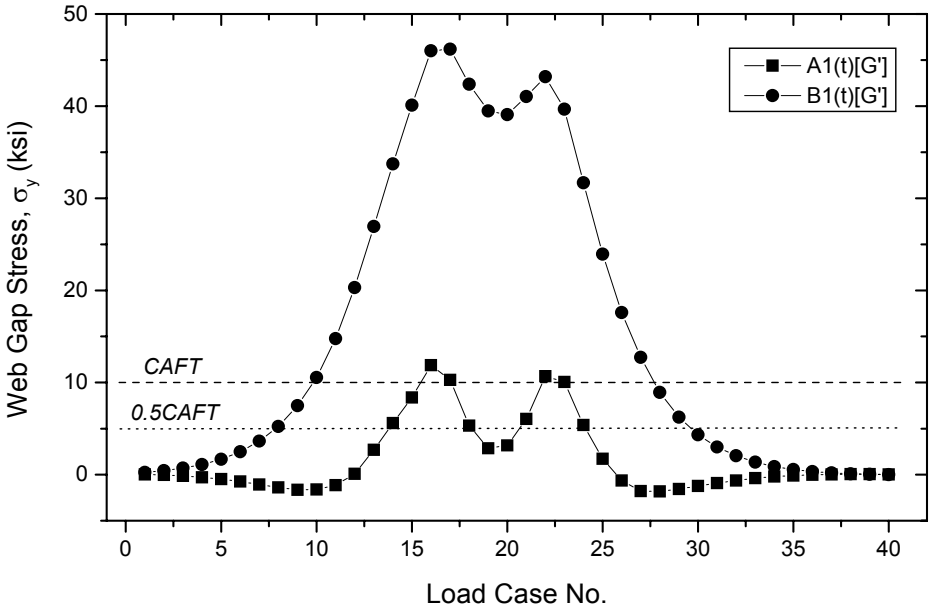

FIGURE 9-12: Top Flange Web Gap σ_y Stress Variation of Mid-Span Connections

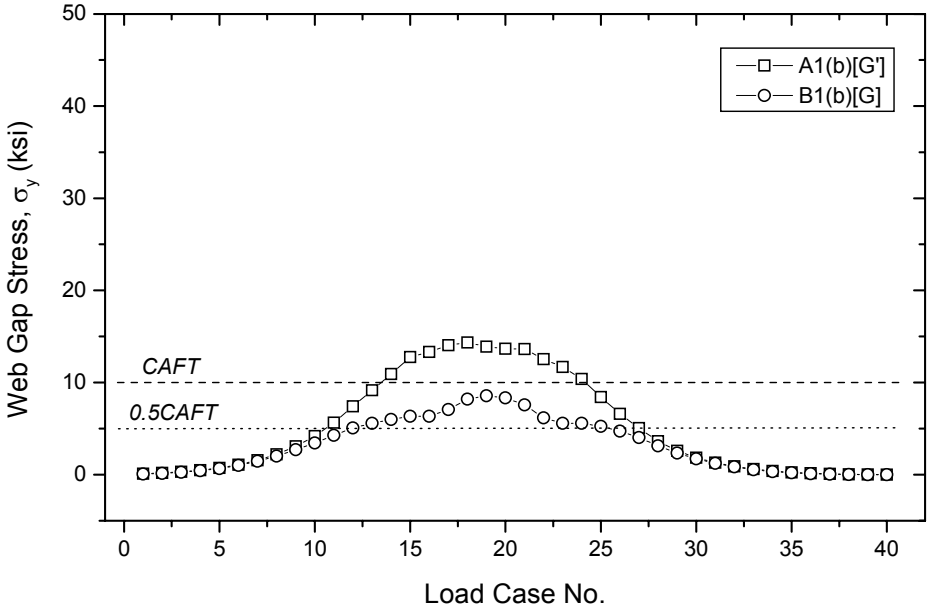

FIGURE 9-13: Bottom Flange Web Gap σ_y Stress Variation of Mid-Span Connections

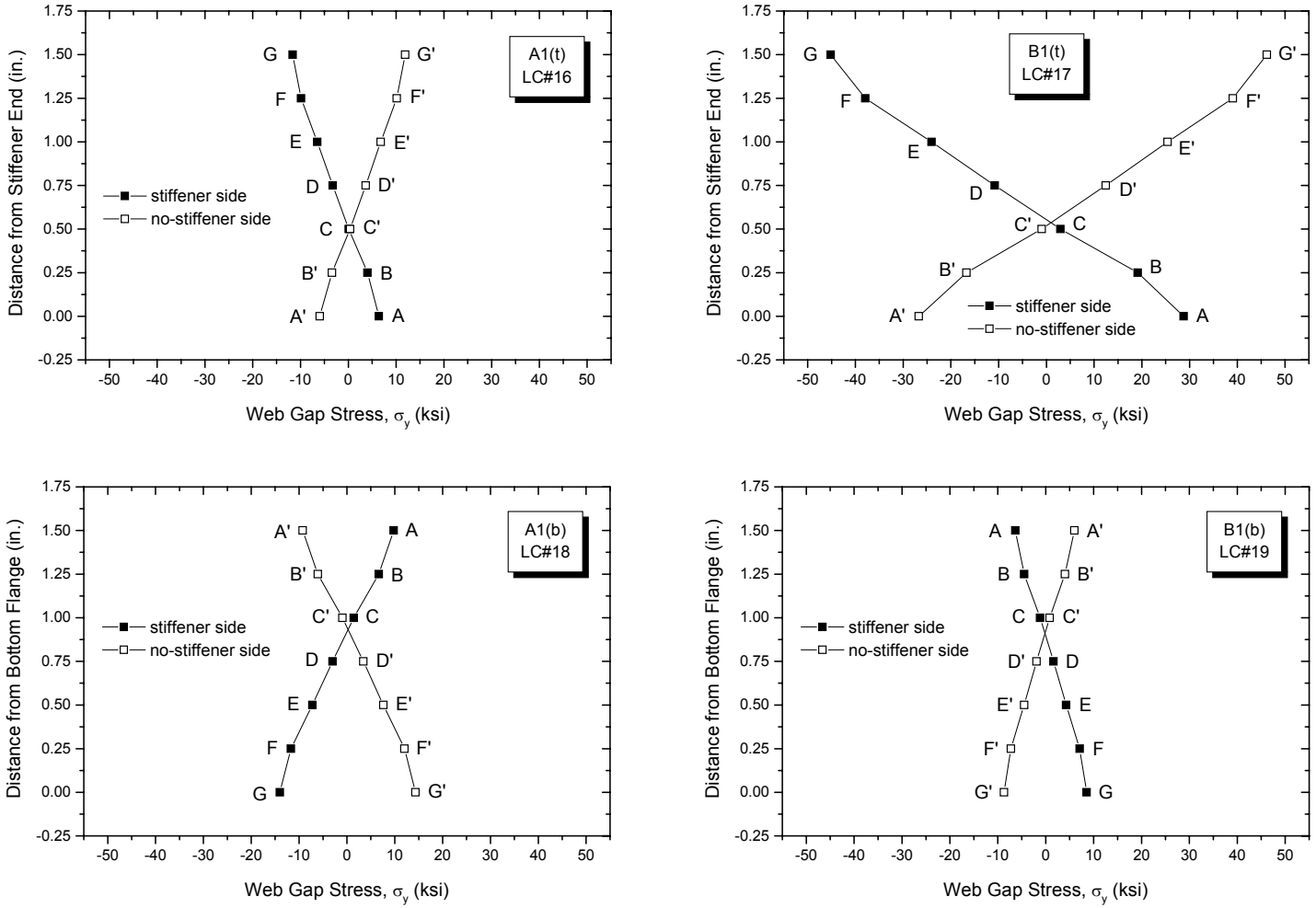

FIGURE 9-14: Web Gap σ_y Stress Gradient of the Mid-Span Cross-Frame/Girder Connections

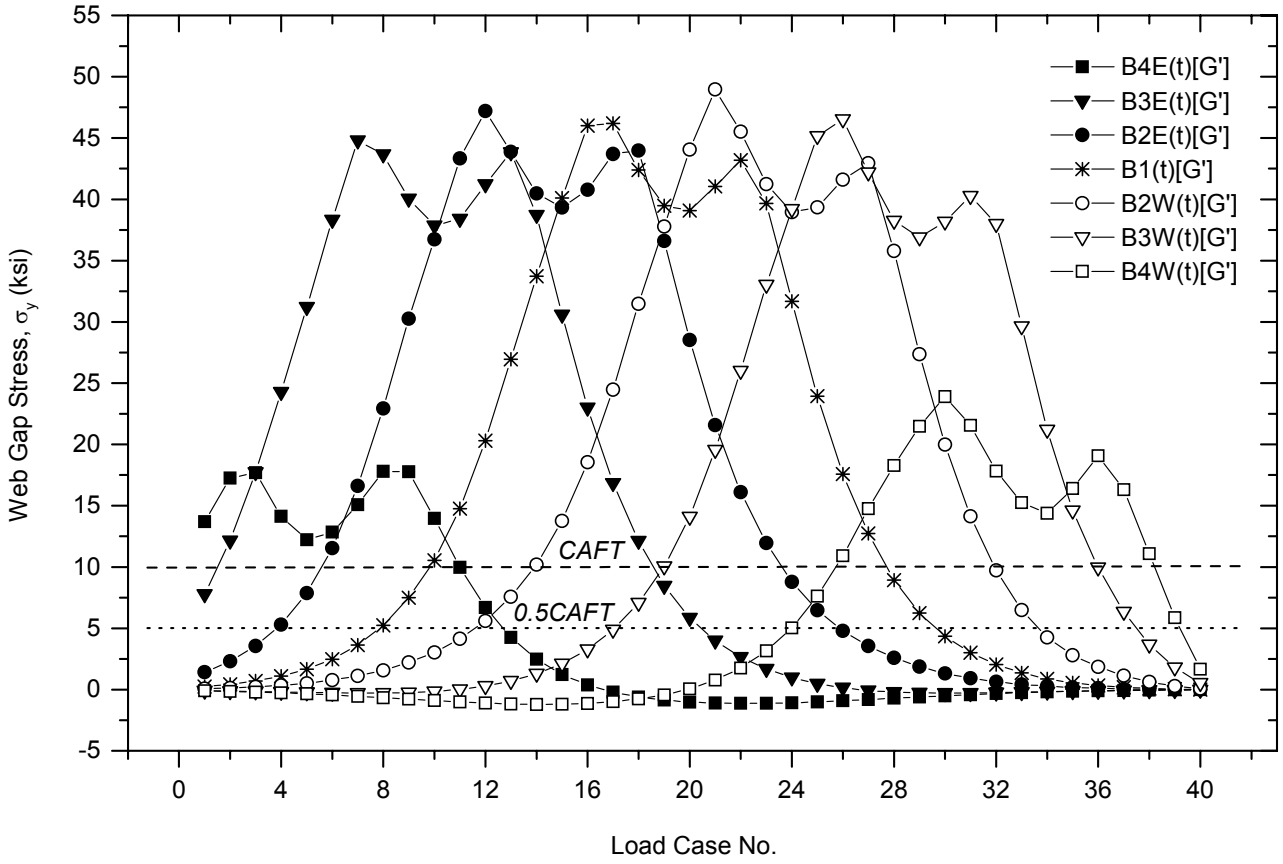

FIGURE 9-15: Web Gap σ_y Stress Variation of Girder B Top Flange Submodels

Since both connections are at the girder mid-span cross section, the corresponding stress variation experienced by connection A1 (or B1) due to the westbound traffic should be the same as that experienced by connection B1 (or A1) due to the eastbound traffic. So in general, as can be seen from the results of Figures 9-12 and 9-13, the stress ranges developed in the top flange web gaps are much higher than those developed in the bottom flange web gaps. This is why so many web gap fatigue cracks have already been found in the bridge close to the top flanges, but not yet in the bottom flanges. Based on the above observation, all the Girder B cross-frame connections are chosen for top flange submodel analysis as presented in Section 9.4.2.2 and only half span of the cross-frame connections of Girder A are chosen for bottom flange submodel analysis as presented in Section 9.4.2.3.

TABLE 9.2: Maximum Web Gap Stresses of Mid-Span Girder Connections

Connection	A1 (t)	B1 (t)	A1 (b)	B1 (b)	AASHTO Fatigue Detail Category	CAFT
Girder	A	B	A	B		
Web Gap Location	Top Flange	Top Flange	Bottom Flange	Bottom Flange		
Δ_{max}	1.82×10^{-3} in.	6.17×10^{-3} in.	1.33×10^{-3} in.	8.89×10^{-4} in.		
	L.C. # 16	L.C. # 16	L.C. # 18	L.C. # 19		
$\sigma_{x, max}$	4.2 ksi	18 ksi	6.0 ksi	-3.7 ksi	C'	12 ksi
	L.C. # 16	L.C. # 17	L.C. # 18	L.C. # 19		
	Point A	Point A	Point A	Point A		
$\sigma_{y, max}$	12 ksi	46 ksi	14 ksi	8.6 ksi	C	10 ksi
	L.C. # 16	L.C. # 17	L.C. # 18	L.C. # 19		
	Point G'	Point G'	Point G'	Point G		
$\sigma_{z, max}$	3.5 ksi	22 ksi	8.5 ksi	-4.0 ksi	C'	12 ksi
	L.C. # 16	L.C. # 17	L.C. # 18	L.C. # 19		
	Point A	Point A	Point A	Point A		

9.4.2.2 Girder B Top Flange Submodels

Submodel analyses are carried out for the top flange web gap details of all the cross-frame to Girder B connections shown in Figure 9-9. From the east to west, these connections are B4E, B3E, B2E, B1, B2W, B3W, and B4W. Figure 9-15 shows the web gap σ_y stress variation of the details under the westbound truck loading. Each detail experiences two stress cycles with the peak stresses occurring about 5 ~ 6 load cases in between. The minimum σ_y stresses of all seven connections are close to zero. The maximum σ_y stresses of the two negative moment region connections, B4E and B4W, are between 15 ~ 25 ksi. The maximum σ_y stresses of the other five connections in the positive and transition moment regions are between 45 ~ 50 ksi. Figure 9-16 shows the top flange web gap σ_y stress contour on both sides of the girder web of connection B2W at Load Case No. 21. Figures 9-17 and 9-18 show the web gap σ_x and σ_z stress contours of the same connection at the same load case on the interior web side. Other connections are found to have the same distribution pattern but with different stress magnitude. The maximum σ_x and σ_z stresses always occur at Point A. The minimum and maximum σ_y stresses always occur at Points G and G'. Table 9-3 summarizes the significant out-of-plane displacements and stresses of the seven top flange submodels under investigation. The maximum σ_x, σ_y, and σ_z stresses developed in these submodels are all higher than ½ CAFT. In particular, stresses developed in the positive and transition moment region connections are of very high magnitude. This is why cracks have been found in high percentage of cross-frame/girder connections in this bridge. Figures 9-19 and 9-20 plot the web gap σ_y stress gradient of the top flange submodels on the east and west half spans of Girder B. The stress gradient of the mid-span connection B1 has been plotted in Figure 9-14. A symmetric stress distribution is observed about the mid web thickness, but not about the mid web gap length. The zero stresses

are located about $^1/_3$ of the web gap length close to the vertical fillet weld ends. Figure 9-21 plots the σ_y stress distribution along the top-flange-to-web welds of connection B2W, as this is the detail that experiences the highest fatigue stress of the seven top flange connections. Stresses start to drop below ½ CAFT (5 ksi) at 5 in. away from each side of the stiffener plate. So a total of 10 in. affected zone can still be defined for the area of stress concentration.

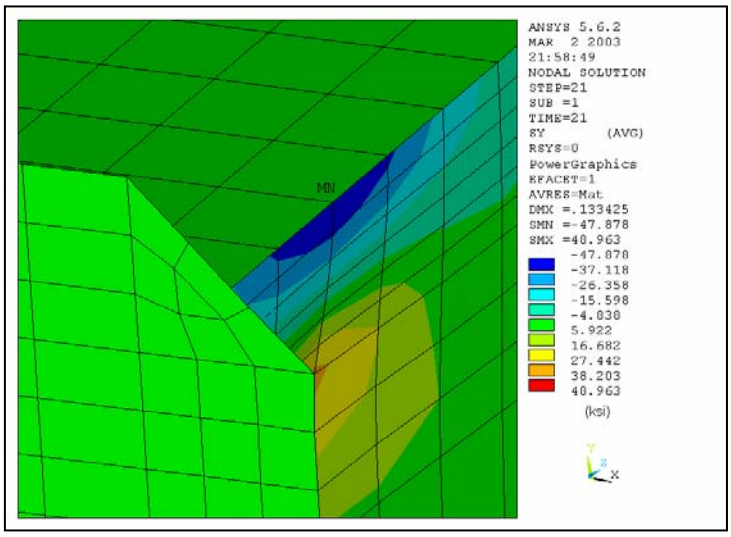

(a) the interior web side

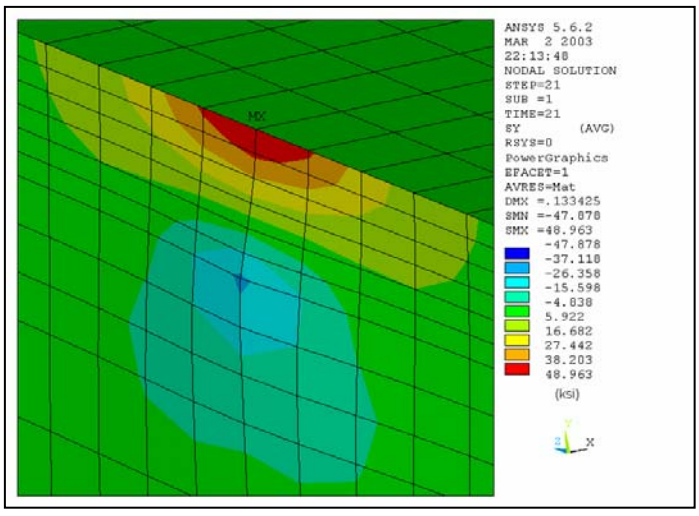

(b) the exterior web side

FIGURE 9-16: Load Case No. 21 Web Gap σ_y Stress Contour of Top Flange Submodel B2W

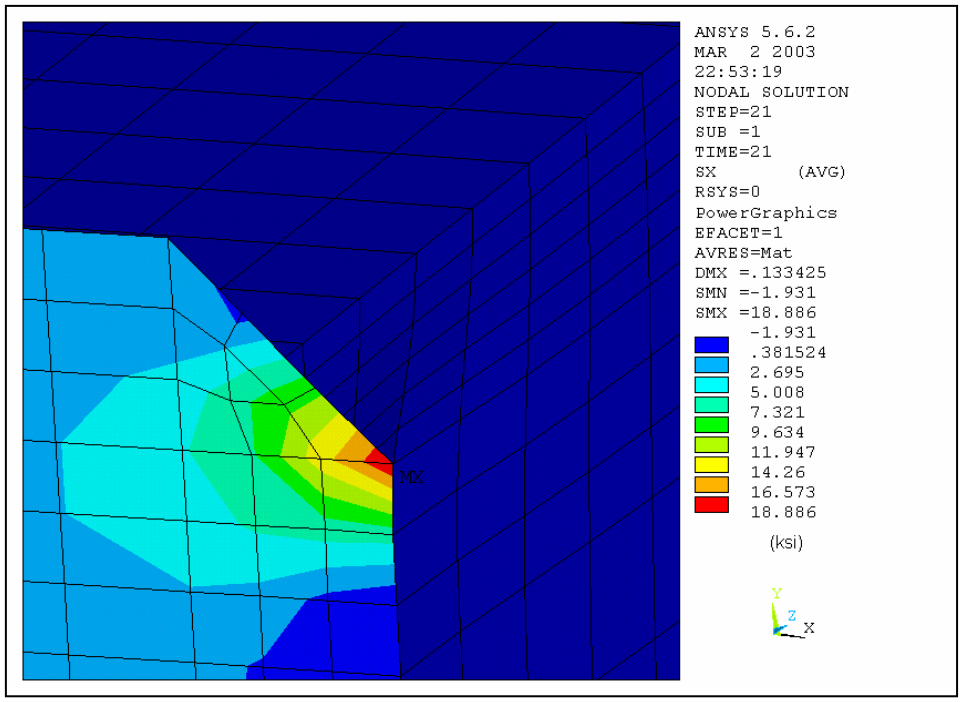

FIGURE 9-17: Load Case No. 21 Web Gap σ_x Stress Contour of Top Flange Submodel B2W

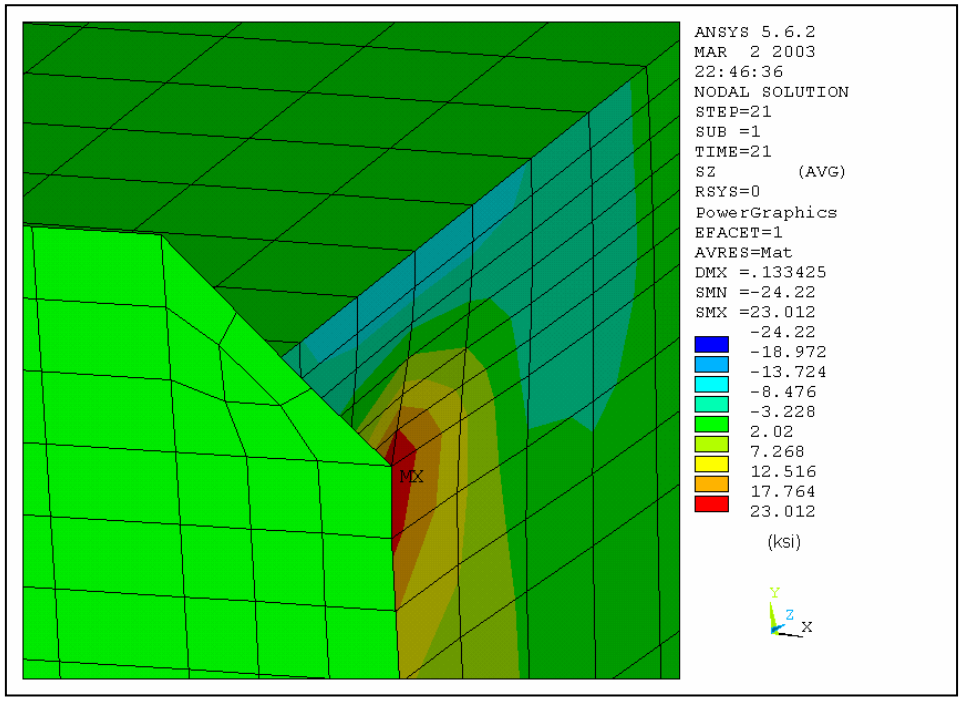

FIGURE 9-18: Load Case No. 21 Web Gap σ_z Stress Contour of Top Flange Submodel B2W

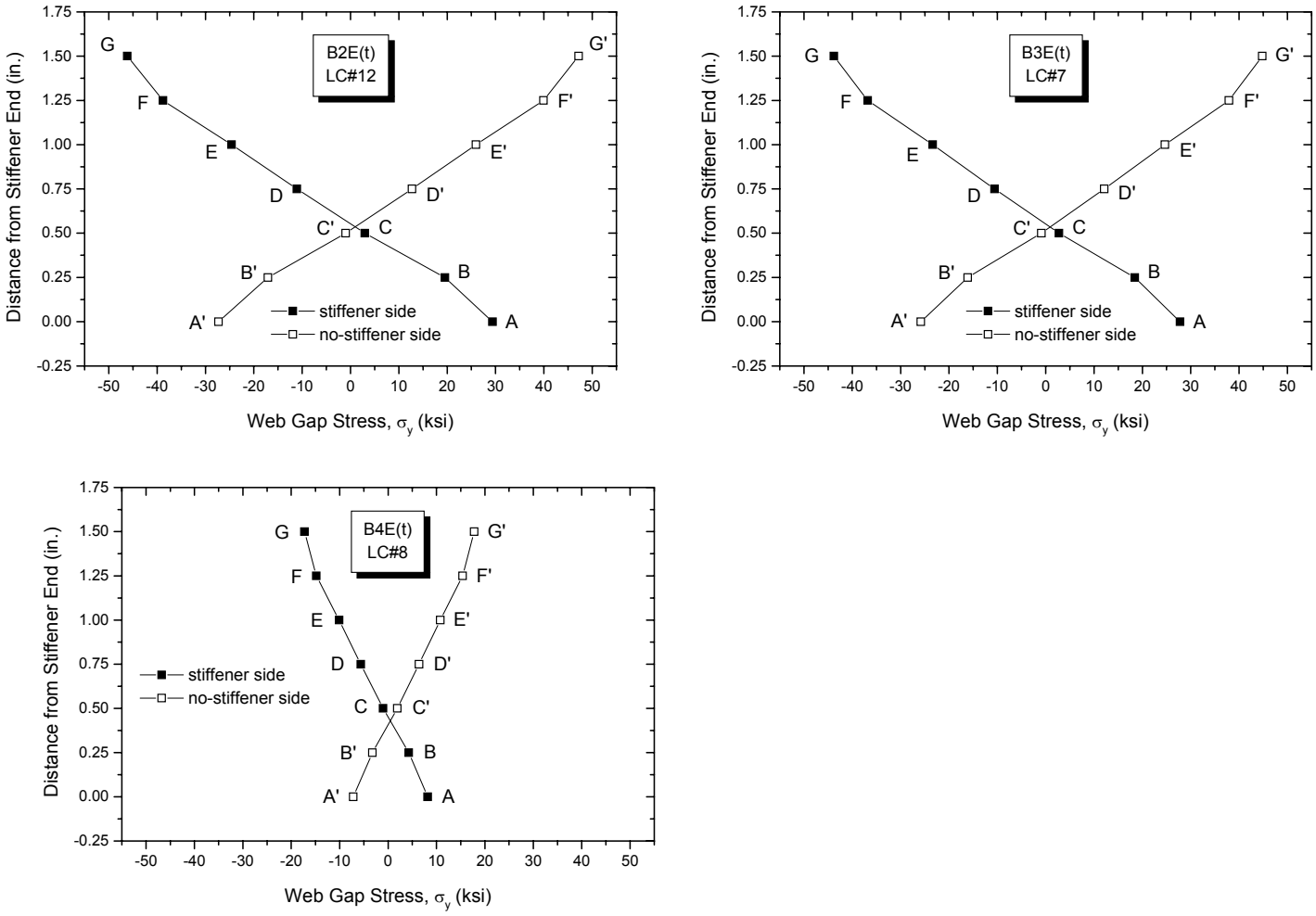

FIGURE 9-19: Top Flange Web Gap σ_y Stress Gradient of the East Half Span Girder B Connections

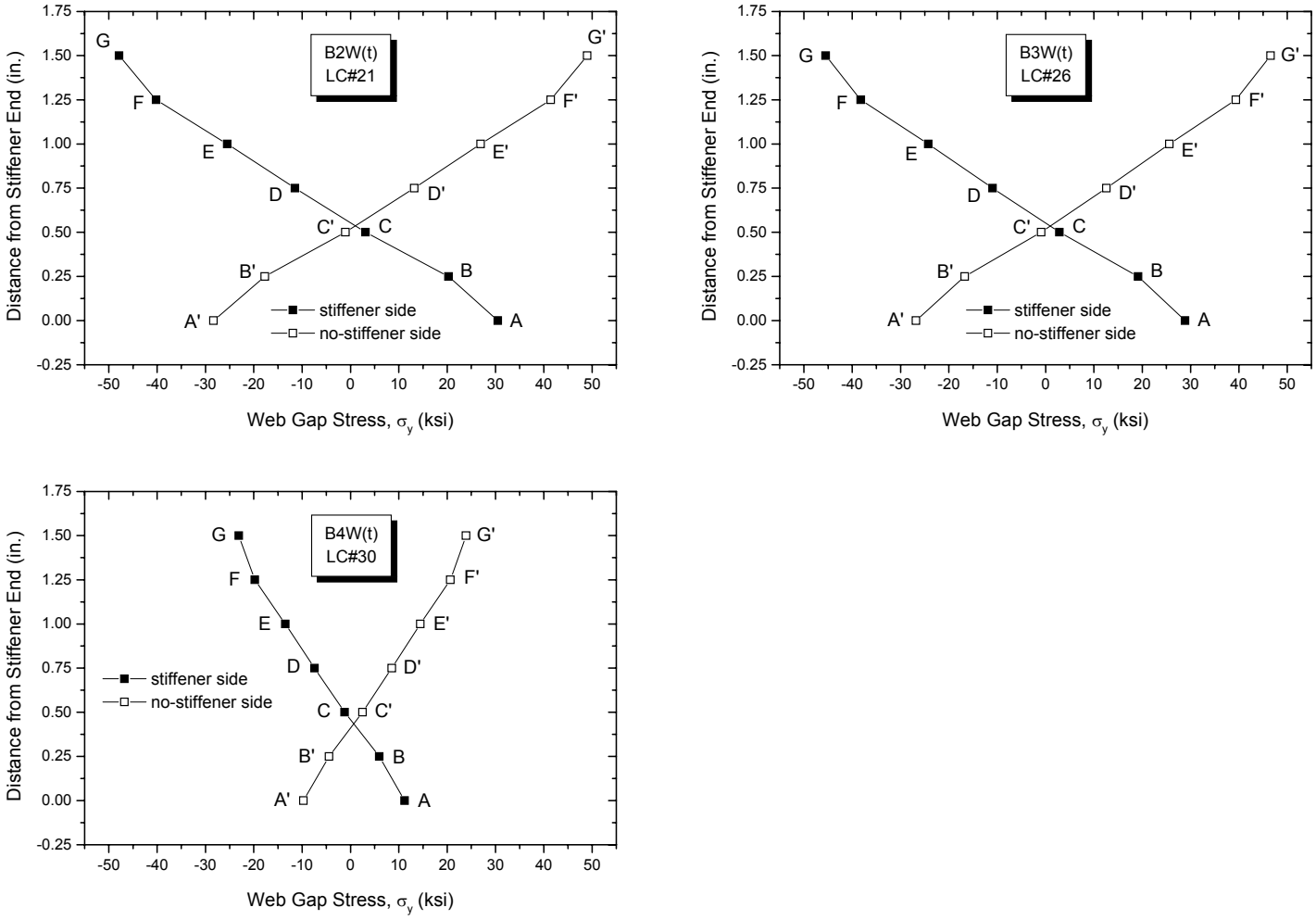

FIGURE 9-20: Top Flange Web Gap σ_y Stress Gradient of the West Half Span Girder B Connections

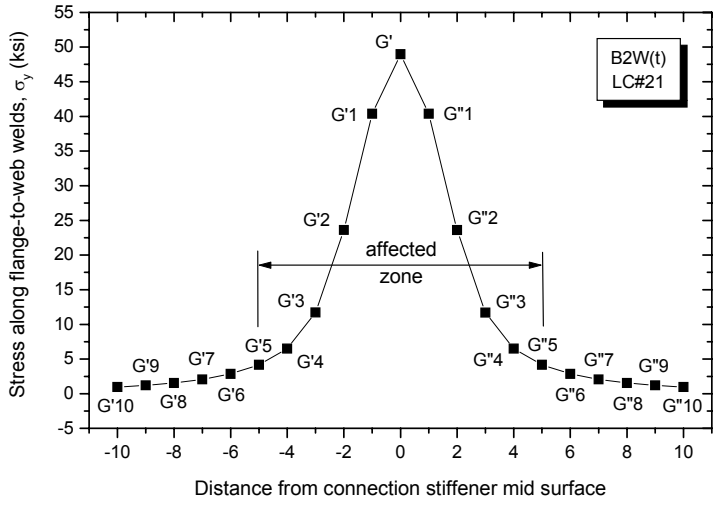

FIGURE 9-21: Load Case No. 21 σ_y Stress Distribution of Connection B2W Along the Top-Flange-to-Web Welds

9.4.2.3 Girder A Bottom Flange Submodels

Stresses developed in the bottom flange web gaps are not as significant as those developed in the top flange web gaps, so only the cross-frame connections in the west half span of Girder A are selected for bottom flange submodel analyses. As shown in Figure 9-9, these are connections A1, A2W, A3W, and A4W. Figure 9-22 plots the σ_y stress variation of these four connections for the entire truck passage. Compared to the curves in Figure 9-15 of the top flange submodels, the stresses experienced by the bottom flange submodels are of very low magnitude. The stress range experienced by the negative moment region connection A4W is below ½ CAFT, so fatigue cracks are not expected to occur at this location. However, the stress ranges experienced by the positive and transition moment region connections are still above CAFT, between 10~15 ksi. So cracks may still have the change to develop in the bottom flange web gaps, as long as the details are subjected to sufficient number of load cycles. Connection A2W is found to experience the highest fatigue stresses, so its web gap stress contours are plotted in Figures 9-23 to 9-25 for σ_y, σ_x, and σ_z, respectively. The overall stress distributions of the other

three connections are very similar to that of connection A2W, but with lower stress magnitude. Table 9-4 summarizes the maximum out-of-plane displacements and stresses of the four bottom flange submodels under investigation. As observed in the top flange submodels, the maximum σ_x and σ_z stresses also occur at Point A and the maximum σ_y stresses also occur at Point G'. Figure 9-26 shows the σ_y stress gradient of these bottom flange submodels within the web gap. Again, stresses are found symmetric about the mid web thickness, but not about the mid web gap length. The zero stresses are also located at about $^1/_3$ of the web gap length close to the end of the vertical stiffener-to-web welds. Figure 9-27 shows the σ_y stress distribution of connection A2W along the bottom-flange-to-web welds. The area affected by stress concentration is also within a 10 in. zone of the girder web (5 in. on each side of the stiffener plan).

TABLE 9.3: Maximum Web Gap Stresses of Girder B Top Flange Submodels

Conn-ection	B4E (t)	B3E (t)	B2E (t)	B1 (t)	B2W (t)	B3W (t)	B4W (t)	AASHTO Fatigue Detail Category	CAFT
Δ_{max}	1.83×10^{-3} in.	6.50×10^{-3} in.	6.56×10^{-3} in.	6.17×10^{-3} in.	6.72×10^{-3} in.	6.63×10^{-3} in.	2.54×10^{-3} in.		
	L.C. # 3	L.C. # 7	L.C. # 12	L.C. # 16	L.C. # 21	L.C. # 26	L.C. # 30		
$\sigma_{x, max}$	9.0 ksi	17 ksi	18 ksi	18 ksi	19ksi	18 ksi	12 ksi	C'	12 ksi
	L.C. # 9	L.C. # 7	L.C. # 12	L.C. # 17	L.C. # 21	L.C. # 26	L.C. # 30		
	Point A	Point A	Point A	Point A	Point A	Point A	Point A		
$\sigma_{y, max}$	18 ksi	45 ksi	47 ksi	46 ksi	49 ksi	47 ksi	24 ksi	C	10 ksi
	L.C. # 8	L.C. # 7	L.C. # 12	L.C. # 17	L.C. # 21	L.C. # 26	L.C. # 30		
	Point G'	Point G'	Point G'	Point G'	Point G'	Point G'	Point G'		
$\sigma_{z, max}$	7.4 ksi	21 ksi	22 ksi	22 ksi	23 ksi	22 ksi	10 ksi	C'	12 ksi
	L.C. # 9	L.C. # 7	L.C. # 12	L.C. # 17	L.C. # 21	L.C. # 26	L.C. # 30		
	Point A	Point A	Point A	Point A	Point A	Point A	Point A		

TABLE 9-4: Maximum Web Gap Stresses of Girder A Bottom Flange Submodels

Connection	A1 (b)	A2W (b)	A3W (b)	A4W (b)	AASHTO Fatigue Detail Category	CAFT
Δ_{max}	1.33×10^{-3} in.	1.47×10^{-3} in.	1.39×10^{-3} in.	2.12×10^{-4} in.		
	L.C. # 16	L.C. # 23	L.C. # 27	L.C. # 33		
$\sigma_{x, max}$	6.0 ksi	6.1 ksi	5.0 ksi	2.5 ksi	C'	12 ksi
	L.C. # 18	L.C. # 22	L.C. # 27	L.C. # 29		
	Point A	Point A	Point A	Point A		
$\sigma_{y, max}$	14 ksi	15 ksi	12 ksi	4.5 ksi	C	10 ksi
	L.C. # 18	L.C. # 22	L.C. # 27	L.C. # 29		
	Point G'	Point G'	Point G'	Point G'		
$\sigma_{z, max}$	8.5 ksi	8.7 ksi	6.5 ksi	1.7 ksi	C'	12 ksi
	L.C. # 18	L.C. # 22	L.C. # 27	L.C. # 30		
	Point A	Point A	Point A	Point A		

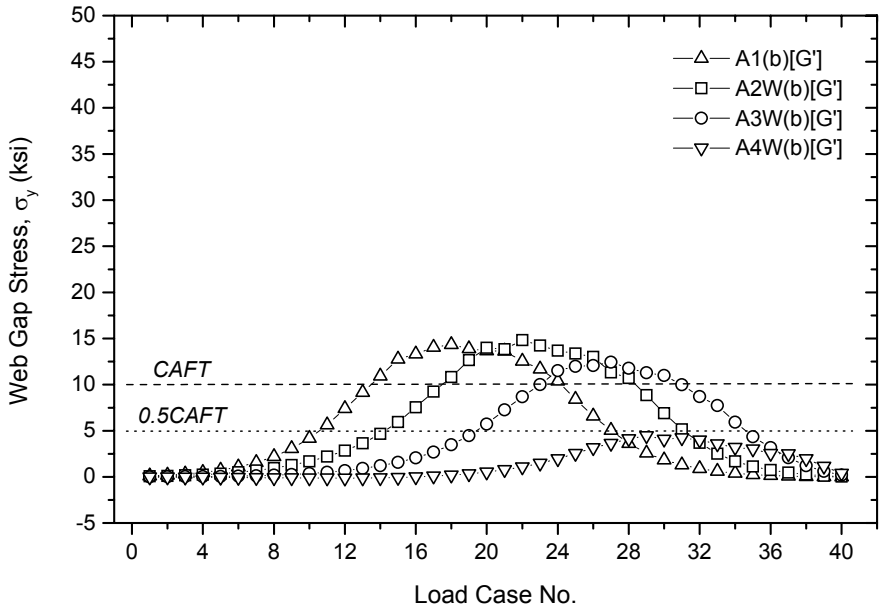

FIGURE 9-22: Web Gap σ_y Stress Variation of the West Half Span Girder A Bottom Flange Submodels

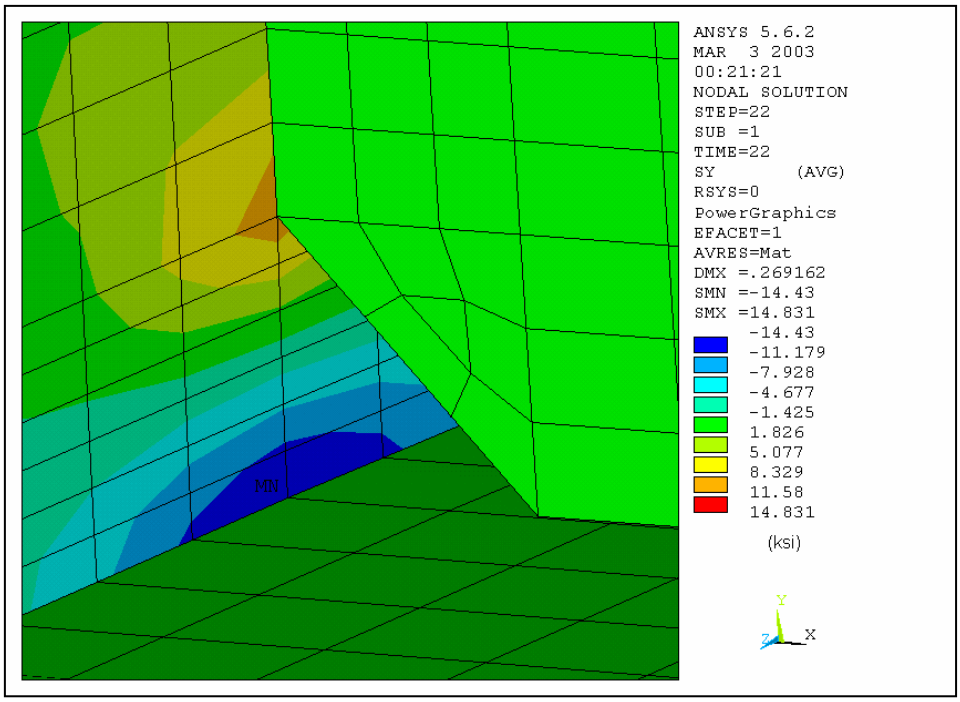

(a) the interior web side

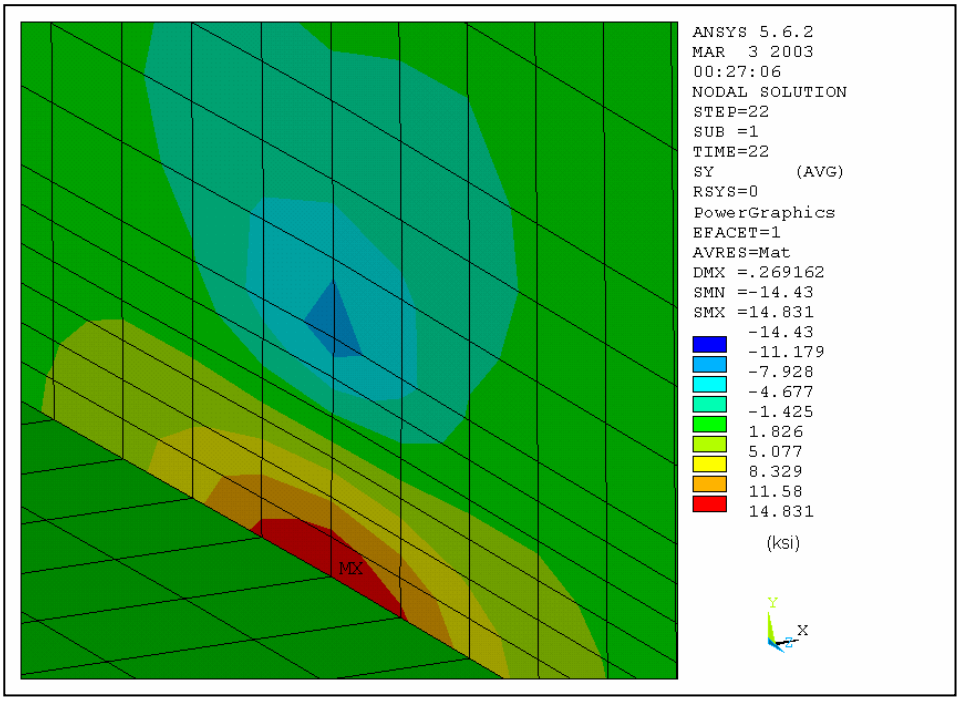

(b) the exterior web side

FIGURE 9-23: Load Case No. 22 Web Gap σ_y Stress Contour of Bottom Flange Submodel A2W

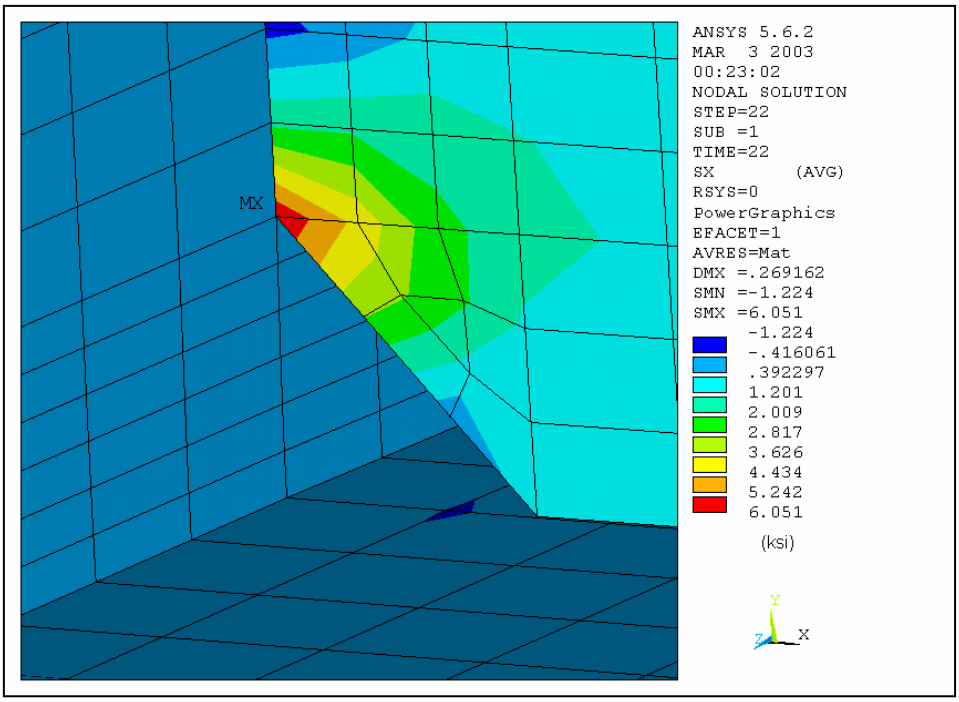

FIGURE 9-24: Load Case No. 22 Web Gap σ_x Stress Contour of Bottom Flange Submodel A2W

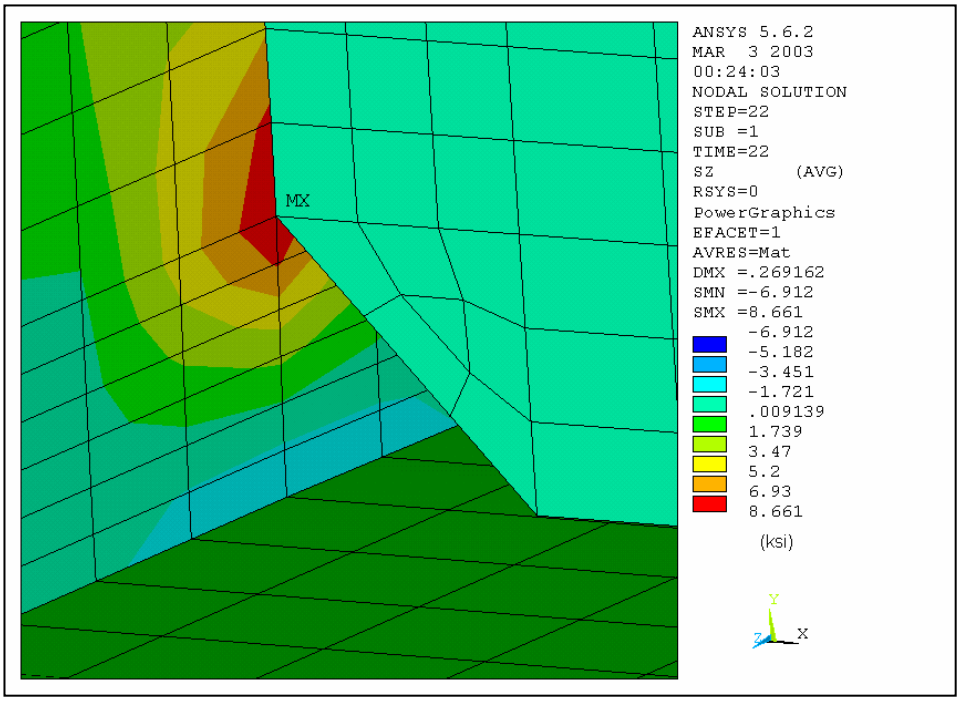

FIGURE 9-25: Load Case No. 22 Web Gap σ_z Stress Contour of Bottom Flange Submodel A2W

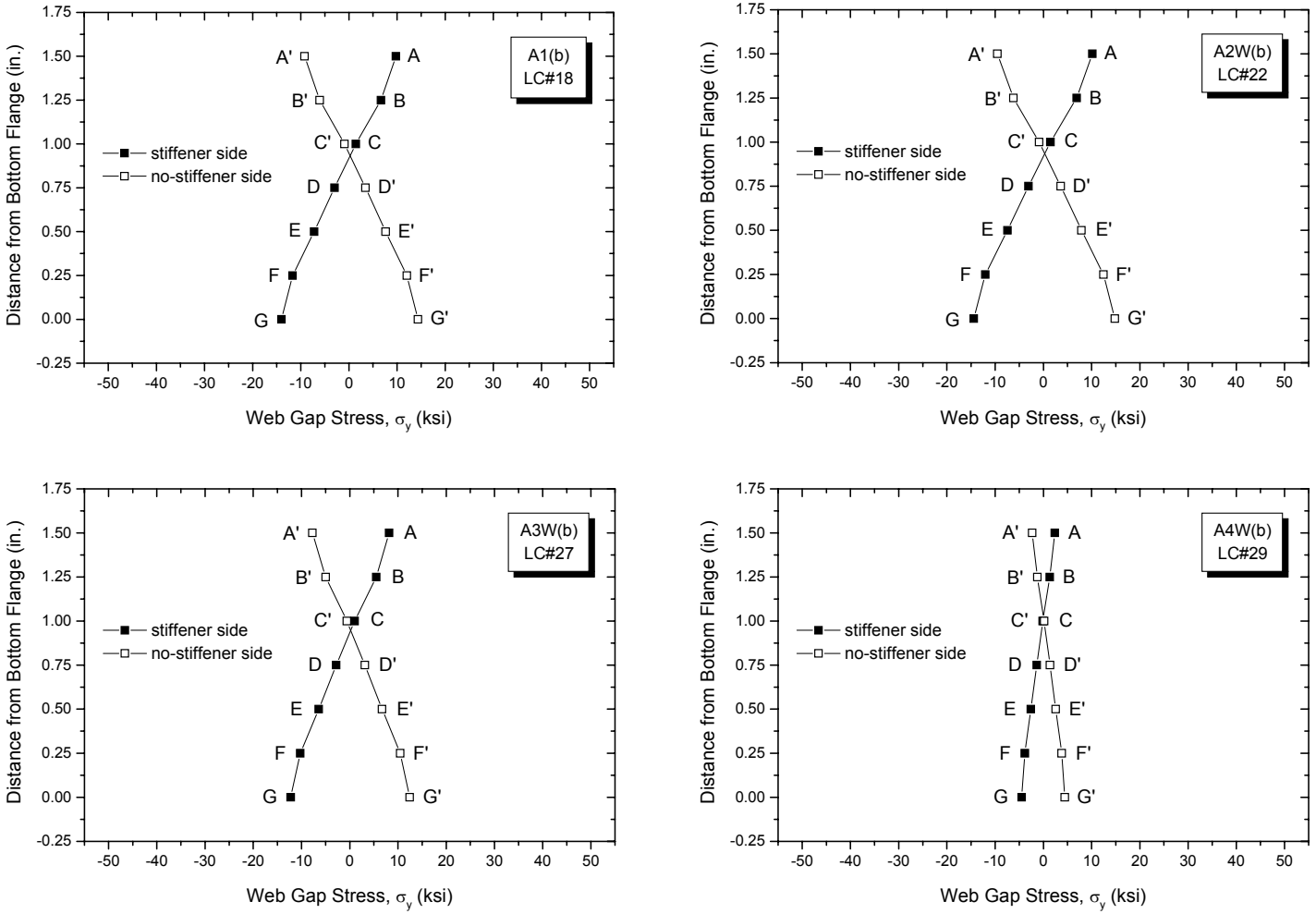

FIGURE 9-26: Bottom Flange Web Gap σ_y Stress Gradient of the West Half Span Girder A Connections

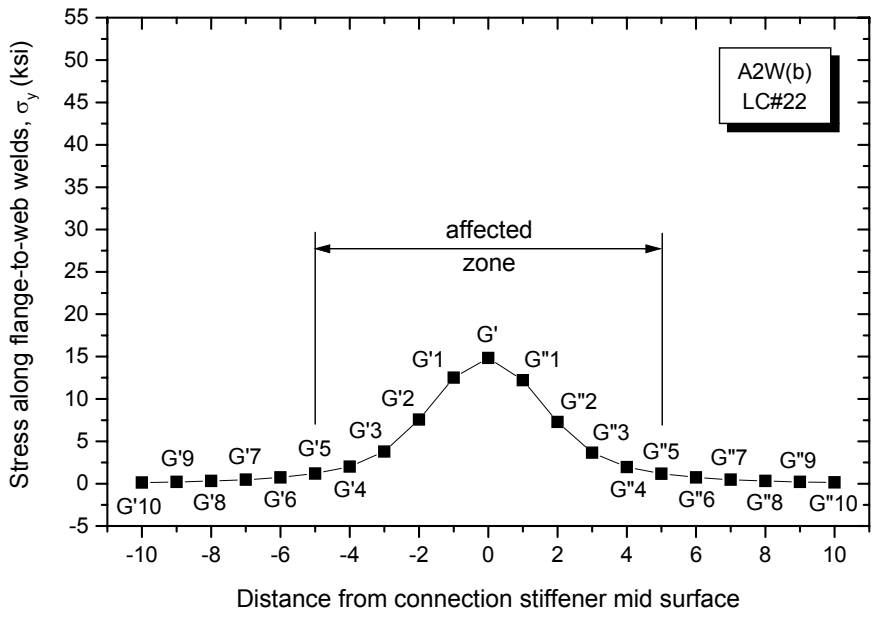

FIGURE 9-27: Load Case No. 22 σ_y Stress Distribution of Connection A2W Along the Bottom-Flange-to-Web Welds

9.5 Repair Analysis

The above finite element study indicates that B2W and A2W are the connections that experiences the highest top and bottom flange web gap stresses. So the truck loading causes the maximum out-of-plane distortion at the cross-section of west cross-frame F2. Since the stresses developed in the top flange web gaps are more significant, the following repair study is carried out only for the top flange submodel of connection B2W. Four different repair schemes are evaluated as shown in Figure 9-28: 1) 4.5 in. slot repair [Figure 9-28(a)], 2) 12.5 in. slot repair [Figure 9-28(b)], 3) broken first intermittent welds [Figure 9-28(c)], and 4) welded connection stiffener to flange attachment [Figure 9-28(d)]. The out-of-plane displacements and stresses resulted from the four repair solutions are summarized in Table 9-5. The details of each repair investigation are discussed in Sections 9.5.1 to 9.5.4 as follows.

9.5.1. 4.5 inch Slot Repair

The 1986 bridge repair was performed by loosening the web gap area with a slot retrofit. The slots were terminated 1 in. below the observed crack ends at the web surface and were all found intercepted within the first intermittent welds. Thus, a 4.5 in. slot length (4 in. net web gap length plus 0.5 in. radius) is selected for the repair evaluation, as it represents a typical cut dimension used in the crack repair [Figure 9-28(a)]. Both the coarse model and submodel are reanalyzed with modified web gap geometry and the highest fatigue stresses are again found to occur at Load Case No. 21. Figures 9-29 to 9-31 show the stress contours of σ_x, σ_y, and σ_z of the 4.5 in. slot repair model at Load Case No. 21. The maximum σ_x, σ_y, and σ_z stresses are 27 ksi, 34 ksi, and 32 ksi, respectively. All occur at locations very close to the end of the radius, which is also the cut end of the vertical fillet welds. Compared to the pre-retrofit stresses developed at the original clipped stiffener end (Point A, 1.5 in. below the top flange), the post-retrofit stresses developed near the slot end (4.5 in. below the top flange) indicate increases of 42%, 12%, and 39%, respectively, for σ_x, σ_y, and σ_z. The post-retrofit σ_y stress at the flange end of the web gap (Point G') is reduced by 48%, but the stress magnitude (25 ksi) is still much higher than CAFT. Figure 9-32 shows the comparison of web gap σ_y stress gradient before and after the 4.5 in. slot repair. Though the stress gradient is decreased after the repair, high magnitude σ_y stresses for crack growth at both the flange-to-web weld and the stiffener-to-web weld still exist. The post-retrofit stress distribution is also symmetric about the mid web thickness and the zero stresses on both sides of the lengthened web gap are located at about 2.5 in. below the top flange. Due to the increased web gap length, the out-of-plane displacements measured within the slot length are significantly large as compared with the displacements obtained prior to the repair within the 1.5 in. web gap. To make sure the results are comparable, the post-retrofit out-of-plane displacement

is still calculated using the relative X-axis deformation between Points A and G, the top and bottom of the original 1.5 in. web gap depth. As shown in Table 9-5, a 40% decrease of the maximum out-of-plane displacement is resulted due to the 4.5 in. slot repair. However, it should be noted that this is a reference displacement used only for comparison purposes, it is not the actually web gap out-of-plane displacement of the repair model and should not be used in Equation 6-3 (Fisher's $\sigma - \Delta$ expression) for post-retrofit stress evaluation.

Though the out-of-plane displacements, the web gap stress gradient, and the fatigue stresses along the flange-to-web welds are reduced after the repair, the stresses developed at the bottom web gap end are elevated and a new stress riser is formed at the cut-short stiffener-to-web weld termination. So the 4.5 in. slot does not relax the web gap region to a satisfactory level. Contrary to the intent to help release the stress field, this repair actually introduced severer stress concentration at the slot end due to the inadequate loosening length. The newly developed high magnitude fatigue stresses, as well as the possible exposure of weld root defects at the slot end, led to the crack reinitiation and propagation observed in many of the repaired locations of this bridge.

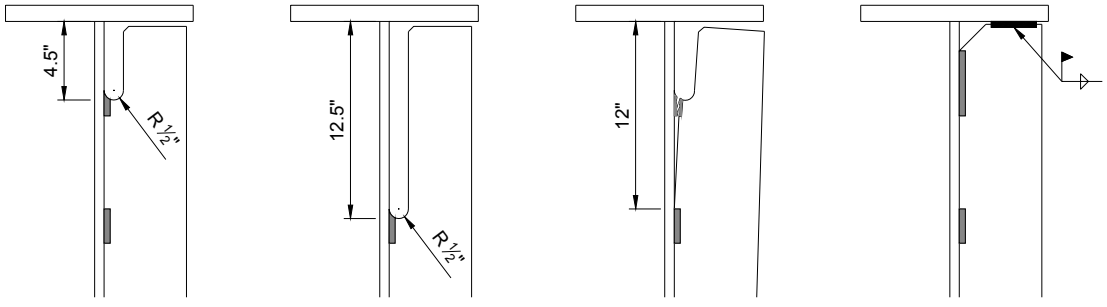

(a) 4.5 in. slot (b) 12.5 in. slot (c) broken first intermittent welds (d) welded repair

FIGURE 9-28: Repair Schemes Investigated Using Finite Element Methods

TABLE 9.5: Stress Changes of Connection B2W Due to Four Different Repair Schemes

	No Repair	4.5 in. Slot Repair		12.5 in. Slot Repair		Broken 1st Intermittent Welds		Welded Repair		AASHTO Fatigue Detail Category	CAFT
Δ_{max}	6.72×10^{-3} in.	4.04×10^{-3} in.	-40%	6.33×10^{-4} in.	-91%	7.37×10^{-4} in.	-89%	3.04×10^{-4} in.	-95%		
	L.C. # 21	L.C. # 21		L.C. # 23		L.C. # 23		L.C. # 14			
$\sigma_{x, max}$	19 ksi	27 ksi	+42%	12 ksi	-39%	5.9 ksi	-69%	0.089 ksi	-100%	C'	12 ksi
	L.C. # 21	L.C. # 21		L.C. # 21		L.C. # 21		L.C. # 19			
	Point A	Slot End		Slot End		12" Below Top Flange		Point A			
$\sigma_{y, max}$	30 ksi	34 ksi	+12%	17 ksi	-43%	17 ksi	-43%	2.3 ksi	-92%	–	–
	L.C. # 21	L.C. # 21		L.C. # 21		L.C. # 21		L.C. # 21			
	Point A	Slot End		Slot End		12" Below Top Flange		Point A			
	49 ksi	25 ksi	-48%	7.5 ksi	-85%	8.0 ksi	-84%	4.2 ksi	-91%	C	10 ksi
	L.C. # 21	L.C. # 21		L.C. # 21		L.C. # 21		L.C. # 21			
	Point G'	Point G'		Point G'		Point G'		Point G'			
$\sigma_{z, max}$	23 ksi	32 ksi	+39%	15 ksi	-34%	13 ksi	-45%	0.68 ksi	-97%	C'	12 ksi
	L.C. # 21	L.C. # 21		L.C. # 21		L.C. # 21		L.C. # 21			
	Point A	Slot End		Slot End		12" Below Top Flange		Point A			

Note: Positive sign indicates percentage increase after the repair and negative sign indicates percentage decrease after the repair

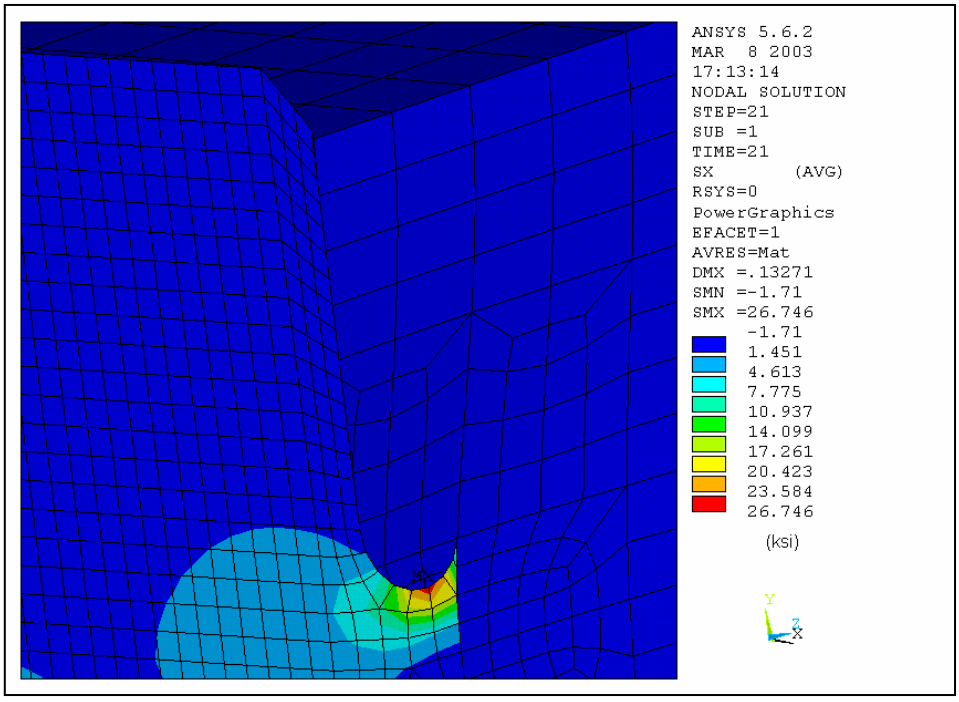

FIGURE 9-29: Load Case No. 21 Web Gap σ_x Stress Contour of the 4.5 inches Slot Repair

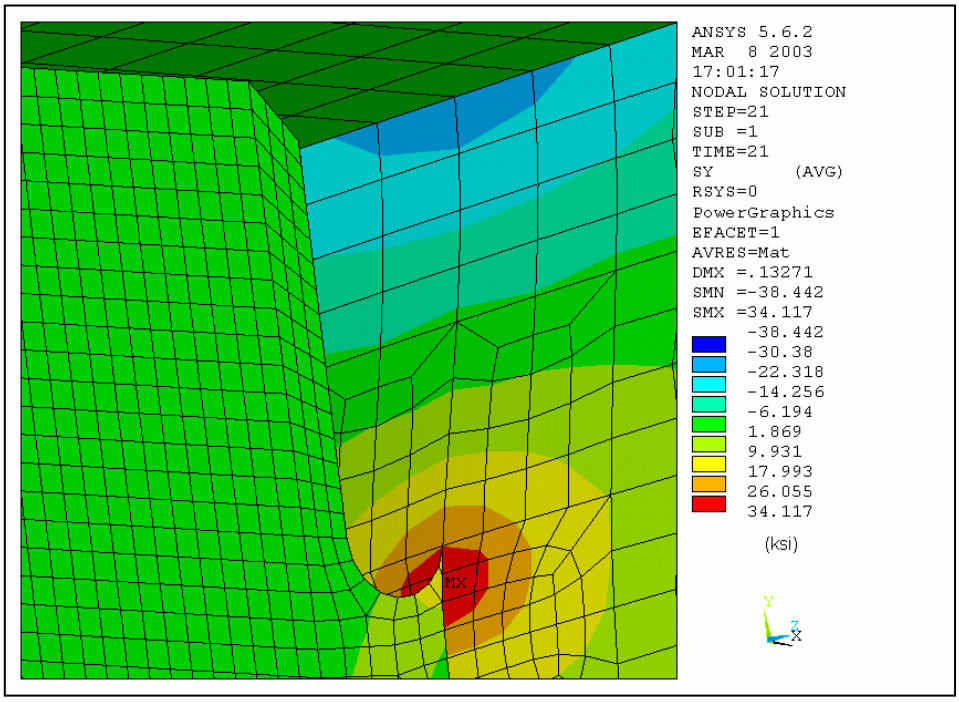

FIGURE 9-30: Load Case No. 21 Web Gap σ_y Stress Contour of the 4.5 inches Slot Repair

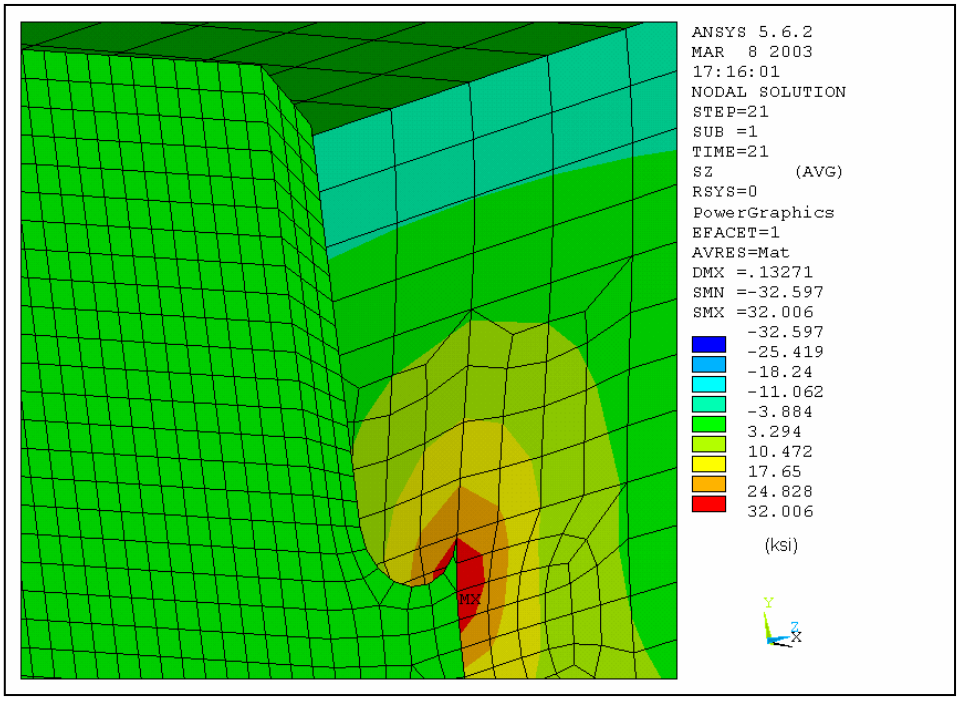

FIGURE 9-31: Load Case No. 21 Web Gap σ_z Stress Contour of the 4.5 inches Slot Repair

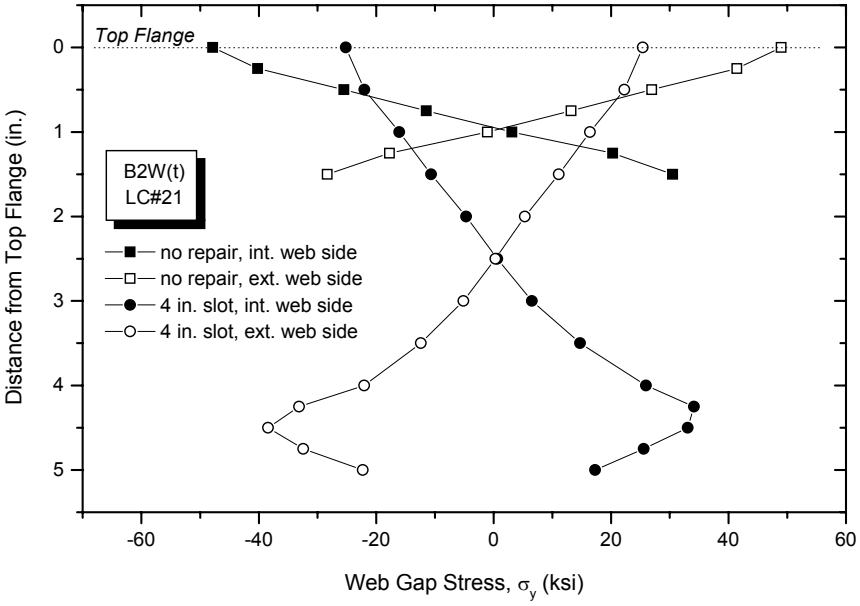

FIGURE 9-32: Comparison of Web Gap σ_y Stress Gradient Before and After the 4.5 inches Slot Repair

9.5.2 12.5 in. Slot Repair

The web thickness is $^{3}/_{8}$ in at connection B2W, so the slot length used in the current repair is less than either the twenty times of the web thickness (7½ in.) or 12 in. A 12.5 in slot length (12 in. net web gap length plus 0.5 in. radius) is then evaluated to see if a longer slot could have reduced the web gap stresses, as shown in Figure 9-28(b). Figures 9-33 to 9-35 show the stress contours of σ_x, σ_y, and σ_z based on the submodel investigation. The maximum σ_x, σ_y, and σ_z stresses are 12 ksi, 17 ksi, and 15 ksi, respectively, all occurring at Load Case No. 21 at the slot end close to the vertical fillet weld termination. A 91% reduction of the out-of-plane displacement is observed due to this repair. Compared to the pre-retrofit stresses developed at the original stiffener end of the web gap (Point A, 1.5 in. below the top flange), the post-retrofit stresses developed near the slot end (12.5 in. below the top flange) are reduced by 39%, 43%, and 34% for σ_x, σ_y, and σ_z. The σ_y stress at the top of the web gap (Point G') is reduced by 85%. Figure 9-36 shows the web gap σ_y stress gradient before and after the repair. The distribution is still symmetric about the mid web gap thickness after the repair, but the zero stress point on each side of the web gap is moved to about 7 in. below the top flange.

The maximum web gap stresses due to the 12.5 in. slot repair are found less than 50% of the corresponding stresses due to the 4.5 in. slot repair, so the 12.5 in. slot repair is apparently more effective in terms of stress reduction. However, the post-retrofit stress magnitude is still higher than ½ CAFT. In addition, the narrow slot is only 1 in. wide, which makes it difficult to achieve a well-finished cut surface, especially at the weld end intersecting with the cut radius. Therefore, fatigue cracks may still be able to reinitiate from the slot end along the vertical welds, even though the web gap stresses have been greatly reduced.

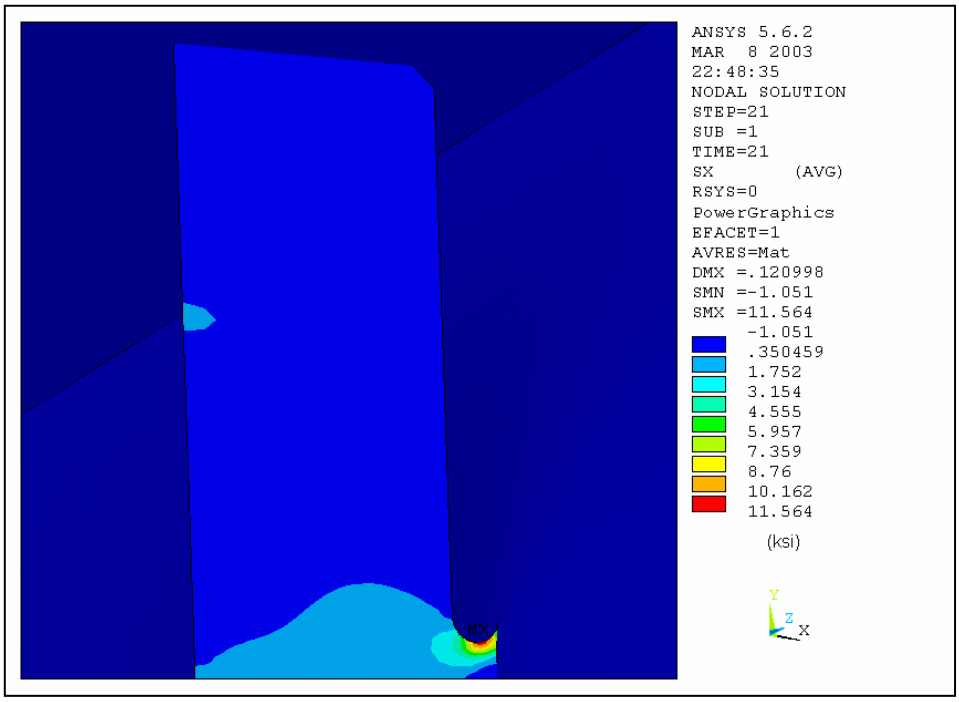

FIGURE 9-33: Load Case No. 21 Web Gap σ_x Stress Contour of the 12.5 inch Slot Repair

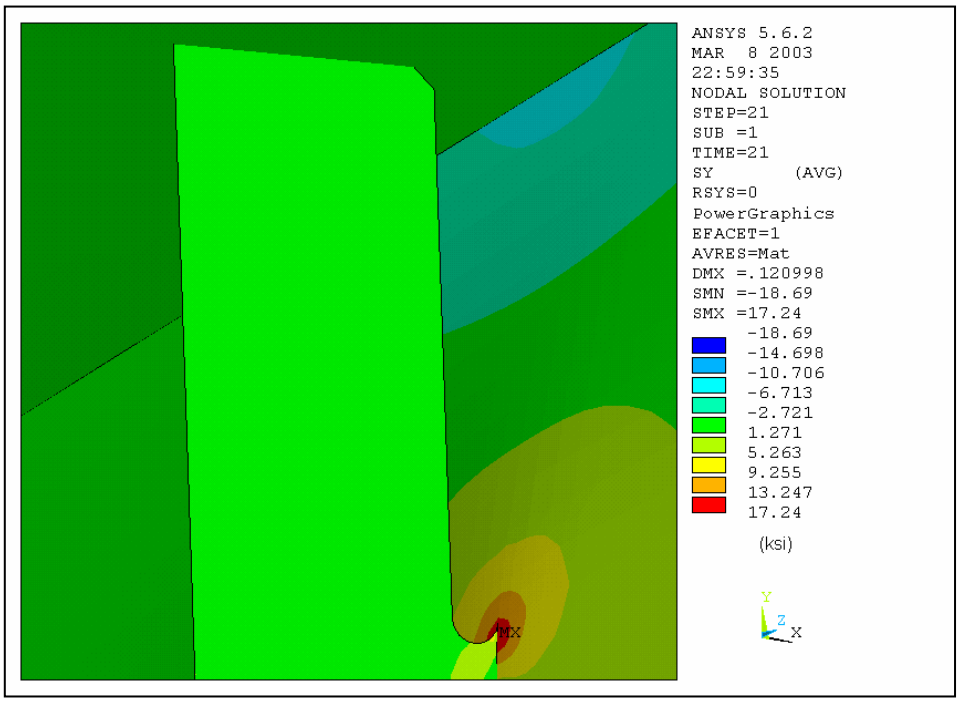

FIGURE 9-34: Load Case No. 21 Web Gap σ_y Stress Contour of the 12.5 inch Slot Repair

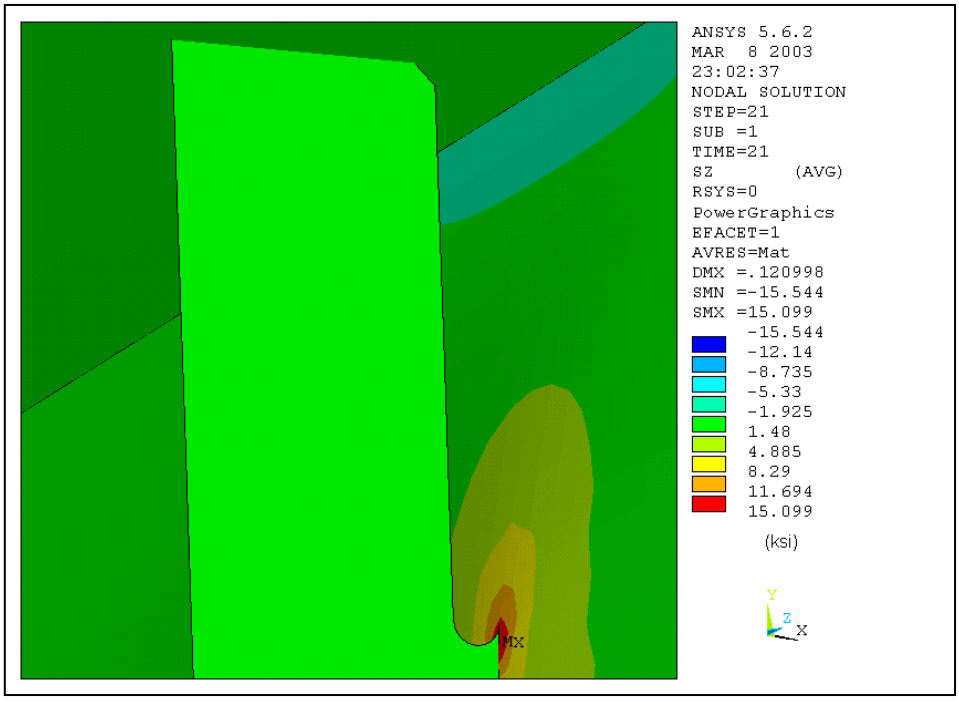

FIGURE 9-35: Load Case No. 21 Web Gap σ_z Stress Contour of the 12.5 inch Slot Repair

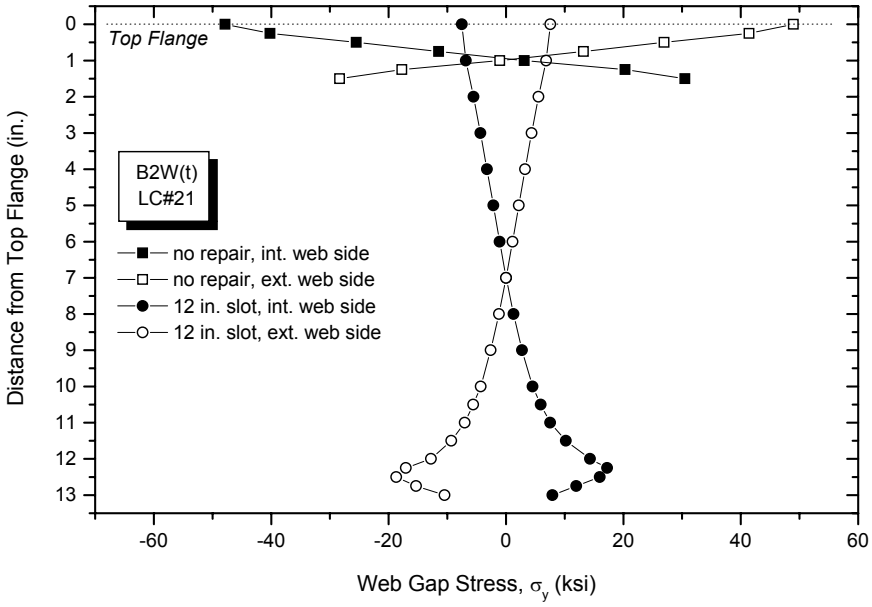

FIGURE 9-36: Comparison of Web Gap σ_y Stress Gradient Before and After the 12.5 inch Slot Repair

9.5.3 Broken First Intermittent Welds

Crack re-initiation and propagation have been observed in many of the details previously repaired in 1986. It is interesting to know whether the cracks could self-stabilize once the first intermittent welds are broken. As shown in Figure 9-28(c), a detached length of 12 in. is considered during the submodel analysis, since most of the second intermittent welds start at about 12 in. below the top flange. Figures 9-37 to 9-39 show the stress contours of Load Case No. 21 for σ_x, σ_y, and σ_z. The maximum σ_x, σ_y, and σ_z stresses are 5.9 ksi, 17 ksi, and 13 ksi, respectively, all located at the point where the second intermittent welds start. Compared to the stresses developed at the original bottom end of the web gap prior to any repair (Point A, 1.5 in. below the top flange), the stresses developed at the top of the second intermittent welds (12 in. below the top flange) after the first intermittent welds are broken are found to be reduced by 69%, 43%, and 45%, respectively, for σ_x, σ_y, and σ_z. The σ_y stress at the top of the web gap (Point G') is reduced by 84%. The maximum out-of-plane displacement is reduced by 89%. Figure 9-40 shows the σ_y stress gradient of the conditions without any repair and with the first intermittent welds broken. The distribution is again symmetric about the mid web thickness after the first intermittent welds are broken, but the zero stresses on both web sides are lowered to about 7 in. below the top flange.

Compared to that of the 4.5 in. slot repair, the web gap stress intensity is greatly reduced after the first intermittent welds are broken. However, the maximum σ_y and σ_z stresses are found higher than ½ CAFT, so cracks may still be able to develop from the top of the second intermittent welds. Additional repair measures are thus needed in order to reduce the secondary stresses to a satisfactory level and to stop crack propagation at those repaired details. In general, the stress condition resulted from the broken first intermittent welds is similar to that of the 12.5

in. slot repair.

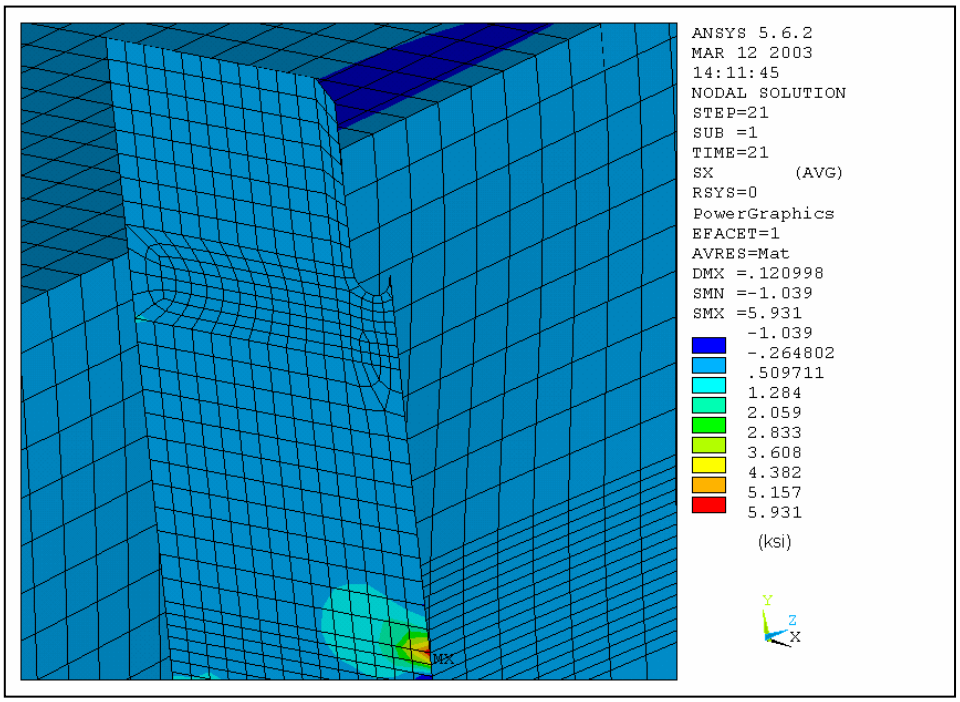

FIGURE 9-37: Load Case No. 21 Web Gap σ_x Stress Contour Due to Broken First Intermittent Welds

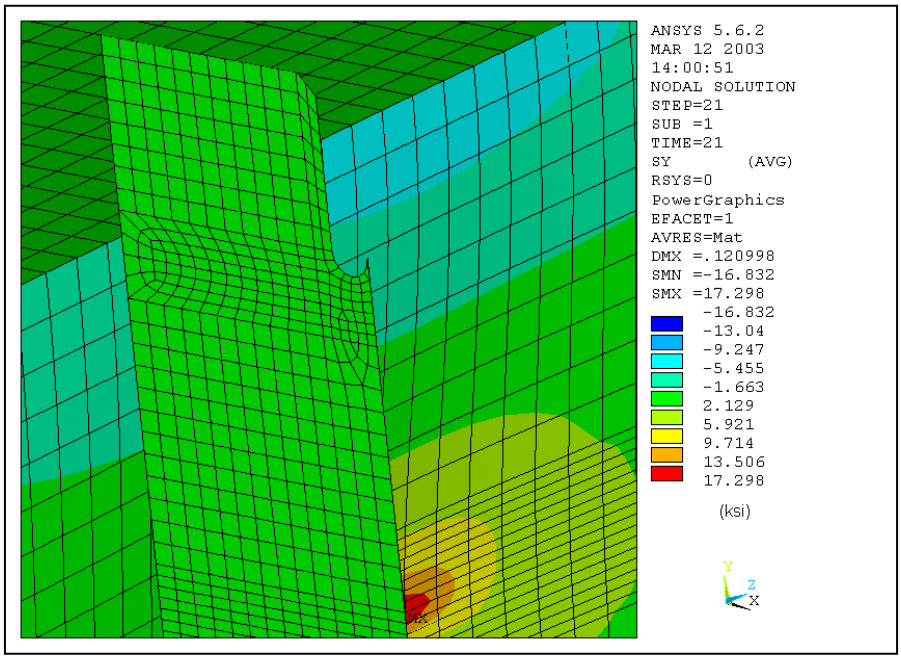

FIGURE 9-38: Load Case No. 21 Web Gap σ_y Stress Contour Due to Broken First Intermittent Welds

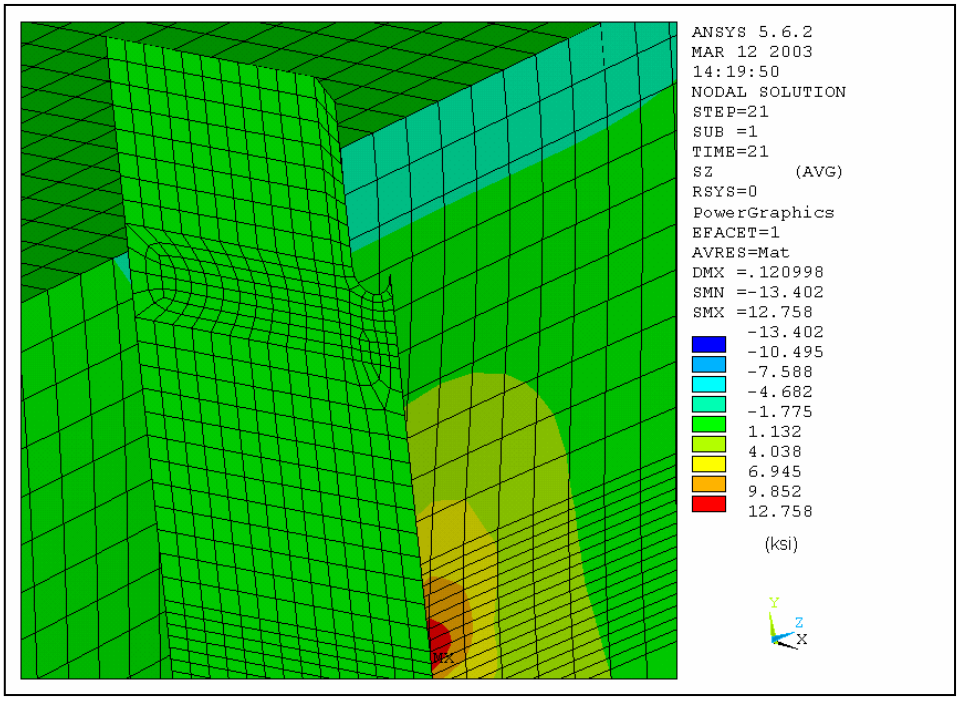

FIGURE 9-39: Load Case No. 21 Web Gap σ_z Stress Contour Due to Broken First Intermittent Welds

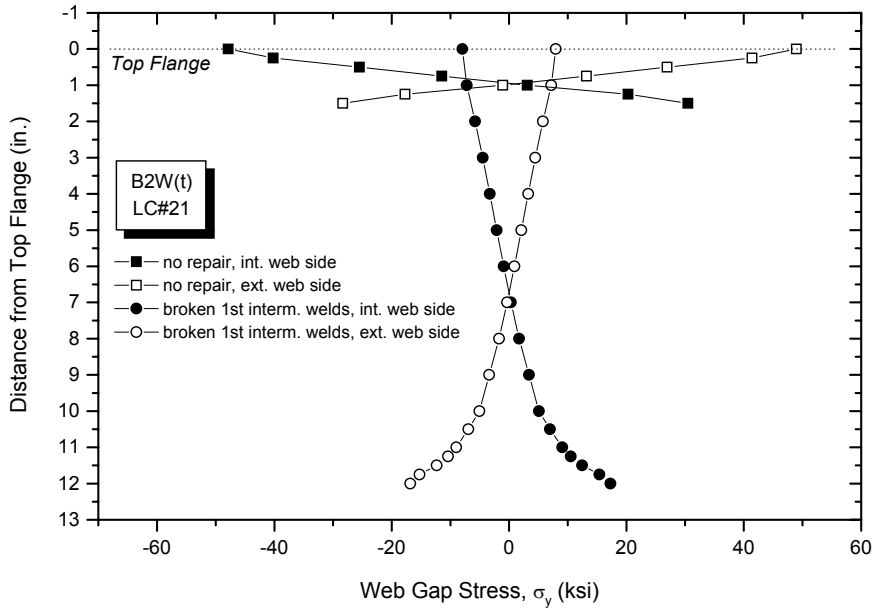

FIGURE 9-40: Change of Web Gap σ_y Stress Gradient Due to Broken First Intermittent Welds

9.5.4 Welded Repair

The fourth repair scheme, as shown in Figure 9-28(d), is to weld the connection stiffener to girder flange. Figure 9-41 shows the web gap σ_y stress contour of Load Case No. 21 for the repair model. Figure 9-42 shows the σ_x stress contour of Load Case No. 19 and Figure 9-43 shows the σ_z stress contour of Load Case No. 21. For most load cases, the maximum σ_z stress of the submodel still occurs at Point A, but the maximum σ_x and σ_y stresses are not located in the web gap region. Figure 9-44 shows the σ_y stress gradient on the exterior side of the web gap for the conditions without repair and with the welded repair. The stress variation between Points A' and G' drops from 77 ksi to 5.2 ksi after the connection stiffener is attached to the top flange. Table 9-5 shows that the maximum out-of-plane displacement and stresses can be reduced by at least 90% if the welded repair is used. The maximum σ_x, σ_y, and σ_z stresses at Point A are 0.089 ksi, 2.3 ksi, and 0.68 ksi. The maximum σ_y stress at Point G' is 4.2 ksi. So the post-retrofit web gap stresses are all reduced to below ½ CAFT. Compared to the other three repair schemes mentioned above, the welded repair could achieve the highest percentage of stress reduction, decrease the web gap stresses to below the infinite life fatigue limit, and at the same time eliminate the chance of forming new stress risers. This is apparently the most effective repair solution and is thus recommended for future bridge retrofit in order to stop both the initiation of new cracks and the propagation of existing cracks.

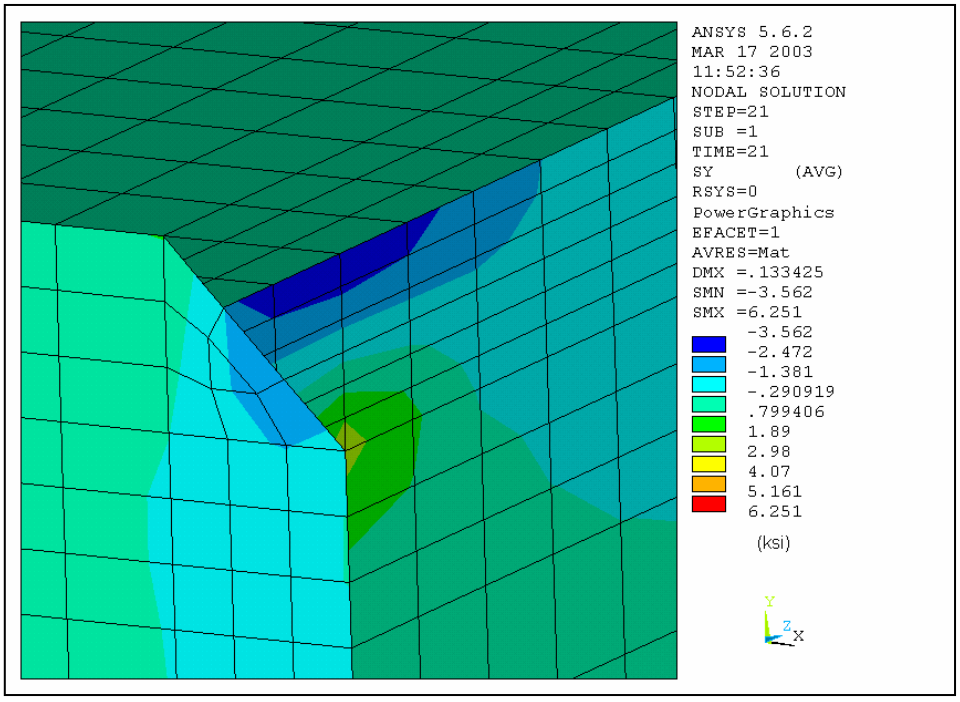

(a) the interior web side

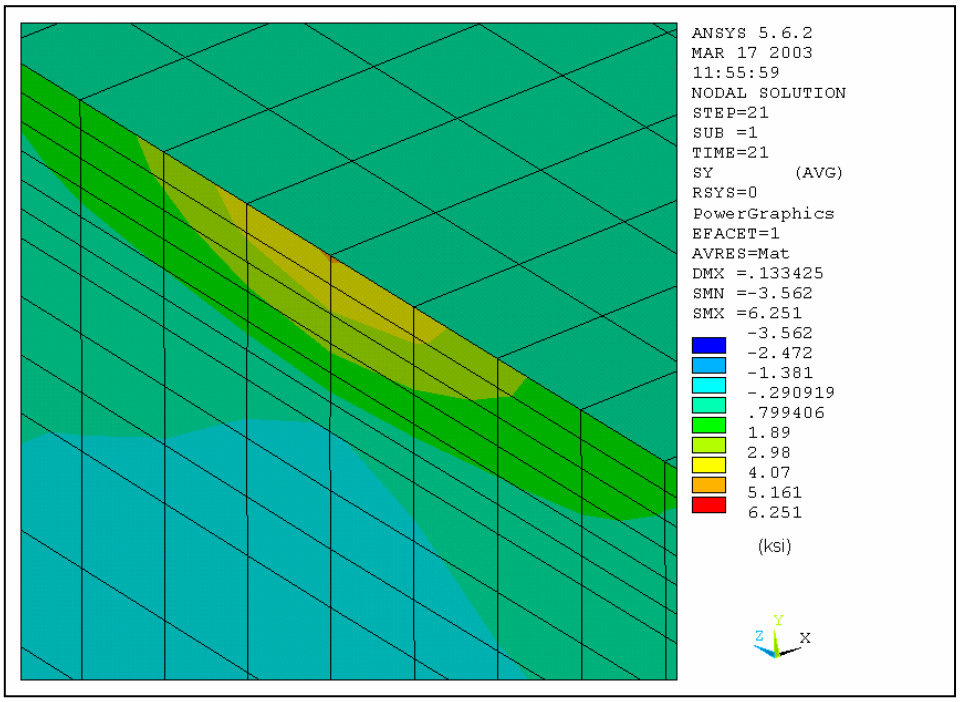

(b) the exterior web side

FIGURE 9-41: Load Case No. 21 Web Gap σ_y Stress Contour Due to Welded Repair

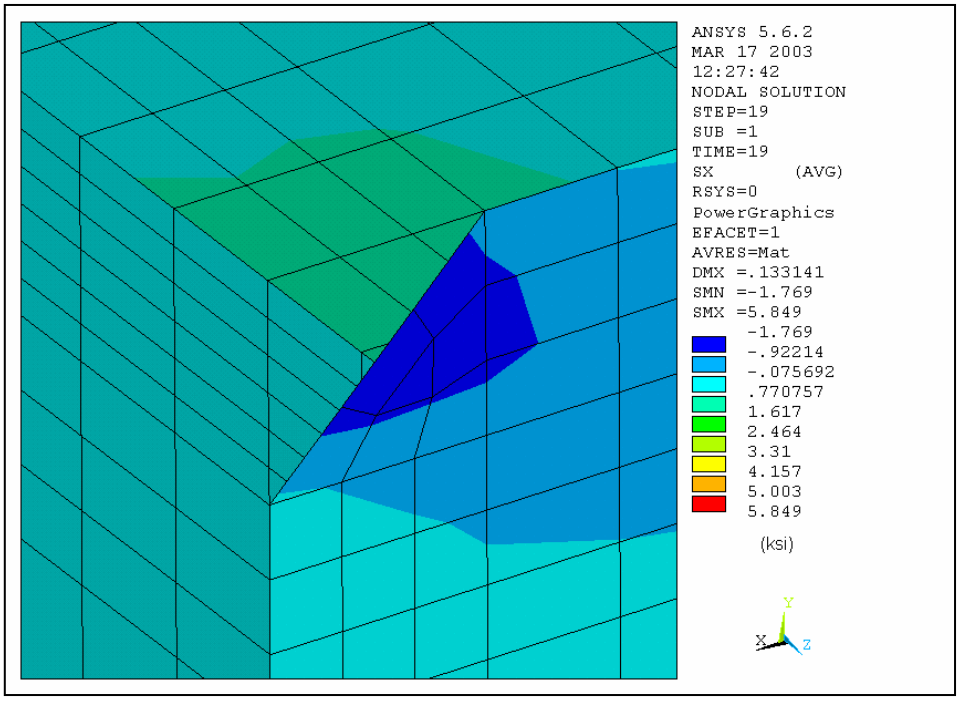

FIGURE 9-42: Load Case No. 19 Web Gap σ_x Stress Contour Due to Welded Repair

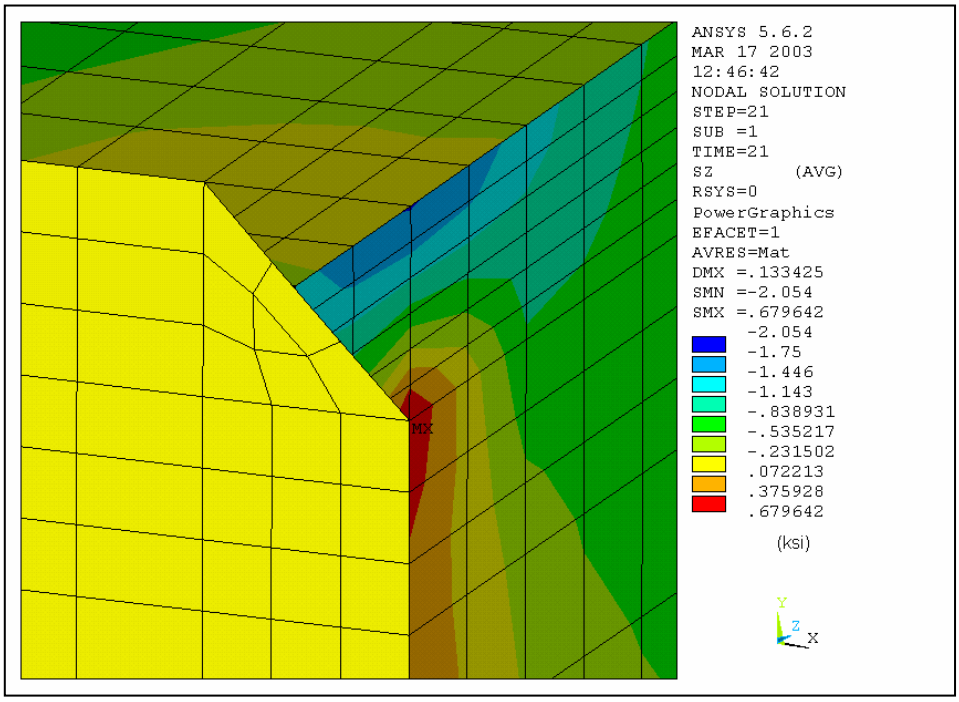

FIGURE 9-43: Load Case No. 21 Web Gap σ_z Stress Contour Due to Welded Repair

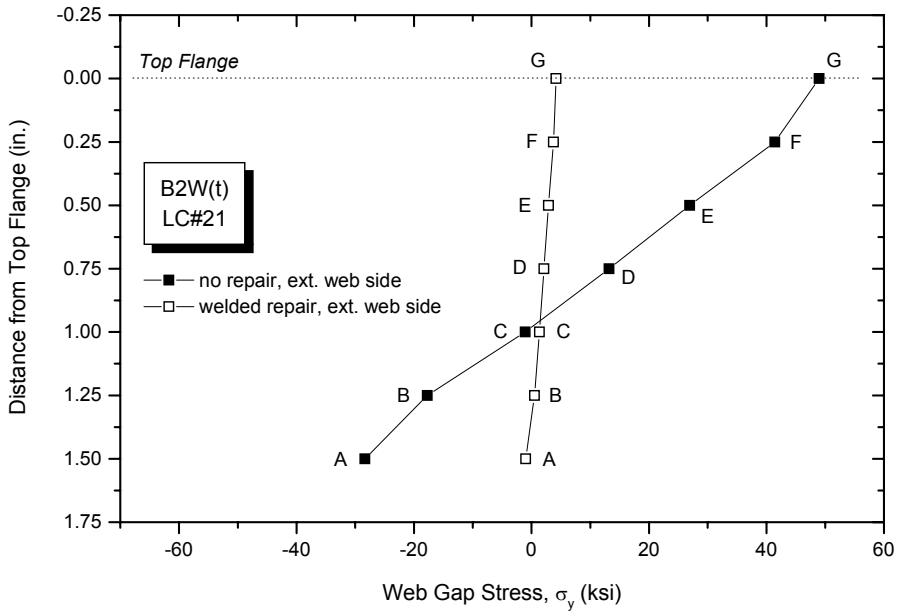

FIGURE 9-44: Change of Web Gap σ_y Stress Gradient Due to Welded Repair

9.5.5 Repair Recommendations

The foregoing repair study shows that the current slot repair used in the bridge is ineffective. Increased web gap stresses are observed due to the insufficient cut-short length, which caused crack propagation and re-initiation at some of the repaired details. Use of a longer, 12.5 in. slot could release the constraints and reduce the stress concentration to a certain degree, but would not make a permanent repair as it is not able to decrease the fatigue stresses to below ½ CAFT. The same conclusion is drawn as with the condition of leaving the crack to propagate until the first intermittent welds are broken. The most effective repair method is to stiffen the web gaps by providing positive attachment between the connection stiffeners and girder flanges.

Based on the observed crack condition and the finite element analysis results, it is recommended that all the non-pier cross-frame/girder connections be repaired with welded stiffener-to-flange attachment. In particular, the top flange web gaps should be repaired at the

earliest convenience, because the slot repair was previously carried out in 1986 only at locations found with cracks by that time. Additional crack details have developed afterwards, and even those repaired details have since then been found with crack propagation and re-initiation. Though cracks have not been found at bottom flange web gaps in this bridge, it is recommended that these details also be repaired to prevent from crack development during future service. However, the bottom flange cross-frame/girder connection is an intersection of multiple lateral bracing and cross-frame members, so the web gap area could be difficult to reach and prepare for a good quality weld repair. It is recommended that strain gauging be carried out at selected details of this bridge. If the actual stresses developed in the bottom flange web gaps are much lower than predicted by finite element analysis, the suggested repair may not need to be carried out.

9.6 Fisher's $\sigma - \Delta$ Expression

Table 9-6 shows the comparison of web gap σ_y stresses calculated using Fisher's $\sigma - \Delta$ formula vs. finite element methods. In general, the stresses obtained from Fisher's formula are much higher than those yielded by ANSYS, especially for the top flange connections. Only at the bottom flange of connection A4W are the stresses obtained from these two methods found close. The average ratio of the maximum ANSYS solution over the Fisher's solution is 0.61, so this is recommended as an adjustment factor to the Fisher's formula for prediction of secondary stresses of this bridge.

TABLE 9.6: Comparison of Web Gap Stresses Obtained from Fisher's Formula and ANSYS Analysis

Connection or Submodel	Load Case No.	Out-of-Plane Displacement Δ (in.)	Web Thickness t_w (in.)	Fisher $\sigma=3E\Delta t_w/L^2$ (ksi)	ANSYS σ_y (ksi) @ Point			
					A	G	A'	G'
A1 (t)	16	1.82×10^{-3}	0.375	± 26	6.4	-12	-6.0	12
B1 (t)	17	6.17×10^{-3}	0.375	± 89	29	-45	-27	46
B2E (t)	12	6.56×10^{-3}	0.375	± 95	29	-46	-27	47
B3E (t)	7	6.50×10^{-3}	0.375	± 94	28	-44	-26	45
B4E (t)	8	1.76×10^{-3}	0.5	± 34	8.2	-17	-7.2	18
B2W (t)	21	6.72×10^{-3}	0.375	± 97	30	-48	-28	49
B3W (t)	26	6.63×10^{-3}	0.375	± 96	29	-45	-27	47
B4W (t)	30	2.54×10^{-3}	0.5	± 49	11	-23	-9.7	24
B1 (b)	19	8.89×10^{-4}	0.375	± 13	-6.4	8.6	6.0	-8.7
A1 (b)	18	1.33×10^{-3}	0.375	± 19	9.8	-14	-9.2	14
A2W (b)	22	1.46×10^{-3}	0.375	± 21	10	-14	-9.5	15
A3W (b)	27	1.39×10^{-3}	0.375	± 20	8.1	-12	-7.7	12
A4W (b)	29	1.74×10^{-4}	0.5	± 3.4	2.4	-4.5	-2.3	4.5

Note: L = 1.5 in., E = 29000 ksi.

9.7 Summary

Fatigue cracks have been observed at about 400 cross-frame to girder connections in the Tuttle Creek Bridge. Finite element study is performed in this chapter for a typical intermediate girder span, to determine the magnitude of distortion-induced fatigue and to evaluate the effectiveness of the different repair schemes. The following points represent the summary of the analytical investigation:

1. The distortion-induced stresses developed at the top flange web gaps are much higher than those of the bottom flange web gaps. In particular, the top flange web gaps of the positive and transition moment region connections experience fatigue stresses higher than yielding. This explains the field observation that a large number of web gap cracks have been found close to the girder top flange.
2. Cracks have not been found in the bridge at the bottom flange web gaps. However, the finite element study indicates that the stresses developed in this region, though in a relatively low magnitude, may still be able to cause fatigue cracking during future service.
3. For both the top and bottom flange web gaps, the σ_y stress distribution is found symmetric about the mid web thickness, but not about the mid web gap depth. For most of the details, the location of zero stress is found approximately $^1/_3$ of the web gap length close to the stiffener end of the web gap.
4. The area subject to stress concentration is found within a 10 in. affected zone, 5 in. on each side of the stiffener plate at the web gap region. Stresses outside this zone soon decrease to zero.
5. It is recommended that an adjustment factor of 0.61 be applied to the Fisher's $\sigma - \Delta$ formula for web gap stress estimation of this bridge.
6. The current slot repair used in the bridge is found to have introduced higher magnitude fatigue stresses in the web gap, which is believed to be the cause of crack reinitiation and propagation found in many of the

repaired details. Another two softening methods considered during the repair study are to use a longer, 12.5 in. slot, or to leave the cracks propagating until the first intermittent welds are broken. Both approaches could help loosen the constraints and relieve the stress intensity at the web gap region, but are not able to reduce the stresses to below the infinite life fatigue limit. To achieve a permanent repair of the bridge, it is recommended that a rigid, welded stiffener-to-flange connection be used during future bridge retrofit. The web gap details should be able to withstand unlimited number of load cycles once this additional repair is performed.

7. It is recommended that the four proposed repair schemes be field tested during future research and their performance be evaluated under real traffic loading. The selected connection stiffeners should be welded to the top flange once the test is completed. Strain gauging is also recommended for the bottom flange web gap details. If the field measurement indicates lower than ½ CAFT stresses, the welded stiffener-to-flange repair can be disregarded for the bottom flange web gaps.

Chapter 10

Conclusions and Recommendations

Much research has been performed over the past thirty years in steel bridge fatigue. This research adds to existing studies the implementation of advanced computational methods for interpretation of fatigue characteristics and evaluation of remedial actions. Intensive finite element investigations were carried out for five KDOT bridges that experienced fatigue cracking at local stress concentration region due to out-of-plane distortion. Through proper modeling of the interaction between longitudinal girders and transverse structural members, insights are obtained as to how the out-of-plane fatigue cracks were formed and what repair method should be recommended for the continued use of the bridges. Analytical results obtained from each case study are summarized at the end of Chapters 5 to 9. This chapter highlights key research findings, summarizes contributions of the study, and suggests extensions to future work.

10.1 Effectiveness and Advantage of Finite Element Modeling

A two-level finite element modeling procedure is adopted in this research to approach the fatigue behavior of crack-prone details and to correlate the global structural response under truck loading with the local stress concentration effect due to out-of-plane distortion. Four of the five bridges, the Arkansas River Bridge, the Winfield Bridge, the Hump Yard Bridge, and the Tuttle Creek Bridge, were investigated using direct 3-D finite element coarse-to-fine submodeling. The other bridge, the Westgate Bridge, was investigated using 2-D stick frame to 3-D finite element modeling. Both modeling procedures successfully explained the cracking scenarios observed in the bridges and predicted potential crack initiation sites during future service.

Though all driven by distortion-induced fatigue, cracks developed in individual bridges are found at different locations and caused by different structural interactions. Crack-prone details in two-girder bridges, such as the Westgate Bridge and the Tuttle Creek Bridge, are easy to identify, because they are located mostly at both girder connections and close to girder top flanges. For multi-girder bridges, however, the critical crack locations are sometimes difficult to determine, depending on the superstructure layout, the detail of the transverse/longitudinal member connection, the frequent truck loading position, etc. For example, the Arkansas River Bridge was found to have developed out-of-plane fatigue cracks only at the exterior girder connections, while the Winfield Bridge was found only possible to develop cracks at the interior girder connections, and the Hump Yard Bridge was found to have developed bottom flange web gap cracks only at the connections with horizontal brace intersection. In these circumstances, it is hard to address the crack phenomena and to identify the direct cause of fatigue cracking unless a systematic and comprehensive investigation is conducted, as is the case of this research. The Arkansas River Bridge developed fatigue cracks at the coped floor-beam top flange to connection plate welds, and the other four bridges developed fatigue cracks at the unstiffened web gap areas. For all five bridges, the finite element modeling approach effectively analyzed the fatigue performance of the crack details and provided appropriate repair suggestions as well.

In particular, web gap cracking is the mostly encountered fatigue problem caused by out-of-plane distortion. Other research carried out for this type of cracking focused on experimentation, both in the field [Koob et al., 1985; Fisher et al., 1987; Stallings et al., 1993; Cousins et al., 1998; Wipf et al., 1998], and in the laboratory [NCHRP 336, 1990; Cousins & Stallings, 1998; D'Andrea et al., 2001]. Fisher et al. reviewed the available studies performed on bridges with web gap cracking and summarized the experimental data as follows [NCHRP 336,

1990]:

"*These studies indicated that floorbeam-girder web gaps adjacent to the top flange generally experienced the largest out-of-plane movement. The displacements were equal to 0.02 in. to 0.04 in. with corresponding stress ranges between 20 and 40 ksi. When no cracks formed at the floorbeam-girder web gap, the distortion was generally less than 0.004 in. and the cyclic stress was generally less than 10 ksi.*"

"*Multigirder bridges without staggered diaphragms were found to experience distortions less than 0.02 in., which caused cyclic stresses between 10 and 20 ksi. Measurements were not available on staggered diaphragms, but the degree of cracking in actual bridges appeared comparable to floorbeam-girder bridges. Also, the bottom flange web gap often cracked in structures with staggered diaphragms.*"

Similar results were obtained from field and laboratory tests of other research. However, the measurements varied in a certain range due to the different structural system, test condition, and evaluation criteria designed for individual bridges. For example, the following two field studies showed large differences in the corresponding web gap stress and displacement measurements. The I-65 Mobile Delta Crossing Bridge [Stallings et al., 1993] is a two-girder bridge with floor-truss/girder connections. The maximum effective stress range under random truck traffic was found to be 30 ksi. This was measured at a detail with 2 in. web gap length and 0.25 in. crack development. At the same detail, the maximum single stress range measurement under random truck traffic was 58 ksi due to an out-of-plane displacement of 0.0107 in., and the maximum single stress range measurement resulted from side-by-side, two 5-axle test truck fast runs was 71 ksi with a corresponding displacement of 0.0130 inch. The highest single stress range obtained from this study was 92 ksi corresponding to an out-of-plane displacement of 0.0170 in., occurring at an uncracked detail with 1.5 in. long web gap, due to side-by-side, two 3-axle test truck fast runs. Linear extrapolation technique was used in this study to estimate the

stresses at the critical locations. Wipf et al. [1998] tested selected details of five Iowa DOT cross-frame bridges with different combinations of straight/skewed, staggered/non-staggered, and X or K type cross-frame arrangement. The maximum web gap stress due to a single test truck was found to be 5.80 ksi with a corresponding displacement of 0.0056 in. The stresses reported in this research were direct translation of strain gauge readings (no extrapolation), so the magnitudes are relatively low. Though the stress measurements obtained from these two studies are quite different, the results are still considered consistent as it is typical to have a wide range of fatigue response at the web gap details due to the following variables:

- Transverse structure member type: floor-beam, diaphragm, or cross-frame
- Structural layout, framing plan, roadway width division
- Selected test location (moment region, top/bottom flange connection, etc.)
- Web gap detail such as depth, thickness, crack dimension, etc.
- Test truck configuration (axle spacing, width, weight), driving speed, loading pattern
- Strain gauge location, data extrapolation or not

Similarly, the finite element study conducted in this project also indicated different magnitude of web gap stresses and displacements at different bridge details. Table 10-1 summarizes the maximum out-of-plane stresses and the corresponding displacements of the four KDOT bridges that experienced web gap cracking. For all four bridges, the maximum web gap stresses are close to or exceed yielding, but the corresponding displacements are only in an order of 0.001 in. A review of the analytical results presented in Chapters 6 to 9 shows that both the distortion-induced displacements and stresses obtained from this study using finite element methods fall in the range of the test data reported by the aforementioned field studies. However, at the same amount of out-of-plane displacements, the critical web gap crack opening stresses

yielded by this study are a little higher than those obtained from the experimental measurement. This could be caused by one or more of the following. In most of the field tests, strain gauges were mounted on the web at a very small distance aside the flange-to-web and stiffener-to-web weld toes, because the web gap is usually only 1~2 in. long and direct placement of strain gauges within this area is very difficult. The extreme stress values at the web gap ends were then determined from linear extrapolation. Thus, the measured stresses could be less than what actually occurred within the web gap at the connection stiffener plane. While the computer modeling procedure used in this research has no constraints in accessing the stresses at the concentration point, the magnitude of the peak stresses is mesh-dependant. Theoretically speaking, the stresses at the concentration point can be infinitely large if the element size is continuously reduced. The magnitude of crack opening stresses reported in this study was obtained from using a 0.25 in. mesh size within the web gap depth. The results were relatively stable at this mesh density and further refinement did not indicate much increase in the stress values. In fact, compared with the experimental results, the critical stresses yielded by the analytical models are a little higher at this mesh size when subjected to the same out-of-plane displacements. In general, both the web gap stress distribution and magnitude predicted in this research using finite element methods agreed well with the findings obtained from the field measurements of other experimental studies.

TABLE 10-1: Summary of Web Gap Stresses and Displacements at Critical Locations

Bridge Name	Superstructure Type	Maximum Web Gap Stress, σ_y (ksi)	Out-of-Plane Displacement, Δ (in.)	Connection Detail
Westgate Bridge	Two-girder / floor-truss / stringer	25 ksi	1.37×10^{-3} in.	-FM1, mid-span, top flange -web gap length 11/16 inch, thickness 3/8 inch
Winfield Bridge	Skewed four-girder / staggered diaphragm	37 ksi	3.73×10^{-3} in.	-3g(b), positive moment region, bottom flange -web gap length 1inch, thickness 5/16 inch
Hump Yard Bridge	Skewed multi-girder / intermittent cross-frame	38 ksi	4.67×10^{-3} in.	-8c(t), positive moment region, top flange -web gap length 1 inch, thickness 3/8 inch
Tuttle Creek Bridge	Two-girder / cross-frame	49 ksi	6.72×10^{-3} in.	B2W(t), positive moment region, top flange -web gap length 1 ½ inch, thickness 3/8 inch

Other benefits of performing the finite element studies are observed during the evaluation of crack-prone details and in the process of retrofit decision-making. For example, in many multi-girder bridges, due to the arrangement of traffic lanes across the bridge roadway width, high magnitude secondary stresses may only develop in some of the bridge girders at specific moment regions. Computer modeling can help in this circumstance to identify the details that are exposed to stress ranges higher than the fatigue limit and consequently allow the repairs to be carried out at these details only. Different repair approaches can also be compared through finite element modeling, as has been performed in this research for all five KDOT bridges. In some situations, the seemingly workable retrofit may not be able to decrease the fatigue stress to a satisfactory level, or it may unexpectedly result in a new stress riser at another location after the original crack detail is repaired. Thus, it is helpful to perform an analytical study of the bridge before the final retrofit is determined and actually carried out in the field.

10.2 Correlation between Out-of-Plane Stresses and Displacements

Figures 10-1 to 10-4 show the web gap stress-displacement plots of all the bridge connections studied in this research using finite element methods. For most of the details, an almost linear stress vs. displacement relationship can be established when subjected to out-of-plane distortion. The plotted stresses are the higher of the tensile σ_y stresses developed at the flange or the stiffener end of the web gap. For all four bridges, the curves of those details experiencing high-magnitude stress ranges are well grouped with better linearity and less variation in slopes. However, for those details subjected to low stress ranges, the data are in a relatively high degree of scatter with poor linearity and large difference in slopes, as noticed especially in the Winfield Bridge (Figures 10-2) and the Hump Yard Bridge (Figure 10-3). Most of the details experiencing low stress ranges are located close to the bridge piers, so the boundary conditions used in the

model analyses may have some influence on the detail behavior. In addition, the Winfield Bridge and the Hump Yard Bridge are both skewed, multi-girder bridges. The Winfield Bridge has staggered diaphragms. The Hump Yard Bridge has different cross-frame type and arrangement in different bays. The skew, the girder location, the connection detail, etc. may also affect the distribution of the stress-displacement data, even for the same type of connections in the same bridge. The Westgate Bridge (Figure 10-1) and the Tuttle Creek Bridge (Figure 10-4) present much more uniform stress-displacement distribution. Both of them are straight, two-girder bridges, so the connection behavior is affected by fewer factors. This is believed to have resulted in the nice grouping of the curves.

Based on finite element solution, a linear relationship between out-of-plane stresses and displacements is obtained, as shown in Equations 10-1 to 10-4 and alsoin Table 10-2, for each of the four KDOT bridges that experienced web gap cracking:

$$\sigma = 17.8 \times 10^3 \Delta \quad \text{for the Westgate Bridge} \qquad (10\text{-}1)$$

$$\sigma = 9.9 \times 10^3 \Delta \quad \text{for the Winfield Bridge} \qquad (10\text{-}2)$$

$$\sigma = 8.3 \times 10^3 \Delta \quad \text{for the Hump Yard Bridge} \qquad (10\text{-}3)$$

$$\sigma = 7.5 \times 10^3 \Delta \quad \text{for the Tuttle Creek Bridge} \qquad (10\text{-}4)$$

where σ is in ksi and Δ is in inches

The equations are generated based on linear regression of the data plotted in Figures 10-1 to 10-4 at 95% confidence level. It is noticed that the σ - Δ equation of the Westgate Bridge (Equation 10-1) has a much higher slope than those of the other three bridges, which is most possibly caused by the different modeling procedure used for this bridge. The global structural response of the other three bridges were investigated using 3-D finite element coarse models, while that of the Westgate Bridge was analyzed using 2-D stick frame models. Another factor

could be the web gap length. As indicated by Fisher's σ - Δ expression (Equation 6-3), the web gap stress is proportional to the web thickness and the out-of-plane displacement, but inversely proportional to the square of the web gap length. So the web gap length has the most important effect on the slope of the σ - Δ correlation. For example, reducing the web gap length by half would result in an increase of the slope by a factor of 4. As indicated in Table 10-2, the web gap length modeled in the Westgate Bridge is the shortest ($^{11}/_{16}$ in.) and that modeled in the Tuttle Creek Bridge is the longest (1½ in.), the stress-displacement slopes of these two bridges are consequently the highest and the lowest.

Equations 10-1 to 10-4 are generated based on specific case studies. For cautious use of these equations, before additional studies are carried out, they should be limited only to the respective bridges for prediction of secondary stresses.

Table 10-2 also summarizes the adjustment factor α suggested for Fisher's σ - Δ expression (Equation 6-3), based on the analytical results presented in Chapters 6 to 9. This factor is calculated based on the maximum web gap stress and the corresponding out-of-plane displacement obtained from ANSYS solution for each of the connection under investigation. It is believed that more reasonable results can be obtained when this adjustment factor is introduced to Fisher's σ - Δ expression. Equation 6-3 is thus modified as follows:

$$\sigma = \alpha \frac{3 E \Delta t_w}{L^2} \qquad (10\text{-}5)$$

When the web gap thickness (t_w) and length (L) are input, Equation 10-5 yields stresses very close to those obtained from Equations 10-1 to 10-4 for the same connection under consideration. Again, since the α factors are generated based on individual case studies, the use

of Equation 10-5 should also be limited to the connections of the corresponding bridges and to those of the bridges with similar structures.

TABLE 10.2: Out-of-Plane Stress-Displacement Correlation

Bridge Name	**Superstructure Type**	**Web Gap Stress-Displacement Correlation σ (ksi), Δ (in.)**	**Adjustment Factor α for Fisher's $\sigma - \Delta$ Formula** $\alpha = \sigma_{y, ANSYS} / \sigma_{y, Fisher}$
Westgate Bridge	-two-girder floor-truss bridge -web gap length 11/16 inch, thickness 3/8 inch	$\sigma = 17.8 \times 10^3 \Delta$ (Equation 10-1)	0.26
Winfield Bridge	-skewed four-girder bridge with staggered diaphragms -web gap length 1inch, thickness 5/16 inch	$\sigma = 9.9 \times 10^3 \Delta$ (Equation 10-2)	0.38
Hump Yard Bridge	-skewed multi-girder bridge with intermittent cross-frames -web gap length 1 inch, thickness 3/8 inch	$\sigma = 8.3 \times 10^3 \Delta$ (Equation 10-3)	0.35
Tuttle Creek Bridge	-two girder cross-frame bridge -web gap length 1 ½ inch, thickness ½ inch or 3/8 inch	$\sigma = 4.5 \times 10^3 \Delta$ (Equation 10-4)	0.61

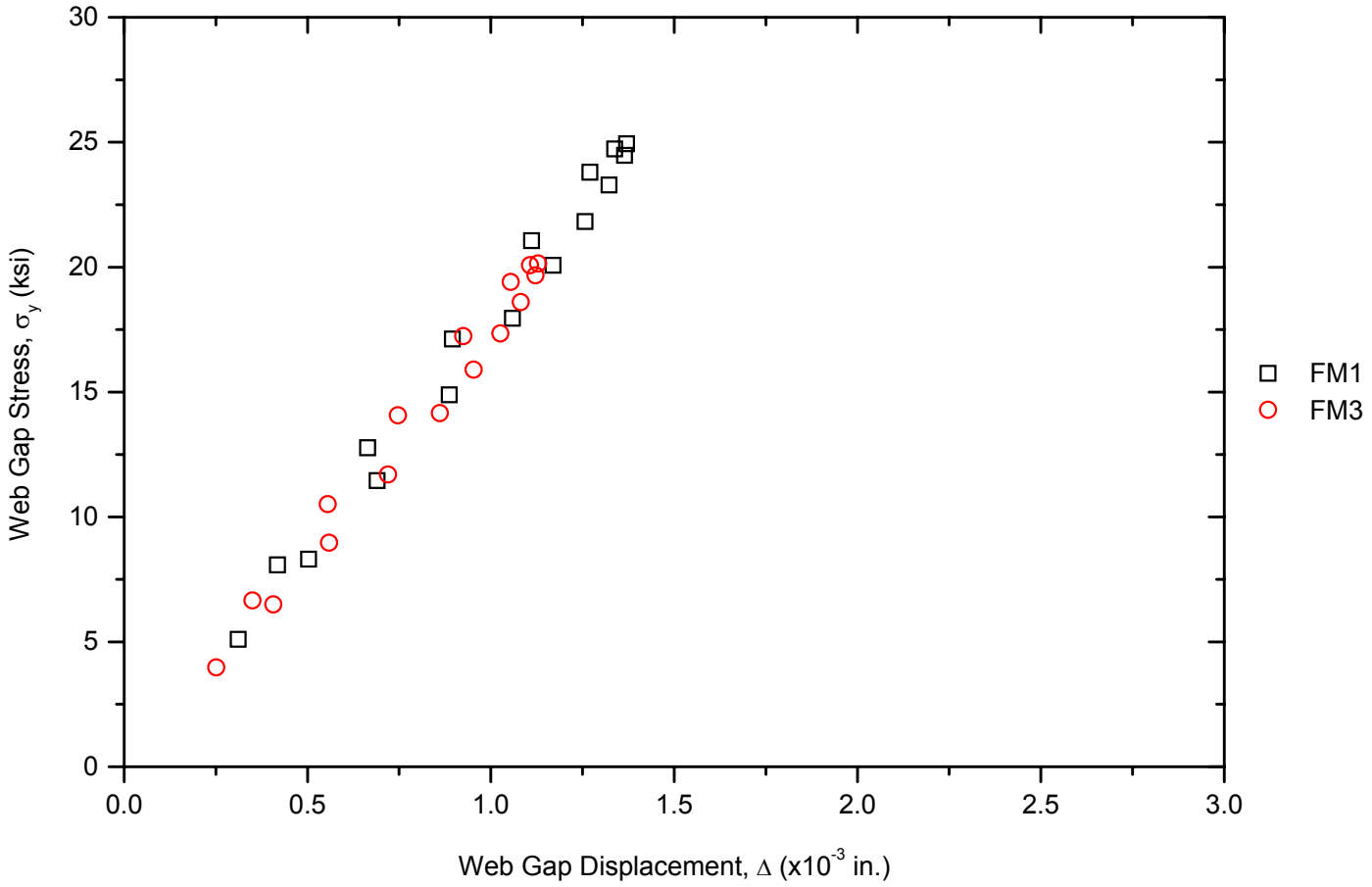

FIGURE 10-1: The Westgate Bridge Web Gap Stress-Displacement Relationship

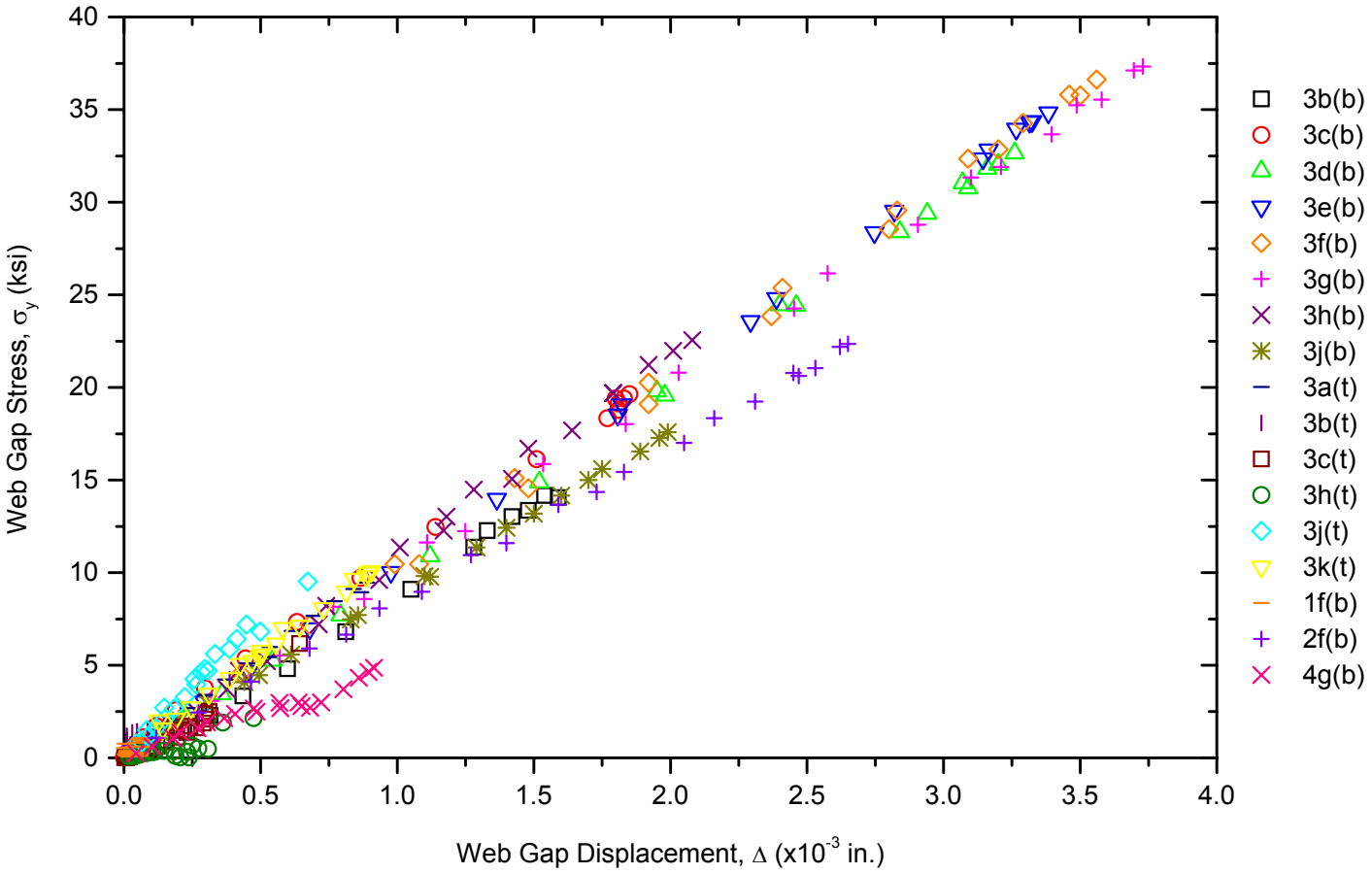

FIGURE 10-2: The Winfield Bridge Web Gap Stress-Displacement Relationship

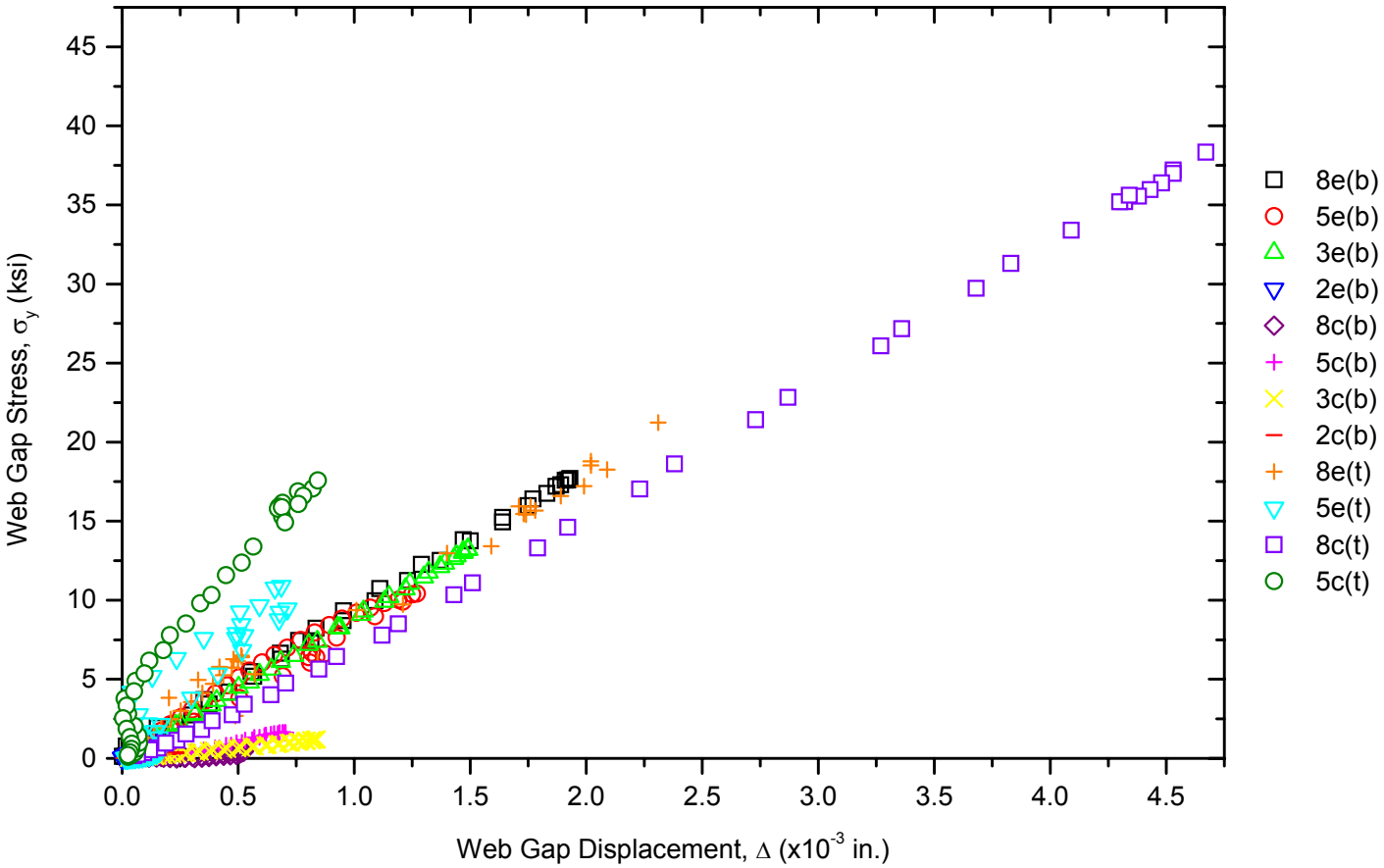

FIGURE 10-3: The Hump Yard Bridge Web Gap Stress-Displacement Relationship

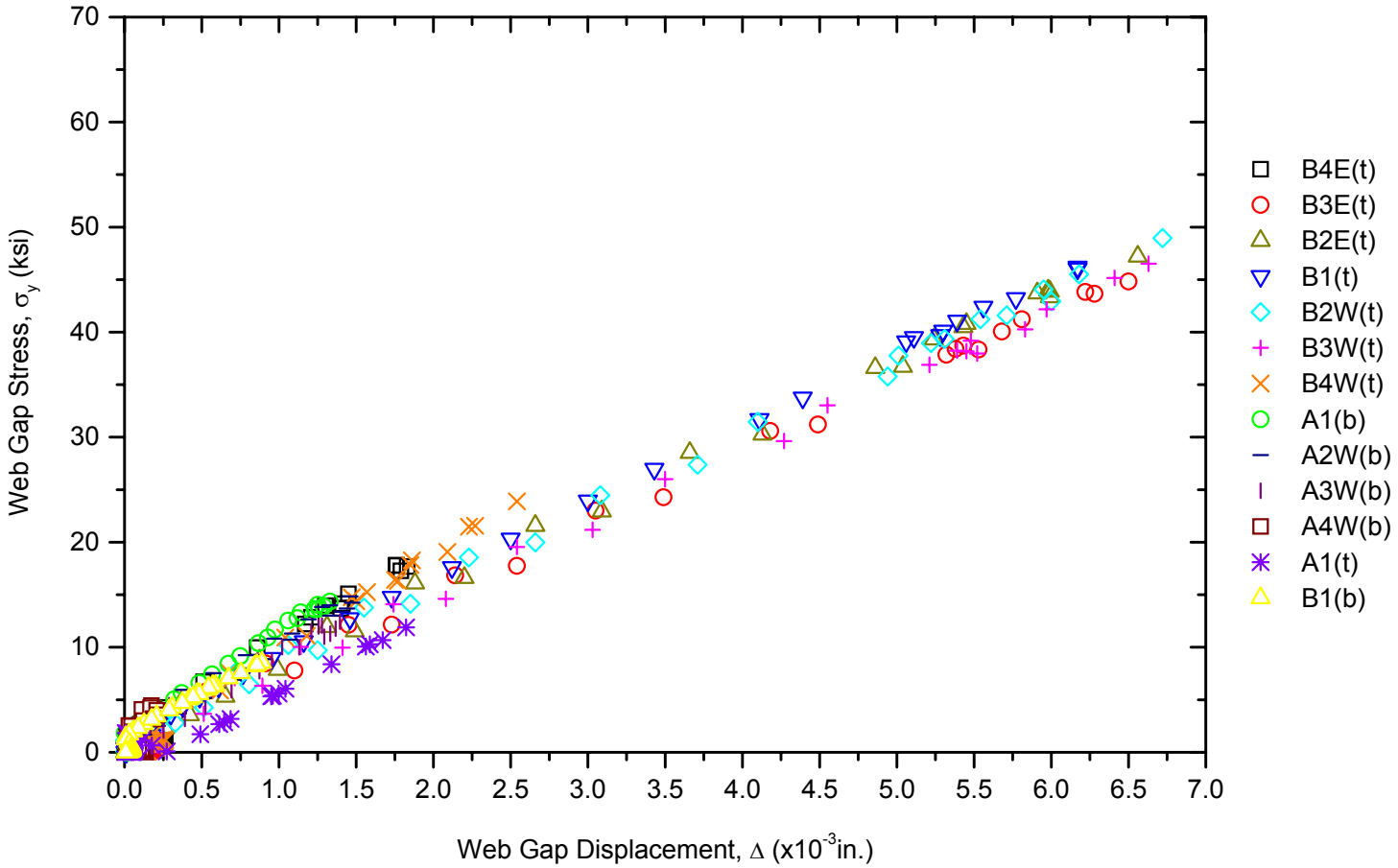

FIGURE 10-4: The Tuttle Creek Bridge Web Gap Stress-Displacement Relationship

10.3 Conclusions and Recommendations

Steel bridge fatigue is addressed in this research through effective finite element analyses of five KDOT bridges with different structure types and cracking scenarios. Results obtained from the case studies verified crack severity observed in the field and provided suggestions to future retrofit. The broader goals of this research program are to develop applicable finite element procedures for the analysis of bridge fatigue, especially in the aspects of stress prediction and repair recommendation, and to extend the same analytical procedures to the study of other bridges as an alternative to experimental testing.

Findings obtained from this research support the following conclusions:

- The finite element modeling procedures used in this study provide an approach for mathematic determination of secondary stresses developed in the existing steel bridges due to out-of-plane distortion. For all five bridges under investigation, the details that experienced fatigue cracking were found subjected to stress ranges much higher than the fatigue limit. Other potential crack initiation sites were also examined and those critical details were identified. It is recommended that this procedure be included in the future update of AASHTO *Guide Specifications for Fatigue Evaluation of Existing Steel Bridges* as a method for evaluation of distortion-induced fatigue.
- Distortion-induced stresses are highly localized in the vicinity of crack initiation sites. For details subjected to web gap cracking, the area affected by stress concentration is only within 5 in. on each side of the stiffener centerline. Stresses outside this 10 in. zone are close to zero. High stress magnitude and gradient were observed on each side of the web within the small gap length. The maximum web gap stresses were found close to or above yielding with corresponding displacements of only thousandths of an inch. Both the distortion-induced stresses and displacements obtained in this research through computational analysis

agree well with the strain gauge measurements of other experimental studies.

- For each of the four bridges with details prone to web gap cracking, a linear out-of-plane stress-displacement relationship was established based on the regression analysis of the results obtained from finite element analysis. These equations can be used as hands-on tools for estimate of web gap stresses or displacements, as most bridge engineers do not have expertise in finite element implementation. However, before further studies are carried out and more data are obtained, it is recommended that these equations be used only for the corresponding bridges.
- To effectively use Fisher's stress-displacement formula for web gap stress prediction, it is recommended that an adjustment factor less than 1.0 be applied. This factor is found between 0.26 and 0.61 for the four KDOT bridges that experienced web gap cracking.
- Different repair methods were evaluated during the case studies for the purposes of eliminating crack initiation site, reducing stress variation magnitude, and extending bridges' service life. The stiffening repair methods were found more effective in stress reduction than the softening repair methods, so rigid attachment between connection plate and girder flange was recommended for the repair of the four bridges subjected to web gap cracking. The details are expected to have an infinite fatigue life after the retrofit is carried out. However, the stiffening repair was not practical to the Arkansas River Bridge due to constraints of field implementation. A softening repair was thus used by cutting the connection plate short to relieve the stress concentration and rewelding the connection plate to restore the cracked section. This repair was found able to provide a minimum remaining service life of 15 years.
- The common strategy used in fatigue repair, especially for bridges with a small number of crack occurrence, is to apply the retrofit only to those details that have developed cracks. This is, in part, to avoid the expensive effort to repair all crack-prone details, and also in some circumstances,

due to the lack of knowledge to recognize the critical details. It is recommended that for bridges with unusual cracking conditions, analytical studies be requested to help determine the locations that need urgent repair and to provide guidance for future field test or retrofit implementations.

10.4 Future Work

Field testing is recommended for future research to investigate the fatigue stress variation under actual traffic loading and to verify the accuracy of the finite element results. The test results in turn can help calibrate and modify the finite element models during future finite element studies. In addition, fatigue and fracture behavior of metals and welds are fundamentally experimental studies. The finite element methods approach used in this research allows the study of steel bridge fatigue performance solely from the perspective of stress variation. Other issues such as weld defects, residual stresses, heat affected zones, and material toughness could also affect the crack development in the bridge connections, but these factors are usually difficult to manipulate in finite element models. It is thus recommended that core samples be collected from the crack details during future research for fractographic examination, in order to study the material properties, crack formation and propagation characteristics, and to gain a comprehensive understanding of the detail performance due to fatigue cracking.

10.5 Implementation Plan

This study is performed to address specific KDOT concerns regarding fatigue cracking and corresponding repair methods in welded steel bridges. For the five KDOT bridges investigated in this research, the retrofit analyses and recommended solutions are presented in Section 5.5 for the Arkansas River Bridge, Sections 6.4.2 and 6.5.2 for the Westgate Bridge, Section 7.4 for the Winfield Bridge, Section 8.4 for the Hump Yard Bridge, and Section 9.5 for the Tuttle Creek

Bridge. These sections provide necessary information and a sound approach for prescription of future repair procedures. Additional field testing is also recommended before the actual implementation is carried out so that the repair plans can be adjusted according to the field conditions.

REFERENCES

AASHTO Guide Specifications, 1990

Guide Specifications for Fatigue Evaluation of Existing Steel Bridges. American Association of State Highway and Transportation Officials, Washington, D.C.

AASHTO LRFD, 1998

LRFD Bridge Design Specifications, 2nd edition. American Association of State Highway and Transportation Officials, Washington, D.C.

AASHTO Standard Specifications, 1996

Standard Specifications for Highway Bridges, 16th edition. American Association of State Highway and Transportation Officials, Washington, D.C.

Aktan et al., 1994

A. E. Aktan, C. Chuntavan, K. L. Lee, and D. N. Farhey. Nondestructive Testing and Identification for Bridge Rating, Phase 2: Steel-Stringer Bridges. Report No. FHWA/OH-95/021, Cincinnati Infrastructure Institute, University of Cincinnati, Cincinnati, Ohio.

ANSYS Release 5.6, 2000

ANSYS, Inc., Canonsburg, Pennsylvania.

Barsom & Rolfe, 1999

John M. Barsom and Stanley T. Rolfe. Fracture and Fatigue Control in Structures: Applications of Fracture Mechanics, 3rd edition. ASTM, West Conshohocken, Pennsylvania.

Bassetti et al., 2000

Andrea Bassetti, Alain Nussbaumer, and Manfred A. Hirt. "Crack Repair and Fatigue Life Extension of Riveted Bridge Members Using Composite Materials", Proceedings of Bridge Engineering Conference, ESE-IABSE-FIB, March 2000, Sharm El Sheikh, Egypt, Vol. 1, pp. 227-238.

Cannon et al., 1986

D. F. Cannon, J. Sinclair, and K. A. Sharpe. "Improving the Fatigue Performance of Bolt Holes in Railway Rails by Cold Expansion", Fatigue Life: Analysis and Prediction, pp.353-369. American Society for Metals.

Cousins et al., 1998

T. E. Cousins, J. M. Stallings, D. A. Lower, and T. E. Stafford. "Field Evaluation of Fatigue Cracking in Diaphragm-Girder Connections", Journal of Performance of Constructed Facilities, Vol. 12, No. 1, pp. 25-32. ASCE, Reston, Virginia.

Cousins & Stallings, 1998

T. E. Cousins and J. M. Stallings. "Laboratory Tests of Bolted Diaphragm-Girder Connections", Journal of Bridge Engineering, Vol. 3, No. 2, pp. 56-63. ASCE, Reston, Virginia.

D'Andrea et al., 2001
Mark D'Andrea, Gilbert Y. Grondin, and Geoffrey L. Kulak. Behavior and Rehabilitation of Distortion-Induced Fatigue Cracks in Bridge Girders. Structural Engineering Report No. 240, Department of Civil & Environmental Engineering, University of Alberta. Edmonton, Alberta, Canada.

Dexter & Fisher, 1996
Robert J. Dexter and John W. Fisher. Memo to the State Bridge Engineer of Minnesota DOT. Center for Advanced Technology for Large Structural Systems, Lehigh University, Bethlehem, Pennsylvania.

Dexter & Fisher, 2000
Robert J. Dexter and John W. Fisher. "Fatigue and Fracture", Bridge Engineering Handbook, edited by Wai-Fah Chen and Lian Duan, CRC Press, Boca Raton, Florida.

Dowling, 1999
Norman E. Dowling. Mechanical Behavior of Materials: Engineering Methods for Deformation, Fracture, and Fatigue, 2nd edition. Prentice Hall, Upper Saddle River, New Jersey.

Microsoft Excel 2000
Microsoft Corporation.

Fisher, 1984
John W. Fisher. Fatigue and Fracture in Steel Bridges: Case Studies. John Wiley & Sons, New York.

Fisher et al., 1987
John W. Fisher, Ben T. Yen, and David C. Wagner. "Review of Field Measurements for Distortion-Induced Fatigue Cracking in Steel Bridges", Transportation Research Record 1118, pp. 49-55. Transportation Research Board, National Research Council, Washington, D.C.

Fisher & Menzemer, 1990
John W. Fisher and Craig C. Menzemer. "Fatigue Cracking in Welded Steel Bridges", Transportation Research Record 1282, pp. 111-117. Transportation Research Board, National Research Council, Washington, D.C.

Fisher, 1997
John W. Fisher. "Evolution of Fatigue-Resistant Steel Bridges". Transportation Research Record 1594, pp. 5-17. Transportation Research Board, National Research Council, Washington, D.C.

Fisher, 1998
John W. Fisher, Geoffrey L. Kulak, and Ian F. C. Smith. A Fatigue Primer for Structural Engineers. National Steel Bridge Alliance.

Fisher et al., 2001

John W. Fisher, Efim Statnikov, and Lionel Tehini. "Fatigue Strength Enhancement by Means of Weld Design Change and the Application of Ultrasonic Impact Treatment". http://www.appliedultrasonics.com/pdf/pdf4.pdf.

Haagensen et al., 1998

P. J. Haagensen, E. S. Statnikov, and L. Lopez-Martinez. "Introductory Fatigue Tests on Welded Joints in High Strength Steel and Aluminum Improved by Carious Methods Including Ultrasonic Impact Treatment (UIT)", International Institute of Welding, IIW Doc. XIII-1748-98.

KDOT Design Manual, 2001

Kansas Department of Transportation Design Manual, Volume III, Bridge Section. Topeka, Kansas.

Keating et al., 1996

Peter B. Keating, Scott D. Wilson, and Terry L. Kohutek. Evaluation of Repair Procedures for Web Gap Fatigue Damage. Report No. FHWA/TX-97/1360-1, Texas Department of Transportation, Austin, Texas.

Koob et al., 1985

Michael J. Koob, Phillip D. Frey, and John M. Hanson. Evaluation of Web Cracking at Floor Beam to Stiffener Connections of the Poplar Street Bridge Approaches, FAI Route 70, East St. Louis, St. Clair County, Illinois. Wiss, Janney, Elstner Associates, Inc. Northbrook, Illinois.

Lai, 1996

Leon L-Y Lai. "Fatigue Cracks at Stringer-Floorbeam Connections", Building an International Community of Structural Engineers: Proceedings of Structures Congress XIV, Chicago, Illinois, April 15-18, 1996, Vol. 1, pp. 483-490. ASCE.

Miller, 1997

Duane K. Miller. "Consider Overall Structural Performance When Specifying Fatigue Details", Modern Steel Construction, March 1997, Vol. 37 no. 3, pp. 61. The American Institute of Steel Construction, Inc., (AISC), Chicago, Illinois.

NCHRP 227, 1980

J. W. Fisher, B. M. Barthelemy, D. R. Mertz, and J. A. Edinger. National Cooperative Highway Research Program Report 227: Fatigue Behavior of Full-Scale Welded Bridge Attachments. Transportation Research Board, National Research Council, Washington, D.C.

NCHRP 299, 1987

F. Moses, C. G. Schilling and K. S. Raju. National Cooperative Highway Research Program Report 299: Fatigue Evaluation Procedures for Steel Bridges. Transportation Research Board, National Research Council, Washington, D.C.

NCHRP 321, 1989

E. N. Gregory, G. Slate, and C. C. Woodley. National Cooperative Highway Research Program Report 321: Welded Repair of Cracks in Steel Bridge Members. Transportation Research Board, National Research Council, Washington, D.C.

NCHRP 336, 1990

John W. Fisher, Jian Jin, David C. Wagner, and Ben T. Yen. National Cooperative Highway Research Program Report 336: Distortion-Induced Fatigue Cracking in Steel Bridges. Transportation Research Board, National Research Council, Washington, D.C.

NCHRP 354, 1993

J. W. Fisher, A. Nussbaumer, P. B. Keating, and B. T. Yen. National Cooperative Highway Research Program Report 336: Resistance of Welded Details under Variable Amplitude Long-Life Fatigue Loading. Transportation Research Board, National Research Council, Washington, D.C.

Roddis, 1988

W. M. Kim Roddis. Heuristic, Qualitative, and Quantitative Reasoning about Steel Bridge Fatigue and Fracture. Ph.D. dissertation. Department of Civil Engineering, Massachusetts Institute of Technology, Cambridge, Massachusetts.

Ross et al., 1994

Timothy Ross, Harold Sorensen, Sunil Donald, Scott Pringle, Kelly Riddick, and Rebecca Thompson. Investigation of Intermediate Diaphragm Loads on Steel Bridges. Report No. FHWA-HPR-NM-91-02. New Mexico State Highway and Transportation Department, Santa Fe, New Mexico.

Small & Cooper, 1998

Edgar P. Small and James Cooper. "Condition of the Nation's Highway Bridges: A Look at the Past, Present, and Future". TR News, January-February 1998. No. 194. Transportation Research Board, National Research Council, Washington, D.C.

STAAD/Pro Release 3.1, 1999

Research Engineers, Inc., Yorba Linda, California, 1999.

Stallings et al., 1993

J. Michael Stallings, Thomas E. Cousins, and Scott K. Rutland. Evaluation of Fatigue Cracking in I-65 Mobile Delta Crossing Bridges, Volume III: Floortruss-Girder Connections. Highway Research Center, Harbert Engineering Center, Auburn University, Alabama.

Stallings et al., 1996

J. M. Stallings, T. E. Cousins, and T. E. Stafford. "Effects of Removing Diaphragms from Steel Girder Bridge", Transportation Research Record 1541, pp. 183-188. Transportation Research Board, National Research Council, Washington, D.C.

Stallings et al., 1999

J. M. Stallings, T. E. Cousins, and T. E. Stafford. "Removal of Diaphragms from Three-Span Steel Girder Bridge", Journal of Bridge Engineering, Vol. 4, No. 1, pp. 63. ASCE, Reston, Virginia.

Stallings, 2001

J. M. Stallings. "Maintenance of Diaphragm-Girder Connections", 2001 Structures Congress, May 21-23, 2001, Washington, D.C., CD-ROM, ASCE.

Statnikov, 1997

Efim Statnikov. "Applications of Operational Ultrasonic Impact Treatment (UIT) Technologies in Production of Welded Joints", International Institute of Welding, IIW Doc. XIII-1667-97.

Tada et al., 2000

Hiroshi Tada, Paul C. Paris, and George R. Irwin. The Stress Analysis of Cracks Handbook, 3rd edition. ASME, New York.

Takamori & Fisher, 2000

Hiroyuki Takamori and John W. Fisher. "Tests of Large Girders Treated to Enhance Fatigue Strength", Transportation Research Record 1696, pp. 93-99. Transportation Research Board, National Research Council, Washington, D.C.

Tedesco et al., 1995

J. W. Tedesco, J. M. Stallings, and D. R. Tow. "Finite Element Method Analysis of Bridge Girder-Diaphragm Interaction", Computers & Structures, Vol. 56, No. 2/3, pp. 461-473. Elsevier Science Ltd., Oxford, England.

Uppal et al., 2002

A. Shakoor Uppal, Dio Yoshino, and Lionel Tehini. "Ultrasonic Impact Treatment of Vertical Stiffener Welds at FAST Bridge", Technology Digest, Transportation Technology Center, Inc.

Welsch, 1990

Winfried H. Welsch. "A Concept for Preventing Repeated Weld Repairs of Bridge Structures", Extending the Life of Bridges, pp. 44-52. ASTM, Philadelphia, Pennsylvania.

Walker et al., 1992

W. H. Walker, M. D. Holbrook, and P. A. Cassity. Three Case Histories of Cracking Problems Associated with Steel Bridge Floor Beams. University of Illinois at Urbana-Champaign, Department of Civil Engineering, Urbana, Illinois.

Wipf et al., 1998

T. J. Wipf, L. F. Greimann, A. H. Khalil, and D. Wood. Preventing Cracking at Diaphragm/Plate Girder Connections in Steel Bridges. Iowa State University, Ames, Iowa.

Wright, 1996

William Wright. Post-Weld Treatment of a Welded Bridge Girder by Ultrasonic Impact Treatment. Federal Highway Administration, Turner-Fairbank Highway Research Center, McLean, Virginia.

Zwerneman et al., 1993

Farrel J. Zwerneman, Adam B. West, and Kee S. Lim. "Fatigue Damage to Steel Bridge Diaphragms", Journal of Performance of Constructed Facilities, Vol. 7, No. 4, pp. 207-224. ASCE, Reston, Virginia.